Numerical Simulations of Large River Plumes in the Pacific Northwest

Ryan Wesley Kilgren
B.S., Environmental Engineering, Michigan Technological University, 2003

A thesis presented to the faculty of the
OGI School of Science & Engineering
at Oregon Health & Science University
in partial fulfillment of the requirements
for the degree
Master of Science
in
Environmental Science and Engineering

October 2006

The thesis “Numerical Simulations of Large River Plumes in the Pacific Northwest” by Ryan Wesley Kilgren has been examined and approved by the following Examination Committee:

António M. Baptista, Ph.D., Thesis Advisor
Professor
OGI School of Science & Engineering, OHSU

Yinglong Zhang, Ph.D.
Research Scientist
OGI School of Science & Engineering, OHSU

Michael G. G. Foreman, Ph.D.
Research Scientist
Institute of Ocean Sciences, Fisheries and Oceans, Canada

DEDICATION

To my family: Wendy, Steven, Meg, Brett, Nicholas, and Ruby.

ACKNOWLEDGEMENTS

I would like to extend a special thank you to my advisor António Baptista for his direction and guidance in this research. Additionally, I would like to thank my thesis committee members for participating in this process with me; it has been rewarding.

The unwavering support of family and friends has given me encouragement for each challenge and they have also provided much appreciated reprieve. Thank you to several people for proofreading portions of this document, including my advisor and thesis committee, Bill Johnston, Meg Koenemann, Carri Marschner, and Wendy, Steven, John, and Nicholas Kilgren.

The National Science Foundation (ACI-0121475; OCE-0424602) and National Oceanic and Atmospheric Administration (AB133F-04-CN-0033) provided financial support for this research. Any statements, opinions, findings, conclusions or recommendations expressed in this material are those of the authors and do not necessarily reflect the views or policies of the federal sponsors, and no official endorsement should be inferred.

TABLE OF CONTENTS

LIST OF TABLES

LIST OF FIGURES

ABSTRACT

Numerical Simulations of Large River Plumes in the Pacific Northwest

Ryan Wesley Kilgren, B.S.

M.S., OGI School of Science & Engineering
at Oregon Health & Science University
October 2006

Supervising Professor: Dr. António M. Baptista

Estuarine and coastal waters present complex physical systems, which support unique habitats, areas of high population density and growth, and large economic sectors (e.g. shipping, fishing, and tourism). Understanding the physical nature of these systems, including the circulation and transport, is necessary to guide management decisions which balance habitat, economic development, and urbanization. Numerical models present a means to simulate these systems under a wide array of realistic scenarios in an effort to fill knowledge gaps that may be cost prohibitive or impossible to fill via observations alone. Therefore, it is important that decisions inherent to model operation and the resulting outcome be properly assessed to ensure that the highest quality model results are available for managing agencies.

This thesis presents modeling studies of two large river plume systems in the Pacific Northwest and southern British Columbia: the Columbia River and the Fraser River. Choices of the algorithm used to solve for the advection of salt and heat are investigated for each of these systems, while the choice of wind forcing is included for the Fraser River experiments. Assessment of the results for each experiment is provided in the context of retrospective observations. The modeling framework of a coastal

margin observatory, CORIE [1, 5, and 6], developed with the study of the Columbia River in mind and the most current code, SELFE [7], used within this framework are utilized in these experiments and adapted from the Columbia River application to that of the Fraser River. Within SELFE, solution of the transport equations with an Upwind Method (UWM) is clearly shown to produce better plume salinities than an equivalent solution with an Eulerian-Lagrangian Method (ELM).

CHAPTER 1

INTRODUCTION

1.1 Context

Numerical models may be applied to estuaries, river plumes, and near coastal waters to better understand transport and circulation processes. Environmental observation and forecasting systems [1] present a framework for using numerical models in the context of measured data (e.g. the Gulf of Maine Ocean Observing System or GoMOOS [2, 3], the Mediterranean Forecasting System: Toward Environmental Predictions or MFSTEP [4], and a coastal margin observatory for the Columbia River or CORIE [1, 5, 6]). However, an environmental observation and forecasting system is not necessary for using numerical models to simulate these waters. Ultimately, the improved understanding gained by use of models and observations may be used to direct management and policy decisions regarding the future use of river and coastal water bodies. For these purposes, it is critical that the influence of model inputs and solution methods are carefully evaluated to ensure a meaningful result.

1.2 Objective

Finely tuned models are able to produce representations of circulation features being studied. The objective of this thesis is to better understand model decisions through the influence each choice has on the model results. The choice of the advection algorithm is investigated for modeling the Columbia River and Fraser River plumes. Additionally, the choice of wind input is tested for simulating the Fraser River plume. In both cases, the new hydrodynamic model SELFE [7] is used and comparisons are made with observed data and between each experiment variation. An increased knowledge of the influence of these modeling decisions on the model results will provide a method to improve the simulation of these river-plume systems.

1.3 Background

Estuarine and coastal waters have physical, biological, and economic resources that are unique to each particular area. Physical processes associated with these waters lead to conditions that are utilized by various trophic levels. The increased tidal ranges of most estuaries allow for pumping of saltier water in and fresher water out; causing a constant mixing and alteration of environmental conditions. During tidal ebbs, large tidal flats can be exposed, while shallower waters are more easily warmed. River inputs provide not only a source of freshwater, but also nutrients and sediments. Nutrients are used by lower trophic level organisms, while turbidity from sediment in the water column creates shelter from predators.

These waters are a rich economic resource for a variety of activities, including both commercial (e.g. shipping, fishing, municipal and industrial outfall, and real estate development) and recreational (e.g. boating and swimming). Over 50% (153 million persons) of the US population lives in areas near coastal waters, which comprise only 17% of total US land area, and an increase of 7 million is estimated by 2008 [8]. This high population density stems from the vast availability of economic opportunities in these areas. Among US states, California and Washington have experienced the first and fourth highest population growth, respectively, from 1980-2003, indicating the large amount of growth along the west coast. Projected growth for the US west coast, including Alaska and Hawaii, is large, with a population increase of 2.2 million predicted by 2008 [8].

A proper balance between economic and environmental resources is imperative for sustaining viability of estuarine and coastal waters. Managing agencies require an ever-increasing level of scientific understanding of the transport and circulation within these waters in order to assist in the decisions affecting the development of this balance. It is in that spirit that a coastal margin observatory and forecasting system for the Columbia River (CORIE [1]), was developed and continues to operate.

The CORIE framework combines observation and modeling systems in an effort to increase the ability to predict the physical properties of the Columbia River, its estuary and freshwater plume, and nearby coastal waters. Observations are made continuously with a network of instruments at several fixed locations within the Columbia River estuary and at two additional moorings located offshore and to the south of the river's mouth. The variables measured include salinity, temperature, velocity and elevation. These measurements are provided publicly through the CORIE website in a real time fashion, as well as in a reanalysis mode which includes quality assessments. The other common method for measuring these parameters (except for water elevations) is by scientific cruises. Cruises, by nature, are limited by financial resources and both ship and crew availability. Therefore, cruises generally utilize only a few vessels operating for a short time period, usually from April-October. Cruises typically capture point, profile, and flow-through measurements at locations which are either fixed or quasi-random in their selection. While the data collected using this method is valuable, it inhibits the ability to understand these physical parameters for the whole domain and for time periods outside of the sampling periods. The CORIE sampling strategy presents a means to monitor conditions and changes in conditions of the Columbia River beyond the usual spatial and temporal constraints of cruises.

Scarcity of observations provides motivation for the use of models to understand the system for the less sampled locations and time periods. The modeling half of the CORIE framework is designed to meet these needs. It is driven by the numerical codes ELCIRC [5, 9] and, more recently, SELFE [7]. These codes were developed for simulating estuarine, plume, and coastal processes, which occur over scales varying from less than 1 meter to several kilometers. Each of these codes is used to generate daily forecasts for the Columbia River estuary/plume and also to create databases of longer term historical simulations (1999-2005). The retrospective databases rely on numerous calibration experiments to adjust the many model parameters, such as bottom drag coefficients and surface mixing lengths.

In the modeling process [10], the preliminary application of a model to a given problem is followed by calibration and subsequent confirmation or validation. The work presented in this thesis is comprised of two experiments. The first presents a further calibration of two recent CORIE databases with data collected during the most extensive winter field survey of the Columbia River plume [11]. The second experiment extends the CORIE modeling framework to the Fraser River as the preliminary application of the modeling process. The Fraser River is the second largest estuarine system in the Pacific Northwest and southern British Columbia. The SELFE code is used for both experiments, and in both cases the use of two different advection algorithms for the transport of salt and heat, Eulerian-Lagrangian (Section 1.4.2) and Upwind (Section 1.4.3), is investigated. Additionally, the Fraser River experiment investigates the choice of wind forcing (Section 1.5) on the influence of the Fraser River plume, using three different weather models for wind inputs and a reference case without wind.

The Columbia River and the Fraser River systems, are linked through seasonal interactions of their buoyant plumes with the coastal waters near the entrance to Juan de Fuca Strait [12-14]. Recent studies [15-17] suggest that this interaction may occur at higher frequencies than the seasonal perspective indicates. Both are large sources of freshwater, nutrients, and sediment to the Pacific Northwest and southern British Columbia coastal waters, draining watersheds of 673,000km^2 for the Columbia River and 230,000km^2 for the Fraser River (Figure 1.1, p. 12). The regional economy depends heavily on these systems, which directly affect the commercial shipping and fishing of Oregon, Washington, and British Columbia.

1.4 Numerical model

1.4.1 General model description

The SELFE model [7] solves forms of the continuity equation (equation 1.1), free surface equation (equation 1.2), Navier Stokes equations (equation 1.3), transport equations for salinity (equation 1.4) and temperature (equation 1.5), and turbulence closure, for the free surface elevation (η), velocity (u, v, w), salinity (S) and temperature (T) fields within the defined spatial/temporal domain. Turbulence closure is used to compute viscosities within the Navier Stokes equations and diffusivities within the transport equations. The conservation of momentum (equation 1.3) includes the advection and diffusion of momentum and the additional terms (**f**) are each identified by the letters (a-e) on the lower brace, for the Coriolis (a), potential acceleration of the free surface (b), tidal potential (c), atmospheric pressure (d), and density differences, or baroclinic differences (e).

$$\nabla\cdot\mathbf{u}+\frac{\partial w}{\partial z}=0 \qquad (1.1)$$

$$\frac{\partial\eta}{\partial t}+\nabla\cdot\int_{-h}^{\eta}\mathbf{u}\,dz=0 \qquad (1.2)$$

$$\frac{D\mathbf{u}}{Dt}=\nabla\cdot(\mu\nabla\mathbf{u})+\frac{\partial}{\partial z}\left(\nu\frac{\partial\mathbf{u}}{\partial z}\right)+\mathbf{f}$$

$$\mathbf{f}=-\underbrace{fk\times u}_{a}-\underbrace{g\nabla\eta}_{b}+\underbrace{\alpha g\nabla\hat{\psi}}_{c}-\underbrace{\frac{1}{\rho_o}\nabla p_A}_{d}-\underbrace{\frac{g}{\rho_o}\int_{z}^{\eta}\nabla\rho\,d\zeta}_{e},\ u=u,v \qquad (1.3)$$

$$\frac{DS}{Dt}=\frac{\partial}{\partial z}\left(\kappa\frac{\partial S}{\partial z}\right)+F_S \qquad (1.4)$$

$$\frac{DT}{Dt}=\frac{\partial}{\partial z}\left(\kappa\frac{\partial T}{\partial z}\right)+\frac{\dot{Q}}{\rho_0 C_p}+F_h \qquad (1.5)$$

The spatial domain is discretized in an unstructured fashion, using triangles in the horizontal direction, allowing for simulation of processes at varying scales and focus of higher grid resolution within regions of interest. Also, unstructured triangles conform better to complex boundaries than structured grids. The vertical domain uses a mixed coordinate system of both S-coordinates and Z-coordinates. S-coordinates are terrain following [18] and provide a method to more accurately represent processes occurring in the surface and bottom layers of the water column. Z-coordinates are assigned at level surface depths and offer a means to provide consistent resolution of the water column over regions of rapidly changing bathymetry. In a typical application of SELFE for simulating a river plume, it is suggested by [7] that S-coordinates be used for depths most influenced by the plume. It should be noted that this hybrid vertical grid system is used to designate the level depths, but that the governing equations are solved at these depths in untransformed Z-space.

1.4.2 Eulerian-Lagrangian transport algorithm

Initial versions of SELFE employ an Eulerian-Lagrangian method (ELM) to find solutions for the transport of salt (Equation 1.4) and heat (Equation 1.5). Eulerian methods evaluate temporal derivatives of fluid flows at fixed spatial locations ($\frac{\partial C}{\partial t}$), while Lagrangian methods evaluate these derivatives along trajectory paths ($u\frac{\partial C}{\partial x}+v\frac{\partial C}{\partial y}+w\frac{\partial C}{\partial z}$). Eulerian-Lagrangian Methods (ELM) incorporate both of these techniques to deal with the material derivative ($\frac{DC}{Dt}=\frac{\partial C}{\partial t}+u\frac{\partial C}{\partial x}+v\frac{\partial C}{\partial y}+w\frac{\partial C}{\partial z}$) [19].

Within SELFE, ELM is implemented numerically by accounting for advection of salt or heat within the material derivative, similar to the application of [9]. Beginning at the grid node location at which variables are being evaluated $(x,y,z)^{n+1}$, the position of the foot of the characteristic line $(x,y,z)^{n}$ is solved for by backwards tracking (from time step t^{n+1} to t^{n}) using the method of characteristics as either a multi-step Euler or a 5th order Runge-Kutta method (Figure 1.2a, p. 13). Along the characteristic lines the values of salinity and temperature do not vary (velocities do vary along characteristic lines). The multi-step Euler tracking is used in the experiments performed for this thesis, which is related to single-step Euler (as below) using smaller time steps.

$$x^n = x^{n+1} - u^{n+1}\Delta t$$
$$y^n = y^{n+1} - v^{n+1}\Delta t$$
$$z^n = z^{n+1} - w^{n+1}\Delta t$$

After backtracking, the element within which the foot of the characteristic line is located is split into four sub-elements (Figure 1.2b, p. 13). The vertices of the sub-element within which the foot lies are used to interpolate the variable of interest to the position of the foot (Figure 1.2b, p. 13). Interpolation may be performed using either a linear or a quadratic method. For the experiments comprising this thesis, quadratic interpolation is used within river and estuarine regions, while linear interpolation is used elsewhere. Finally, the value found for the foot of the characteristic line is placed within the total derivative as the value for the prior time step (t^n), for the nodal location being evaluated (Figure 1.2c, p. 13), as

$$\frac{DS}{Dt} = \frac{S^{n+1} - S^n}{\Delta t}.$$

Also, it is important to note that within the ELM SELFE version the heat exchange module is inactive due to the non-conservative nature of the algorithm for the treatment of mass [20]. Therefore, model temperatures are not affected by inputs from solar radiation ($\dot{Q}$), but are treated as a passive tracer similar to salt.

1.4.3 Upwind transport algorithm

Recent versions of SELFE allow for a finite volume upwind method (UWM), as an alternative to the ELM, for the treatment of the advection terms of the transport equations for salt (equation 1.4) and heat (equation 1.5). The upwind scheme is a non-centered approach for solving the advective term and is generally considered better than a centered approach, since it removes the numerical dispersion associated with centered space methods and more appropriately represents the physical nature of advection [21]. The drawback of UWM is its inherent numerical diffusion, which tends to smear out gradients [20]. Essentially, the direction of the normal ($\underset{\sim}{n}$) velocity (u_n) at each face is used to determine the locations of values (of salt and heat) to use in the computation of spatial derivatives.

In SELFE, this scheme is implemented by using a finite volume method advecting heat and salinity into and out of each face of a control volume [20]. Since the horizontal grid is composed of triangles, the control volumes ($V_{i,k}^{n}$) are prisms (Figure 1.3a and indexed as i, p. 13) with three faces in the horizontal direction (Figure 1.3b with areas $\hat{P}_{j,k}$, p. 13) and two in the vertical direction (Figure 1.3c with areas $\hat{S}_{i,k}$, p. 13). Values of salinity (S), temperature (T), and addition of heat from solar radiation ($\dot{Q}$) are defined at the center of each prism (Figure 1.3a, p. 13). The normal velocity at each face is used to compute the advective flux into or out of the prism, depending on the direction of the normal velocity. The value advected is taken from the upwind prism. This method is written as (for advection of salinity)

$$\int \frac{DS}{Dt} = V_{i,k}^{n} \frac{S_{i,k}^{m+1} - S_{i,k}^{m}}{\Delta t'} + \sum_{j=1}^{3} \left(\hat{P}_{j,k} \left(u_n \right)_{j,k}^{n+1} S_{j*}^{m} \right) + \underset{\sim}{\overline{u}}_k \cdot \underset{\sim}{n}_k S_{k*}^{m+1} \hat{S}_{i,k} - \underset{\sim}{\overline{u}}_{k-1} \cdot \underset{\sim}{n}_{k-1} S_{k-1*}^{m+1} \hat{S}_{i,k-1},$$

where the superscript m designates a sub-time index with spacing $\Delta t'$. The sub-time interval is determined to ensure that multiple prism faces are not crossed during the specified amount of time (Courant number restriction). This method reduces to the continuity equation (equation 1.1) when salinity is held constant or for temperature when temperature is held constant and the flux of solar radiation is set to zero [20]. The heat exchange module within SELFE is used in the UWM version and inputs from solar radiation ($\dot{Q}$) are evaluated in the control volume.

1.5 Wind datasets

Weather model datasets present a method to apply spatially and temporally varying wind and solar radiation values as surface boundary conditions to hydrodynamic models. This serves as an alternative to imposing seasonal winds or interpolated winds from buoy or shore based measurement locations. The CORIE project systematically archives several different wind datasets, including the three used for the experiments presented in this thesis. Datasets archived include the forecast data from the Mesoscale Model 5 (MM5) run at the University of Washington and the National Weather Service ETA-12 (ETA), and the reanalysis data assimilated National Weather Service North

American Regional Reanalysis (NARR). These datasets offer varying spatial and temporal resolutions (Table 1.1, p. 13), and subsequently varying levels of quality for the Columbia River and Fraser River regions (Sections 2.4 and 3.4).

1.6 Thesis format

The remainder of this comprises three chapters. The next two chapters present methodology and results pertaining to the numerical experiments for the winter Columbia River plume (Chapter 2) and the summer Fraser River plume (Chapter 3). Finally, Chapter 4 presents a synthesis of these experiments as they relate to improving simulations and knowledge of these two systems.

1.7 References

1. Baptista, A.M., *Environmental observation and forecasting systems.*, in *Encyclopedia of Physical Science and Technology*, R.A. Meyers, Editor. New York: Academic Press, 2002. 565-581.

2. Gulf of Maine Ocean Observing System (GoMOOS), http://www.gomoos.org, [Viewed July 2006]

3. Richert, E.D., N. Pettigrew, M.K. Beard, C. Roesler, L.S. Incze, A. Thomas, J. Irish, D. Townsend, V. Pachang, and H. Xue, *A Proposal To Implement The Gulf of Maine Ocean Observing System*. 2000, Proposed to Office of Naval Research.

4. Mediterranean Forecasting System: Toward Environmental Predictions (MFSTEP), www.bo.invg.it/mfstep, [Viewed July 2006]

5. Baptista, A.M., Y.L. Zhang, A. Chawla, M. Zulauf, C. Seaton, III E.P. Myers, J. Kindle, M. Wilkin, M. Burla, and P.J. Turner, *A cross-scale model for 3D baroclinic circulation in estuary-plume-shelf systems: II. Application to the Columbia River.* Continental Shelf Research, 2005. **25**: 935-972.

6. Coastal Margin Observatory for the Columbia River (CORIE), www.ccalmr.ogi.edu/CORIE, [Viewed July 2006]

7. Zhang, Y. and A.M. Baptista, *A semi-implicit Eulerian-Lagrangian finite-element model for cross-scale ocean circulation, with hybrid vertical coordinates.* International Journal for Numerical Methods in Fluids, in-review.

8. Crossett, K.M., T.J. Culliton, P.C. Wiley, and T.R. Goodspeed, *Population Trends Along the Coastal United States: 1980-2008*. 2004, National Oceanic and Atmospheric Administration.

9. Zhang, Y., A.M. Baptista, and E. Myers, *A cross-scale model for 3D baroclinic circulation in estuary-plume-shelf systems: I. Formulation and skill assessment.* Continental Shelf Research, 2004. **24**(18): 2187-2214.

10. Chapra, S.C., *Surface water-quality modeling*. New York, N.Y.: McGraw-Hill, 1997. 317-326.

11. Hickey, B.M., L.J. Pietrafesa, D.A. Jay, and W.C. Boicourt, *The Columbia River plume study: Subtidal variability in the velocity and salinity fields.* Journal of Geophysical Research, 1998. **103**(C5): 10,339-10,368.

12. Masson, D., *Seasonal water mass analysis for the Straits of Juan de Fuca and Georgia.* Atmosphere-Ocean, 2006. **44**(1): 1-15.

13. Hickey, B.M. and N.S. Banas, *Oceanography of the U.S. Pacific Northwest Coastal Ocean and Estuaries with Application to Coastal Ecology.* Estuaries, 2003. **26**(4B): 1010-1031.

14. Barnes, C.A., A.C. Duxbury, and B.A. Morse, *Circulation and selected properties of the Columbia River effluent at sea*, in *The Columbia River Estuary and Adjacent Ocean Waters*, A.T. Pruter and D.L. Alverson, Editors. Seattle: University of Washington Press, 1972. 41-80.

15. Hickey, B., S. Geier, N. Kachel, and A. MacFadyen, *A bi-directional river plume: The Columbia in summer.* Continental Shelf Research, 2005. **25**(14): 1631-1656.

16. MacFadyen, A., B.M. Hickey, and M.G.G. Foreman, *Transport of surface waters from the Juan de Fuca eddy region to the Washington coast.* Continental Shelf Research, 2005. **25**(16): 2008-2021.

17. Thomas, A.C. and R.A. Weatherbee, *Satellite-measured temporal variability of the Columbia River plume.* Remote Sensing of Environment, 2006. **100**(2): 167-178.

18. Song, Y. and D. Haidvogel, *A semi-implicit ocean circulation model using a generalized topography-following coordinate system.* Journal of Computational Physics, 1994. **115**(1): 228-244.

19. Baptista, A.M., E.E. Adams, and K.D. Stolzenbach, *Eulerian-Lagrangian analysis of pollutant transport in shallow water, Technical Report 296*. 1984, MIT R.M. Parsons Laboratory: Cambridge, MA.

20. Zhang, Y. of Oregon Health & Science University, *Personal communication*. 2006.

21. Roache, P.J., *Computational Fluid Dynamics*. Albuquerque, NM: Hermosa Publishers, 1982.

1.8 Figures and Tables

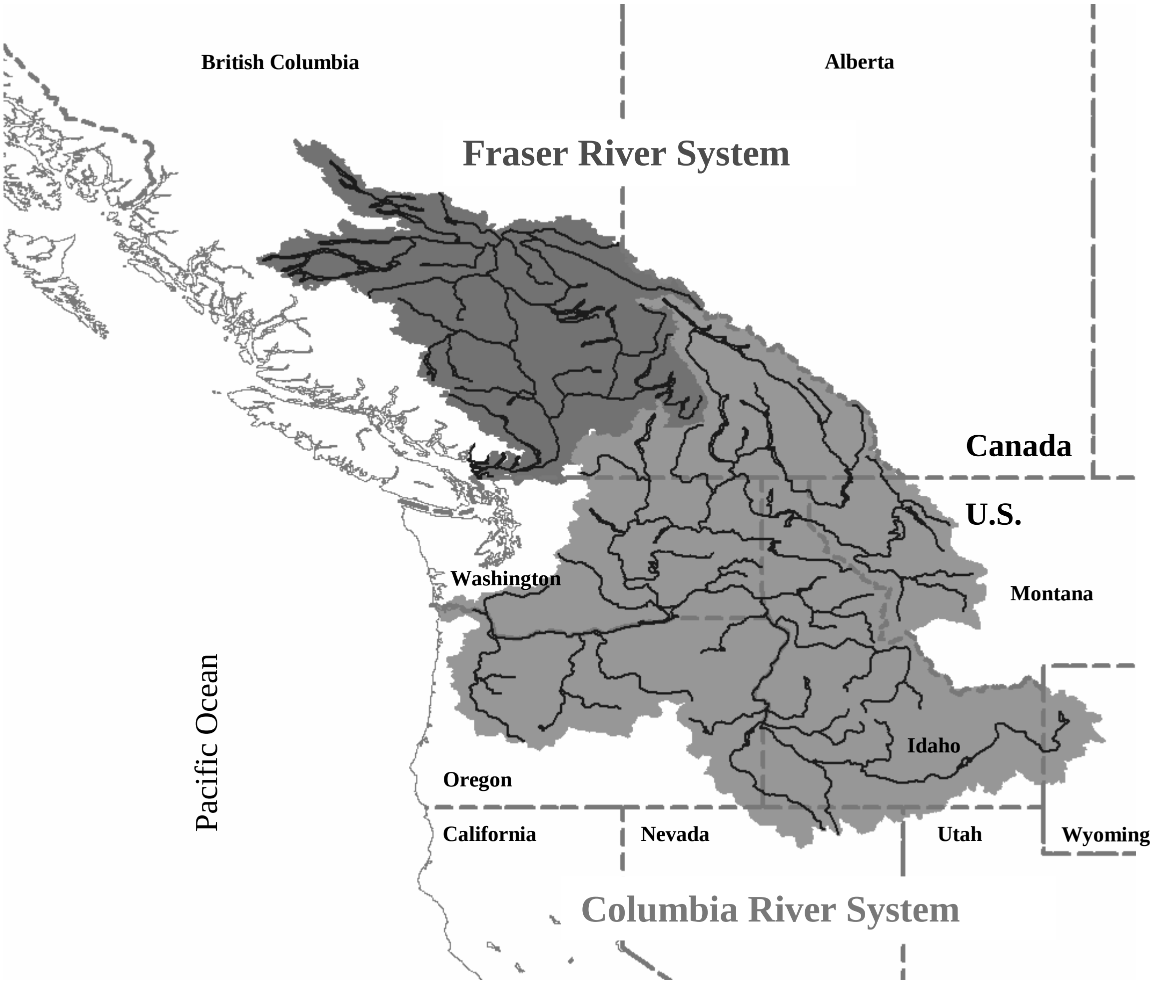

Figure 1.1 The Fraser and Columbia River watersheds drain a large portion of the Pacific Northwest and southern British Columbia region.

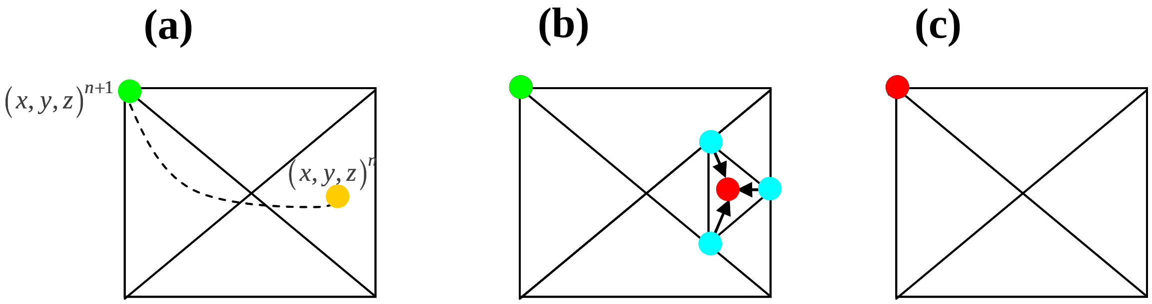

Figure 1.2 The Eulerian-Lagrangian Method within SELFE is illustrated by three actions **(a)** backtracking of the characteristic line for the grid position being evaluated from time t^{n+1} (●) to t^{n} (●), **(b)** splitting of the element in which the foot of the characteristic line is located and interpolation from sub-element vertices (●) to the position of the foot (●), and **(c)** placing the value at the foot of the characteristic line in the total derivative at the node being evaluated (●).

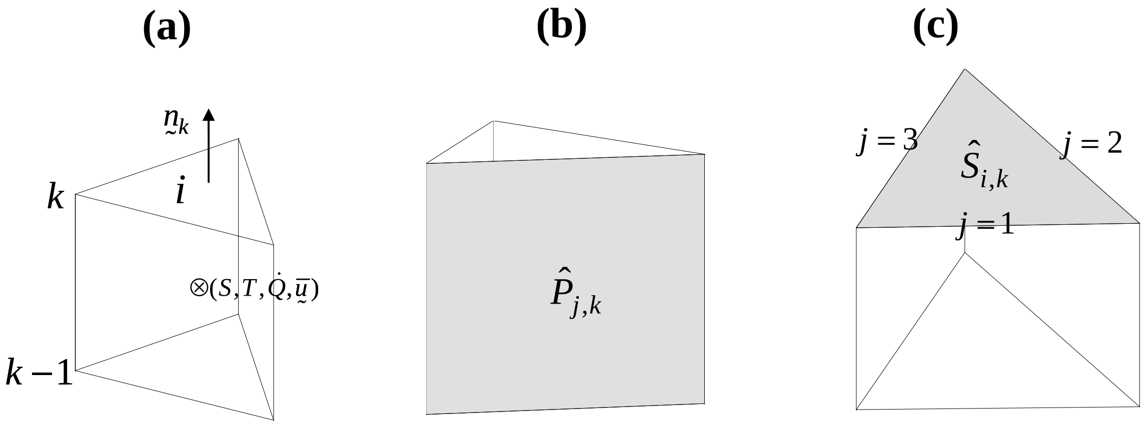

Figure 1.3 The finite volume Upwind Method within SELFE is illustrated with prisms depicting **(a)** the definition of normal vectors ($\underset{\sim}{n}_k$), prism indices (i), centroid variable definions (S, T, $\dot{Q}$, $\underset{\sim}{u}$), and vertical level indicies (k and $k-1$), **(b)** horizontal prism faces ($\hat{P}_{j,k}$), and **(c)** vertical prism faces ($\hat{S}_{i,k}$).

Table 1.1 Resolution of the three wind datasets used in the experiments presented in this thesis.

	Resolution	
Dataset	Spatial (km)	Temporal (h)
MM5	4	1
ETA	12	3
NARR	32	3

CHAPTER 2

INFLUENCE OF TRANSPORT ALGORITHMS ON THE SIMULATION OF THE COLUMBIA RIVER PLUME DURING THE EARLY WINTER OF 1990-1991

2.1 Abstract

Hindcast simulations are performed using calibrations from two coastal margin observatory for the Columbia River (CORIE [1-3]) databases (DB13 and DB14) to assess the abilities of an Eulerian-Lagrangian Method (ELM, Section 1.4.2) and an Upwind Method (UWM, Section 1.4.3) to advect salt and heat with the hydrodynamic model SELFE [4] to reproduce a winter Columbia River plume. Evaluation of the model salinities, temperatures, and velocities is performed using observed data from an extensive field survey [5], while water elevations are compared with measured tides four tide gauge locations.

The UWM produces smaller and less fresh plumes than the ELM, and better represents the low passed salinities, temperatures, and velocity directions than ELM when compared with the observations. Use of the different advection algorithms has little influence on elevations, and elevations are represented similar to that of the longer term DB13 and DB14 time series. Magnitudes of low passed modeled velocities are generally weaker than those measured. Adjustment of the surface mixing length may help to improve the transfer of momentum from winds to the water surface [6].

An assessment of the wind inputs from the National Weather Service (NWS) North American Regional Reanalysis model (NARR) is also performed using

measurements from wind buoys. Generally, NARR represents the observed wind field mean speeds and directions and variance well. However, comparisons of NARR nearest the mouth of the Columbia River, at buoy 46010, have the larger average bias in mean direction and the direction of maximum variance than the average of all locations.

2.2 Introduction

The Columbia River is the largest source of freshwater on the west coast of North America, supplying an average annual freshwater discharge of 2.28 x $10^{11}m^3$ [7] from a watershed covering 6.73 x 10^5km^2. The transport of this freshwater and the associated suspended organic/inorganic matter is important for the natural resources of the estuary and plume and also for commercial activities not limited to fishing, power generation, and ship navigation. To increase the scientific understanding of this system and help guide decisions impacting the management of the combined natural and economic resources, the Columbia River estuary and plume has been the setting of numerous physical oceanographic and modeling studies.

The breadth of topics investigated includes the variability in seasonal plume location using field or satellite measurements, or modeled results [8-12], salinity transport modeling within estuarine channels [13], extensive field observations of the plume and estuary [1, 5], and multiyear database model simulations including the estuary/plume and offshore regions of Washington and Oregon as part of the pilot environmental observation and forecasting system, a coastal margin observatory for the Columbia River (CORIE [1-3]). A greater understanding of the seasonal position of the plume has been accomplished through several historical and more recent studies. The historical accounts of [8] provide the basic seasonal patterns of a northward downwelling positioned plume and a south-southwestward upwelling positioned plume during summer. Recent studies conclude that this understanding is overly simplistic and inadequately describes the highly dynamic plume for the Columbia River. The plume position is influenced by forcings which vary at higher frequencies than seasonally, including the California Current, river discharge, and wind stress events.

The most comprehensive field survey for the Columbia River plume during the winter was performed from October 8, 1990–February 26, 1991 [5]. Twenty-two moorings, supporting 58 instruments, measured salinities, temperatures, velocities and elevations inside and near the plume, extending approximately 100km in the north-south direction and 50km off shore of the mouth. This study offers the most extensive spatial and temporal coverage of the Columbia River plume during the winter performed to date. It is particularly unique, as most previous and ongoing measurements within the Columbia River plume are typically performed in the summertime.

The CORIE modeling system has focused on providing high quality hindcast and forecast model products for the Columbia River, including its estuary and coastal plume. Within the context of this modeling framework several multiyear databases have been constructed, which utilize both improvements in hydrodynamic codes and representations of the model domain using realistic bathymetries and coastline geometries and smaller subsets of the greater region. In the current study, two recent database calibrations, which both make use of the SELFE model's [4] ability to simulate 3D baroclinic circulation, are assessed for their ability to reproduce the measurements of [5]. The databases are given numeric names with Database 1 (DB1) as the first database simulation and Database 16 (DB16) as the most recent database. Further description of the databases, including the model domain extents, numerical codes, calibration parameters, and time periods simulated within each database are available on the CORIE website at http://www.ccalmr.ogi.edu/CORIE/hindcasts/versionhelp.html. Calibrations used for this thesis are from Database 13 (DB13) and Database 14 (DB14). Both of these databases use SELFE, with DB13 using the Eulerian-Lagrangian Method (ELM, Section 1.4.2) and DB14 the Upwind Method (UWM, Section 1.4.3) to solve for the advection of salinity and heat. These two databases present simulations of the Columbia River domain spanning six years (1999-2005).

Following this introduction there are four remaining sections of this chapter. Section 2.3 focuses on the methodology used for the setup of each numerical experiment and the dataset used for model evaluation. Section 2.4 analyzes the model input wind fields, using comparisons of winds measured at buoys during the modeled time period. Section 2.5 presents the results of the two numerical experiments, including comparisons with measured values of salinity, temperature, velocity, and tidal elevation. Finally, a discussion (2.6) of the results in context of the ability of each transport algorithm to represent the Columbia River plume for the period of study.

2.3 Methods

Two experiments are performed using the hydrodynamic model SELFE to evaluate differences between the two transport algorithms, the ELM and the UWM, with respect to generating a freshwater plume for the Columbia River during the winter of 1990. Specifically, the time period chosen for the study corresponds to the availability of observed field data for the Columbia River plume as part of the study by [5]. Each experiment is initialized on September 10, 1990 using realistic inputs and run for a duration of 63 days ending on November 12, 1990. Storage requirements for one week of simulation are about 17gigabytes, or over 300gigabytes for the entire time series of both ELM and UWM experiments. This places a logistical constraint on the ability to both create and store long term simulations using the setup described below.

2.3.1 Model domain

The numerical grid domain (Figure 2.1, p. 37) includes the Columbia River estuary west of Beaver Army Terminal and extends along the coastline of northern California to southern central Vancouver Island, reaching over 300km offshore. A representative volume is included in the grid for the Strait of Juan de Fuca, Puget Sound and the Strait of Georgia to eliminate tidal reflections apparent in previous CORIE model studies which omitted this volume. This grid domain is consistent with that used for the calibrations of the DB13 and DB14 [2].

The horizontal grid is comprised of 20,736 horizontal nodes forming 39,133 unstructured triangular elements. The unstructured triangles allow the domain to span across varying horizontal resolutions, including spacing less than 100m within the estuary to more than 15km near the open ocean boundary to the west (Figure 2.1, p. 37). Length scales of processes of interest, namely those involved with the development, movement, and mixing of the freshwater plume associated with discharge from the Columbia River span these same scales. For example, gradients of salinity can be high within the estuary and plume at up to 1psu/m [5], while offshore tidal water elevations vary over larger spatial distances.

Interpolation of realistic (unsmoothed) bathymetries provides the nodal depths for the numerical grid. Bathymetries within the Columbia River estuary are a combination of recent US Army Corps of Engineers (USACE) bank to bank and channel surveys [14], National Elevation Dataset [15], and historical CORIE composite bathymetries [16]. The coastal and offshore bathymetries are interpolated from mixtures of ETOPO2 [17] and the Coastal Relief Models [18]. Offshore bathymetries near the mouth of the Columbia River are also interpolated from USACE surveys.

The vertical grid is discretized in a hybrid manner, using a combination of terrain following S coordinates in the upper levels and fixed depth Z coordinates at the lower levels and is consistent with DB13 and DB14. This hybrid grid method provides the ability to more accurately simulate the bottom and surface processes, such as those associated with river plume systems, across varying depth scales – from shallow estuarine, to the inner–mid shelf, and deepest offshore waters [4]. A total of 54 vertical levels are used. The upper 37 of these levels are S levels while the remaining 17 are Z levels, with the transition between S and Z coordinates occurring at 100m depth below the free surface.

2.3.2 Forcings

2.3.2.1 Initial and nudging salinities and temperatures

Typically the CORIE database simulations utilize salinity and temperature values from the Naval Research Laboratory’s (NRL) Navy Coastal Ocean Model (NCOM [19, 20]). NCOM has been run by NRL as a data assimilated global ocean forecast model since August 2000 [19] and it is used to provide initial ocean conditions and provide periodic nudging (equation 2.1) of model solutions away from the mouth of the Columbia River (Figure 2.2, p. 38). However, since the time period of the current study is prior to the availability of NCOM forecast data, climatological salinity [21] and temperature [22] values are interpolated to nodal grid locations for initial and nudging conditions. These values are defined on a 1° horizontal grid, which includes coarse coverage of the Columbia River estuary. Salinity and temperature values within the estuary are initialized using a linear transition from climatology to river conditions between the mouth of the Columbia River and Astoria Tongue Point. Nudging is performed using a vertically constant but horizontally varying nudging factor (α, [2]), providing a method to maintain ambient ocean conditions outside of the primary region of interest.

The nudging factors vary from 0 inside of the Columbia River estuary and near plume region to approximately 5x10^{-4} along the open ocean boundary. In regions where the nudging factor is greater than 0, the weighted average of the nudging value (S^c) and the model variable (S^n) is the final output (S') at each time step (equation 2.1 as in [2, 23]). For the nudging value of 5x10^{-4}, the equivalent relaxation period (r) is approximately 2 simulated days (2*86400s) using the model time step (Δt) of 90s. Nudging factors are defined by equation 2.2 as in [23].

$$S'(x,y,z) = (1-\alpha)S^n(x,y,z) + \alpha S^c(x,y,z) \tag{2.1}$$

$$\alpha = \frac{\Delta t}{r} \tag{2.2}$$

Different nudging factors are used for each of the two experiments. The ELM experiment nudging factors use a radial decreasing factor (Figure 2.2b, p. 38). The UWM application is similar to the ELM, except to the north of the Columbia River mouth, where the lower nudging factors are extended (Figure 2.2a, p. 38). The purpose for these differences is to highlight the ability of UWM SELFE to maintain a conservative representation of the plume to the north along the Washington coast (the seasonal location of the Columbia River plume; e.g. [8]) without the nudging factor being imposed for maintenance of these ambient conditions. Section 2.5 will show that the UWM is capable of maintaining plume size more appropriately without the aid of nudging factors to correct the ambient conditions due to overly large plumes. However, the nudging factors are applied well outside of the region observed by [5] and does not impact any of the quantitative comparisons presented here.

2.3.2.2 Tidal boundary conditions

Interpolated harmonics for eight tidal constituents, including the semi-diurnal components M2, S2, N2, K2 and the diurnal components O1, Q1, K1, P1, are used to impose tidal boundary elevations and are taken from [24]. These conditions are specified for the open ocean boundary nodes, along the western and southern edges of the model domain, and the boundary nodes along the northern Strait of Georgia. A mean sea level (Z0) forcing is imposed for the DB13 and DB14 long term simulations and is derived from NCOM. The mean sea level value (Z0) represents Since the time period of the current study predates NCOM forecasts a Z0 value is not provided as a model forcing.

2.3.2.3 Estuarine river inputs

Using model estimated discharge for the Columbia River and Willamette River, a time history of tidally varying freshwater discharge representing the contributions from these two rivers is computed using a 2D barotropic ELCIRC [25] simulation and supplied for the SELFE model near Beaver Army Terminal (Figure 2.3, p. 39). The discharges for the barotropic simulation are taken from measurements for the Columbia River, from the US Geological Survey gauge (USGS 14128870), and estimated for the Willamette River, as measurements are not available for this time period. Additionally, measured daily discharge from the Environment Canada gauge (08MF005) at Hope, BC provides a representative input for the Fraser River. Water temperatures for each of the combined Columbia River/Willamette River inputs are supplied from daily measured temperatures from the Columbia River; while those for the Fraser River are derived from the nearest climatological values [22].

2.3.2.4 Atmospheric conditions

The time period of the field study is a limiting factor for the availability of atmospheric weather model data that can be used for inputs into the SELFE simulations. Although internal archives include data from 8 weather model products for atmospheric properties, only two of these sources provide data within the time period of this study. These two sources are the National Weather Service (NWS) North American Regional Reanalysis model (NARR) and the NWS Global Reanalysis (NNRP). As reanalysis products, observations are assimilated into NARR and NNRP model outputs. NARR is a more suitable choice, than NNRP, with an approximate resolution of 32km spatially and 3h temporally, compared with the NNRP at approximately 1.875° spatial and 6h temporal resolution. The heat exchange module is inactive for the ELM version of SELFE, but active for the UWM version.

2.3.3 Observations

A total of 58 instruments on 22 moorings were installed, as part of the field study conducted by [5], along depth contours of approximately 30m, 55m, and 90m during the winter 1990–1991 (Figure 2.4, p. 39). The instrument array was designed to capture the wintertime Columbia River plume variability in the inner shelf (30m), shallow mid shelf (55m) and deeper mid shelf (90m) regions, by measuring of salinities, temperatures, velocities, water level pressures, and surface winds. Drifters, CTD casts, and satellite imagery were also collected to help in the study of the wintertime plume variability; however this data is not used for comparisons with this work as it was not included in the supplied dataset.

Three character names were assigned by [5] to each of the moorings for unique identification and this definition scheme is repeated here for clarity. The first character indicates geographic location of each mooring (Figure 2.5, p. 40): “EN” and “ES” for inside the estuary either on the north or south, “N” for north of the mouth, “S” for south of the mouth, “O” for Oregon, “K” and “B” for Klipsan and Long Beach respectively, and “W” for Willapa. For moorings other than those inside the estuary the second character identifies the approximate depth given by a “1” for 10 fathoms, a “3” for 30 fathoms, and a “5” for 50 fathoms, which correspond approximately with the 30m, 55m, and 90m isobaths. The third and final character designates whether the mooring is supported by a surface or a subsurface float, using the designation of “S” or “A” respectively.

The time period of data availability varies across each mooring location (Figure 2.4, p. 39). For the comparison with the model results of the current study, data quality is of a concern. As with any long term oceanographic field installations, each instrument is subject to degradation of signal strength and reliability due to stresses from environmental conditions and also those from commercial ship operations [5]. Metadata indicated that degradation occurred at several locations (e.g. ENA, K5A, S5A, and B1). Therefore, only data collected during the initial weeks of the deployment was used for model comparisons (Figure 2.4, p. 39), minimizing the use of data from instruments that may have moved physically or experienced various problems. The secondary reason supporting the chosen length of each experiment was computational expense, including storage constraints as previously discussed.

Metadata supplied with the dataset includes several suggested adjustments for temperatures. These adjustments were used during the computation of salinities by [5] and are applied for the comparisons presented in this study. However, it is noted that for at least one location, W1S, the suggested reduction in temperature of 1.2°C may be too large. Observations of 1m temperatures are compared for mooring locations within the estuary and the inner shelf north of the plume and from five casts [26] located within Willapa Bay and Grays Harbor (Figure 2.6-7, p. 41). For the casts, the deepest measured value is plotted. Additional cast data during this time period is not available from [26]. The measured and modeled temperatures are generally warmer than those of W1S using the suggested reduction (Figure 2.7, p. 41). These instruments lie in the path of the northward downwelling freshwater plume from the Columbia River; and correlations between the daily and longer term fluctuations between temperatures within the estuary and those in the plume are evident.

Data collected from the moored array presents evidence of the Columbia River plume's response to strong wind forcings associated with 2-10 day storm events and that the plume contains steep gradients of salinity in the vertical direction (up to 1psu/m) [5]. And, the plume is generally confined to within 10m or 20m from the surface depending on whether the plume is separated or attached to the north [5].

2.3.4 Performance metrics

Low-pass filtered model salinities, temperatures, and velocities are evaluated against low-pass filtered data observed by [5] (Figure 2.5b, 40). Low-pass filtering is performed using the pl64.m [27] Matlab code, which removes tidal and higher frequency oscillations from the time series by averaging the neighboring 64 points on either side of each point in the hourly time series using constant weights (Figure 2.8, p. 42). Tidal and higher frequency fluctuations can obscure fluctuations due to wind events [28]. The half amplitude of this filter is 33hours, thus fluctuations occurring at higher frequencies than this are reduced in amplitude by more than 50% (Figure 2.9, p. 42). The reductions in amplitude for the frequencies of the leading 8 tidal harmonics, when using this filter, are shown in Table 2.1 (p. 43). The filter metrics provided above were computed using the code available from [28].

Model elevations are compared with measurements at the National Oceanic and Atmospheric Administration's (NOAA) Center for Operational Oceanographic Products and Services (CO-OPS) tidal gauge stations (Figure 2.5a, p. 40), including Neah Bay, WA (9443090), Astoria Tongue Point, OR (9439040), South Beach, OR (9435380), and Charleston, OR (9432780). Harmonic analysis [29] is used to evaluate the model elevation results, at each of the tide gauge stations, with the eight constituents imposed at the open ocean boundaries. The comparisons of elevations are performed against both raw observations and also against synthesized observations after harmonic analysis. Harmonic analysis is performed using inference for the observed time series of the P1, K2, and NU2 constituents and P1 and K2 for the model time series. The observed elevations are then synthesized using the same 8 harmonics as used in the model. These two forms of analysis for elevations allow for a determination of the model's ability to represent the observed water elevations and to also understand how much error is due to constituents not used in the model.

The first 28 days of both simulations occur prior to the beginning of the dataset provided by [5], and are used as a ramp-up period to properly develop the Columbia River plume as is consistent with previous CORIE database simulations [2]. Results from these initial weeks are shown in plots of time series of computed plume volume and thickness using various salinity isopleths (Figures 2.18-19, p. 56-57).

2.4 Wind field analysis

Winds measured at buoy locations (locations shown on maps in Figure 2.10-11, p. 44-47), and operated by the NOAA's National Data Buoy Center (NDBC) and Environment Canada, are used to assess the quality of the NARR wind model for use as atmospheric inputs to the hydrodynamic experiments. The three variables used for evaluation of time series include mean values of speed and direction, principal axes, and computed wind stress for several wind buoy locations within the northeastern Pacific Ocean. Many of these buoys are outside of the numerical domain providing the reader with a broader review of the NARR quality for this region.

The first and second of these variables (mean values of speed and direction, and principal axes) are also utilized in a recent evaluation of weather model winds for use as ocean model inputs [30]. Similar to the analysis performed by [30], the variables describing the winds are compared using the metrics of magnitude ratios and directional biases. Magnitude ratios allow for quick comparison of modeled to measured values, with ratios approaching 1 indicating winds that are well represented. Directions for this analysis are given with respect to which direction the winds are towards to aid in the interpretation of results in the context of water mass movements.

The analysis of [30] adjusts wind speeds measured at 5m height to 10m for comparison with modeled results using the data of [31]; accordingly a uniform adjustment of 1.08 is applied. However, the anemometer heights were not publicly available for the Environment Canada buoys, so for consistency in the analysis of winds at each location no corrections have been applied for the height of the wind data. The magnitudes of measured wind speed presented may be between 2-8% less than if the corresponding correction from [31] had been applied.

2.4.1 Time series means

Winds farther offshore than the model domain are predominately directed northeastward during the time period studied; while those near the mouth of the Columbia River are predominately directed northward (Table 2.2, p. 43; Figure 2.10, p. 44). Winds south of the Oregon/California border and near the northern California coast, are directed southward. Generally, the NARR winds represent the mean observed wind fields quite well with an average ratio of modeled to measured mean vector winds of 1.1, an average ratio of modeled to measured mean scalar winds of 0.95, and an average bias of mean direction for the model winds of 21° clockwise with respect to the mean direction of the measured winds. The average bias between the measured and modeled mean wind directions is slightly worse for near shore buoys located within 300 km of the Columbia River mouth (46206, 46041, 46010, and 46040) than the average bias for all buoys at 33.8° clockwise with respect to the mean direction of the measured winds.

2.4.2 Principal axes

Principal axes ([32]; Appendix A.2) of modeled and measured wind velocities are computed to measure variance within each wind field in the major and minor directions of variance and compare the ability of a model to resolve the observed variance. The principal axes values are typically shown as standard deviations for consistency in units with velocity (m/s). The NARR weather model represents a large amount of the variance in the observed wind field from September 1 to November 12, 1990 for the locations used for comparisons (Table 2.2, p. 43; Figure 2.11, p. 46). The average ratios of modeled to measured major and minor principal axes are 0.89 and 0.91 respectively. The bias between the modeled and measured principal direction shows that the NARR results are directed an average of 15° counter-clockwise of the measured winds. However, the direction of principal axes for locations nearest the mouth of the Columbia River (46206, 46041, 46010, and 46040) is biased by an average of 71° counter-clockwise of the observed major axes. Comparisons with buoys that are in the SELFE model domain show similar results as the near shore locations outside of this region.

2.4.3 Wind stress

Observed and NARR winds are used to compute wind stress, using the method of [33], at buoys located within the model domain (Figure 2.12, p. 48). These time series plots reveal patterns similar to those of the mean and principal axes metrics; mainly, that the NARR winds are representative of the direction reversals, although a bias exists between the measured and modeled wind directions, and that the NARR winds are weaker and show less variance than the observed. However, several strong wind events associated with the summer to winter transition period storms are evident within both the observed and NARR modeled time series. As an example, attention is given [5] to the strong wind event during approximately October 25-28 which causes a northward downwelling plume position. Increases in observed and modeled wind stress, for this described event, are shown at buoy 46010 (Figure 2.12b, p. 48) near the mouth of the Columbia River.

2.5 Results of the SELFE experiments

Differences are seen in the results of the two experiments. The ELM simulations produce larger fresher plumes while the UWM simulations produce plumes that are both saltier and smaller than the ELM. As a result of these algorithm derived plume differences, ELM and UWM model water velocities are different, particularly at locations farther offshore (e.g. K5S and N5S). Since the ELM plume is larger, it has a greater baroclinic forcing on model velocities farther offshore than UWM. Generally UWM agrees more favorably with the observations of [5] than ELM. Similar to the results presented by [5], the observed and modeled salinities, temperatures, and velocities have been filtered to assess the subtidal variations, such as influence by wind events.

2.5.1 Elevations

Model water elevation results are similar for both experiments, with the ELM performing slightly better, indicating a need to further calibrate the drag coefficients for the UWM, or DB14, simulations [6]. These results are compared with observed elevations at four tidal gauges including Astoria Tongue Point, Charleston, South Beach, and Neah Bay (Figure 2.13, p. 49). These elevations represent the observed tidal signal similar to those of the longer simulations comprising DB13 and DB14. It should be noted that for these tide gauge locations the model domain is best resolved to capture the elevation at Astoria Tongue Point. The numerical grid is much less resolved near the remaining three gauges. Accordingly, the smallest errors of elevation are at Astoria Tongue Point, although differences in elevation indicate that these errors fluctuate throughout the experiment (Figure 2.14, p. 50). RMS errors are 0.115m, 0.167m, 0.114m, and 0.252m for the ELM results at Astoria Tongue Point, Charleston, South Beach, and Neah Bay respectively. Elevations (Figure 2.15, p. 52) and difference of elevation (Figure 2.16, p. 53) are also compared by performing harmonic analysis [29] on the observed tides using inference at each station for the P1, K2, and NU2 constituents and subsequently synthesizing the time series of observed elevations using only the 8 modeled constituents. These comparisons result in decreased RMS errors for both the ELM and UWM simulations and at each observation location. These reductions are attributed to the removal of constituents not used in the model from the observed time series. Thus, these errors are primarily factors of boundary condition and grid errors.

Harmonic analysis [29] is performed using the 8 modeled tidal constituents for both the model results and the observed values during the simulated period, the P1, K2, and NU2 constituents are obtained with inference for the observed while inference of the P1 and K2 are used for the model (Table 2.3, p. 51). The distance in the complex plane (Appendix A.1), between modeled and measured constituents, is used as a measurement of error, and is shown in Table 2.3 (p. 51) as the value D. The largest differences at Astoria Tongue Point for both experiments are in the semi-diurnal constituents M2 and N2. Average differences in the complex plane for each constituent (Table 2.4, p. 51) further indicate that the ELM results are slightly better than the UWM results. When this same analysis is used to compare the synthesized observed elevations and model results, reductions in the error the N2 constituent is most apparent (Table 2.5, p. 54 and Table 2.6, p. 54). This reduction occurs due to the removal of the NU2 constituent from overlapping with the N2 harmonic by using inference. The differences in complex distance, when comparing the synthesized observations and model results, are less than 1cm for the constituents other than the N2 (Table 2.5, p. 2.5 and Table 2.6, p. 2.6). This again indicates that much of the remaining error is not due to missing harmonics within the model results, but is due to errors in the boundary conditions and the grid.

2.5.2 Salinities

The choice of transport algorithm causes differences in simulated salinities. These differences are readily apparent in surface contours of salinities for the final time step (November 12, 1990) of each of the two simulations (Figure 2.17, p. 55). The plume generated using ELM is substantially larger in volume (Figure 2.18, p. 56), extends to greater depths within the water column (Figure 2.19, p. 57), and is fresher than the UWM plume. UWM represents the mean salinities measured by each instrument and also several of the fluctuations in the measured time series better than the ELM. Examples of well represented salinity fluctuations (Figure 2.20a, d, f, g, and h, p. 58-59) include the increases during October 25-26 and decreases during October 26-27 apparent at 1m depth within the estuary (ENS) and northern plume region on both the inner (N1S, B1, and K1S) and shallow mid shelf (K3S). The use of UWM improves the representation of inner shelf northern (N1S, B1, and W1S) and mid shelf northwestern (K3S and W3S) plume salinities as opposed to ELM (Figure 2.20d, f, h, i, and j, p. 58-60). UWM also represents the data measured at 1m and 5m depth along the edges and turning regions of the plume better than the ELM (Figure 2.20e, k, l, m, and n, p. 59-61) as shown for the shallow mid shelf (N3S and S3S) and the deep mid shelf (S5S, N5S, and K5S). Finally, estuarine and near plume representations (Figure 2.20a, b, c, and d, p. 58) are better using UWM as shown for 1m locations (ENS, N1S) and deeper estuarine instruments at 5m (ENS) and 8m (ENA). RMS errors of salinities are shown for all instruments (Figure 2.21, p. 62 and Table 2.7, p. 63). Except for two of the instruments (O3A at 45m and

S5A at 35m) located both deeper and south of the majority of the plume, UWM out performs ELM at each location.

2.5.3 Temperatures

A larger number of instruments capable of measuring temperature were deployed than the number for measuring salinity; 39 temperature instruments are used for model-data temperature comparisons, while only 21 are used for salinity comparisons. It is important to remind the reader that for the ELM experiments performed, the heat module within SELFE was inactive. Therefore, the comparisons between the two experiments can not be directly attributed to the choice of transport algorithm. Similar to the salinity results, UWM temperatures (with the heat exchange module) compare more favorably with measurements than ELM (without the heat exchange module) within the estuary and near plume (Figure 2.22a, b, c, and d, p.64), the inner and shallow mid shelf northern and northwestern plume (Figure 2.22e, f, g, h, i, and j, p. 65-66), and the deep mid shelf (Figure 2.22k, l, m, and n, p. 66).

During the wintertime, the difference between air and water temperature for the Columbia River plume region is less than during the summertime [34]. This leads to low pass temperatures with little fluctuation near the surface. However, at deeper depths larger fluctuations in temperature are measured (S3A at 41m, 46m, 51m, and 56m; O3A at 35m, 45m, and 50m). These larger fluctuations in measured temperature occur during northward wind events and are likely due to the downwelling of warmer waters to these deeper layers (October 18, 21, 30 and 31, and November 3 and 7; see Figure 2.12b for wind stress events occurring on these same dates, p. 48). UWM represents the fluctuations in temperature at depth better than the ELM results at S3A (Figure 2.22p, q, r, and s, p. 67) and slightly better at O3A (Figure 2.22u, v, w, and x, p. 68). RMS errors of temperatures are shown for all instruments (Figure 2.23, p. 69 and Table 2.8, p. 70). Similar to the two instances when ELM resulted in lower RMS error of salinity than UWM, there are locations where the RMS error of temperature is lower for ELM than for UWM. These locations are mostly outside of the plume region and are at depths greater than those generally influenced by the UWM modeled plume (Figure 2.19, p. 57). This indicates that the larger errors in the UWM results, for locations outside of the plume influence, are primarily due to differences in the climatological values, used for initial and nudging conditions, and those observed during the simulated time period.

2.5.4 Velocities

Velocity data from 15 instruments is used to analyze the model results. Except for the measurements made inside of the estuary near the river mouth (ENS), the velocities have a mean northward direction during the time period studied (Figure 2.24-26, p. 71-79 and Table 2.9, p. 77), as is consistent with the findings of [5]. The ELM and UWM model velocities are generally weaker in magnitude and variance than the measurements (Figure 2.26-27, p. 78-83 and Table 2.9-10, p. 77-80).

The velocities for the longer term simulations of DB13 and DB14 are also weak [6]. The parameterization of the surface mixing length is believed to be too shallow [6]. The mixing length used throughout the domain for the ELM and UWM is 10cm and 4cm respectively. This input parameter acts to transfer momentum from wind stress to the water column, thus a more accurate calibration of this parameter should improve the influence of wind on water velocities.

The average ratios of modeled to measured vector mean speeds at 5m are 0.55 and 0.65 for the ELM and UWM respectively. The average directions of model currents are aligned to the right (clockwise) of the measured directions by an average of 49.6° for the ELM and 7.5° for the UWM. And, at 10m depth, the average ratios of modeled to measured vector mean speeds are 0.34 for the ELM and 0.36 for the UWM, and with an average bias in mean direction of 38.7° for the ELM and 27.9° for the UWM. The UWM is therefore shown to provide improvements in representing the direction of the measured currents at both the 5m and 10m depths, while the averaged ratios of modeled to measured mean scalar speed at 5m, 0.62 for the ELM and 0.61 for the UWM, show that both models represent the magnitude of the observed currents with a similar skill (Figure 2.24-25a, p. 71-74).

Analysis of principal axes ([32]; Appendix A.2) indicates that the ELM at 5m represents the observed variance in velocity better than the UWM results. However, the

ELM suffers from a higher bias between the measured and modeled average principal direction at 50.7° to the left (counter-clockwise) than the UWM at 34.7° to the left. The average ratio of the modeled to measured principal major axes are 0.96 for the ELM and 0.81 for the UWM, thus quantifying the smaller modeled variance than that of the observed currents (Figure 2.27, p. 81-83 and Table 2.10, p. 80). The modeled currents are more rectilinear than the measured currents at 5m, with mean degrees of polarization of 0.19, 0.21, and 0.41 for the ELM, UWM, and measured data respectively.

Although the two models produce magnitudes and variances of velocities weaker than the observed, the models do show some similar fluctuations and occurrences of maxima of magnitude. This is particularly apparent with the only inner shelf mooring used for comparison W1S at 5m (Figure 2.23-24d, p. 69-71) on October 29, November 3, and November 7. The model velocities are better resolved at W1S than at other offshore locations (e.g. N5S and K5S), because the plume, as shown by the salinity comparisons, is better defined in this location. Velocities at W1S are therefore controlled more strongly by the baroclinic forcing than by winds or mean sea slope.

Harmonic analysis of the u and v components of the instantaneous (not low pass filtered) velocities, for the M2 (Table 2.11, p. 84) and K1 (Table 2.12, p. 85) constituents also indicates that errors exist outside of the low pass signal. The distances (D) in the complex plane (Appendix A.1) are computed between each modeled and measured tidal velocity component to assess the representation of the observed values. This analysis does not provide any consistent trends, except that the model results do not match the observed. As the plumes are different for both simulations and that observed, the effect of the plume on the tidal velocities is different for each case, contributing to the differences in the tidal velocities.

2.6 Discussion

Generally, the simulations represented the seasonal northward orientation [8-12] of the Columbia River wintertime plume. Water elevations were also well resolved by the model, and have similar fits to those of the longer term simulations using the two different transport algorithms (DB 13 and DB14). Errors are not due to missing tidal constituents within the model.

Comparisons between measured and modeled water elevations, salinities, temperatures, and velocities reveal differences between the abilities of ELM SELFE and UWM SELFE to simulate the wintertime conditions of the Columbia River plume for 1990-1991. Results indicate that UWM produces smaller and less fresh plumes than ELM, thus better representing the observed temperature and salinity values. The decreased nudging factors used to the north of the Columbia River mouth help to emphasize that the UWM conserves the plume preventing the unrealistic growth into this region that occurs with ELM. Modeled plume thicknesses for the 30psu contour during the period of study by [5] vary between 5-10m and 18-25m for the UWM and ELM respectively. These thicknesses are similar to those reported in the field study.

UWM transport leads to improvements in mean values and fluctuations of salinities, temperatures, and velocity directions. However, UWM velocities at the southern and western most moorings (O3S, O5S, N5S, and K5S) are weaker than observed. Further calibration of the surface mixing length should improve these results, as this model parameter influences the transfer of wind stress into momentum into the upper most portion of the water column [6]. Additionally, a recently discovered error in the application of wind direction (see discussion below) likely contributes to the average model clockwise (right) bias in water velocities.

Ratios of modeled to measured low pass filtered mean vector speeds at ENS, within the estuary and near the mouth, indicate that the model freshwater input is generally appropriate, with 1.13 for the ELM and 1.51 for the UWM. Here, the mean modeled directions are directed out of the estuary, but have biases of 14.2° and 25.6° counter-clockwise with respect to the measured mean direction for the ELM and UWM respectively. This discrepancy in direction may be due to differences in the representation of the model grid domain and the actual channel during the survey time period, causing the currents to turn in a different manner at this location.

Comparison of mean directions of winds at buoy 46010 shows that the model winds are directed 21.1° to the right of the observed winds. A portion of this difference most likely contributes to the biases directed to the right for the 5m and 10m modeled currents with respect to the observed currents. Upon completion of each of these experiments, it was noted that an error in the application of wind input directions was systematically imposed [34]. Wind inputs were used within the model in the geographic projection, with north directed towards the model grid positive y direction. However, the model grid used the Oregon State Plane Coordinate System North (OSPCSN) North American Datum 1927 (NAD27) projection, in which the positive y direction does not correspond to northward. The directional errors associated with this projection error are approximately 2.5° to the right of the correct direction near the mouth of the Columbia River [16].

Future modeling studies of the Columbia River plume using the CORIE framework should incorporate the lessons learned from the analyses presented in this thesis. The use of the UWM scheme in these experiments was generally more computationally expensive than ELM (UWM requires 28% more time to simulate 1 week than ELM), its use should continue to be pursued as the improvements are substantial. Recently improvements in the UWM algorithm have increased its computational efficiency and will aid in its future use [6] Next, these experiments have indicated that the nudging factors may be decreased north of the plume while still properly resolving the observed salinities using UWM. Further exploration of decreased nudging in the regions nearest the plume (Figure 2.2, p.38), including those to the south of the plume (i.e. the seasonal summer location of the plume [5, 9, 10, 12]), can be investigated for how plume influences coastal waters outside of the current nudging over long time periods. Errors in wind application should be corrected. Finally, efforts should be directed towards improving model velocities, which may improve with corrections in wind application, application of a mean sea slope (Z0) and further calibration of the mixing parameters which transfer wind energy into and through the water column [6].

2.7 Acknowledgements

We would like to thank the following people and organizations for the use and availability of their data: Dr. Barbara Hickey for the Columbia River plume observations [5] and Susan Geier both of University of Washington, NCAR/NCEP for NARR weather data, the Levitus climatologies for salinity and temperature [21, 22], NOAA/NDBC and Environment Canada for wind measurements, NOAA/CO-OPS for water elevations, USGS for bathymetry and discharge data, USACE and NGDC for bathymetric data and additional research staff and students of the Center for Coastal and Land-Margin Research group: Michela Burla, Arun Chawla, Sergey Frolov, Nate Hyde, Aaron Racicot, Charles Seaton, Paul Turner, and Ethan VanMatre.

2.8 References

1. Baptista, A.M., *Environmental observation and forecasting systems.*, in *Encyclopedia of Physical Science and Technology*, R.A. Meyers, Editor. New York: Academic Press, 2002. 565-581.

2. Baptista, A.M., Y.L. Zhang, A. Chawla, M. Zulauf, C. Seaton, III E.P. Myers, J. Kindle, M. Wilkin, M. Burla, and P.J. Turner, *A cross-scale model for 3D baroclinic circulation in estuary-plume-shelf systems: II. Application to the Columbia River.* Continental Shelf Research, 2005. **25**: 935-972.

3. Coastal Margin Observatory for the Columbia River (CORIE), www.ccalmr.ogi.edu/CORIE, [Viewed July 2006]

4. Zhang, Y. and A.M. Baptista, *A semi-implicit Eulerian-Lagrangian finite-element model for cross-scale ocean circulation, with hybrid vertical coordinates.* International Journal for Numerical Methods in Fluids, in-review.

5. Hickey, B.M., L.J. Pietrafesa, D.A. Jay, and W.C. Boicourt, *The Columbia River plume study: Subtidal variability in the velocity and salinity fields.* Journal of Geophysical Research, 1998. **103**(C5): 10,339-10,368.

6. Zhang, Y. of Oregon Health & Science University, *Personal communication*. 2006.

7. Landry, M.R., J.R. Postel, W.K. Peterson, and J. Newman, *Broad-Scale Distributional Patterns of Hydrographic Variables on the Washington/Oregon Shelf*, in *Coastal Oceanography of Washington and Oregon*, M.R. Landry and B.M. Hickey, Editors. Amsterdam: Elsevier Oceanography Series, 47. Elsevier Science, 1989. 1-40.

8. Barnes, C.A., A.C. Duxbury, and B.A. Morse, *Circulation and selected properties of the Columbia River effluent at sea*, in *The Columbia River Estuary and Adjacent Ocean Waters*, A.T. Pruter and D.L. Alverson, Editors. Seattle: University of Washington Press, 1972. 41-80.

9. Fiedler, P.C. and R.M. Laurs, *Variability of the Columbia River plume observed in visible and infrared satellite imagery.* International Journal of Remote Sensing, 1990. **11**(6): 999-1010.

10. García Berdeal, I. , B.M. Hickey, and M. Kawase, *Influence of Wind Stress and Ambient Flow on a High Discharge River Plume.* Journal of Geophysical Research, 2002. **107**(C9): 3130.

11. Hickey, B., S. Geier, N. Kachel, and A. MacFadyen, *A bi-directional river plume: The Columbia in summer.* Continental Shelf Research, 2005. **25**(14): 1631-1656.

12. Thomas, A.C. and R.A. Weatherbee, *Satellite-measured temporal variability of the Columbia River plume.* Remote Sensing of Environment, 2006. **100**(2): 167-178.

13. Hamilton, P., *Modelling salinity and circulation for the Columbia River estuary.* Progress in Oceanography, 1990. **25**: 113-156.

14. USACE, Columbia River Surveys, http://www.nwp.usace.army.mil/op/nwh/home.asp, [Viewed July 2006]

15. USGS, National Elevation Dataset, http://ned.usgs.gov, [Viewed July 2006]

16. Seaton, C. of Oregon Health & Science University, *Personal Communication*. 2006.

17. U.S. Department of Commerce, National Oceanic and Atmospheric Administration, National Geophysical Data Center, *2-Minute Gridded Global Relief Data (ETOPO2).* 2001.

18. Divins, D.L. and D. Metzger, NGDC Coastal Relief Model, http://www.ngdc.noaa.gov/mgg/coastal/coastal.html, [Viewed July 2006]

19. Rhodes, R.C., H.E. Hurlburt, A.J. Wallcraft, C.N. Barron, P.J. Martin, O.M.Smedstad, S. Cross, J.E. Metzger, J. Shriver, A. Kara, and D.S. Ko, *Navy Real-Time Global Modeling Systems.* Oceanography, 2001. **15**(1): 29-43.

20. Martin, P.J., *Description of the Navy Coastal Ocean Model Version 1.0, NRL Formal Report 7322-00-9962*. 2000, Naval Research Laboratory: Stennis Space Center, MS.

21. Levitus, S., R. Burgett, and T.P. Boyer, *Salinity. NOAA Atlas NESDIS 3*. World Ocean Atlas 1994. Vol. 3. Washington, D.C.: U.S. Department of Commerce, 1994. 99.

22. Levitus, S. and T.P. Boyer, *Temperature. NOAA Atlas NESDIS 4.* World Ocean Atlas 1994. Vol. 4. Washington, D.C.: U.S. Department of Commerce, 1994. 117.

23. Foreman, M.G.G., R.E. Thomson, and C.L. Smith, *Seasonal current simulations for the western continental margin of Vancouver Island.* Journal of Geophysical Research, 2000. **105**(C8): 19,665-19,698.

24. Myers, E.P. and A.M. Baptista, *Inversion for tides in the Eastern North Pacific Ocean.* Advances in Water Resources, 2001. **24**(5): 505-519.

25. Zhang, Y., A.M. Baptista, and E. Myers, *A cross-scale model for 3D baroclinic circulation in estuary-plume-shelf systems: I. Formulation and skill assessment.* Continental Shelf Research, 2004. **24**(18): 2187-2214.

26. Washington Department of Ecology, Marine Water Quality Monitoring, Grays Harbor and Willapa Bay, http://www.ecy.wa.gov/programs/eap/mar_wat/mwm_intr.html, [Viewed June 2006]

27. Beardsley, R.C., R. Limeburner, and L.K. Rosenfeld, *Introduction to the CODE-2 moored array and large-scale data report.* 1985, R. Limeburner, ed. Woods Hole Oceanographic Institution Technical Report, WHOI-85-35. 234.

28. Butman, B., M.H. Bothner, P.S. Alexander, F.L. Lightsom, M.A. Martini, B.T. Gutierrez, and W.S. Strahle, *Long-term Oceanographic Observations in Western Massachusetts Bay Offshore of Boston, Massachusetts: Data Report for 1989-2002*. 2004, U.S.G.S. Digital Data Series DDS-74, version 2.0.

29. Pawlowicz, R., B. Beardsley, and S. Lentz, *Classical tidal harmonic analysis including error estimates in MATLAB using T_TIDE.* Computers and Geosciences, 2002. **28**: 929-937.

30. Tinis, S.W., R.E. Thomson, C.F. Mass, and B.M. Hickey, *Comparison of MM5 and Meteorological Buoy Winds from British Columbia to Northern California.* Atmosphere-Ocean, 2006. **44**(1).

31. Smith, S.D., *Coefficients for Sea Surface Wind Stress, Heat Flux, and Wind Profiles as a Function of Wind Speed and Temperature.* Journal of Geophysical Research, 1988. **93**(C12): 15,467-15,472.

32. Emery, W.J. and R.E. Thomson, *Data Analysis Methods in Physical Oceanography*. Amsterdam: Pergamon Press, 2001.

33. Zeng, X., M. Zhao, and R.E. Dickinson, *Intercomparison of Bulk Aerodynamic Algorithms for the computation of Sea Surface Fluxes Using TOGA COARE and TAO Data.* Journal of Climate, 1998. **11**: 2628-2644.

34. Zulauf, M. of Oregon Health & Science University, *Personal Communication*. 2006.

2.9 Figures and Tables

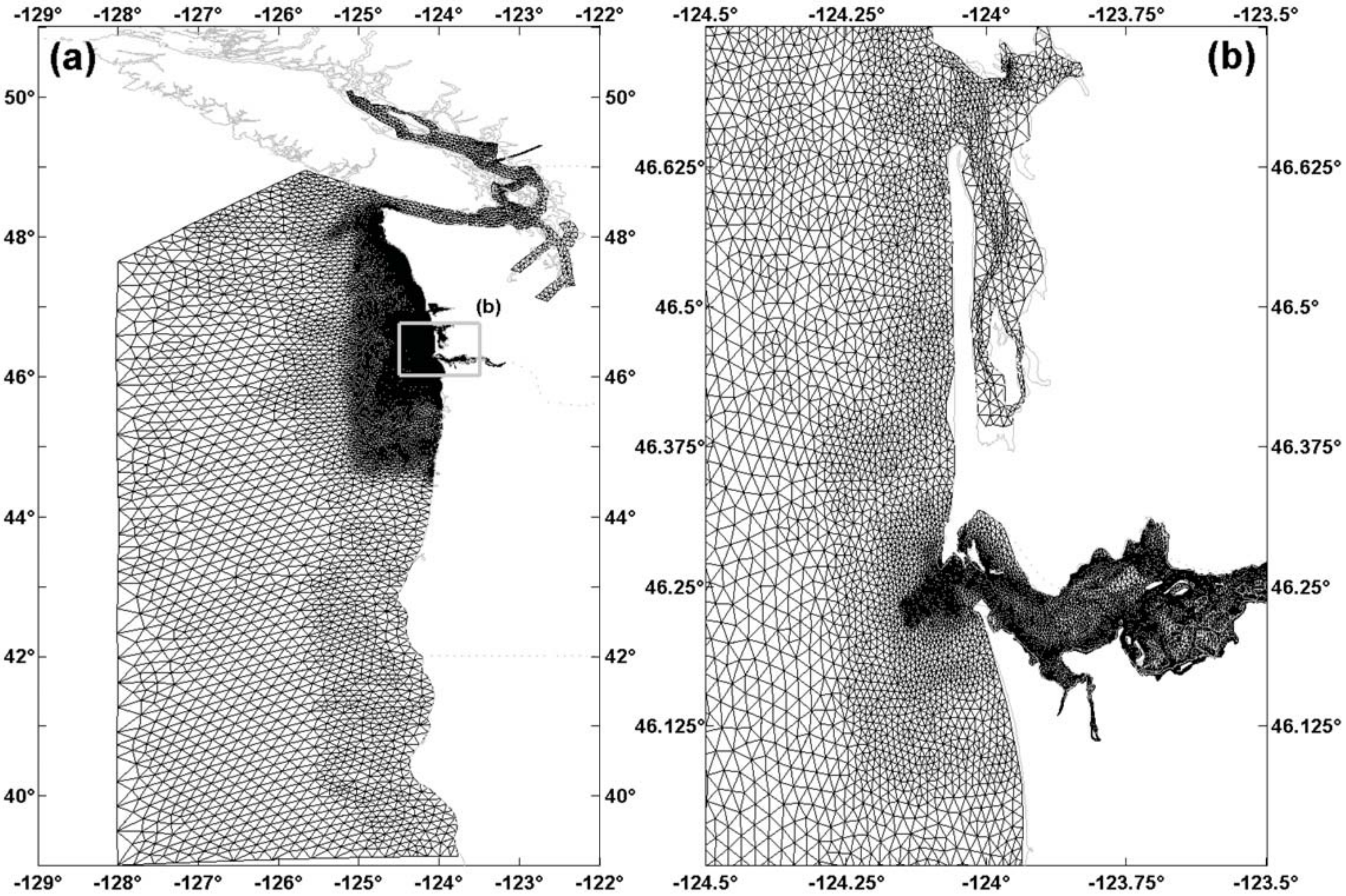

Figure 2.1 **(a)** Full model domain and **(b)** inside the Columbia River estuary and near the mouth of the Columbia River, showing the higher grid resolution in these regions.

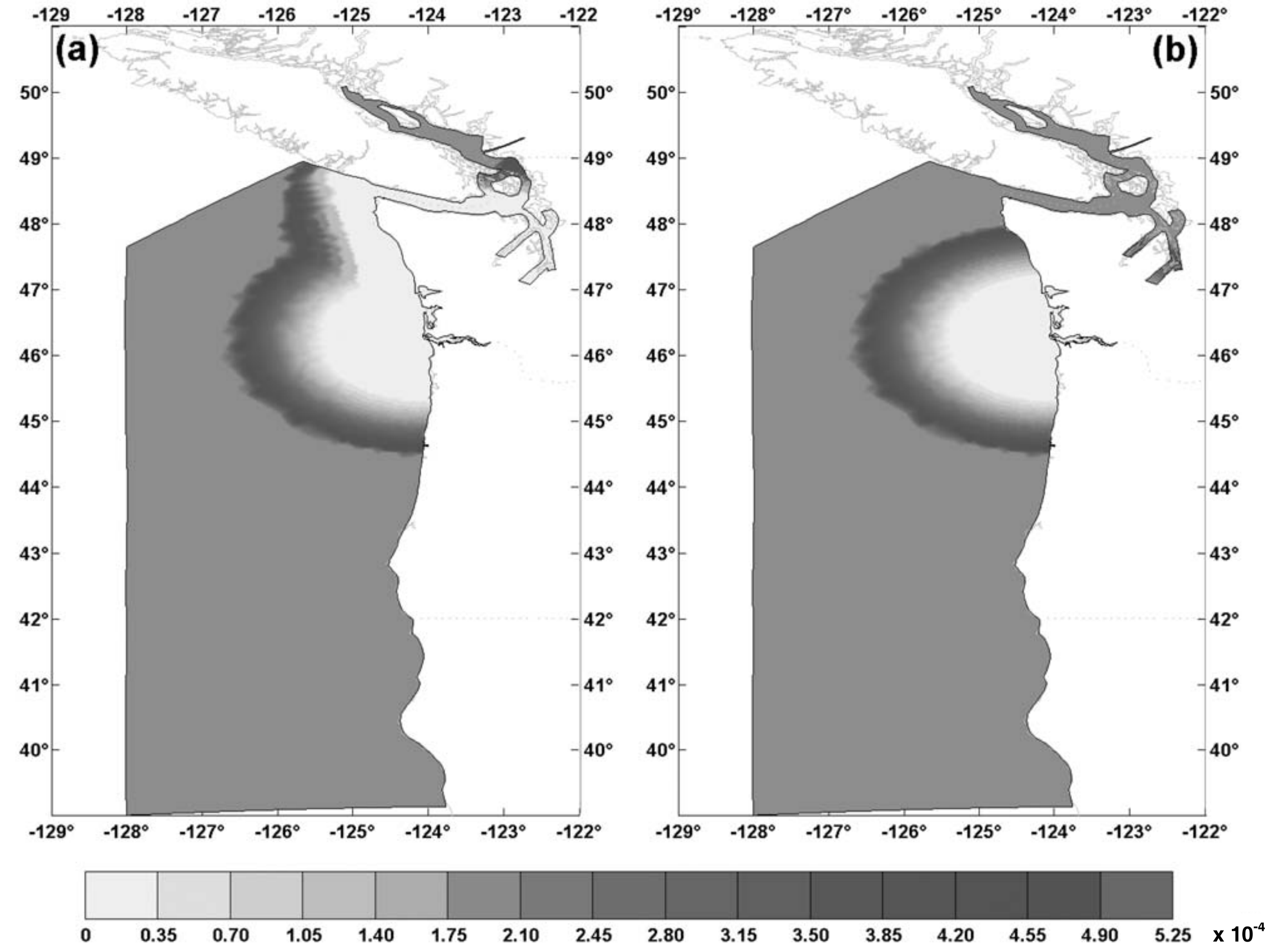

Figure 2.2 Nudging factors (γ) for the **(a)** UWM and **(b)** ELM SELFE Columbia River 1990 experiments.

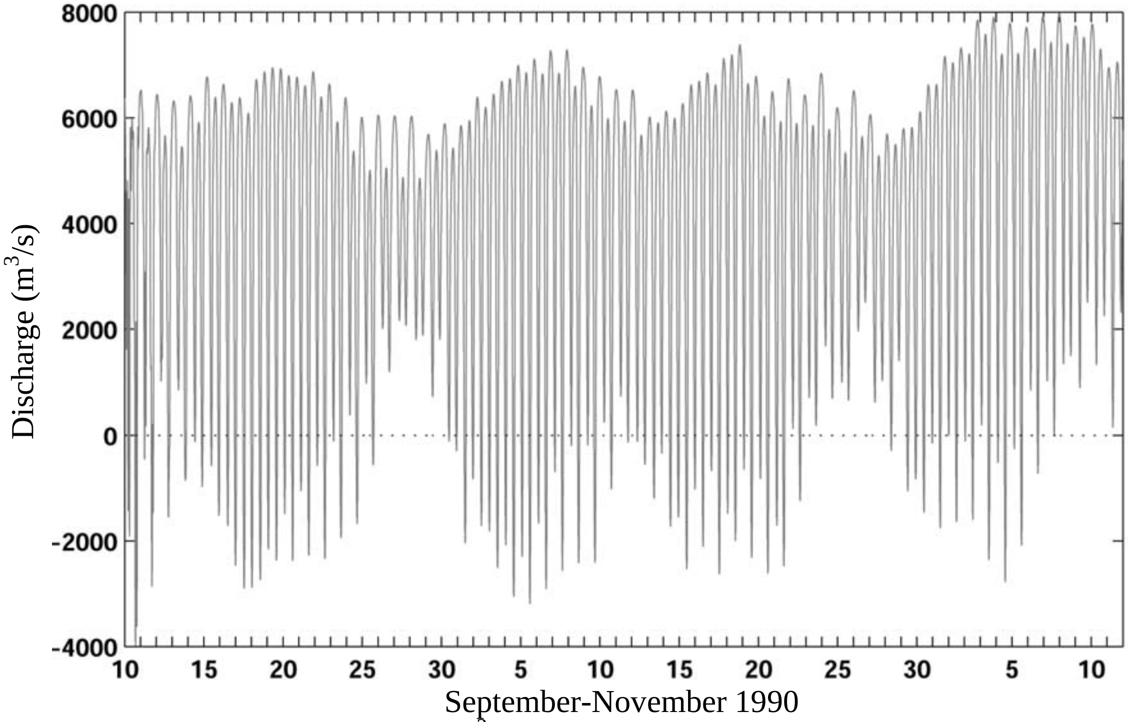

Figure 2.3 Estimated discharge (m^3/s) for the Columbia River estuary at Beaver Army Terminal used for model input.

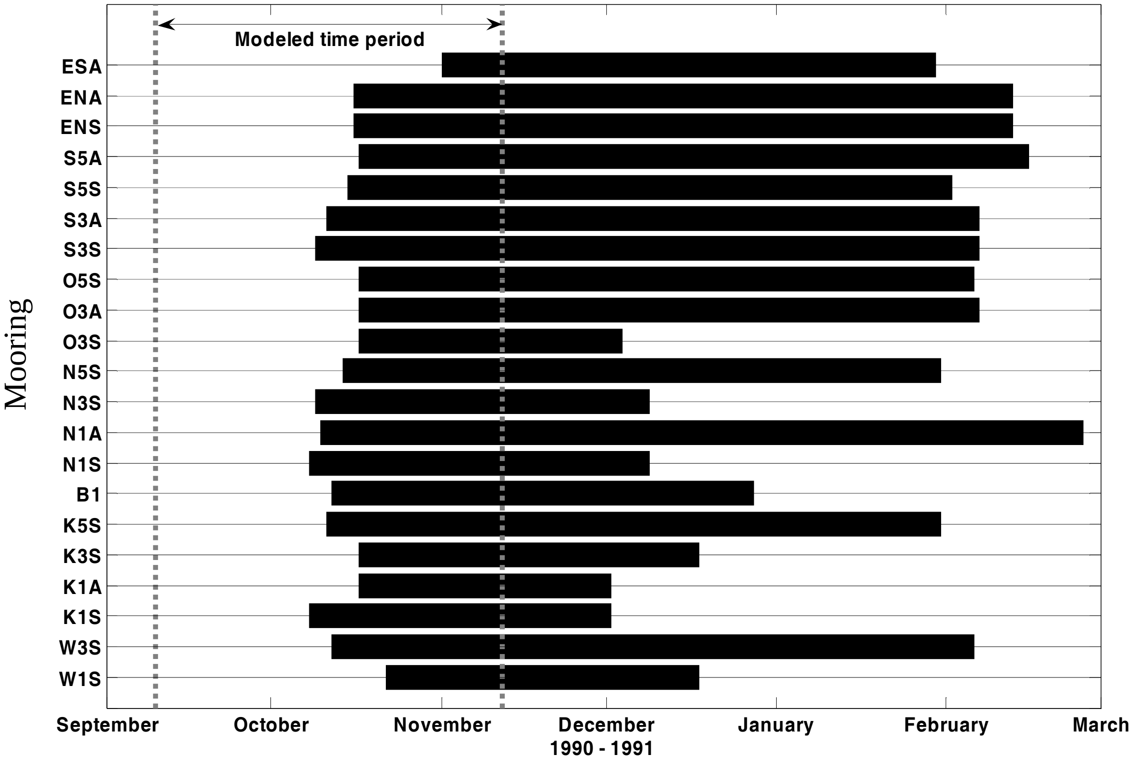

Figure 2.4 Availability of data from the 20 mooring locations of the Hickey et al. (1998) Columbia River plume field study providing observations. The modeled time period from September 10 – November 12, 1990 is also shown.

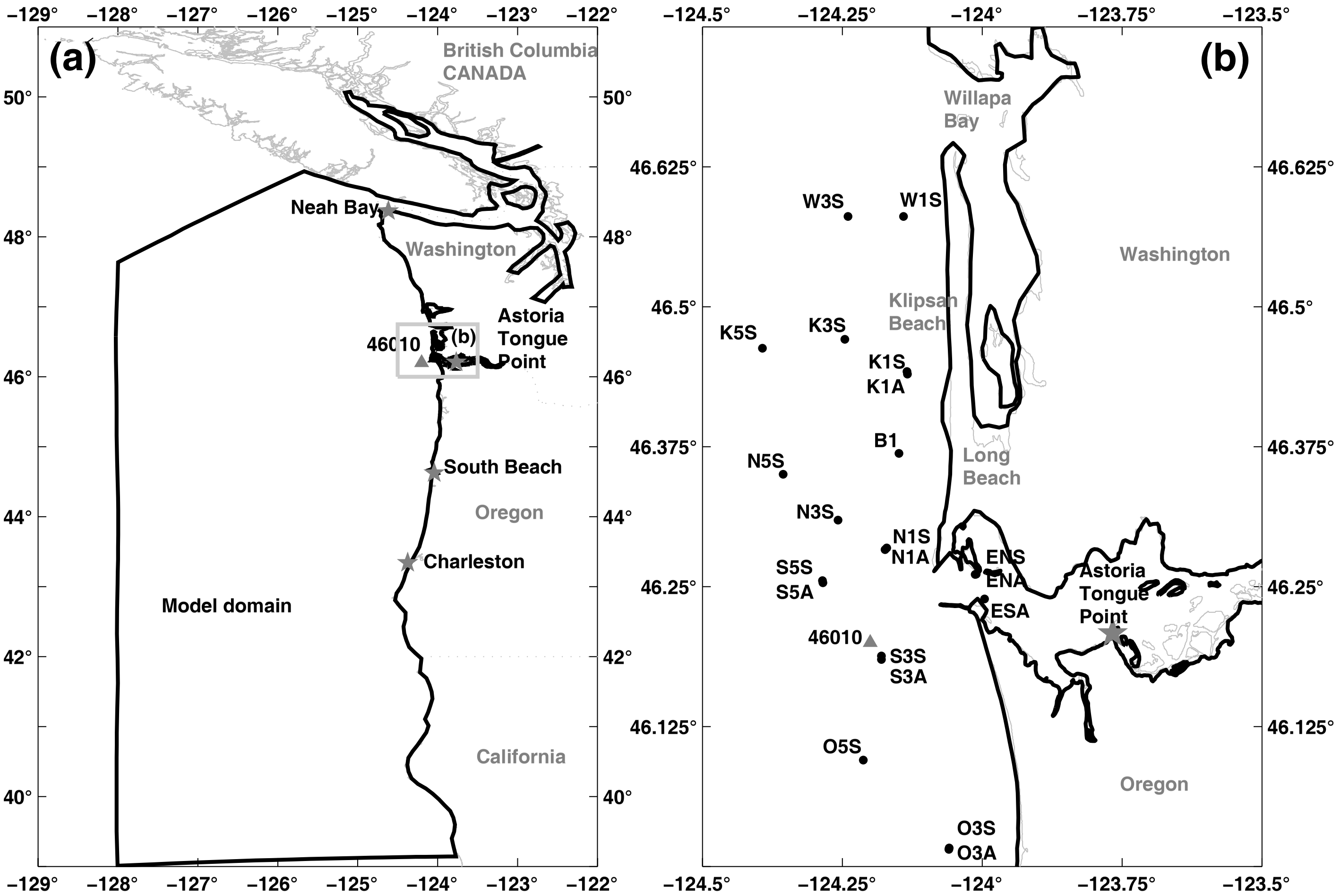

Figure 2.5 Locations of observations of **(a)** tidal water elevations (★) and **(b)** Hickey et al. (1998) moorings (●) used for model comparisons. The NDBC wind buoy 46010 is shown for reference (▲).

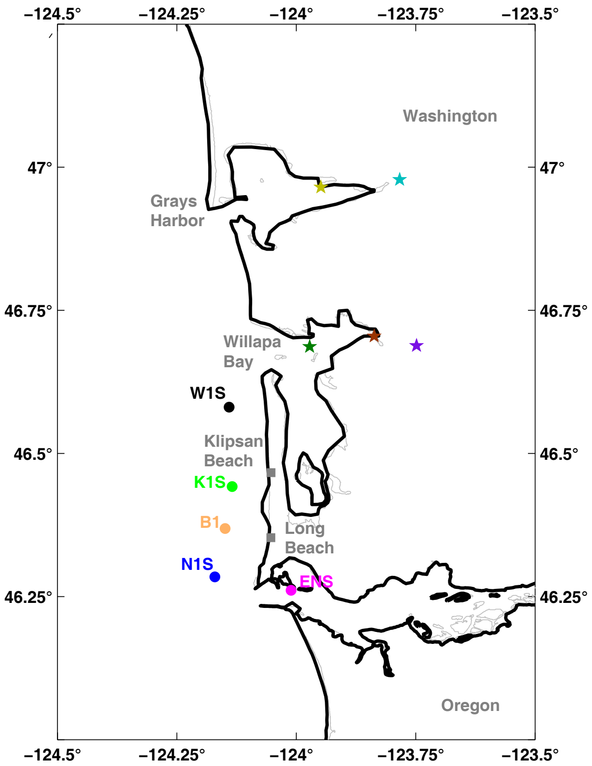

Figure 2.6 Location of moorings and casts used to compare the suggested temperature adjustment provided for W1S. Colors correspond to those of Figure 2.7.

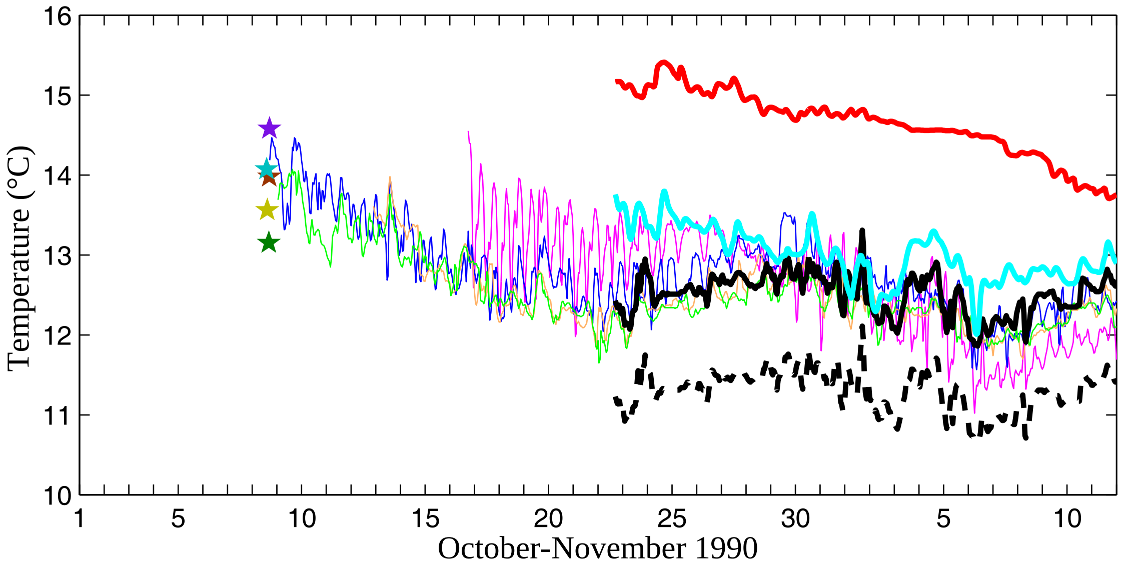

Figure 2.7 Comparison of modeled ELM (▬) and UWM (▬) and measured temperatures at 1m depth at the moorings ENS (▬), N1S (▬), B1 (▬), K1S (▬), and W1S with (▬ ▬) and without (▬) adjustment. Also included are the deepest recorded measurements from casts taken by [25] within Willapa Bay and Grays Harbor, shown as stars with colors corresponding to the locations in Figure 2.6.

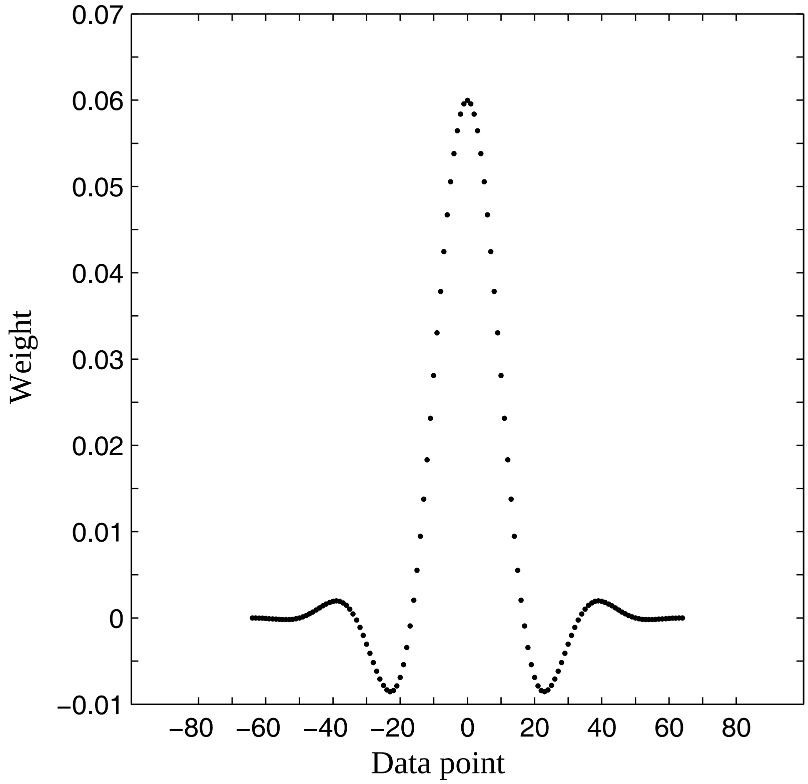

Figure 2.8 Filter weights from the pl64.m low pass filter, applied at each point in an hourly time series.

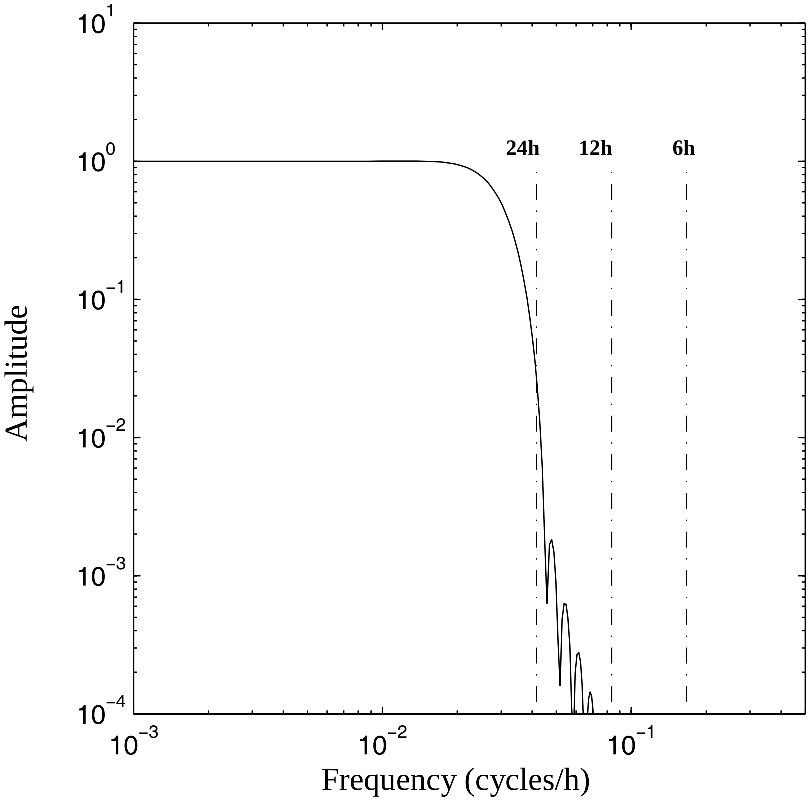

Figure 2.9 Amplitude transfer for the pl64.m low pass filter.

Table 2.1 Percent reduction in amplitude from the pl64.m low pass filter at each of the leading 8 tidal frequencies.

Tidal constituent	M2	S2	N2	K2	K1	O1	P1	Q1
Amplitude reduction (%)	99	99	99	99	98	91	97	87

Table 2.2 Vector (U_v) and scalar (U_s) mean speeds (m/s), mean directions (θ, in ° clockwise with respect to true north), principal major axis (λ_1, m/s), principal minor axis (λ_2, m/s), and principal major axis direction (θ_p, in ° clockwise with respect to true north) are given for modeled and measured winds at buoy locations as computed over the time period September 10 – November 12, 1990. Also shown are various metrics of comparison including the degrees of polarization, ratios of model to data vector and scalar mean speeds, and biases between the average model direction with respect to the average direction of the measured wind.

	DATA							NARR									
Station	$u_{d,v}$	$u_{d,s}$	θ_d	$\lambda_{1,d}^{0.5}$	$\lambda_{2,d}^{0.5}$	$\theta_{p,d}$	$\lambda_{2,d} / \lambda_{1,d}$	$u_{m,v}$	$u_{m,s}$	θ_m	$u_{m,v} / u_{d,v}$	$u_{m,s} / u_{d,s}$	$\theta_m - \theta_d$	$\lambda_{1,m}^{0.5}$	$\lambda_{2,m}^{0.5}$	$\theta_{p,m}$	$\lambda_{2,m} / \lambda_{1,m}$
46014	4.77	6.03	152	4.79	1.45	151	0.0920	5.77	6.53	162	1.21	1.08	10	4.25	0.911	165	0.0460
46022	2.71	4.52	183	4.65	1.40	176	0.0905	3.46	4.86	183	1.28	1.08	0	4.42	0.875	0.113	0.0392
46027	2.71	5.07	172	5.39	1.51	164	0.0782	1.45	3.57	177	0.537	0.705	5	3.85	1.10	174	0.0816
46040	0.602	5.27	350	5.54	2.17	171	0.153	0.667	5.52	58.9	1.11	1.05	69	5.95	1.58	7.84	0.0706
46010	1.50	5.82	24.3	6.05	2.78	177	0.211	1.94	4.80	45.4	1.29	0.825	21.1	4.65	2.51	10.0	0.291
46041	1.05	5.46	359	5.42	2.95	151	0.296	1.10	5.13	19.0	1.05	0.941	20	5.47	2.02	153	0.136
46004	4.57	8.74	66.7	6.58	5.10	139	0.601	4.64	8.58	66.0	1.02	0.982	-0.7	6.58	4.76	143	0.522
46006	2.17	6.48	68.5	5.75	3.62	28.0	0.395	2.78	6.06	65.7	1.28	0.934	-2.8	5.25	3.22	31.5	0.376
46012	4.05	5.08	139	3.76	1.32	145	0.123	4.21	4.88	150	1.04	0.961	11	2.76	1.56	162	0.320
46013	5.85	6.82	129	4.63	1.60	131	0.119	5.02	5.51	133	0.858	0.808	5	3.34	0.930	143	0.0777
46026	3.36	4.92	111	3.98	2.28	130	0.328	2.42	3.09	123	0.722	0.628	12	2.44	1.11	145	0.207
46028	6.19	6.80	146	4.39	1.17	143	0.0710	7.26	7.82	145	1.17	1.15	-1	4.27	0.635	141	0.0221
46036	3.97	7.65	72.8	5.79	4.62	162	0.637	4.37	7.88	73.0	1.10	1.03	0.2	5.82	4.89	170	0.706
46042	4.83	5.71	154	3.88	1.42	154	0.134	4.36	4.79	142	0.903	0.839	-12	2.77	0.698	140	0.0633
46181	0.266	4.02	105	4.94	1.26	13.3	0.0647	3.28	5.30	1.54	12.4	1.32	-104	4.17	3.25	171	0.605
46182	1.63	3.69	196	4.10	1.04	179	0.0643	0.730	1.46	82.9	0.448	0.396	-114	1.33	0.562	104	0.178
46184	4.67	9.12	63.1	6.69	5.70	115	0.726	5.08	9.29	57.6	1.09	1.02	-5.5	6.48	5.83	118	0.810
46204	1.53	6.94	356	7.04	3.71	124	0.278	1.91	6.14	32.6	1.25	0.885	37	6.08	3.17	147	0.273
46205	2.70	8.40	40.3	6.95	5.32	118	0.584	3.43	7.32	43.1	1.27	0.872	2.9	5.49	4.82	86.8	0.771
46206	0.572	5.64	350	6.02	2.88	104	0.229	1.43	5.55	25.2	2.49	0.984	35	5.68	2.40	131	0.179
46207	2.26	7.40	45.6	6.96	4.16	133	0.357	2.60	7.54	55.8	1.15	1.02	10.2	7.00	4.08	150	0.339
46208	6.19	6.78	344	4.21	2.31	158	0.302	2.72	8.05	61.1	0.440	1.19	77	7.56	4.07	135	0.291
Average of stations inside of hydrodynamic model domain						165	0.154				1.1	0.95	21			85	0.111
Standard Error of the sample with stations inside of hydrodynamic model domain						12	0.0860				0.3	0.15	25			87	0.0948

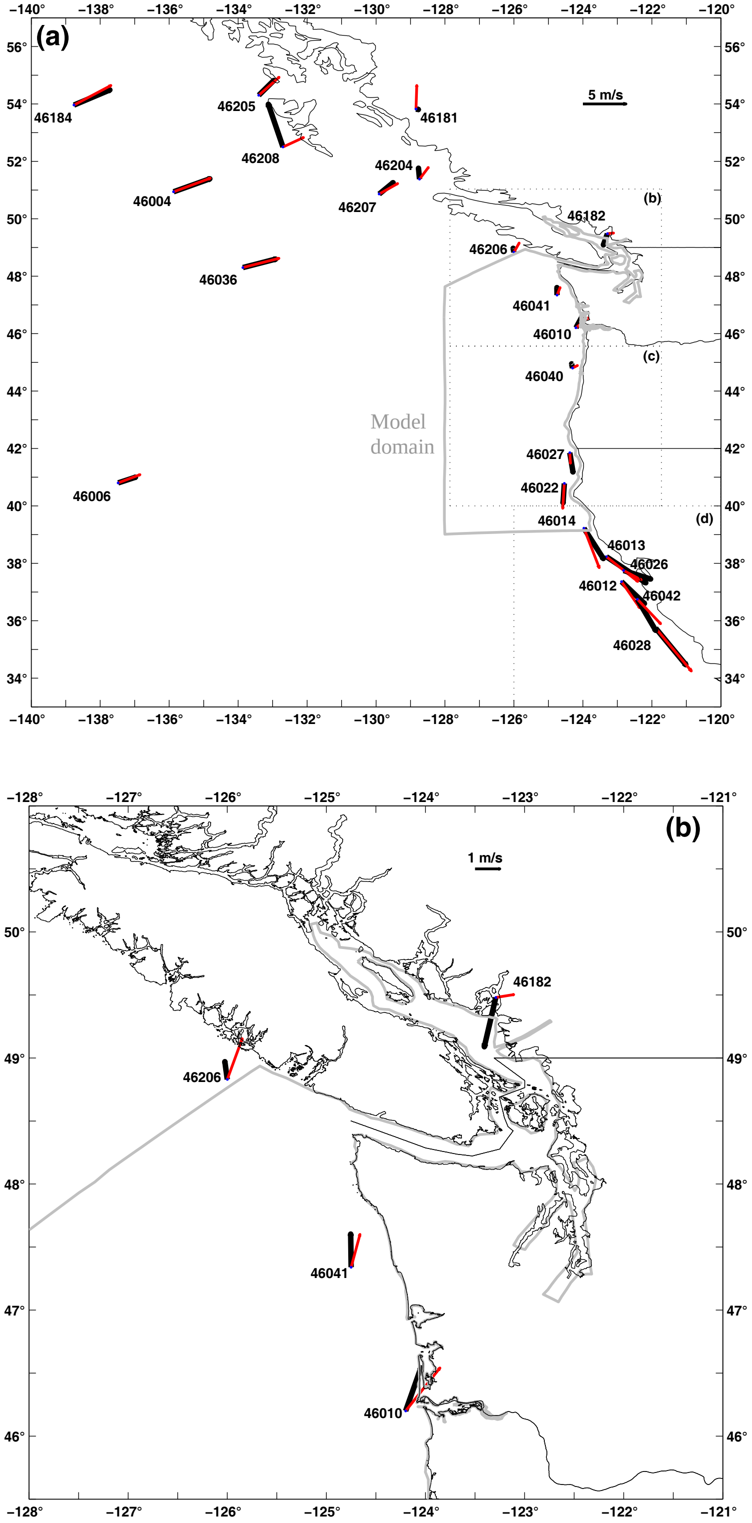

Figure 2.10 Vector mean measured (▬) and the NARR (▬) winds computed for the time period September 10 – November 12, 1990 for buoy locations **(a)** further offshore than the model domain, and near the **(b)** northern, **(c)** central, and **(d)** southern portions of the model domain.

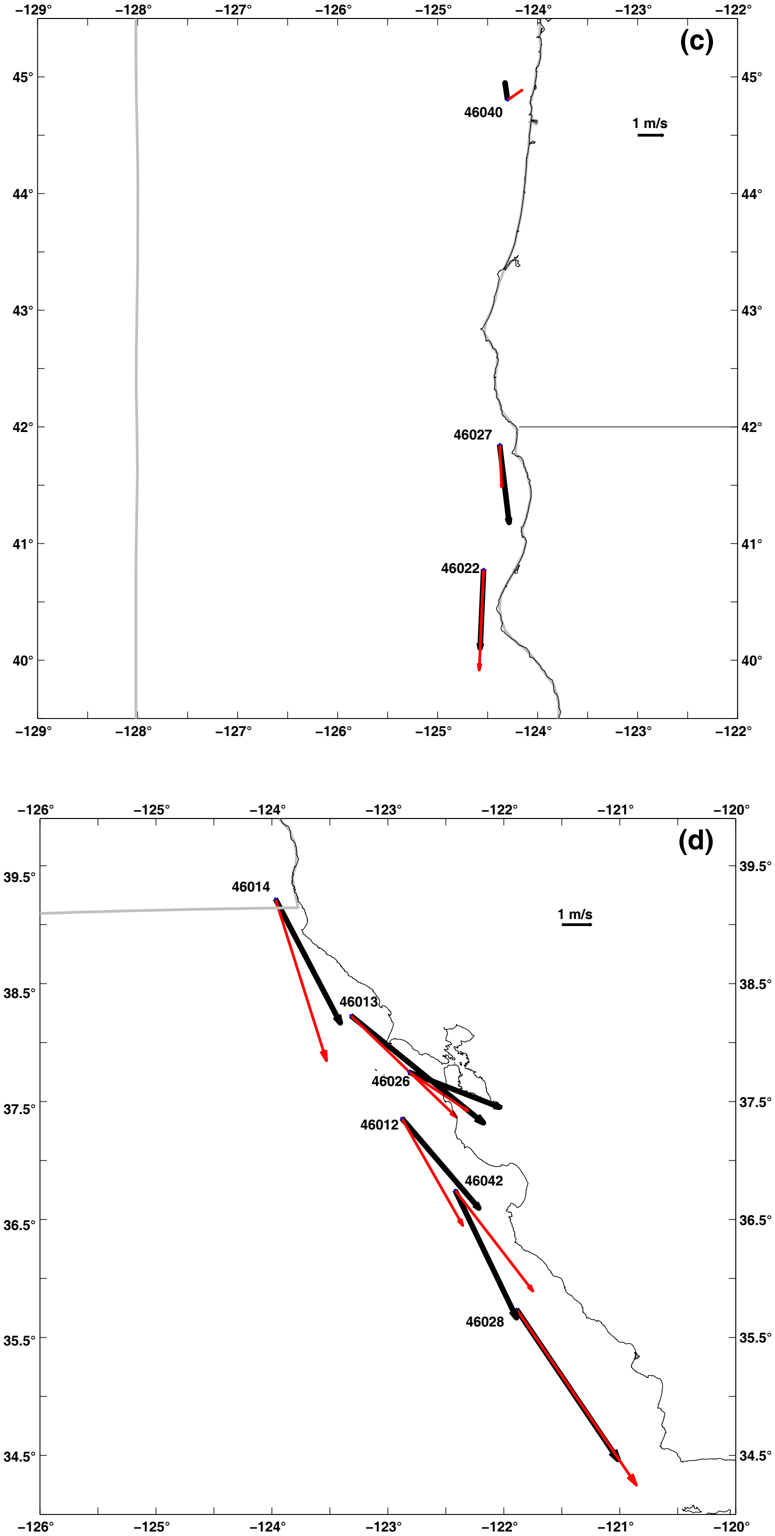

Figure 2.10 Continued.

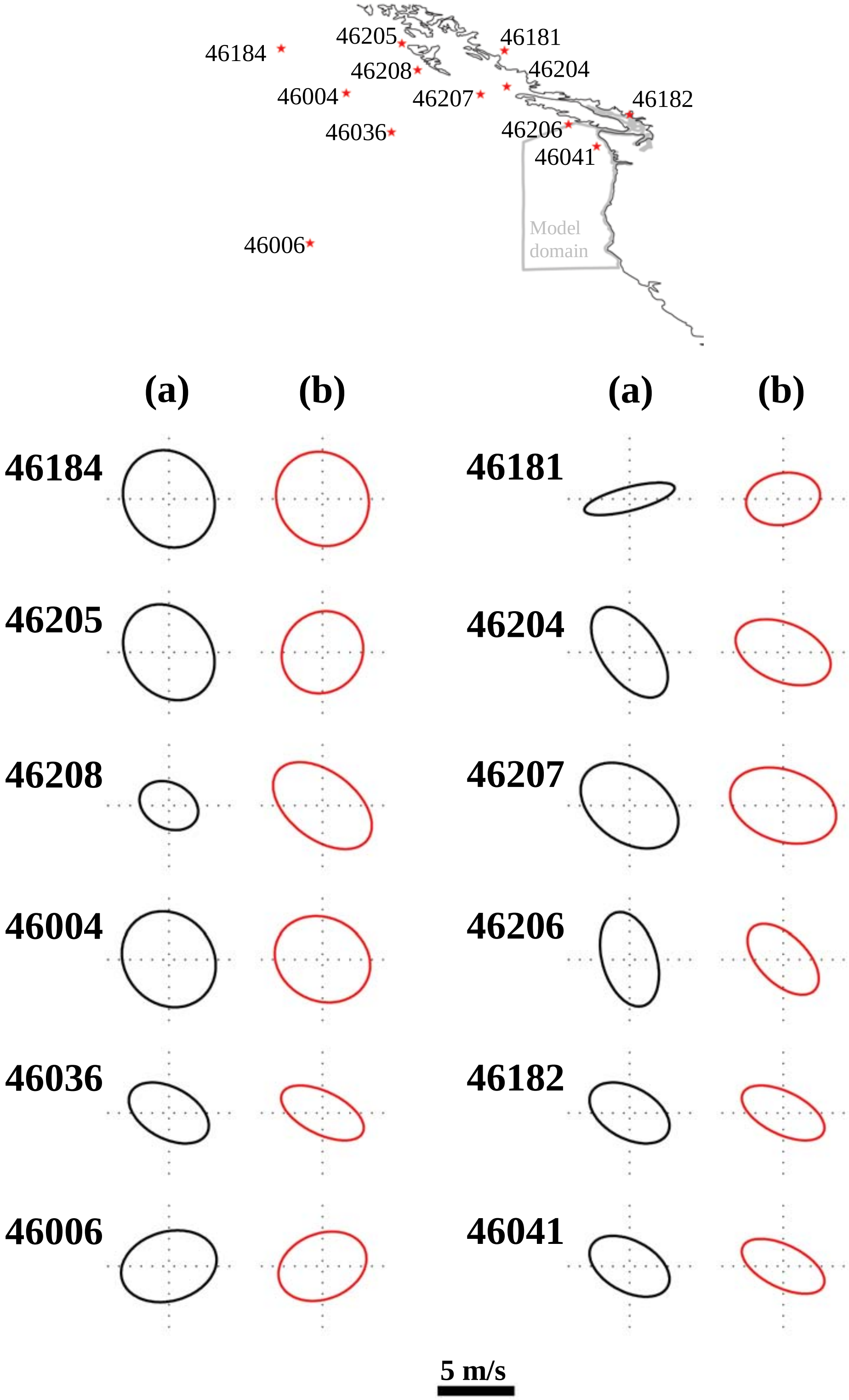

Figure 2.11 Principal ellipses for **(a)** observed (▬) and **(b)** NARR modeled (▬) winds computed for the time period September 10–November 12, 1990 for buoy locations within and outside of the model domain.

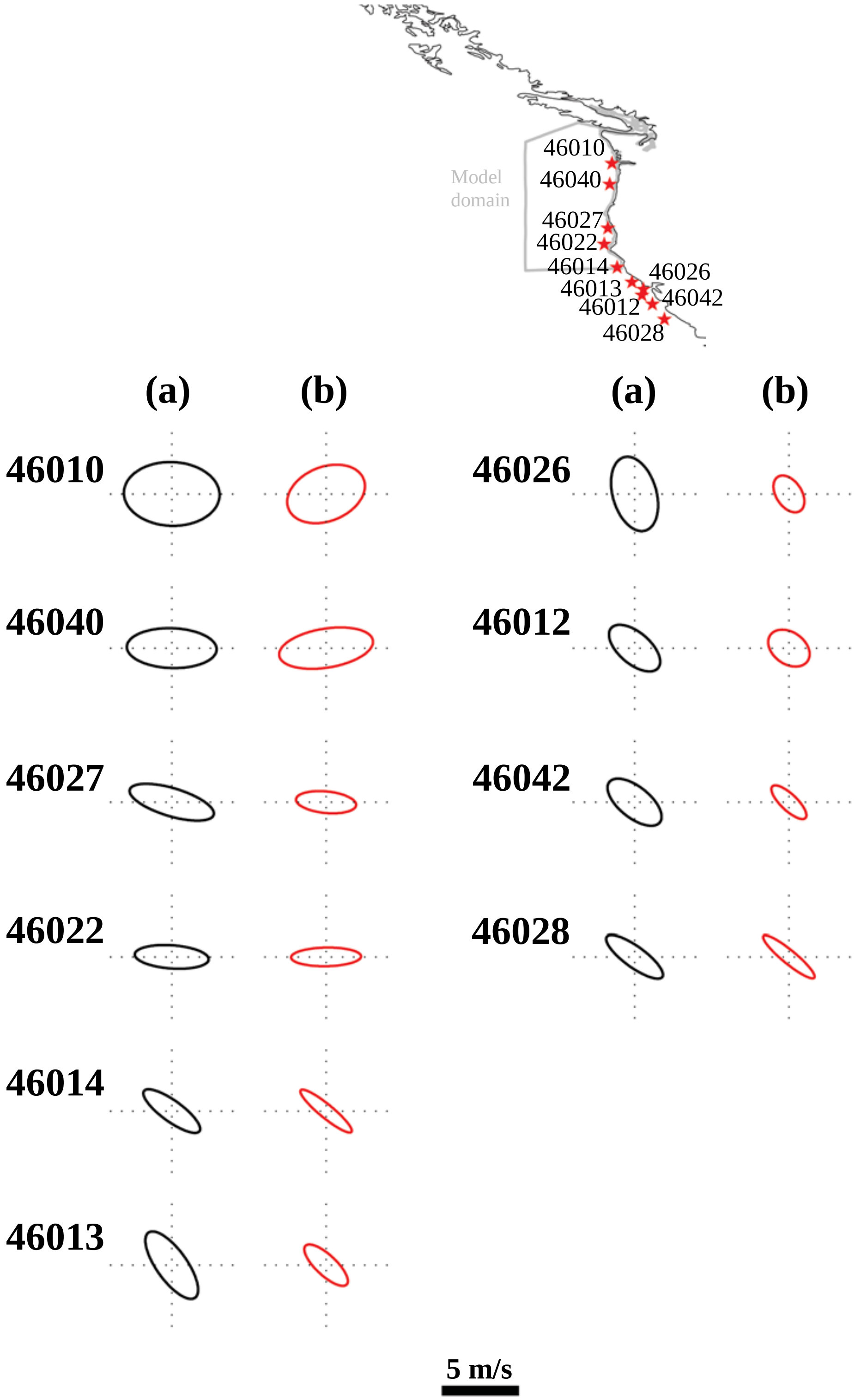

Figure 2.11 Continued.

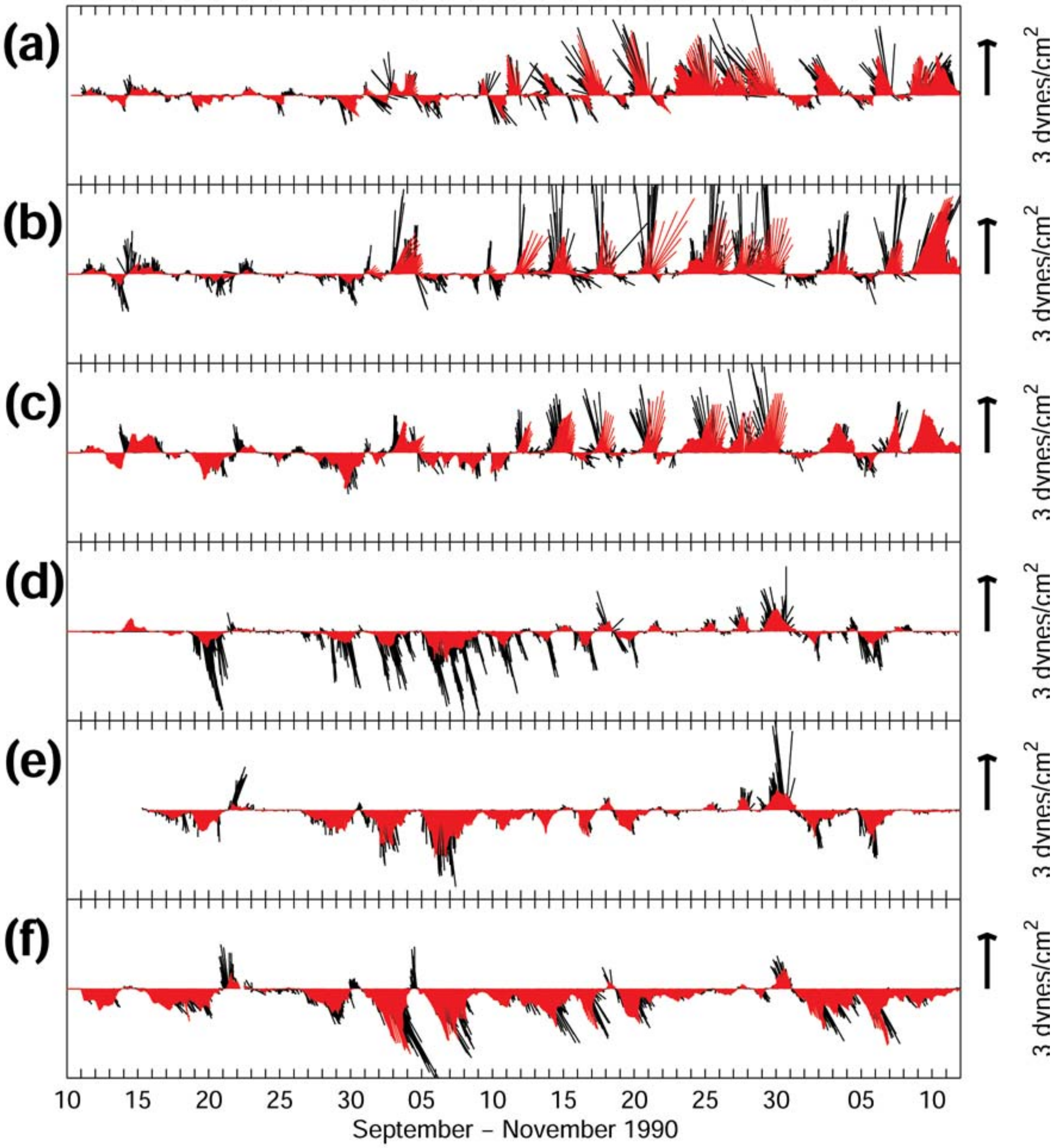

Figure 2.12 Wind stress computed for observed (▬) and NARR (▬) winds at buoys **(a)** 46041, **(b)** 46010, **(c)** 46040, **(d)** 46027, **(e)** 46022, and **(f)** 46014.

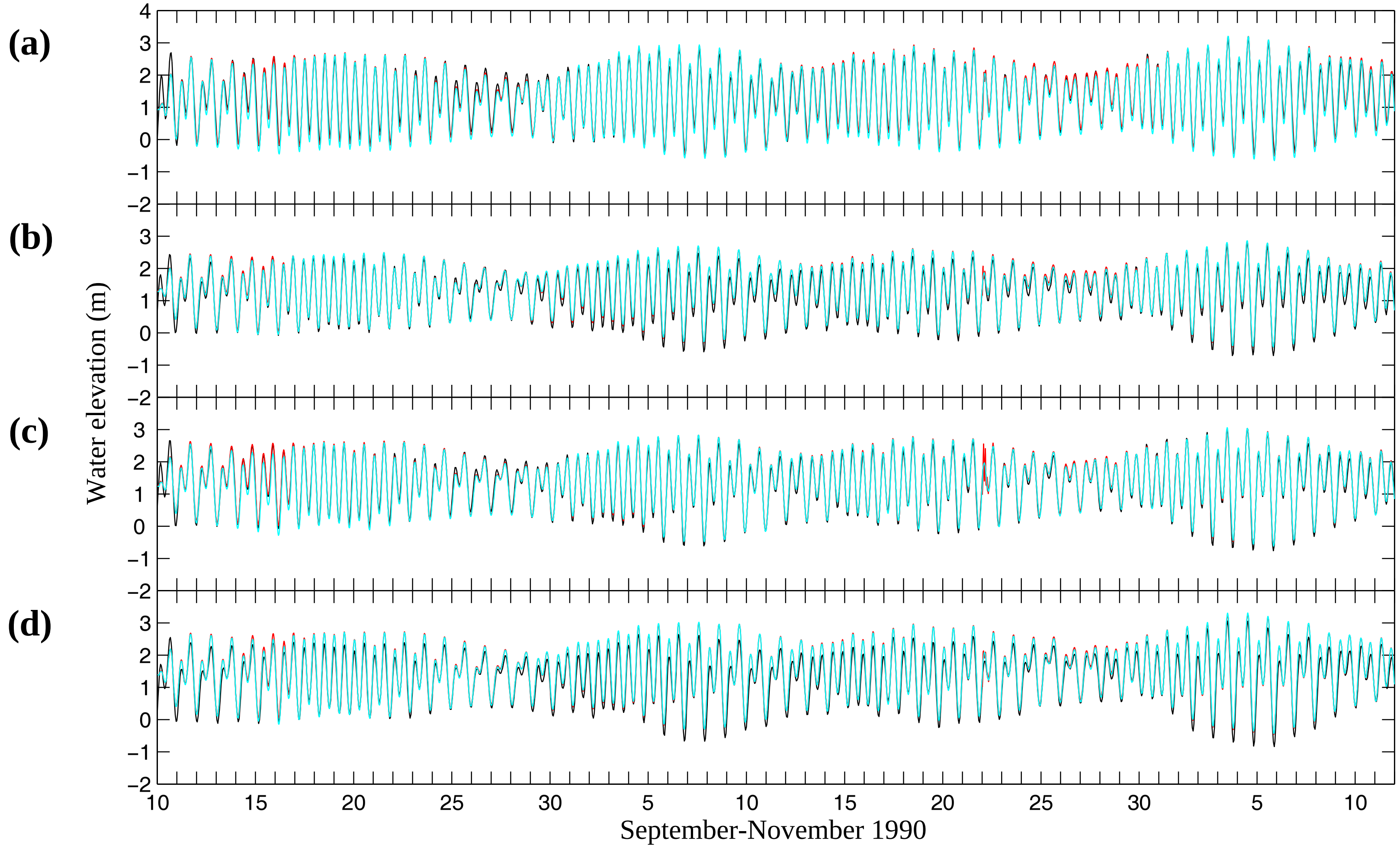

Figure 2.13 Modeled ELM (—) and UWM (—) and measured (—) water elevations (m), with RMS errors (m) given in square brackets for the ELM and UWM simulations respectively, for the tide gauge locations **(a)** Astoria Tongue Point [0.115 and 0.169], **(b)** Charleston [0.167 and 0.163], **(c)** South Beach [0.114 and 0.121], and **(d)** Neah Bay [0.252 and 0.245].

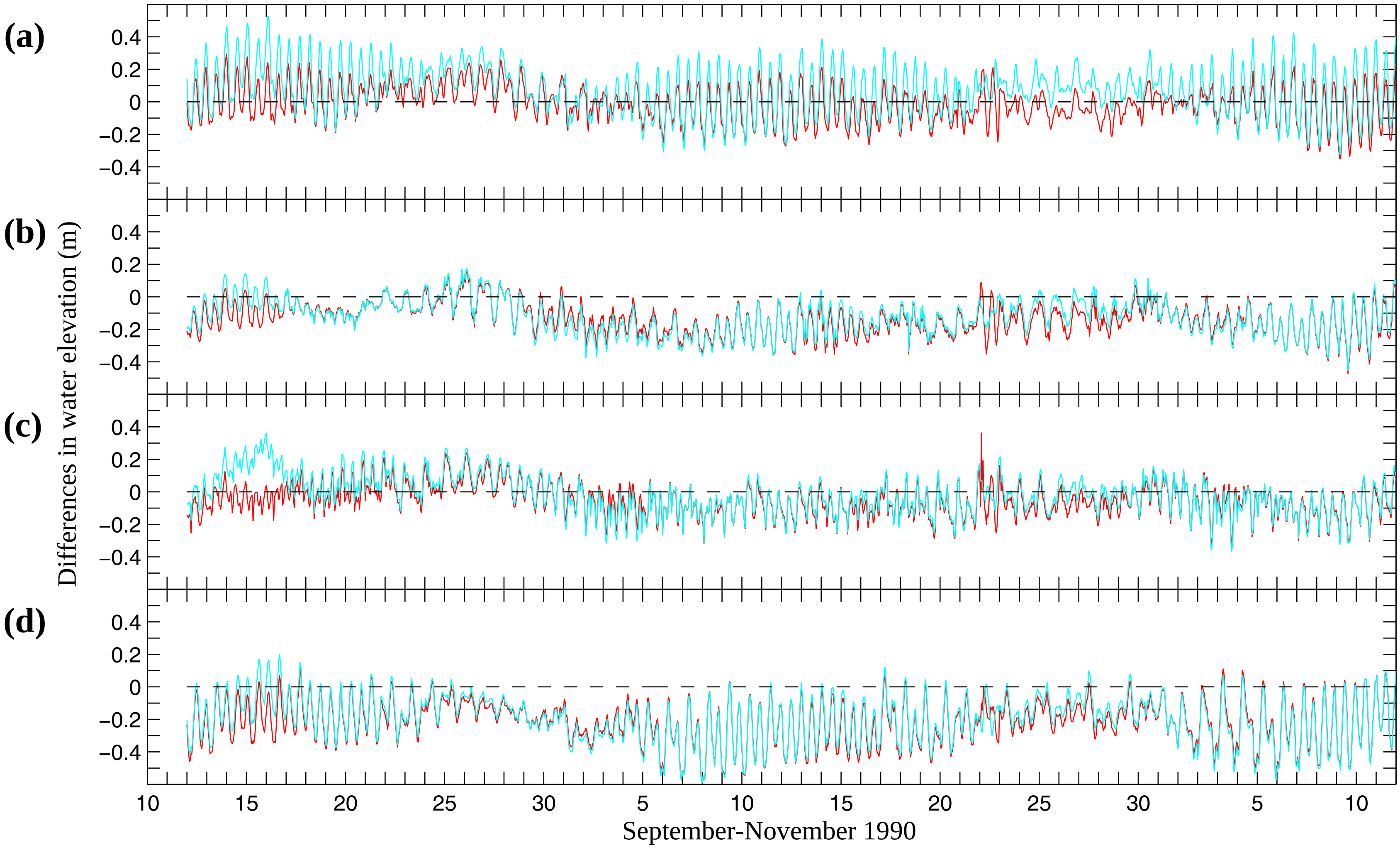

Figure 2.14 Differences [measured-modeled] in water elevation (m) for the ELM (▬) and UWM (▬) experiments for the tide gauge locations **(a)** Astoria Tongue Point, **(b)** Charleston, **(c)** South Beach, and **(d)** Neah Bay.

Table 2.3 Results of harmonic analysis of modeled and measured water elevations at the four tide gauge locations used for comparisons are shown as amplitudes (m) and phase (°UTC) for each of the 8 modeled constituents. Also shown are the differences (m) computed between the ELM and UWM model results and the measured values for each constituent and for model comparison between the ELM and UWM results.

	DATA				ELM						UWM					
	O1		K1		O1			K1			O1			K1		
Tide gauge site	amp	phase	amp	phase	amp	phase	D	amp	phase	D	amp	phase	D	amp	phase	D
Neah Bay	0.3092	216.99	0.4729	234.14	0.2757	214.83	0.035262	0.4381	237.94	0.046065	0.2762	215.11	0.034365	0.4385	237.97	0.045931
South Beach	0.2691	207.72	0.4175	224.76	0.2698	208.03	0.001617	0.4290	227.12	0.020883	0.2710	207.99	0.002287	0.4292	226.71	0.018559
Charleston	0.2483	206.59	0.3822	221.36	0.2561	202.87	0.018133	0.4122	221.32	0.030001	0.2561	202.90	0.018014	0.4122	221.30	0.030003
Astoria Tongue Point	0.2465	222.40	0.3921	242.91	0.2442	219.95	0.01074	0.4094	241.39	0.020304	0.2457	217.94	0.019169	0.4145	239.27	0.034022
	Q1		P1		Q1			P1			Q1			P1		
Tide gauge site	amp	phase	amp	phase	amp	phase	D	amp	phase	D	amp	phase	D	amp	phase	D
Neah Bay	0.0568	227.86	0.1565	241.21	0.0413	222.01	0.016269	0.1450	245.01	0.015233	0.0418	221.52	0.015939	0.1451	245.04	0.015212
South Beach	0.0489	217.50	0.1382	231.83	0.0428	210.84	0.008091	0.1420	234.19	0.006909	0.0425	211.83	0.007829	0.1420	233.78	0.006097
Charleston	0.0429	215.77	0.1265	228.43	0.0420	203.26	0.009293	0.1364	228.39	0.0099	0.0416	202.72	0.009689	0.1364	228.37	0.009901
Astoria Tongue Point	0.0411	242.57	0.1297	249.98	0.0347	236.09	0.007693	0.1355	248.46	0.006783	0.0356	235.39	0.007294	0.1372	246.34	0.011316
	K2		N2		K2			N2			K2			N2		
Tide gauge site	amp	phase	amp	phase	amp	phase	D	amp	phase	D	amp	phase	D	amp	phase	D
Neah Bay	0.0576	257.35	0.1651	203.13	0.0630	261.14	0.006711	0.1805	183.63	0.060463	0.0629	261.19	0.00666	0.1807	183.78	0.060115
South Beach	0.0615	244.31	0.1857	190.45	0.0612	251.75	0.007966	0.1785	174.40	0.051342	0.0615	251.65	0.007873	0.1795	174.57	0.05082
Charleston	0.0545	236.07	0.1696	182.71	0.0537	239.53	0.003363	0.1608	163.70	0.055246	0.0537	239.60	0.003427	0.1614	163.66	0.055367
Astoria Tongue Point	0.0624	276.56	0.1843	223.16	0.0669	279.05	0.005304	0.1911	200.47	0.074148	0.0716	277.28	0.009238	0.203	199.00	0.08309
	M2		S2		M2			S2			M2			S2		
Tide gauge site	amp	phase	amp	phase	amp	phase	D	amp	phase	D	amp	phase	D	amp	phase	D
Neah Bay	0.7839	216.71	0.2118	234.95	0.8832	213.05	0.112626	0.2316	238.74	0.024629	0.8826	213.08	0.111883	0.2312	238.79	0.024418
South Beach	0.8898	203.75	0.2258	221.91	0.8753	205.17	0.026241	0.2248	229.35	0.029252	0.8758	205.23	0.026757	0.2260	229.25	0.02892
Charleston	0.8163	196.42	0.2003	213.67	0.7896	194.11	0.041958	0.1973	217.13	0.012372	0.7896	194.18	0.041206	0.1972	217.20	0.012629
Astoria Tongue Point	0.9752	233.53	0.2294	254.16	0.9891	229.47	0.070954	0.2458	256.65	0.019376	1.0473	227.19	0.133008	0.2632	254.88	0.033941

Table 2.4 Average differences (m) between the measured and the ELM and UWM modeled constituents for the four gauge locations.

	O1	K1	Q1	P1	K2	N2	M2	S2
ELM	0.016438	0.029313	0.010336	0.009706	0.005836	0.0603	0.062945	0.021407
UWM	0.018459	0.032129	0.010188	0.010631	0.0068	0.062348	0.078213	0.024977

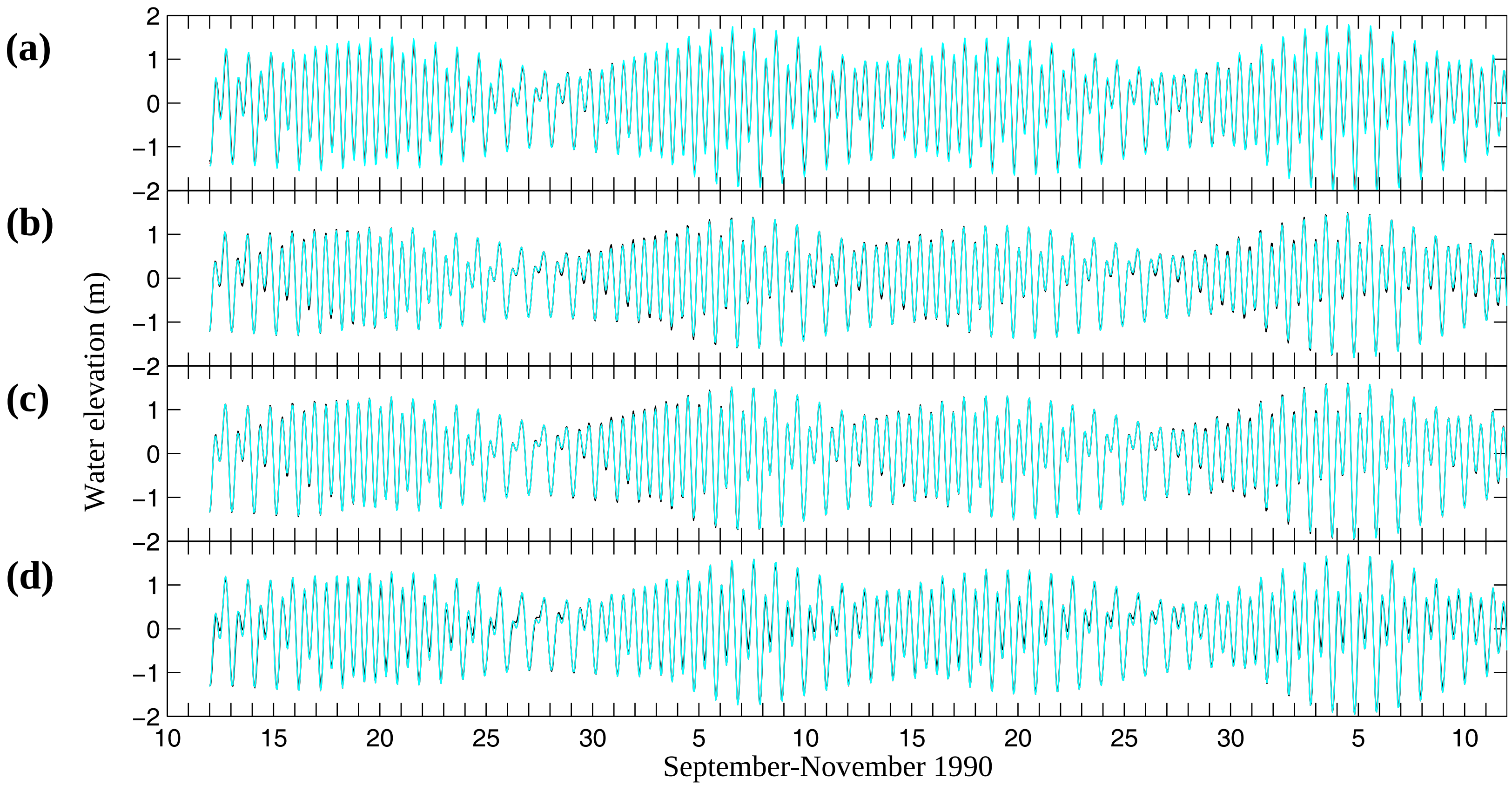

Figure 2.15 Modeled ELM (▬) and UWM (▬) and measured (▬) synthesized water elevations (m) after harmonic analysis using inference of the P1, K2, and NU2 for the measured and fitting only the modeled constituents to the modeled time series, with RMS errors (m) given in square brackets for the ELM and UWM simulations respectively, for the tide gauge locations **(a)** Astoria Tongue Point [0.0612 and 0.1063],**(b)** Charleston [0.0469 and 0.0466], **(c)** South Beach [0.0385 and 0.0376], and **(d)** Neah Bay [0.0953 and 0.0945].

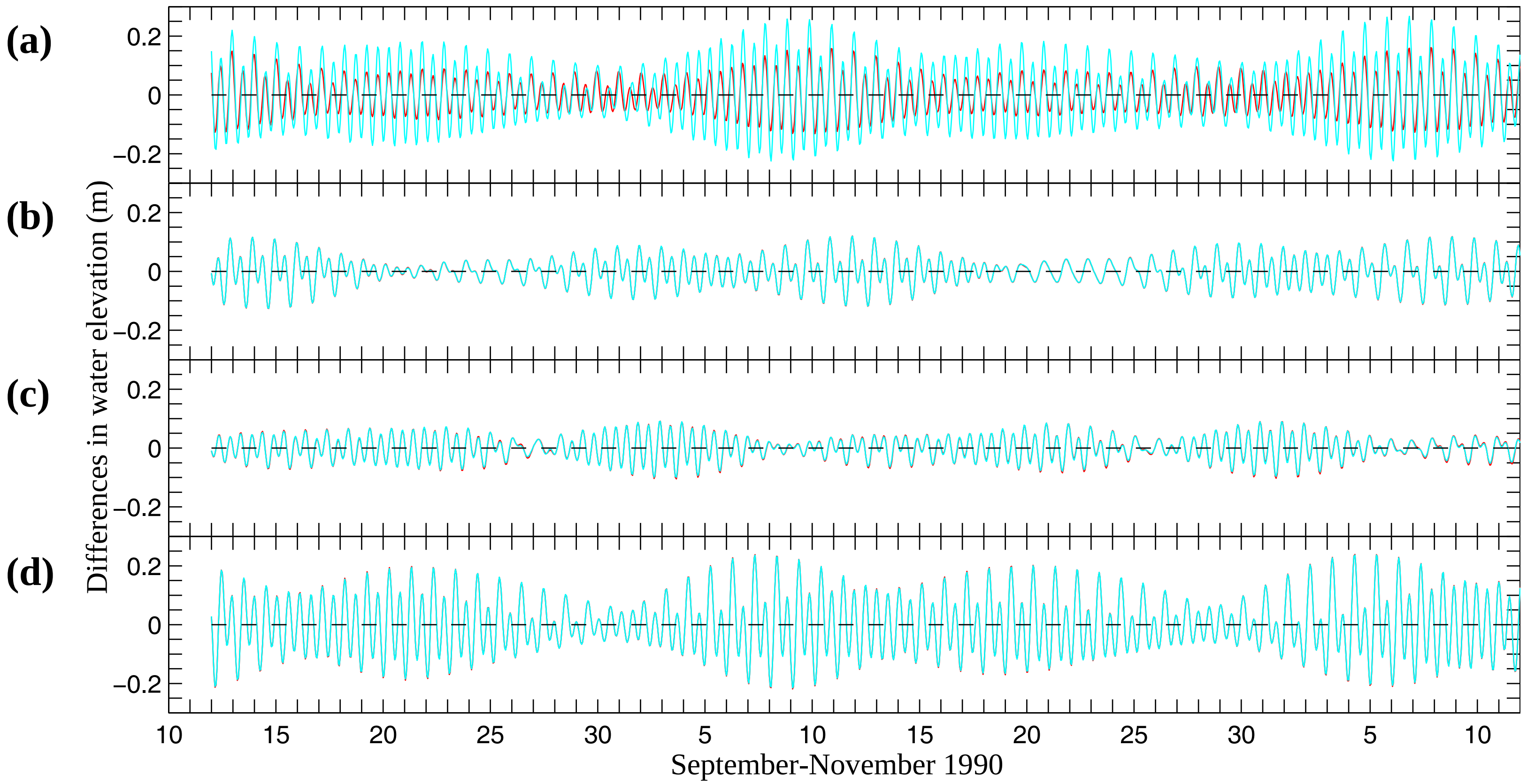

Figure 2.16 Differences [measured-modeled] in synthesized water elevation (m) after harmonic analysis using inference of the P1, K2, and NU2 for the measured and fitting only the modeled constituents to the modeled time series for the ELM (▬) and UWM (▬) experiments for the tide gauge locations **(a)** Astoria Tongue Point, **(b)** Charleston, **(c)** South Beach, and **(d)** Neah Bay.

Table 2.5 Results of harmonic analysis of modeled and measured water elevations using inference of the P1, K2, and NU2 for the observed and fitting only the modeled constituents from the model results at the four tide gauge locations used for comparisons are shown as amplitudes (m) and phase (°UTC) for each of the 8 modeled constituents. Also shown are the differences (m) computed between the ELM and UWM model results and the measured values for each constituent and for model comparison between the ELM and UWM results.

	DATA				ELM						UWM					
	O1		K1		O1			K1			O1			K1		
Tide gauge site	amplitude	phase	amplitude	phase	amplitude	phase	D	amplitude	phase	D	amplitude	phase	D	amplitude	phase	D
Neay Bay	0.3092	216.99	0.4883	232.22	0.2763	214.80	0.034745	0.4525	236.07	0.047738	0.2766	215.08	0.034026	0.453	236.09	0.047485
South Beach	0.2691	207.72	0.4336	222.42	0.2706	207.98	0.001936	0.4456	224.84	0.022105	0.2712	208.00	0.002481	0.4458	224.36	0.019247
Charleston	0.2483	206.59	0.3952	219.47	0.2567	202.81	0.018652	0.4267	219.51	0.031501	0.2565	202.87	0.01832	0.4268	219.48	0.0316
Astoria Tongue Point	0.2465	222.40	0.3987	239.74	0.2453	220.17	0.009645	0.4158	238.30	0.019928	0.2466	218.20	0.018069	0.421	236.16	0.033947
	Q1		P1		Q1			P1			Q1			P1		
Tide gauge site	amplitude	phase	amplitude	phase	amplitude	phase	D	amplitude	phase	D	amplitude	phase	D	amplitude	phase	D
Neay Bay	0.0569	227.83	0.1526	230.52	0.0414	221.47	0.016409	0.1414	234.37	0.014928	0.042	221.04	0.015985	0.1416	234.39	0.014817
South Beach	0.0488	217.52	0.1341	218.92	0.0427	210.21	0.008431	0.1378	221.34	0.00683	0.0426	211.70	0.007738	0.1379	220.86	0.00597
Charleston	0.0428	215.81	0.1242	217.57	0.0419	202.77	0.009659	0.1341	217.61	0.0099	0.0416	202.55	0.009817	0.1341	217.58	0.0099
Astoria Tongue Point	0.0411	242.57	0.1128	238.34	0.0355	235.00	0.007536	0.1176	236.90	0.005605	0.0366	234.36	0.007147	0.1191	234.76	0.009598
	K2		N2		K2			N2			K2			N2		
Tide gauge site	amplitude	phase	amplitude	phase	amplitude	phase	D	amplitude	phase	D	amplitude	phase	D	amplitude	phase	D
Neay Bay	0.0584	233.53	0.1667	193.61	0.0638	237.43	0.006813	0.1806	183.78	0.032821	0.0637	237.50	0.006778	0.1806	183.94	0.032384
South Beach	0.066	218.66	0.1864	180.85	0.0656	226.25	0.008719	0.1785	174.65	0.021252	0.0659	226.17	0.008639	0.1793	174.86	0.02038
Charleston	0.058	212.02	0.1705	172.67	0.0571	215.58	0.003687	0.1607	163.90	0.027143	0.057	215.66	0.003787	0.1611	163.87	0.027112
Astoria Tongue Point	0.0771	257.99	0.184	212.1	0.0822	260.86	0.006474	0.1913	201.16	0.036506	0.0881	259.09	0.011113	0.2032	199.65	0.04612
	M2		S2		M2			S2			M2			S2		
Tide gauge site	amplitude	phase	amplitude	phase	amplitude	phase	D	amplitude	phase	D	amplitude	phase	D	amplitude	phase	D
Neay Bay	0.7839	216.71	0.2286	239.13	0.8828	213.10	0.111926	0.2496	243.03	0.026557	0.8822	213.12	0.111252	0.2493	243.10	0.026495
South Beach	0.8898	203.75	0.2439	227.06	0.8748	205.20	0.026898	0.2423	234.65	0.03222	0.8751	205.26	0.027512	0.2435	234.57	0.031922
Charleston	0.8162	196.42	0.2151	218.52	0.7892	194.15	0.041713	0.2115	222.08	0.013731	0.7891	194.22	0.041035	0.2113	222.16	0.014065
Astoria Tongue Point	0.9752	233.53	0.2355	260.39	0.9894	229.53	0.070017	0.2509	263.26	0.019631	1.0475	227.24	0.132387	0.2688	261.49	0.033649

Table 2.6 Average differences (m) between the measured and the ELM and UWM modeled constituents as in Table 2.5 for the four tide gauge locations.

	O1	K1	Q1	P1	K2	N2	M2	S2
ELM	0.016244	0.030318	0.010509	0.009316	0.006423	0.02943	0.062639	0.023035
UWM	0.018224	0.03307	0.010172	0.010071	0.007579	0.031499	0.078046	0.026533

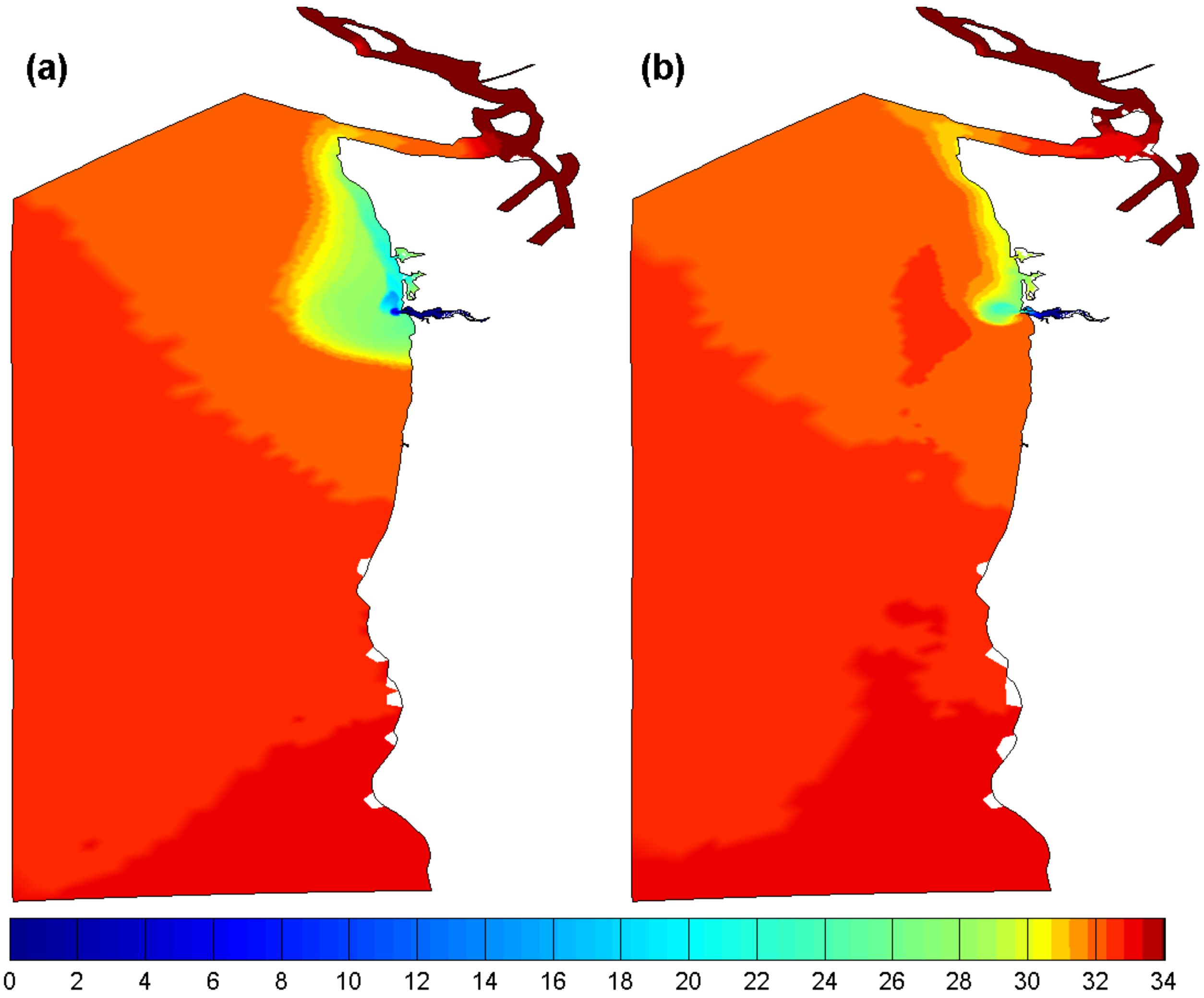

Figure 2.17 Surface salinity contours (psu) for the final time step (November 12, 1990) of the **(a)** ELM and **(b)** UWM model simulations.

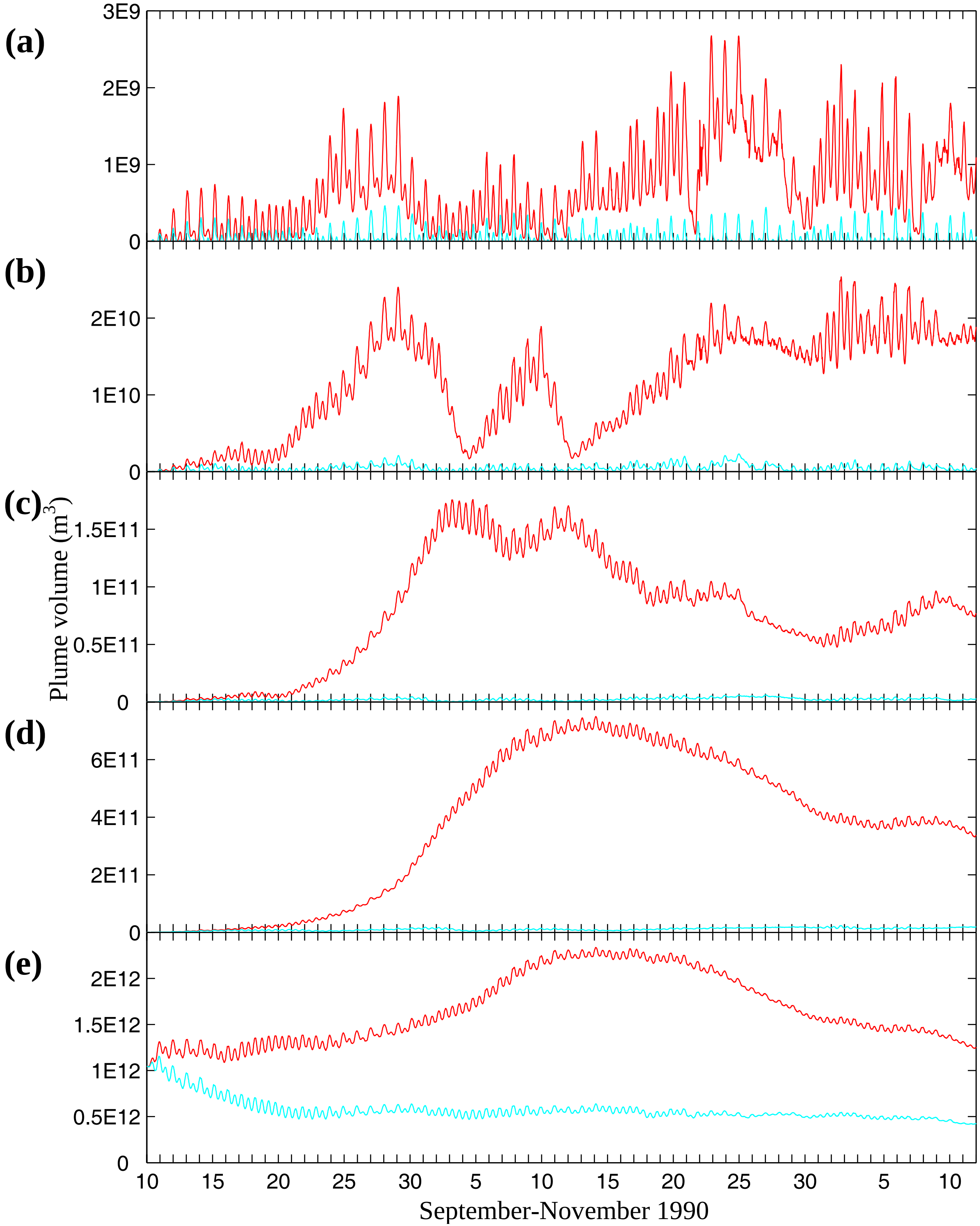

Figure 2.18 Plume volumes (m^3) computed for the **(a)** 20, **(b)** 26, **(c)** 28, **(d)** 30, and **(e)** 32 psu salinity contours for the ELM (▬) and UWM (▬) model results.

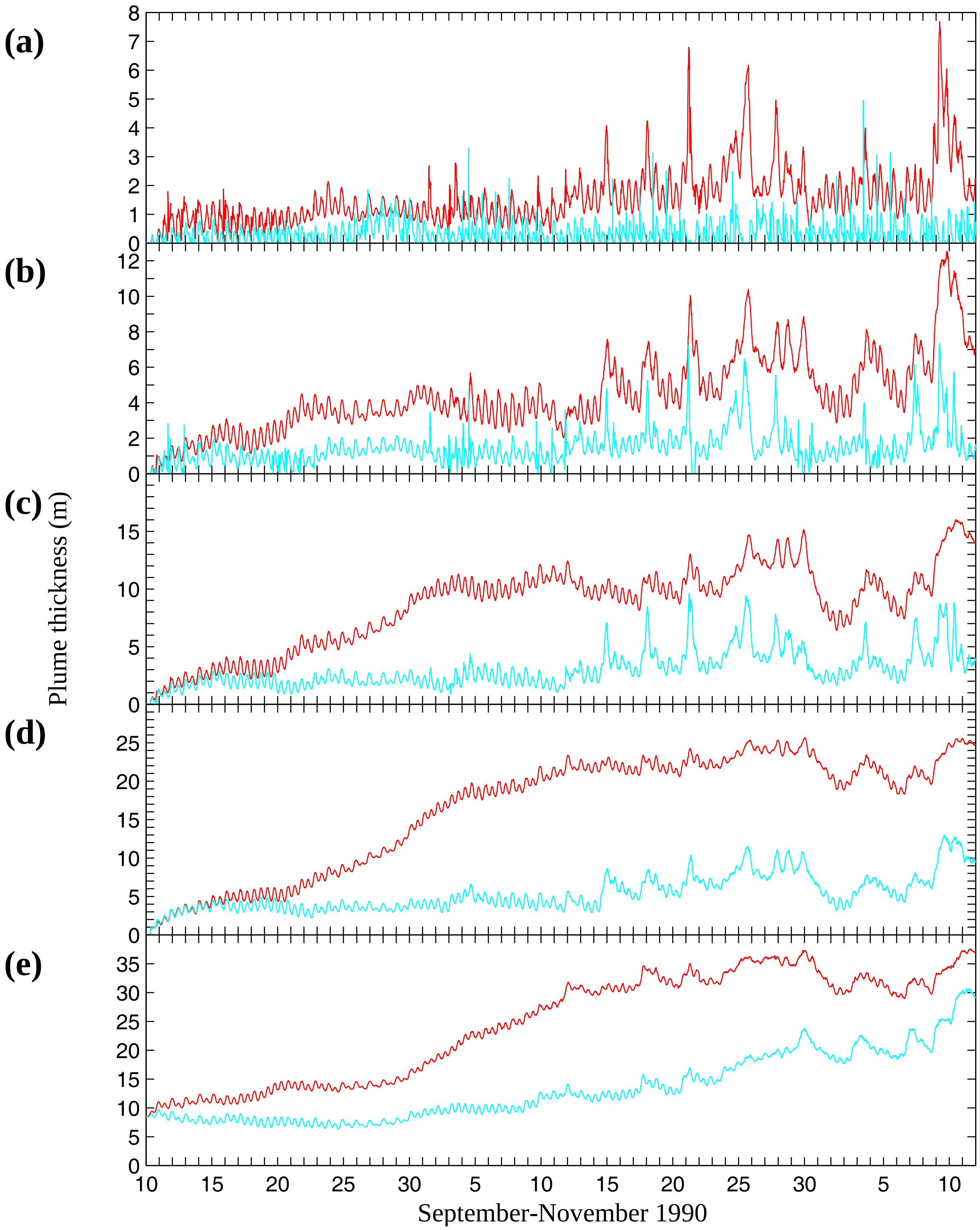

Figure 2.19 Plume thickness (m) computed for the **(a)** 20, **(b)** 26, **(c)** 28, **(d)** 30, and **(e)** 32 psu salinity contours for the ELM (▬) and UWM (▬) model results.

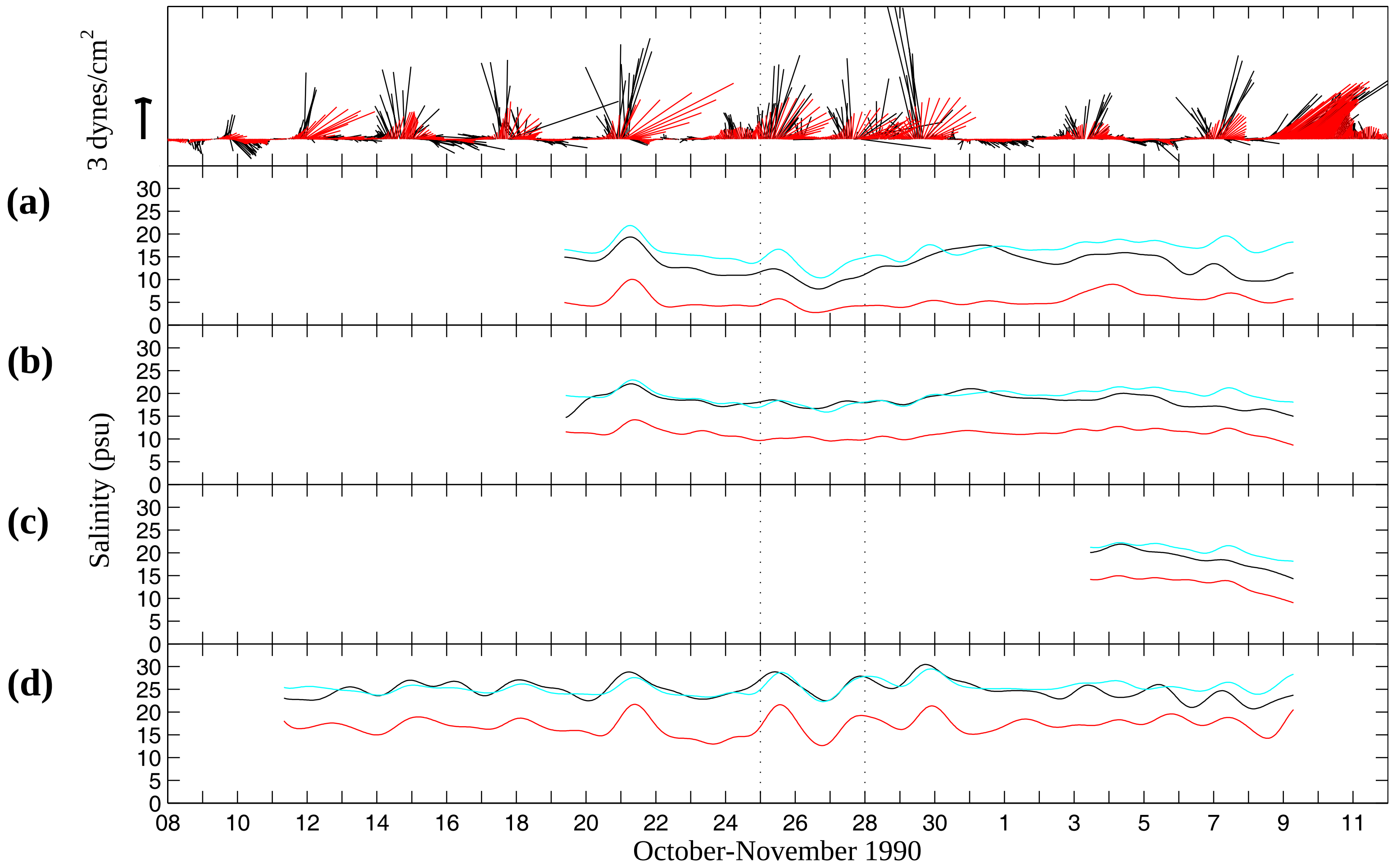

Figure 2.20 Low pass filtered salinities (psu) for ELM (▬) and UWM (▬) model results and measured data (▬) for the instruments with nominal depths: **(a)** ENS at 1m, **(b)** ENS at 5m, **(c)** ENA at 8m, **(d)** N1S at 1m, **(e)** N3S at 1m, **(f)** B1 at 1m, **(g)** K1S at 1m, **(h)** K3S at 1m, **(i)** W1S at 1m, **(j)** W3S at 1m, **(k)** S3S at 1m, **(l)** S5S at 5m, **(m)** N5S at 1m, and **(n)** K5S at 1m. Modeled and measured wind stress at buoy 46010 is shown for reference.

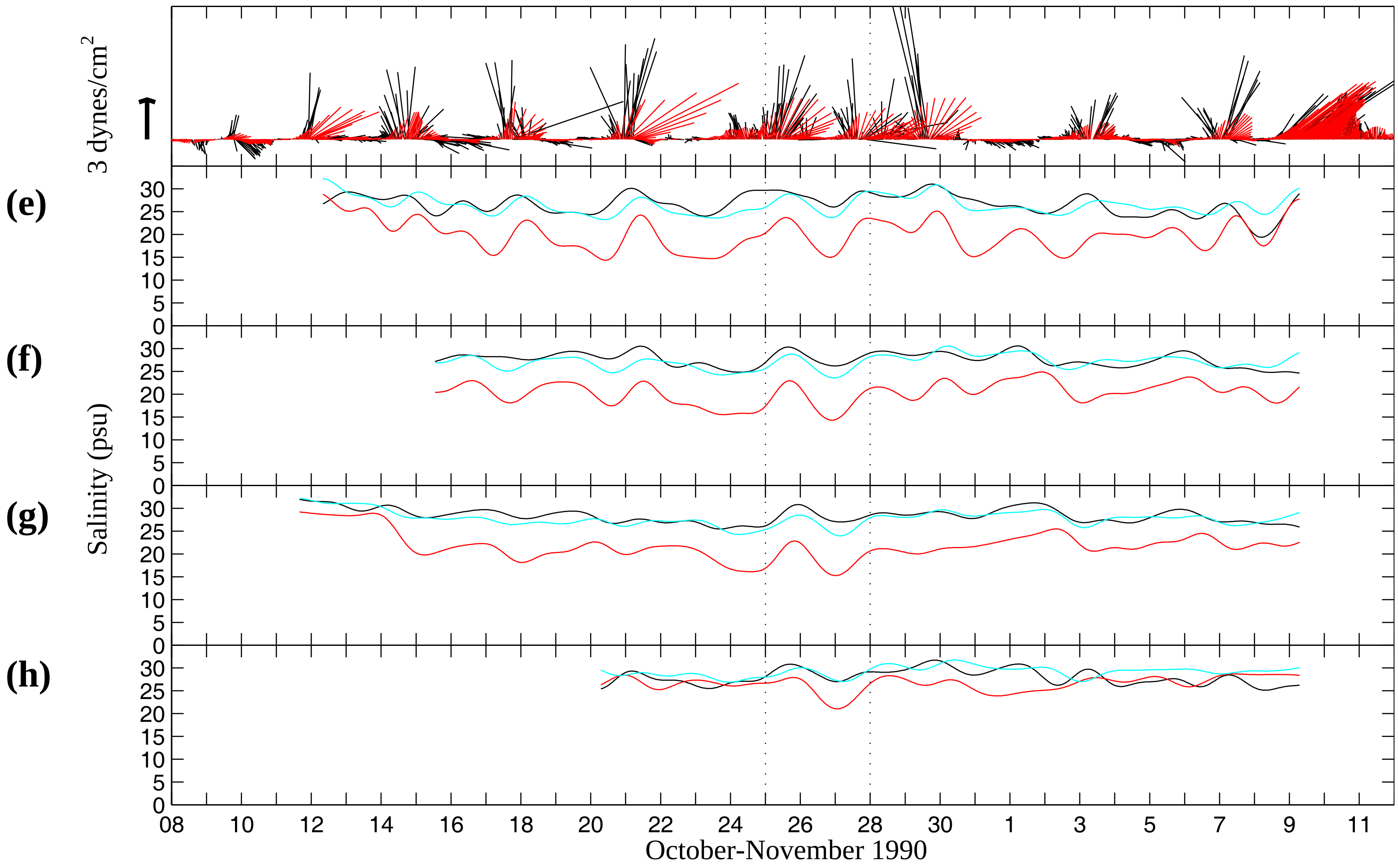

Figure 2.20 Continued.

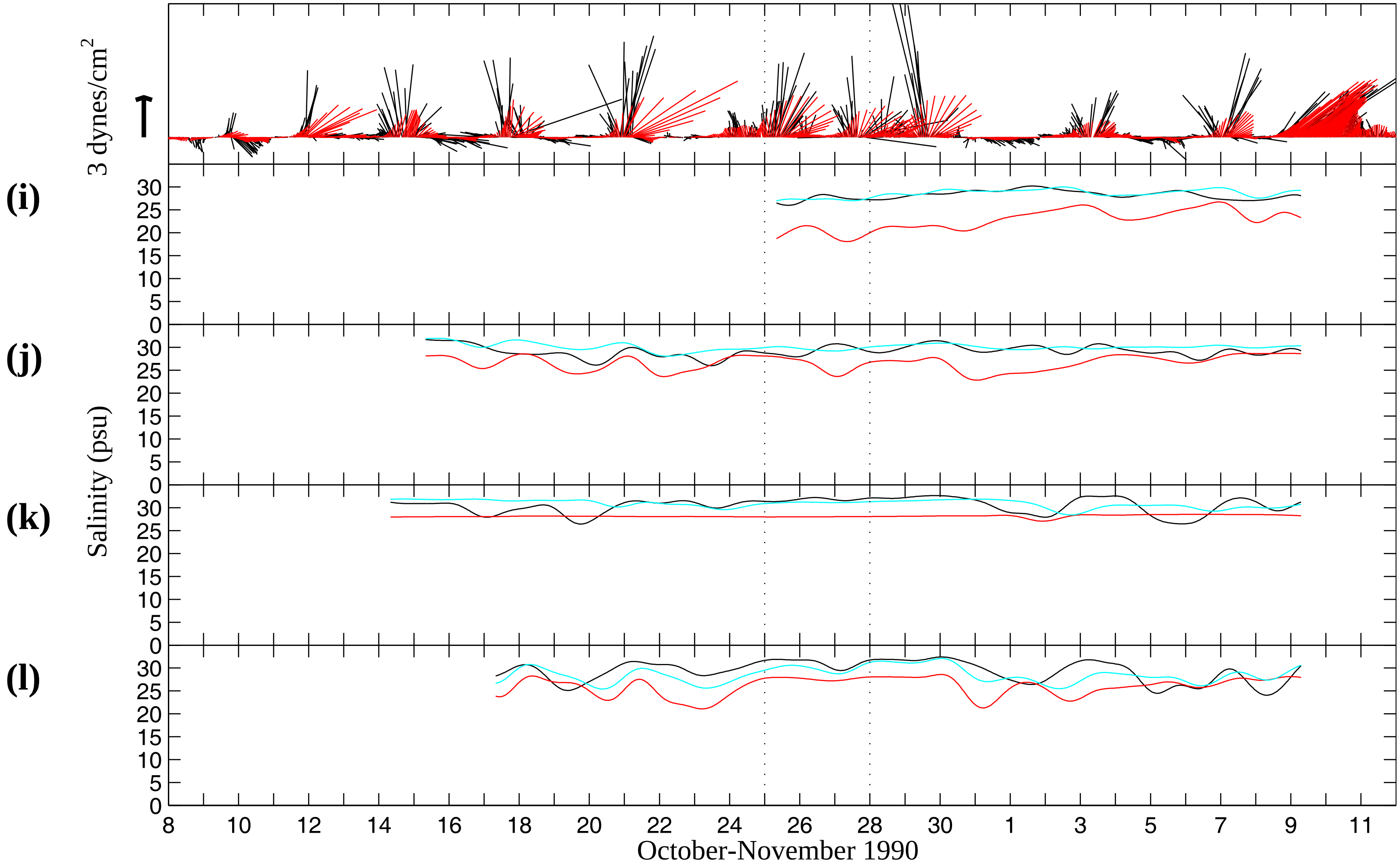

Figure 2.20 Continued.

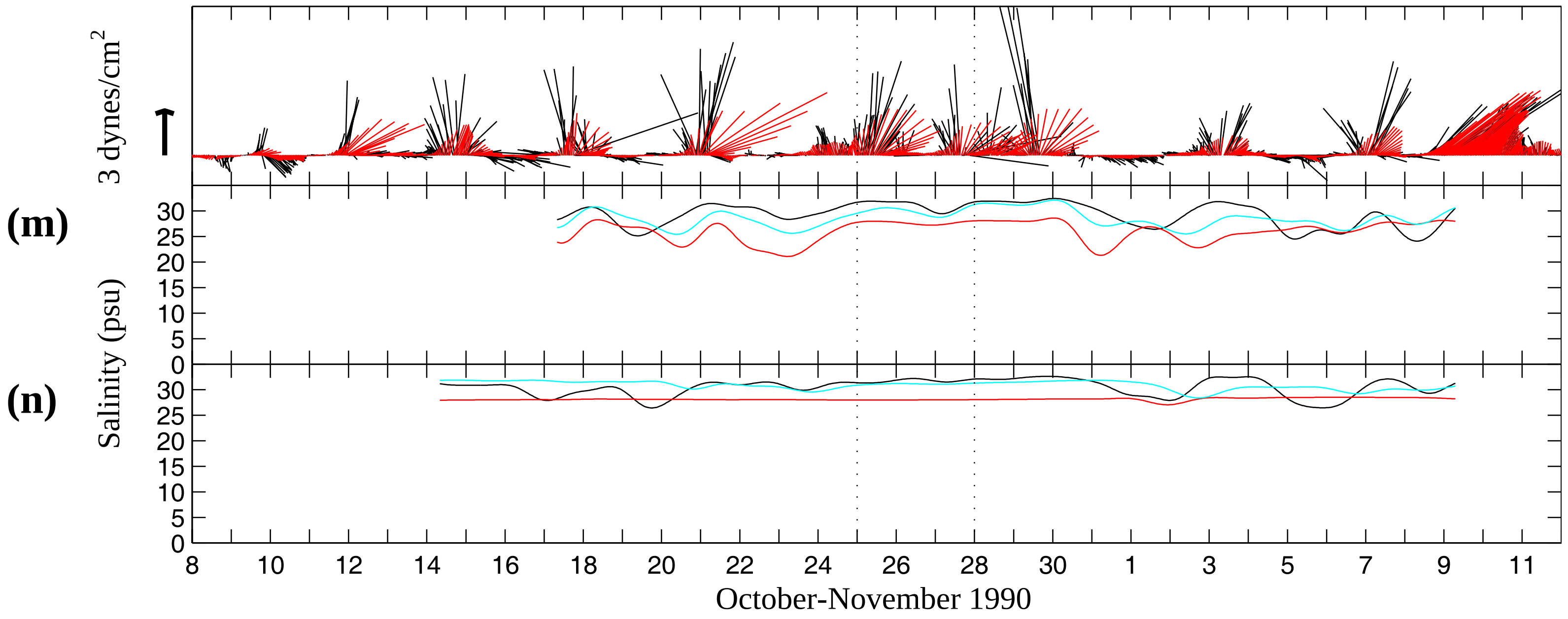

Figure 2.20 Continued.

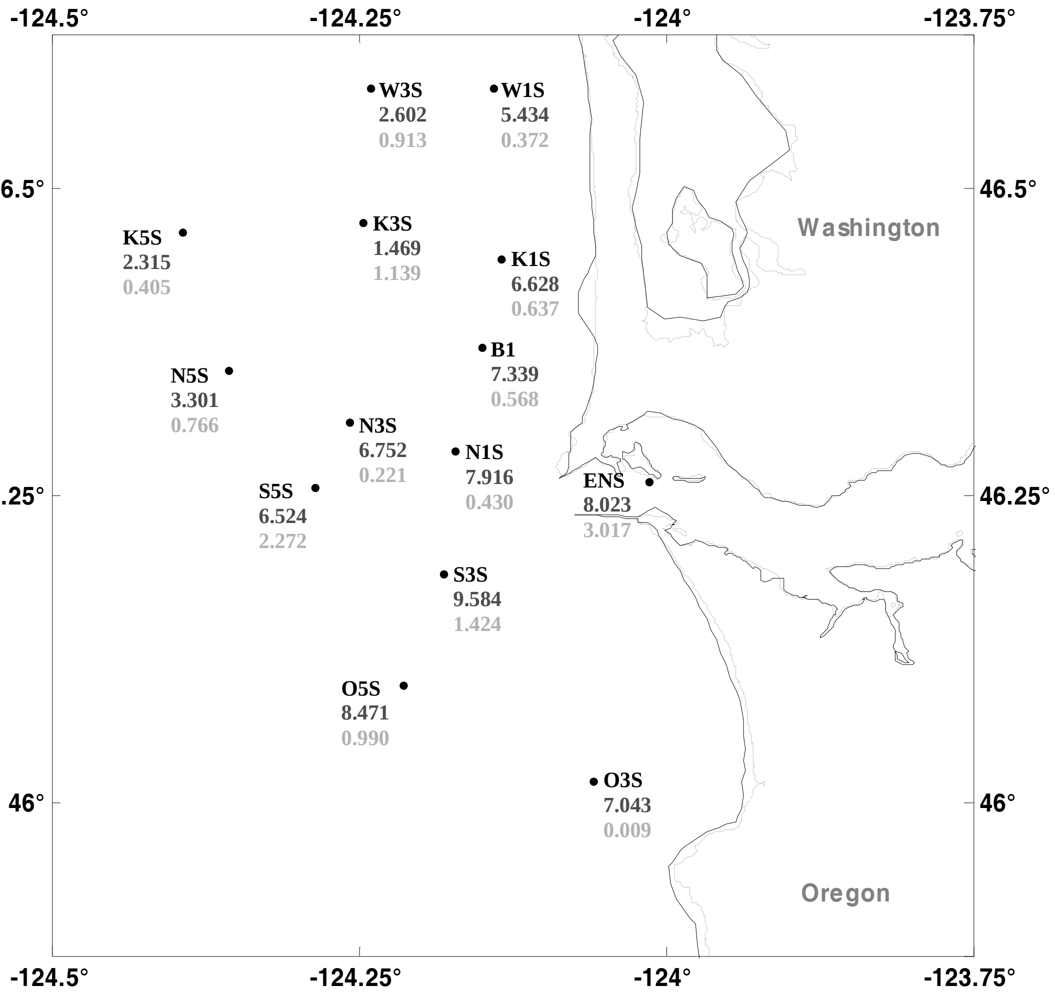

Figure 2.21 RMS errors of low pass filtered salinities (psu) computed between 1m observations and model ELM (▬) and UWM (▬) results, excepting S5S which is computed for 5m results.

Table 2.7 RMS errors of low pass filtered salinities (psu) computed for results of the ELM and UWM experiments at each **(a)** estuarine and near plume, **(b)** northern inner, shallow-deeper mid shelf, and **(c)** southern shallow-deeper mid shelf instruments. Nominal instrument depths are provided next to mooring id.

(a)

	ENS, 1m	ENS, 5m	ENA, 8m	N1S, 1m
ELM	8.023	7.244	5.568	7.916
UWM	3.017	0.900	1.896	0.430

(b)

	B1, 1m	K1S, 1m	W1S, 1m	N3S, 1m	K3S, 1m	W3S, 1m	N5S, 1m	K5S, 1m	K5S, 5m
ELM	7.339	6.628	5.434	6.752	1.469	2.602	3.301	2.315	2.926
UWM	0.568	0.637	0.372	0.221	1.139	0.913	0.766	0.405	0.030

(c)

	O3S, 1m	O3A, 45m	O5S, 1m	S3S, 1m	S3A, 41m	S5S, 5m	S5A, 35m	S5A, 65m
ELM	7.043	0.251	8.471	9.584	1.726	6.524	0.638	2.731
UWM	0.009	0.329	0.990	1.424	0.204	2.272	0.769	2.923

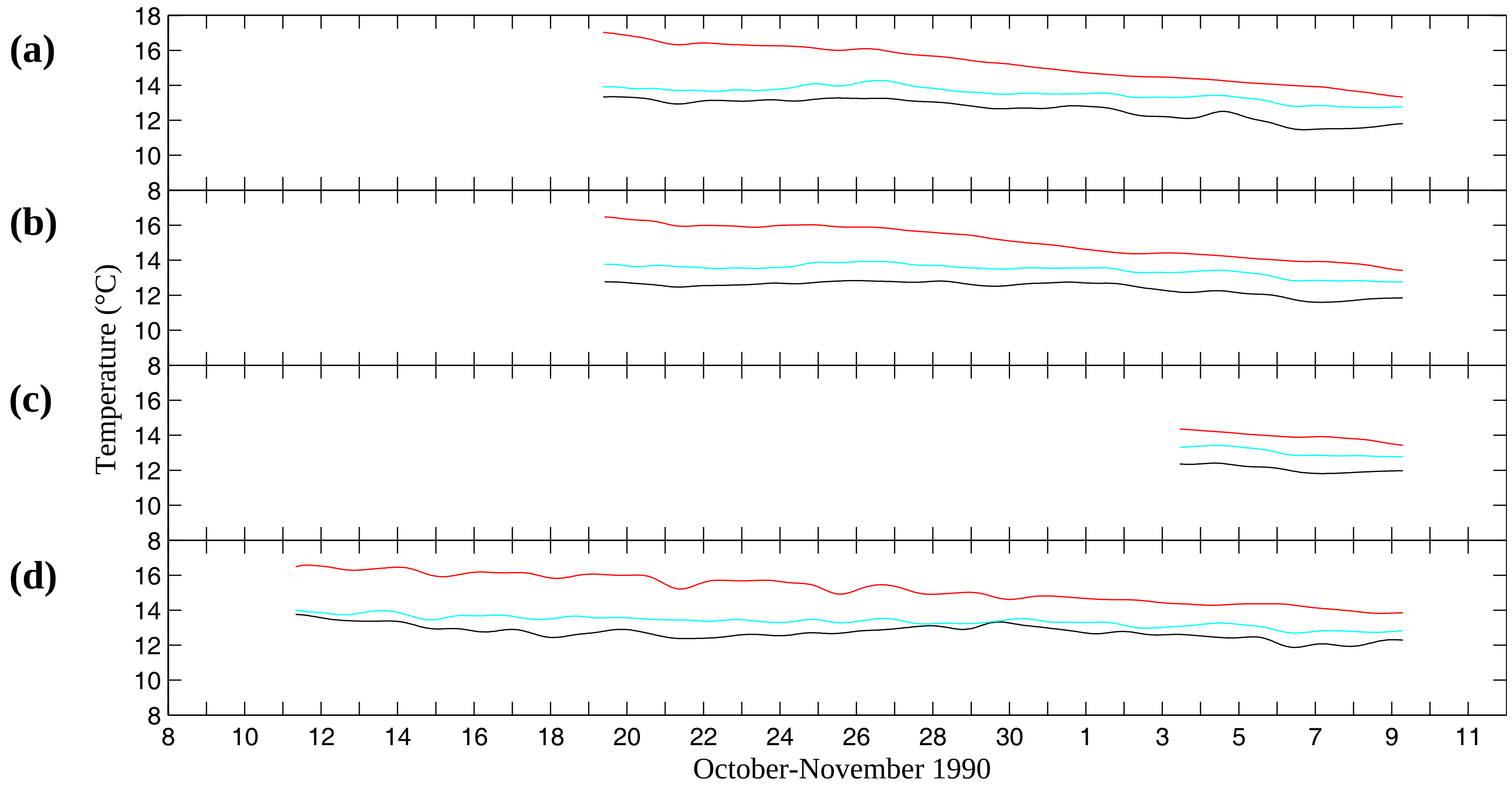

Figure 2.22 Low pass filtered temperatures (°C) for ELM (▬) and UWM (▬) model results and measured data (▬) for the instruments with nominal depths: **(a)** ENS at 1m, **(b)** ENS at 5m, **(c)** ENA at 8m, **(d)** N1S at 1m, **(e)** N3S at 1m, **(f)** B1 at 1m, **(g)** K1S at 1m, **(h)** K3S at 1m, **(i)** W1S at 1m, **(j)** W3S at 1m, **(k)** N5S at 1m, **(l)** N5S at 5m, **(m)** K5S at 1m, **(n)** K5S at 5m, **(o)** S3S at 1m, **(p)** S3A at 41m, **(q)** S3A at 46m, **(r)** S3A at 51m, **(s)** S3A at 56m, **(t)** O3S at 1m, **(u)** O3S at 20m, **(v)** O3A at 35m, **(w)** O3A at 45m, and **(x)** O3A at 50m.

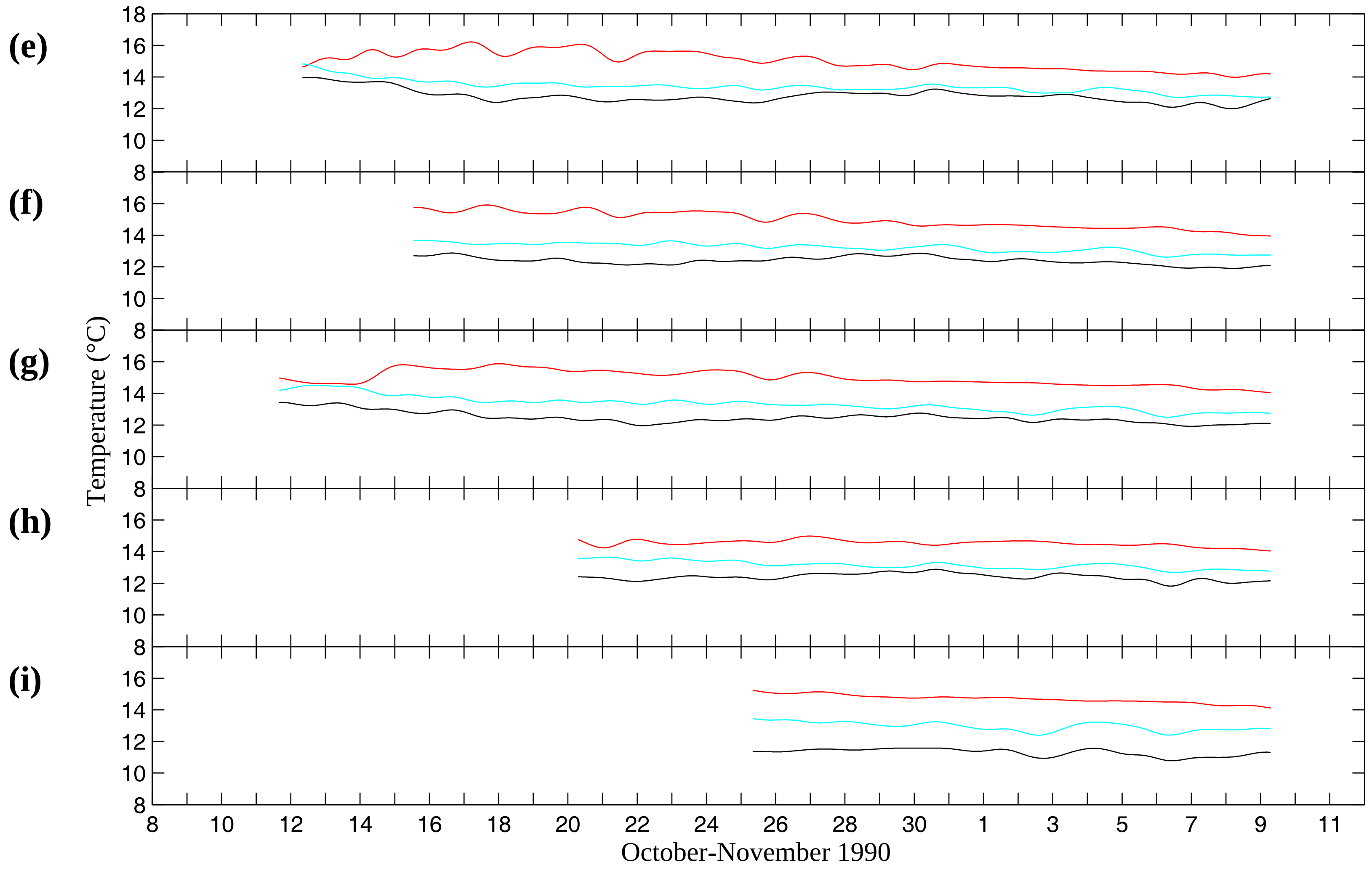

Figure 2.22 Continued.

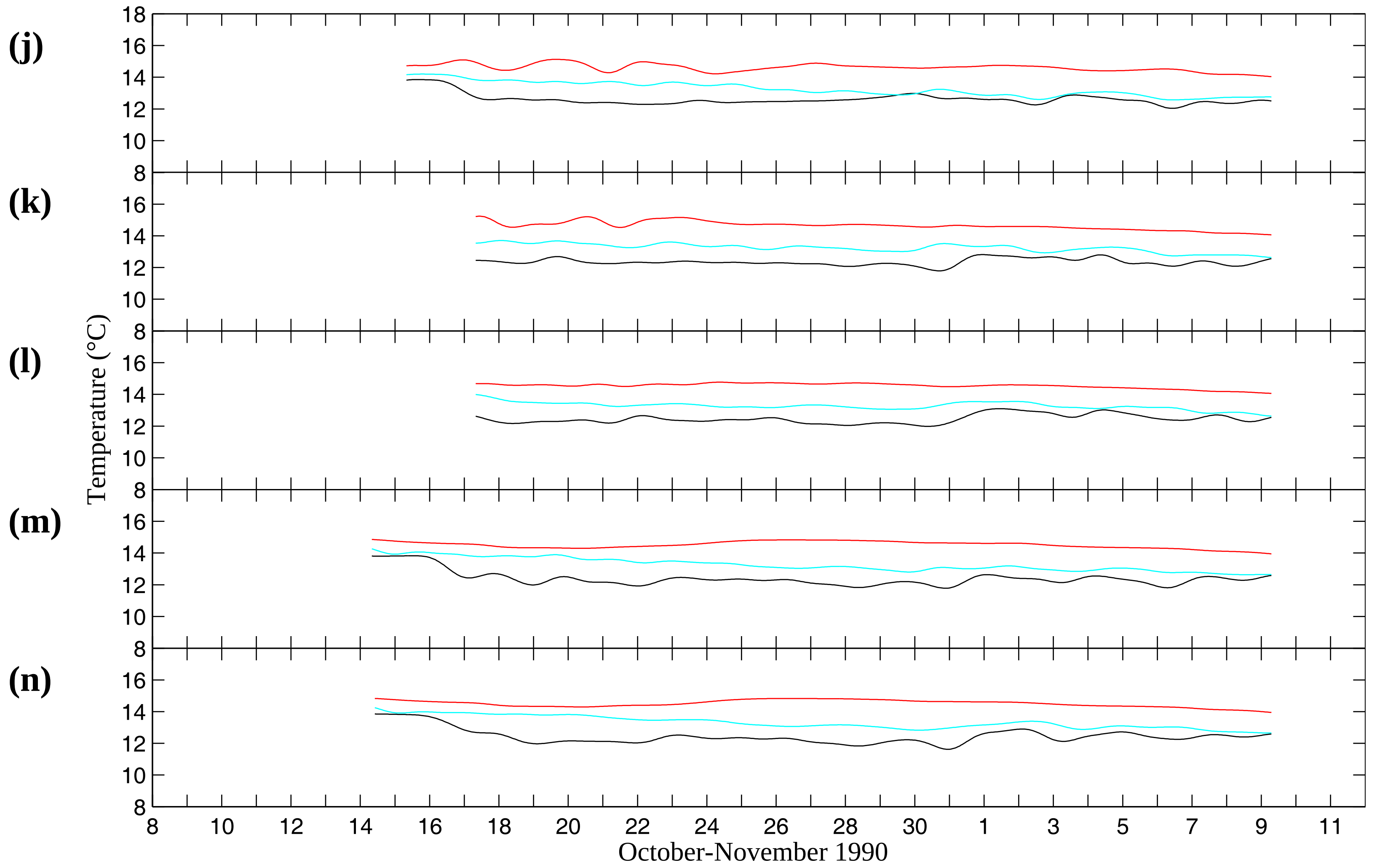

Figure 2.22 Continued.

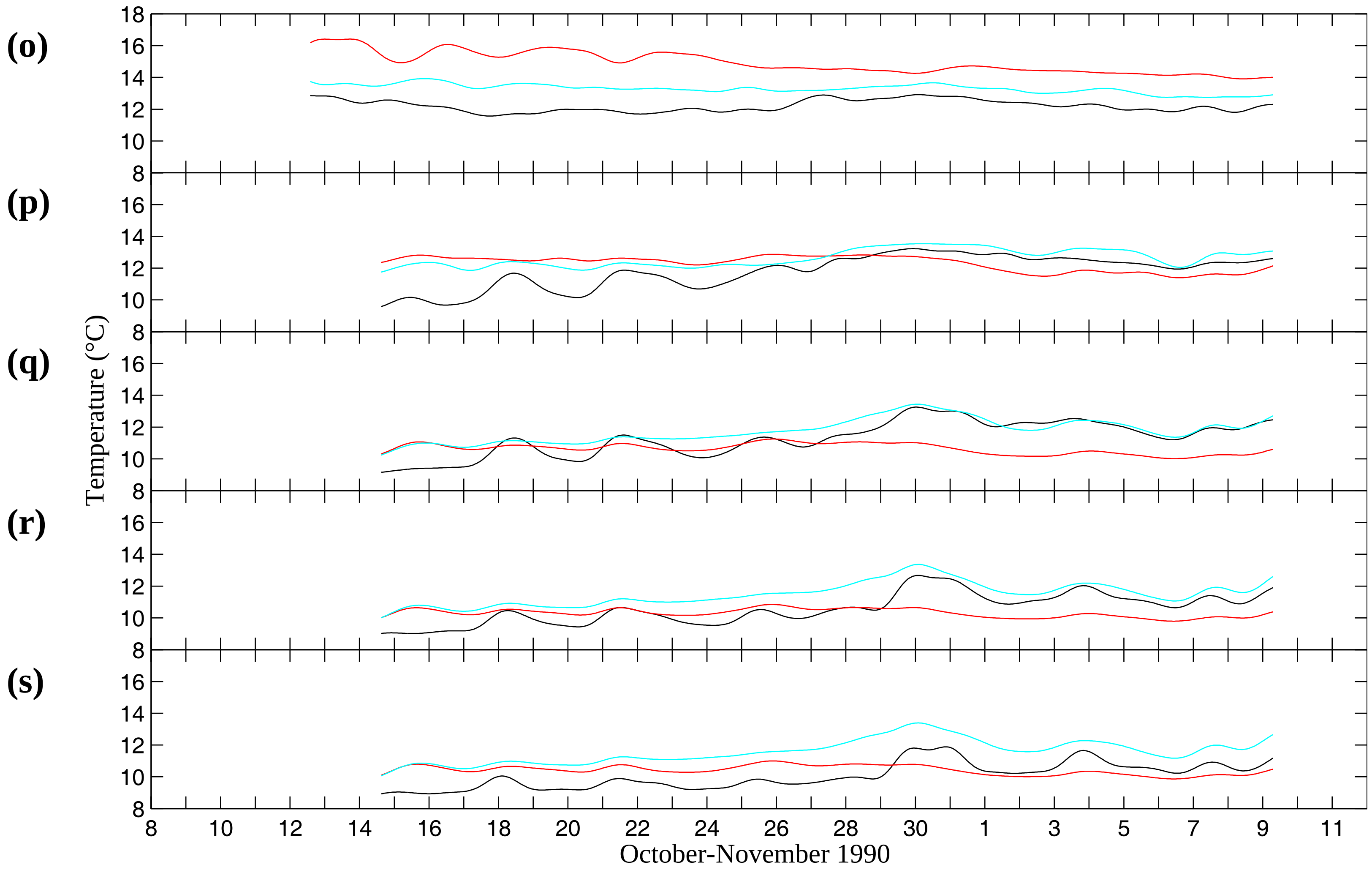

Figure 2.22 Continued.

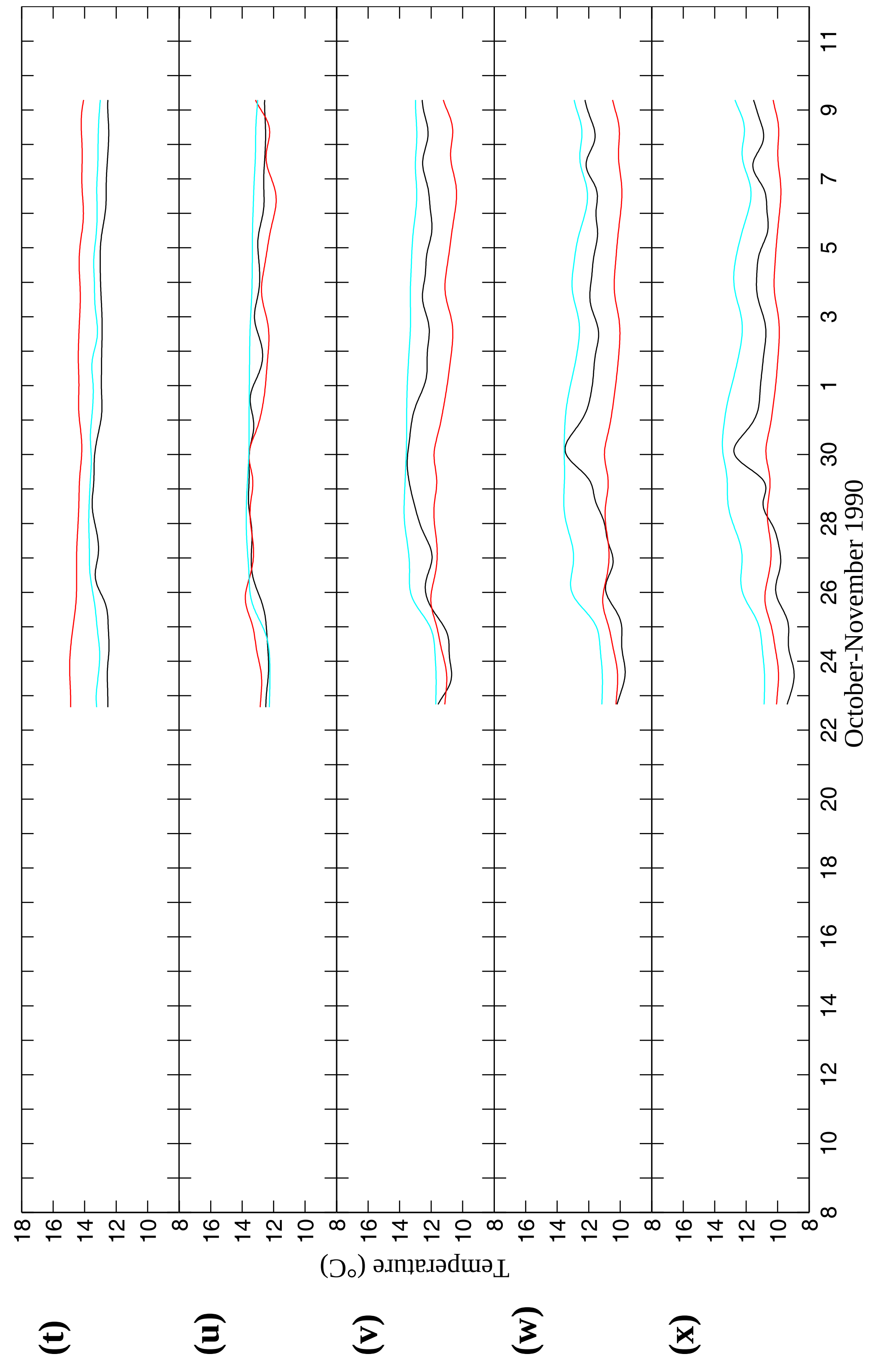

Figure 2.22 Continued.

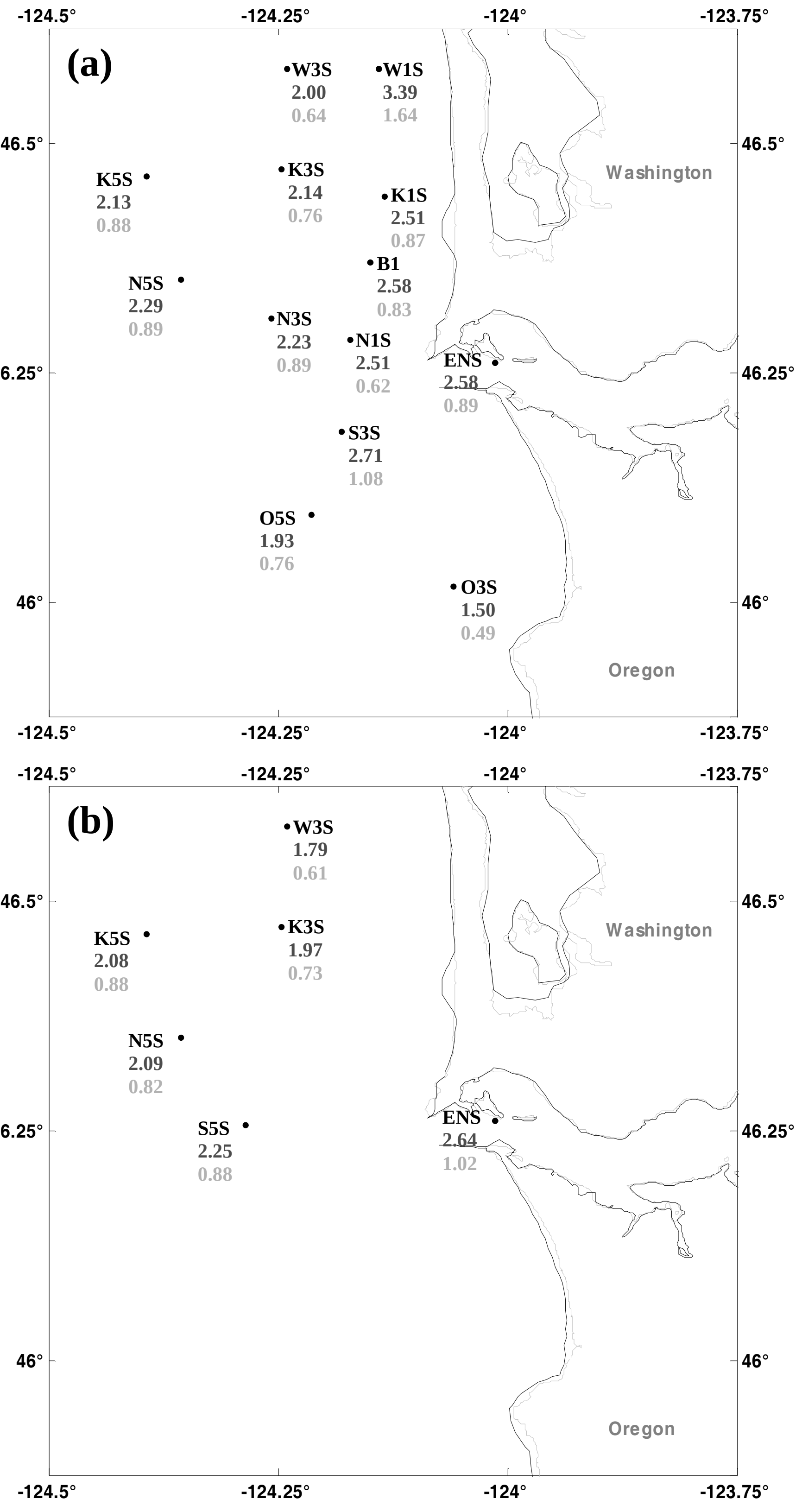

Figure 2.23 RMS errors of low pass filtered temperatures (°C) computed between observations and model ELM (▬) and UWM (▬) results at **(a)** 1m and **(b)** 5m depth.

Table 2.8 RMS errors of low pass filtered temperatures (°C) computed for results of the ELM and UWM experiments at each **(a)** estuarine, **(b)** nearest northern inner, and shallow-deeper mid shelf, **(c)** northern inner, and shallow-deeper mid shelf, **(d)** nearest southern shallow-deeper mid shelf, and **(e)** southern shallow-deeper mid shelf instruments. Nominal instrument depths are provided next to mooring id.

(a)

	ESA, 8m	ESA, 13m	ENS, 1m	ENS, 5m	ENA, 8m	ENA, 13m	ENA, 16m
ELM	1.60	1.65	2.58	2.64	1.87	0.68	1.77
UWM	0.88	1.05	0.89	1.02	0.97	0.13	1.02

(b)

	N1S, 1m	B1, 1m	N3S, 1m	N5S, 1m	N5S, 5m	N5S, 10m
ELM	2.51	2.58	2.23	2.29	2.09	2.12
UWM	0.62	0.83	0.60	0.89	0.82	0.73

(c)

	K1S, 1m	K3S, 1m	K3S, 5m	K5S, 1m	K5S, 5m	K5S, 10m	W1S, 1m	W3S, 1m	W3S, 5m	W3S, 10m
ELM	2.51	2.14	1.97	2.13	2.08	2.07	3.39	2.00	1.79	1.70
UWM	0.87	0.76	0.73	0.88	0.88	0.92	1.64	0.64	0.61	0.59

(d)

	S3S, 1m	S3A, 41m	S3A, 46m	S3A, 51m	S3A, 56m	S5S, 5m	S5A, 35m	S5A, 45m	S5A, 65m	S5A, 89m
ELM	2.71	0.51	0.65	0.26	0.36	2.25	0.08	1.00	1.06	0.86
UWM	1.08	0.84	0.47	0.92	1.53	0.88	0.27	2.06	2.53	1.56

(e)

	O3S, 1m	O3S, 20m	O3A, 35m	O3A, 45m	O3A, 50m	O5S, 1m
ELM	1.50	0.12	1.10	0.97	0.47	1.93
UWM	0.49	0.33	0.81	1.28	1.63	0.76

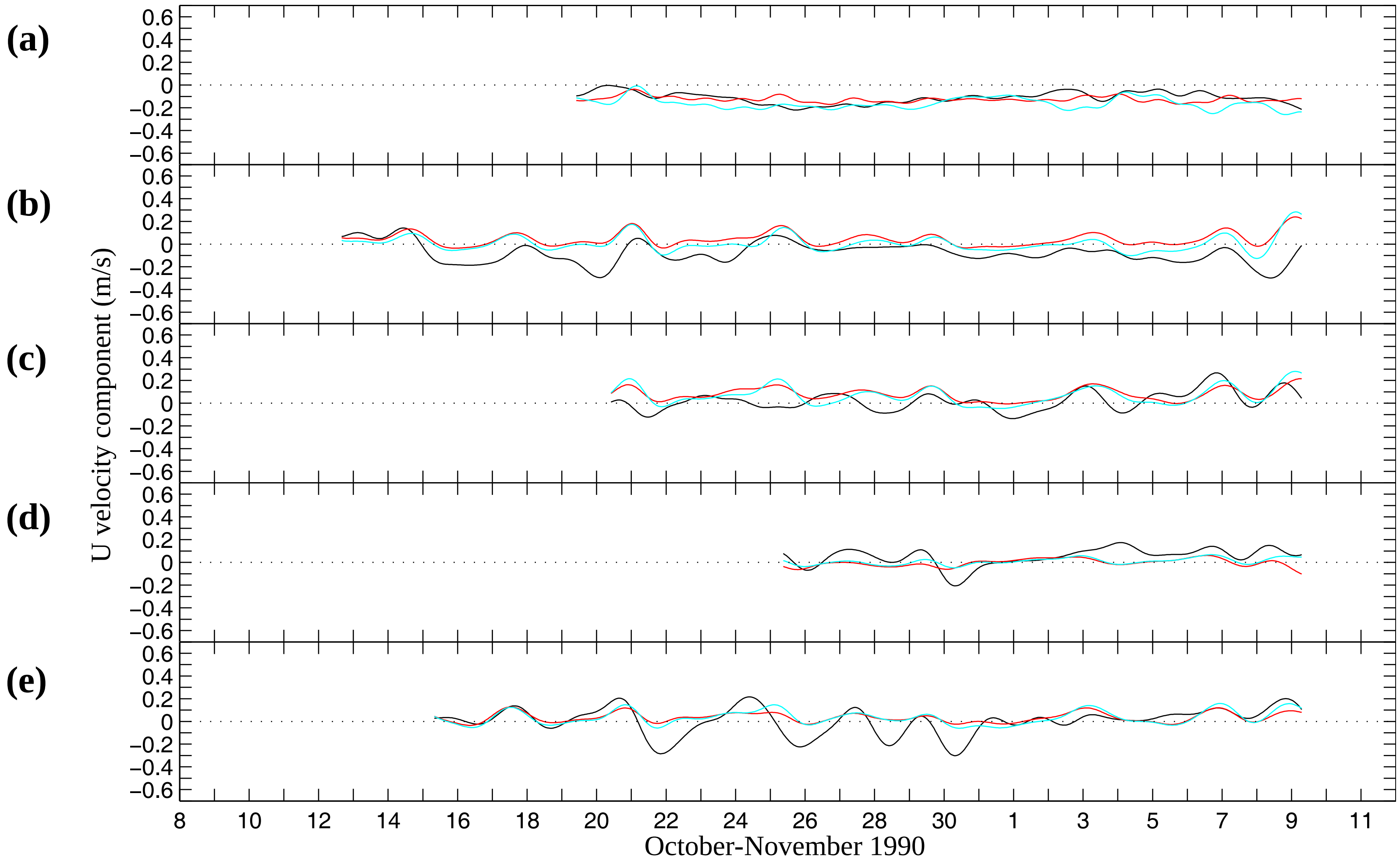

Figure 2.24 Low pass filtered u velocity components for ELM (▬) and UWM (▬) model results and measured data (▬) at **(a)** ENS at 5m, **(b)** N3S at 5m, **(c)** K3S at 5m, **(d)** W1S at 5m, **(e)** W3S at 5m, **(f)** W3S at 10m, **(g)** N5S at 5m, **(h)** N5S at 10m, **(i)** K5S at 5m, **(j)** K5S at 10m, **(k)** S5S at 5m, **(l)** O5S at 5m, **(m)** O3S at 5m, **(n)** O3S at 20m, and **(o)** S5A at 65m.

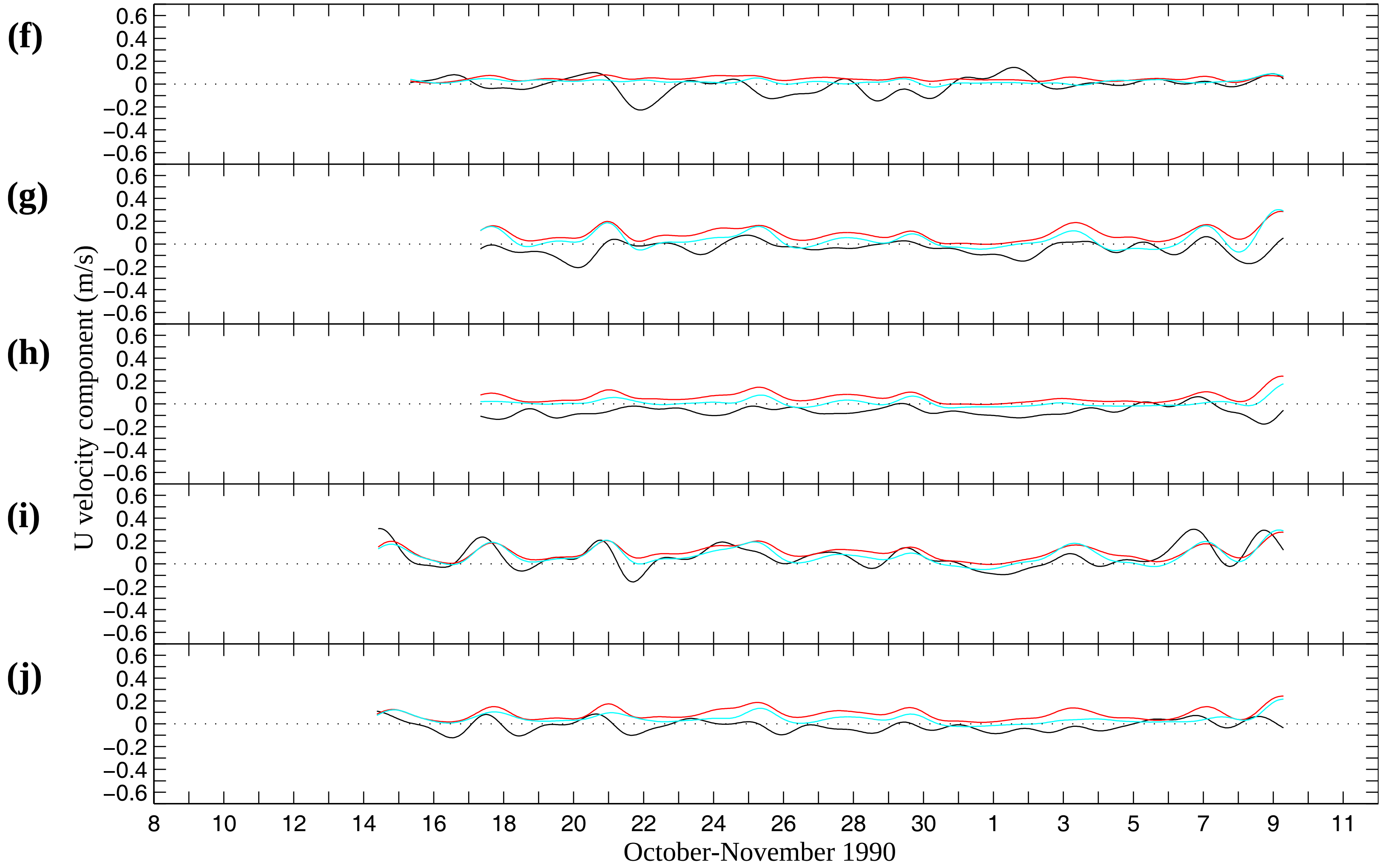

Figure 2.24 Continued.

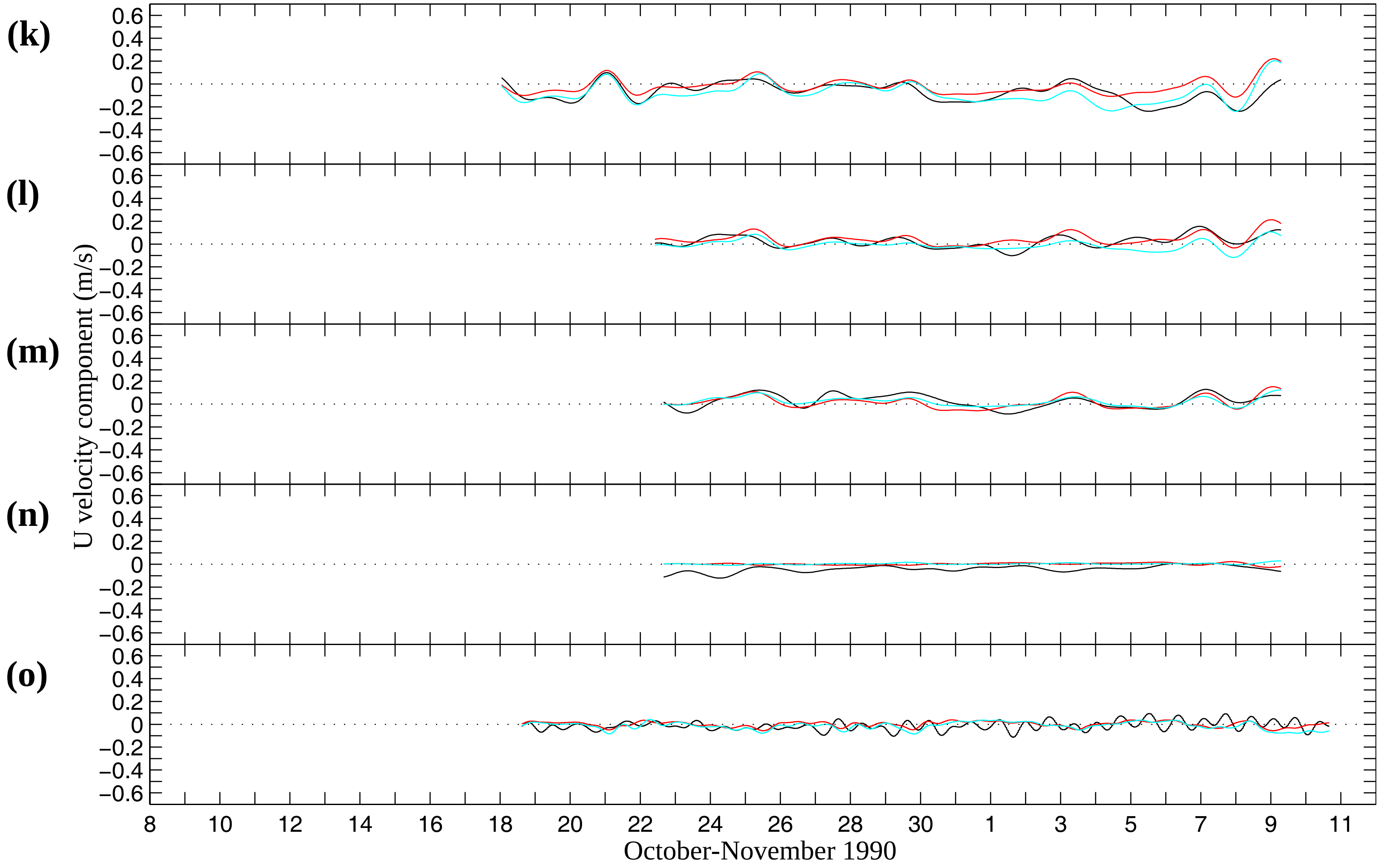

Figure 2.24 Continued.

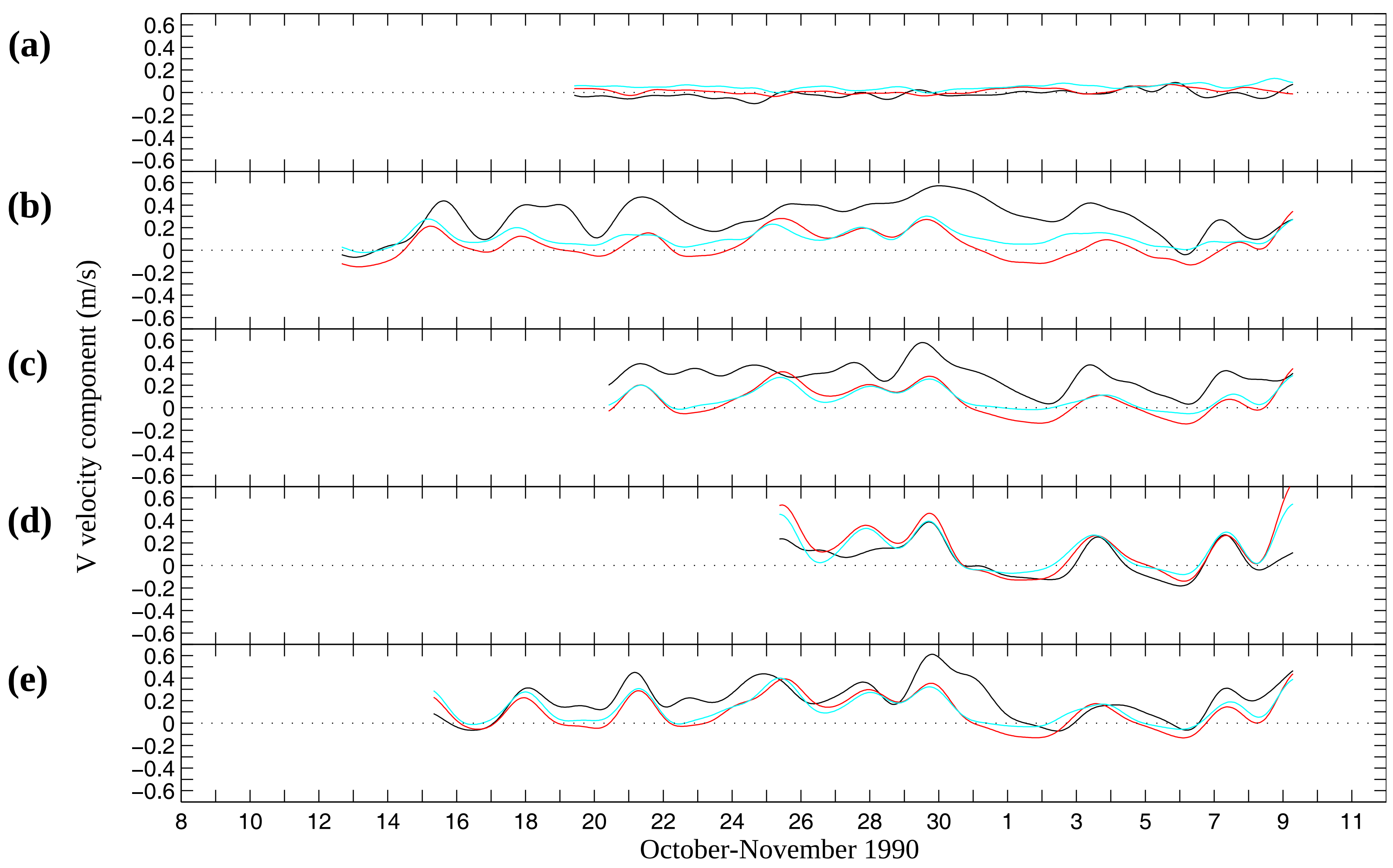

Figure 2.25 Low pass filtered v velocity components for ELM (▬) and UWM (▬) model results and measured data (▬) at **(a)** ENS at 5m, **(b)** N3S at 5m, **(c)** K3S at 5m, **(d)** W1S at 5m, **(e)** W3S at 5m, **(f)** W3S at 10m, **(g)** N5S at 5m, **(h)** N5S at 10m, **(i)** K5S at 5m, **(j)** K5S at 10m, **(k)** S5S at 5m, **(l)** O5S at 5m, **(m)** O3S at 5m, **(n)** O3S at 20m, and **(o)** S5A at 65m.

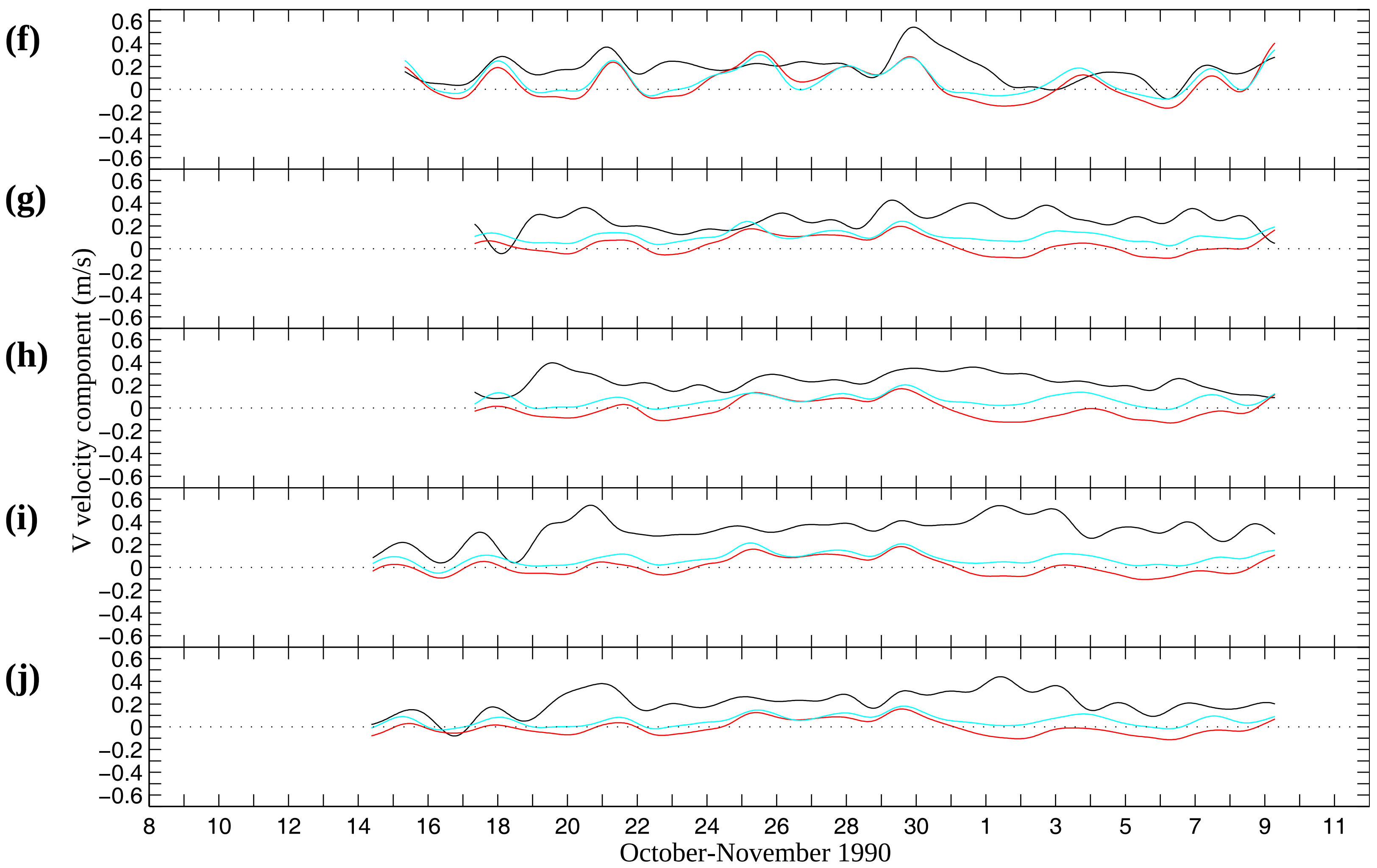

Figure 2.25 Continued.

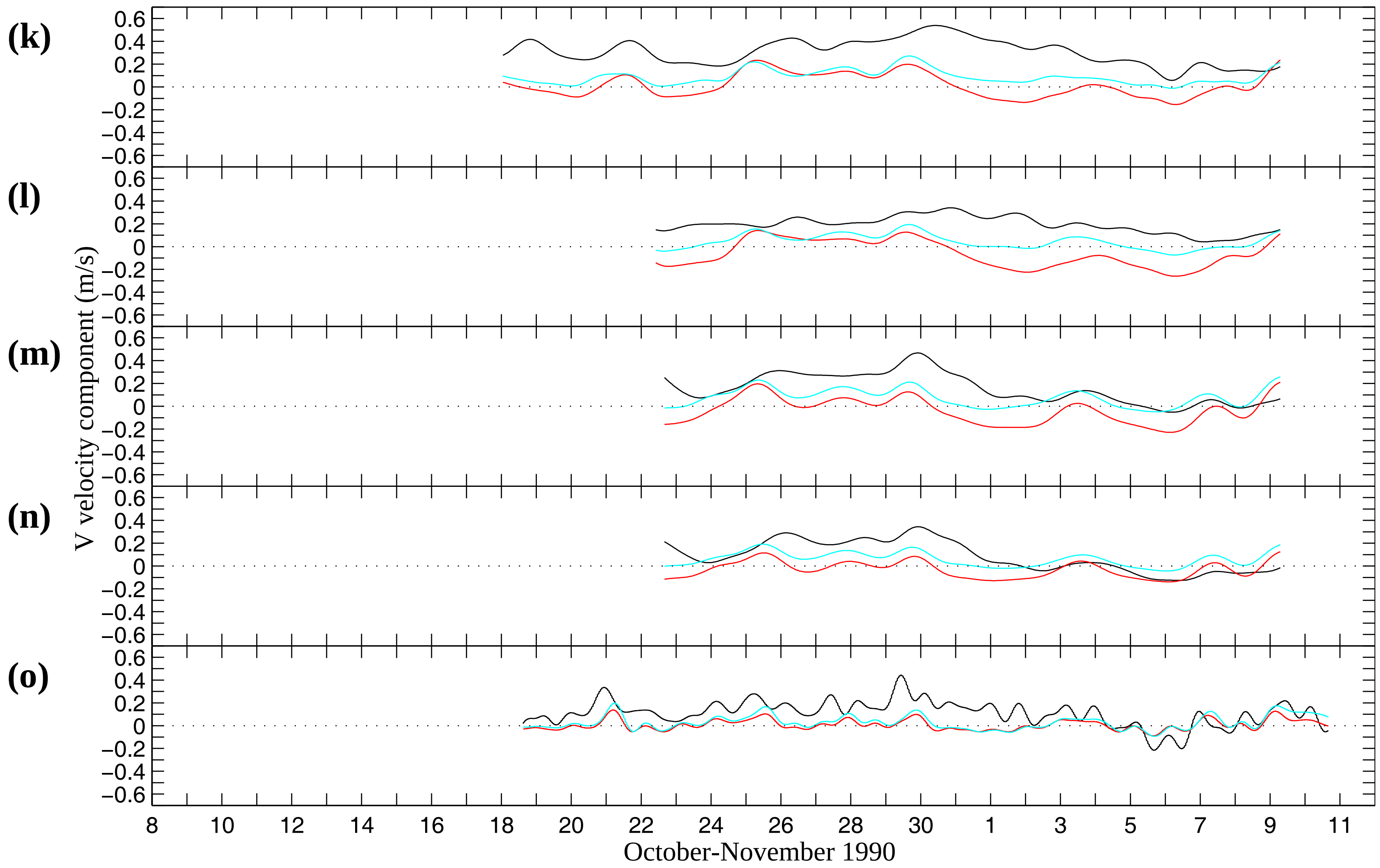

Figure 2.25 Continued.

Table 2.9 Modeled and measured vector (v) and scalar (s) mean speeds (m/s), mean directions (°clockwise with respect to true north) are given for instruments at **(a)** 5m, **(b)** 10m, **(c)** 20m, and **(d)** 65m depth.

(a)

	DATA			ELM						UWM					
Mooring	$u_{d,v}$	$u_{d,s}$	θ_d	$u_{m,v}$	$u_{m,s}$	θ_m	$u_{m,v} / u_{d,v}$	$u_{m,s} / u_{d,s}$	$\theta_m - \theta_d$	$u_{m,v}$	$u_{m,s}$	θ_m	$u_{m,v} / u_{d,v}$	$u_{m,s} / u_{d,s}$	$\theta_m - \theta_d$
O5S	0.19	0.20	6.5	0.078	0.14	147.2	0.41	0.68	140.8	0.045	0.077	347.2	0.23	0.38	-19.3
O3S	0.16	0.18	9.3	0.044	0.11	160.1	0.28	0.65	150.8	0.077	0.093	16.4	0.49	0.53	7.1
S5S	0.31	0.33	346.7	0.026	0.11	298.4	0.08	0.34	-48.3	0.12	0.15	315.9	0.38	0.46	-30.8
N5S	0.25	0.26	350.8	0.091	0.12	69.0	0.36	0.45	78.1	0.12	0.13	18.5	0.46	0.49	27.7
N3S	0.30	0.32	344.5	0.062	0.12	43.4	0.21	0.36	58.9	0.11	0.13	2.4	0.37	0.39	17.9
K5S	0.33	0.35	10.6	0.099	0.13	85.7	0.30	0.36	75.1	0.11	0.12	43.1	0.32	0.34	32.4
K3S	0.28	0.30	4.0	0.10	0.15	51.2	0.36	0.50	47.2	0.11	0.13	38.4	0.38	0.43	34.4
W1S	0.076	0.16	38.9	0.14	0.19	358.6	1.84	1.20	-40.3	0.13	0.16	4.0	1.71	0.99	-35.0
W3S	0.20	0.24	0.9	0.10	0.15	20.3	0.49	0.61	19.4	0.13	0.15	15.4	0.62	0.61	14.6
ENS	0.11	0.12	261.7	0.13	0.13	275.9	1.13	1.09	14.2	0.17	0.17	287.3	1.51	1.45	25.6
Average							0.55	0.62	49.6				0.65	0.61	7.5
Standard error of the sample							0.53	0.30	66.6				0.52	0.35	26.3

(b)

	DATA			ELM						UWM					
Mooring	$u_{d,v}$	$u_{d,s}$	θ_d	$u_{m,v}$	$u_{m,s}$	θ_m	$u_{m,v} / u_{d,v}$	$u_{m,s} / u_{d,s}$	$\theta_m - \theta_d$	$u_{m,v}$	$u_{m,s}$	θ_m	$u_{m,v} / u_{d,v}$	$u_{m,s} / u_{d,s}$	$\theta_m - \theta_d$
W3S	0.18	0.20	357.2	0.066	0.13	44.0	0.37	0.65	46.8	0.081	0.11	16.0	0.46	0.55	18.8
K5S	0.21	0.22	355.3	0.084	0.11	95.5	0.40	0.48	100.3	0.069	0.078	38.7	0.33	0.35	43.4
N5S	0.24	0.25	344.6	0.057	0.097	106.6	0.24	0.39	122.0	0.070	0.076	6.1	0.29	0.31	21.4
Average							0.34	0.51	89.7				0.36	0.40	27.9
Standard error of the sample							0.088	0.13	38.7				0.089	0.13	13.5

(c)

	DATA			ELM						UWM					
Mooring	$u_{d,v}$	$u_{d,s}$	θ_d	$u_{m,v}$	$u_{m,s}$	θ_m	$u_{m,v} / u_{d,v}$	$u_{m,s} / u_{d,s}$	$\theta_m - \theta_d$	$u_{m,v}$	$u_{m,s}$	θ_m	$u_{m,v} / u_{d,v}$	$u_{m,s} / u_{d,s}$	$\theta_m - \theta_d$
O3S	0.091	0.14	334.2	0.033	0.066	176.3	0.36	0.48	-157.9	0.059	0.067	3.5	0.65	0.48	-330.7

(d)

	DATA			ELM						UWM					
Mooring	$u_{d,v}$	$u_{d,s}$	θ_d	$u_{m,v}$	$u_{m,s}$	θ_m	$u_{m,v} / u_{d,v}$	$u_{m,s} / u_{d,s}$	$\theta_m - \theta_d$	$u_{m,v}$	$u_{m,s}$	θ_m	$u_{m,v} / u_{d,v}$	$u_{m,s} / u_{d,s}$	$\theta_m - \theta_d$
S5A	0.11	0.14	353.5	0.0071	0.044	4.5	0.064	0.31	11.0	0.031	0.058	334.3	0.28	0.42	-19.2

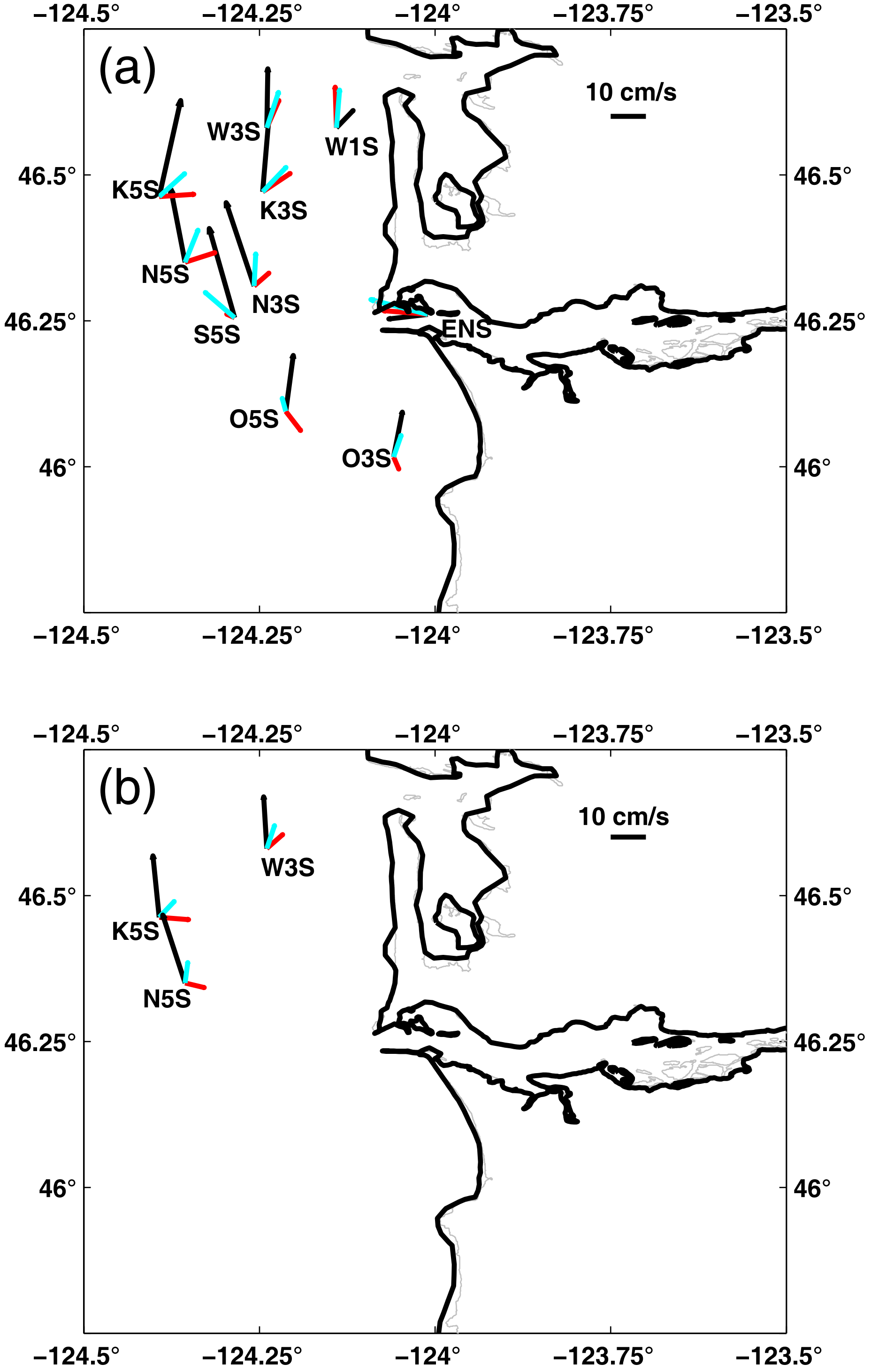

Figure 2.26 Mean vectors of velocity for ELM (▬) and UWM (▬) model results and measured data (▬) at **(a)** 5m, **(b)** 10m, **(c)** 20m, and **(d)** 65m depth.

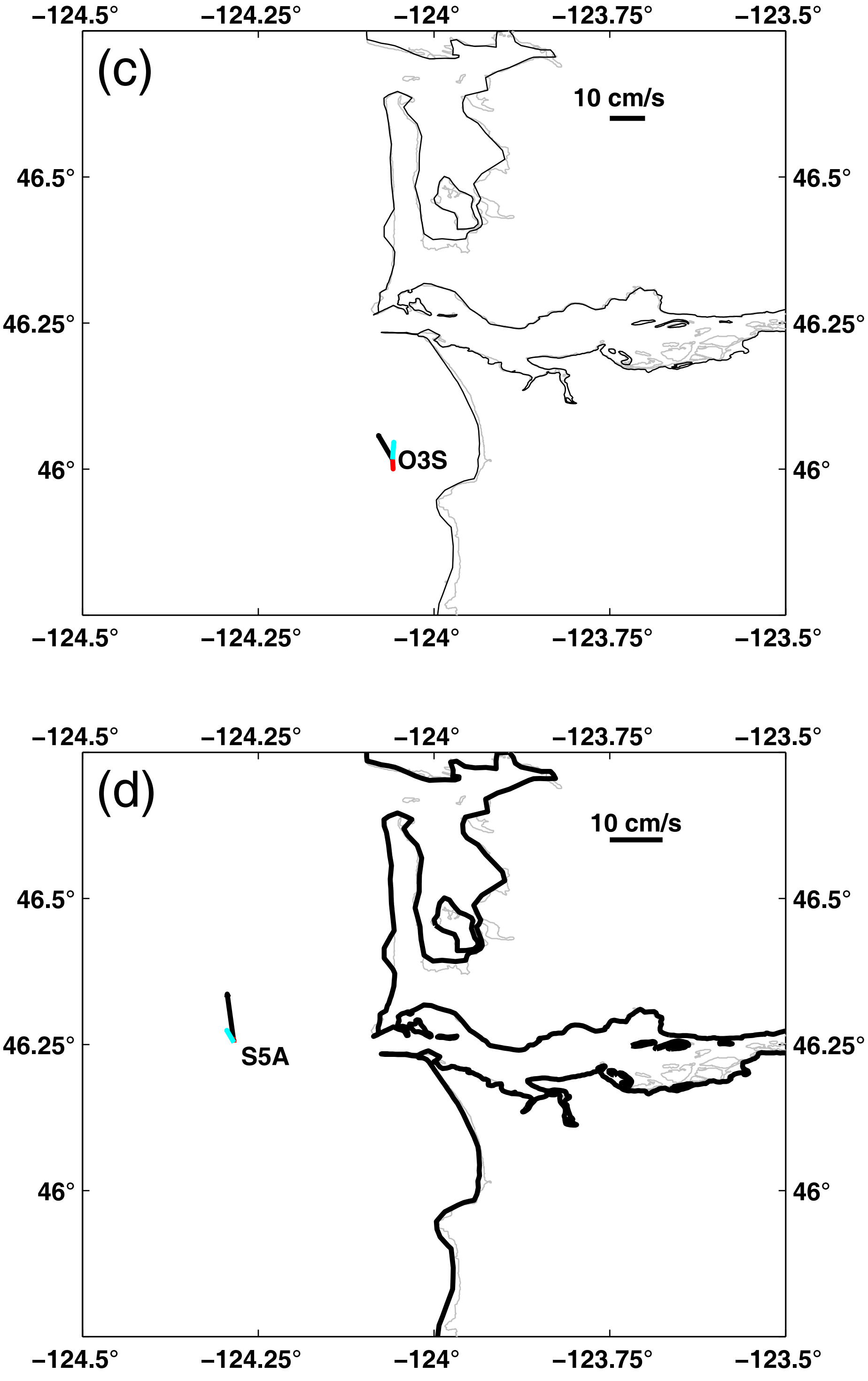

Figure 2.26 Continued.

Table 2.10 Principal major axis (m/s), principal minor axis (m/s), and principal axis direction (°clockwise with respect to true north) of measured and modeled currents are given for instruments at **(a)** 5m, **(b)** 10m, **(c)** 20m, and **(d)** 65m depth.

(a)

	DATA				ELM							UWM						
Mooring	$\lambda_{1,d}^{0.5}$	$\lambda_{2,d}^{0.5}$	$\theta_{p,d}$	$\lambda_{2,d} / \lambda_{1,d}$	$\lambda_{1,m}^{0.5}$	$\lambda_{2,m}^{0.5}$	$\theta_{p,m}$	$\lambda_{2,m} / \lambda_{1,m}$	$\lambda_{1,m}^{0.5}/\lambda_{1,d}^{0.5}$	$\lambda_{2,m}^{0.5}/\lambda_{2,d}^{0.5}$	$\theta_{p,m} - \theta_{p,d}$	$\lambda_{1,m}^{0.5}$	$\lambda_{2,m}^{0.5}$	$\theta_{p,m}$	$\lambda_{2,m} / \lambda_{1,m}$	$\lambda_{1,m}^{0.5}/\lambda_{1,d}^{0.5}$	$\lambda_{2,m}^{0.5}/\lambda_{2,d}^{0.5}$	$\theta_{p,m} - \theta_{p,d}$
O5S	0.082	0.038	151.1	0.21	0.12	0.049	3.2	0.17	1.45	1.31	-147.9	0.069	0.032	25.1	0.22	0.84	0.85	-126.0
O3S	0.13	0.051	12.5	0.14	0.12	0.036	18.3	0.092	0.87	0.69	5.9	0.084	0.013	24.1	0.03	0.63	0.26	11.6
S5S	0.11	0.078	11.4	0.46	0.11	0.054	22.5	0.25	0.94	0.69	11.1	0.096	0.042	57.3	0.19	0.83	0.54	45.9
N5S	0.089	0.059	172.1	0.44	0.080	0.049	29.1	0.37	0.90	0.83	-142.9	0.077	0.037	64.9	0.23	0.87	0.63	-107.2
N3S	0.15	0.090	4.4	0.35	0.12	0.051	12.6	0.20	0.76	0.57	8.2	0.081	0.052	43.0	0.41	0.53	0.58	38.6
K5S	0.11	0.097	7.9	0.76	0.083	0.042	34.9	0.26	0.75	0.43	27.0	0.078	0.043	61.4	0.30	0.70	0.44	53.4
K3S	0.11	0.083	173.5	0.53	0.13	0.042	15.9	0.10	1.14	0.50	-157.5	0.10	0.054	39.3	0.29	0.89	0.65	-134.2
W1S	0.14	0.077	175.3	0.30	0.20	0.020	172.3	0.010	1.39	0.26	-3.0	0.15	0.028	178.8	0.03	1.09	0.36	3.6
W3S	0.16	0.11	168.5	0.50	0.14	0.040	4.8	0.082	0.87	0.35	-163.8	0.12	0.052	15.5	0.19	0.73	0.46	-153.0
ENS	0.051	0.033	80.2	0.41	0.030	0.018	136.4	0.38	0.58	0.57	56.2	0.051	0.022	100.4	0.19	0.99	0.68	20.2
Average				0.41				0.19	0.96	0.62	-50.7				0.21	0.81	0.54	-34.7
Standard error of the sample				0.17				0.12	0.28	0.29	89.7				0.12	0.17	0.17	84.2

(b)

	DATA				ELM							UWM						
Mooring	$\lambda_{1,d}^{0.5}$	$\lambda_{2,d}^{0.5}$	$\theta_{p,d}$	$\lambda_{2,d} / \lambda_{1,d}$	$\lambda_{1,m}^{0.5}$	$\lambda_{2,m}^{0.5}$	$\theta_{p,m}$	$\lambda_{2,m} / \lambda_{1,m}$	$\lambda_{1,m}^{0.5}/\lambda_{1,d}^{0.5}$	$\lambda_{2,m}^{0.5}/\lambda_{2,d}^{0.5}$	$\theta_{p,m} - \theta_{p,d}$	$\lambda_{1,m}^{0.5}$	$\lambda_{2,m}^{0.5}$	$\theta_{p,m}$	$\lambda_{2,m} / \lambda_{1,m}$	$\lambda_{1,m}^{0.5}/\lambda_{1,d}^{0.5}$	$\lambda_{2,m}^{0.5}/\lambda_{2,d}^{0.5}$	$\theta_{p,m} - \theta_{p,d}$
W3S	0.12	0.067	165.3	0.33	0.13	0.015	2.1	0.01	1.10	0.23	-163.2	0.106	0.018	0.9	0.03	0.89	0.27	-164.4
K5S	0.10	0.050	177.1	0.24	0.070	0.038	28.4	0.29	0.69	0.76	-148.7	0.053	0.033	34.8	0.38	0.52	0.66	-142.3
N5S	0.077	0.043	1.1	0.32	0.083	0.036	19.0	0.18	1.08	0.82	17.9	0.051	0.026	21.6	0.26	0.67	0.60	20.5
Average				0.29				0.16	0.96	0.61	-98.0				0.22	0.70	0.51	-95.4
Standard error of the sample				0.05				0.14	0.23	0.33	100.6				0.18	0.19	0.21	101.0

(c)

	DATA				ELM							UWM						
Mooring	$\lambda_{1,d}^{0.5}$	$\lambda_{2,d}^{0.5}$	$\theta_{p,d}$	$\lambda_{2,d} / \lambda_{1,d}$	$\lambda_{1,m}^{0.5}$	$\lambda_{2,m}^{0.5}$	$\theta_{p,m}$	$\lambda_{2,m} / \lambda_{1,m}$	$\lambda_{1,m}^{0.5}/\lambda_{1,d}^{0.5}$	$\lambda_{2,m}^{0.5}/\lambda_{2,d}^{0.5}$	$\theta_{p,m} - \theta_{p,d}$	$\lambda_{1,m}^{0.5}$	$\lambda_{2,m}^{0.5}$	$\theta_{p,m}$	$\lambda_{2,m} / \lambda_{1,m}$	$\lambda_{1,m}^{0.5}/\lambda_{1,d}^{0.5}$	$\lambda_{2,m}^{0.5}/\lambda_{2,d}^{0.5}$	$\theta_{p,m} - \theta_{p,d}$
O3S	0.14	0.026	176.3	0.038	0.070	0.0077	175.4	0.012	0.52	0.29	-0.8	0.061	0.0060	2.1	0.010	0.45	0.23	-174.2

(d)

	DATA				ELM							UWM						
Mooring	$\lambda_{1,d}^{0.5}$	$\lambda_{2,d}^{0.5}$	$\theta_{p,d}$	$\lambda_{2,d} / \lambda_{1,d}$	$\lambda_{1,m}^{0.5}$	$\lambda_{2,m}^{0.5}$	$\theta_{p,m}$	$\lambda_{2,m} / \lambda_{1,m}$	$\lambda_{1,m}^{0.5}/\lambda_{1,d}^{0.5}$	$\lambda_{2,m}^{0.5}/\lambda_{2,d}^{0.5}$	$\theta_{p,m} - \theta_{p,d}$	$\lambda_{1,m}^{0.5}$	$\lambda_{2,m}^{0.5}$	$\theta_{p,m}$	$\lambda_{2,m} / \lambda_{1,m}$	$\lambda_{1,m}^{0.5}/\lambda_{1,d}^{0.5}$	$\lambda_{2,m}^{0.5}/\lambda_{2,d}^{0.5}$	$\theta_{p,m} - \theta_{p,d}$
S5A	0.11	0.036	171.2	0.11	0.049	0.014	155.9	0.080	0.45	0.39	-15.3	0.066	0.016	154.6	0.061	0.60	0.45	-16.6

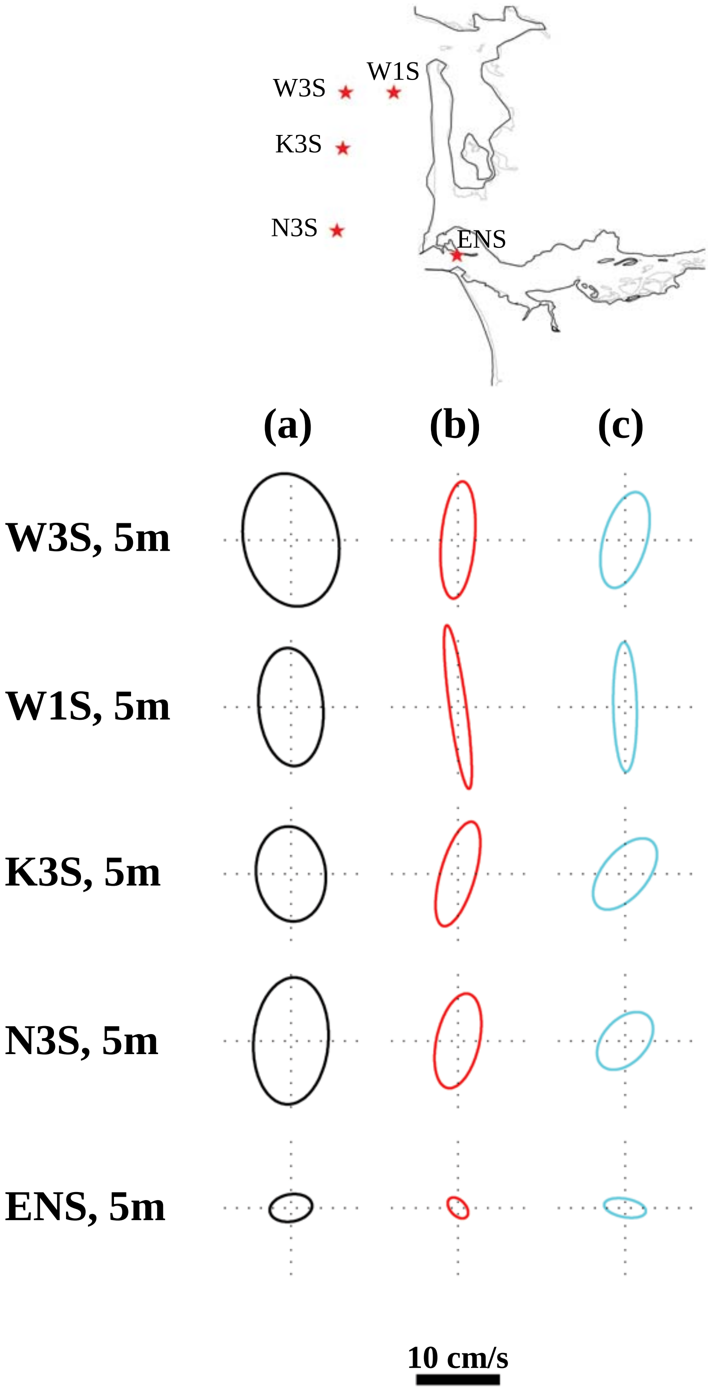

Figure 2.27 Principal ellipses of low-pass filtered velocities for **(a)** measured data (▬), **(b)** ELM (▬) and **(c)** UWM (▬) model results at the specified depth

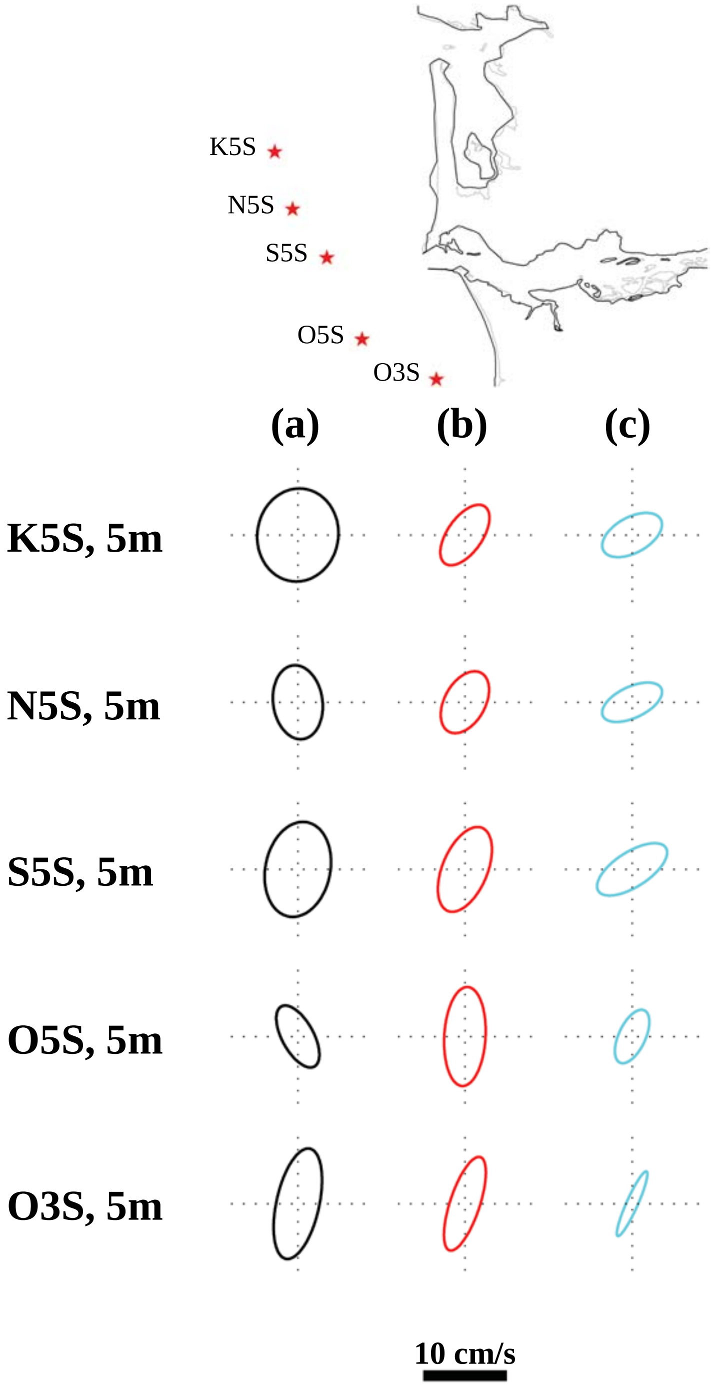

Figure 2.27 Continued.

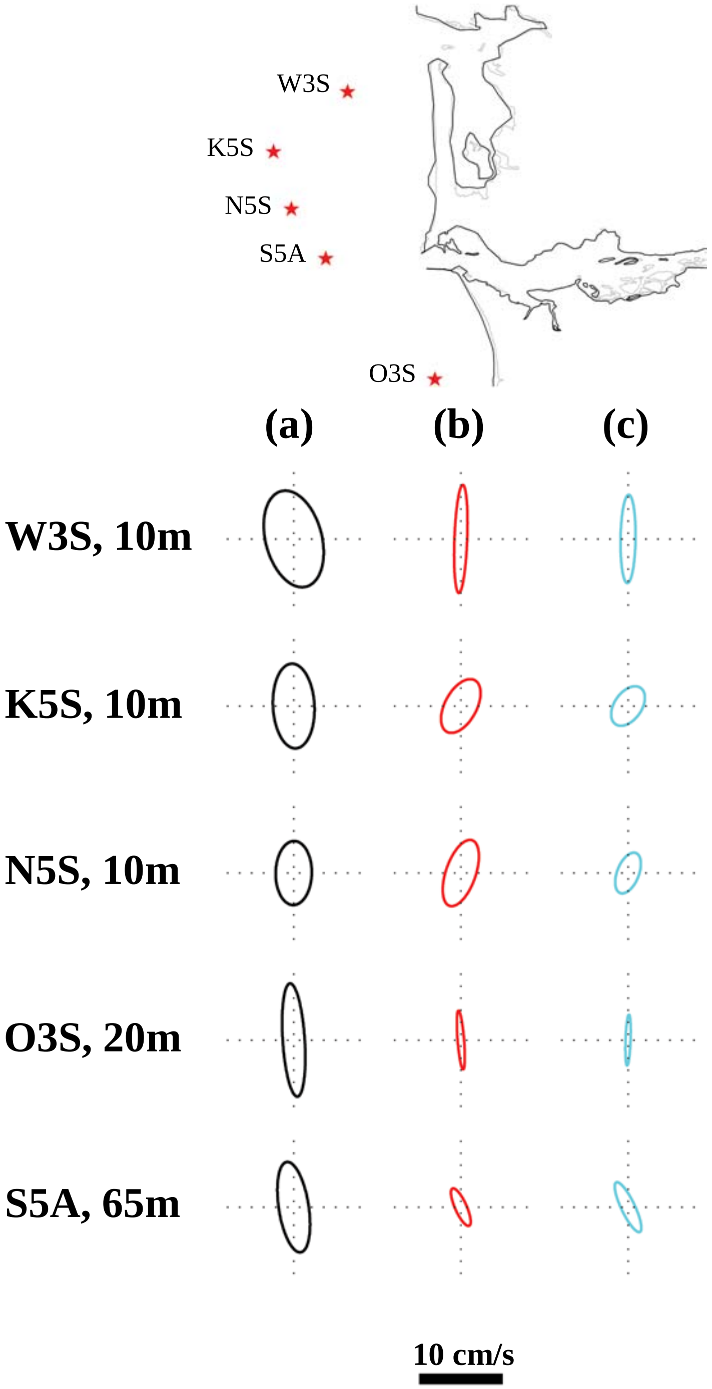

Figure 2.27 Continued.

Table 2.11 Observed and modeled M2 tidal velocity components (m/s), phases (°UTC), and distances (D) in the complex plane between the observed and modeled tidal velocity components (m/s) at **(a)** 5m, **(b)** 10m, **(c)** 20m, and **(d)** 65m instrument depths.

(a)

	Data				ELM						UWM					
	u		v		u			v			u			v		
Mooring	amp	phase	amp	phase	amp	phase	D	amp	phase	D	amp	phase	D	amp	phase	D
O5S	0.0086	282.8	0.0261	160.9	0.0212	108.1	0.0298	0.0545	70.6	0.0605	0.0059	32.2	0.0119	0.0468	84.7	0.0478
O3S	0.0150	34.3	0.0183	103.9	0.0060	38.2	0.0090	0.0372	67.9	0.0249	0.0166	6.9	0.0076	0.0308	45.3	0.0264
S5S	0.1059	128.3	0.0868	24.2	0.1183	132.2	0.0146	0.1196	13.3	0.0381	0.1073	143.4	0.0279	0.0945	27.1	0.0089
N5S	0.0561	92.0	0.0815	60.2	0.0374	95.0	0.0189	0.0814	41.4	0.0266	0.0176	78.5	0.0392	0.0595	52.0	0.0242
N3S	0.0712	125.9	0.0659	15.9	0.0730	109.8	0.0203	0.1427	12.4	0.0770	0.0468	125.6	0.0244	0.1083	23.9	0.0440
K5S	0.0277	68.5	0.0271	53.6	0.0378	46.5	0.0160	0.0289	35.4	0.0090	0.0355	21.3	0.0263	0.0136	31.6	0.0154
K3S	0.0055	153.6	0.0199	56.5	0.0371	56.8	0.0382	0.0368	13.0	0.0262	0.0264	5.8	0.0312	0.0147	29.2	0.0096
W1S	0.0265	30.6	0.0224	52.6	0.0337	18.7	0.0094	0.0433	349.6	0.0387	0.0381	350.3	0.0248	0.0426	333.4	0.0443
W3S	0.0259	5.0	0.0090	324.6	0.0435	51.3	0.0317	0.0480	7.3	0.0418	0.0397	15.2	0.0150	0.0330	5.5	0.0269
Average complex distance							0.0209			0.0381			0.0231			0.0275

(b)

	Data				ELM						UWM					
	u		v		u			v			u			v		
Mooring	amp	phase	amp	phase	amp	phase	D	amp	phase	D	amp	phase	D	amp	phase	D
W3S	0.0433	51.1	0.0285	18.3	0.0462	40.4	0.0089	0.0479	9.9	0.0202	0.0515	25.3	0.0227	0.0439	0.9	0.0188
K5S	0.0459	71.6	0.0448	27.0	0.0426	43.6	0.0216	0.0299	25.4	0.0150	0.0506	33.2	0.0320	0.0258	1.6	0.0242
N5S	0.0766	69.5	0.0515	15.9	0.0447	69.7	0.0319	0.0603	30.5	0.0167	0.0415	61.6	0.0360	0.0501	28.3	0.0111
Average complex distance							0.0208			0.0173			0.0302			0.0180

(c)

	Data				ELM						UWM					
	u		v		u			v			u			v		
Mooring	amp	phase	amp	phase	amp	phase	D	amp	phase	D	amp	phase	D	amp	phase	D
O3S	0.0165	15.6	0.0241	70.3	0.0280	53.2	0.0180	0.0442	35.3	0.0281	0.0241	31.6	0.0094	0.0378	33.1	0.0237

(d)

	Data				ELM						UWM					
	u		v		u			v			u			v		
Mooring	amp	phase	amp	phase	amp	phase	D	amp	phase	D	amp	phase	D	amp	phase	D
S5A	0.0175	180.2	0.0019	192.8	0.0065	226.4	0.0138	0.0043	84.3	0.0052	0.0066	257.6	0.0173	0.0057	110.8	0.0058

Table 2.12 Observed and modeled K1 tidal velocity components (m/s), phases (°UTC), and distances (D) in the complex plane between the observed and modeled tidal velocity components (m/s) at **(a)** 5m, **(b)** 10m, **(c)** 20m, and **(d)** 65m instrument depths.

(a)

	Data				ELM						UWM					
	u		v		u			v			u			v		
Mooring	amp	phase	amp	phase	amp	phase	D	amp	phase	D	amp	phase	D	amp	phase	D
O5S	0.0190	261.6	0.0105	271.9	0.0200	243.3	0.0063	0.0097	150.6	0.0176	0.0266	234.4	0.0130	0.0154	182.9	0.0185
O3S	0.0184	312.9	0.0151	303.5	0.0137	258.5	0.0153	0.0081	277.0	0.0087	0.0122	237.2	0.0194	0.0092	213.2	0.0177
S5S	0.0214	265.6	0.0349	127.0	0.0431	295.9	0.0269	0.0556	141.2	0.0234	0.0499	290.4	0.0318	0.0493	150.0	0.0219
N5S	0.0169	225.6	0.0250	196.4	0.0213	229.0	0.0045	0.0408	173.5	0.0203	0.0267	230.4	0.0100	0.0368	171.1	0.0178
N3S	0.0254	228.4	0.0148	85.8	0.0207	229.7	0.0048	0.0707	151.1	0.0659	0.0280	239.5	0.0057	0.0611	156.4	0.0579
K5S	0.0065	180.8	0.0276	45.7	0.0146	220.2	0.0104	0.0063	165.2	0.0312	0.0180	228.3	0.0144	0.0078	167.5	0.0324
K3S	0.0344	270.2	0.0105	357.6	0.0213	235.7	0.0207	0.0224	181.3	0.0329	0.0228	225.8	0.0241	0.0133	178.8	0.0238
W1S	0.0186	279.7	0.0398	43.5	0.0071	316.9	0.0136	0.0110	139.4	0.0423	0.0068	310.9	0.0133	0.0118	136.0	0.0420
W3S	0.0067	3.9	0.0154	25.1	0.0063	288.6	0.0080	0.0142	190.7	0.0294	0.0058	221.5	0.0118	0.0125	193.3	0.0278
Average complex distance							0.0123			0.0302			0.0159			0.0289

(b)

	Data				ELM						UWM					
	u		v		u			v			u			v		
Mooring	amp	phase	amp	phase	amp	phase	D	amp	phase	D	amp	phase	D	amp	phase	D
W3S	0.0171	264.6	0.0041	76.8	0.0054	262.6	0.0116	0.0159	193.6	0.0182	0.0024	178.2	0.0171	0.0098	188.4	0.0119
K5S	0.0077	303.3	0.0099	349.2	0.0135	226.2	0.0139	0.0052	192.6	0.0149	0.0085	198.1	0.0129	0.0023	81.2	0.0103
N5S	0.0020	338.7	0.0206	275.8	0.0192	211.0	0.0205	0.0230	171.1	0.0346	0.0124	211.2	0.0137	0.0158	162.3	0.0305
Average complex distance							0.0154			0.0225			0.0146			0.0176

(c)

	Data				ELM						UWM					
	u		v		u			v			u			v		
Mooring	amp	phase	amp	phase	amp	phase	D	amp	phase	D	amp	phase	D	amp	phase	D
O3S	0.0141	247.6	0.0131	332.3	0.0050	247.9	0.0090	0.0061	257.6	0.0129	0.0040	244.0	0.0101	0.0062	236.1	0.0151

(d)

	Data				ELM						UWM					
	u		v		u			v			u			v		
Mooring	amp	phase	amp	phase	amp	phase	D	amp	phase	D	amp	phase	D	amp	phase	D
S5A	0.0344	114.8	0.0131	320.2	0.0095	348.0	0.0408	0.0103	109.5	0.0226	0.0127	334.1	0.0449	0.0095	144.7	0.0225

CHAPTER 3

INFLUENCE OF WIND FORCINGS AND TRANSPORT ALGORITHMS ON THE SIMULATION OF THE FRASER RIVER SUMMER PLUME

3.1 Abstract

Six baroclinic numerical experiments are performed with the hydrodynamic model SELFE [1] to assess the influence of atmospheric conditions and the advection algorithm for the transport of salt on the development and representation of a summer freshwater plume for the Fraser River, British Columbia. Wind inputs are derived from the University of Washington Mesoscale Model (MM5), National Weather Service ETA-12 model (ETA), and National Weather Service North American Regional Reanalysis model (NARR) weather models and a reference case without wind forcing. The advection algorithms are based on Eulerian-Lagrangian Methods (ELM, Section 1.4.2) and Upwind Methods (UWM, Section 1.4.3).

Model computed water elevations and salinities are compared with observed tides and a thermosalinograph mounted on the hull of the Tsawwassen-Duke Point (central) BC Ferry. The choice of wind forcing influences the model results due to differences in the strength of each forcing. Water elevations are similar for each of the experiments, with phase and amplitude errors in the tidal signal mainly attributed to inadequate representation of the tidal forcing at open boundaries along the northern Strait of Georgia. Improvements in this boundary condition are shown to reduce errors in elevation through two barotropic SELFE experiments.

The UWM algorithm produces much smaller and saltier plumes, and has results which more closely match observed salinities than the ELM algorithm. Wind forcing is also an important choice for modeling this region, as ETA and NARR have weak winds, while MM5 is overly strong.

3.2 Introduction

The coastal waters of southwestern British Columbia and northwestern Washington, including the Straits of Juan de Fuca and Georgia and Puget Sound, (Fraser Region hereafter) have been the center of numerous studies utilizing observations and/or model simulations. The Fraser Region presents a complex system for studying circulation and other important physical/biological processes, through field or simulated experiments. It is comprised of many narrow deep passages, the largest of which are Juan de Fuca Strait and the Strait of Georgia (Figure 3.1, p.112). The Strait of Georgia is on average 30km wide and 210km long; while Juan de Fuca Strait is narrower at 20km wide and shorter at 130km. The connections from the Strait of Georgia to the northern tip of Vancouver Island are particularly constricted and are dominated by tidal velocities of several meters per second [2]. These high velocities are due to elevation differences caused by the lag of up to 5 hours for tides to travel through these channels instead of around Vancouver Island [2]. Due in part to these high velocities and also to dramatic changes in bathymetry, tidal mixing prevents much subtidal exchange from occurring between the Strait of Georgia and the Pacific Ocean through these northern passages. Therefore, exchange between the Strait of Georgia and the Pacific Ocean primarily occurs through the southern connections around the Gulf and San Juan Islands, including Haro and Rosario Straits, and then through Juan de Fuca Strait (Figure 3.1, p. 112). The Fraser River conveys the largest freshwater discharge for British Columbia, with a watershed covering 230,000km^2 and an annual mean ranging between 700-7,100 m^3/s providing approximately 50% of the annual total discharge to the Fraser Region.

The framework developed for a coastal margin observatory for the Columbia River (CORIE [3-5]), a pilot environmental observation and forecasting system, includes an observation network of instruments within the Columbia River estuary and plume delivering real time measurements of salinity, temperature, elevation, and velocity via telemetry and a hydrodynamic modeling system producing both forecast and hindcast products. Operating since 1996, CORIE has served as a mechanism to increase the understanding of the Columbia River estuary and plume circulation and also changes in the circulation, providing guidance for scientific cruises and the management decisions affecting this resource.

As part of the current research, the modeling portion of the CORIE framework has been extended to the Fraser Region providing a second model proving ground for a large freshwater plume within the Pacific Northwest and southern British Columbia. A strong interest exists in being able to understand and predict the physical and biological oceanic properties within the Fraser Region. Many of the previous modeling studies have been focused on tidal modeling including [2]. Other recent and future model studies intend to focus on oceanographic processes that are wind driven and/or of biological importance, such as the generation and transport of algal blooms [6]. A hydrodynamic forecast [7] is operated by the Institute of Ocean Sciences (IOS) using the Princeton Ocean Model (POM [8]). This forecast is performed in a barotropic mode, forced only by eight tidal constituents (K1, O1, P1, Q1, M2, S2, K2, and N2). An additional forecast for the Fraser Region, operated in a baroclinic mode, was implemented using the CORIE modeling framework and the National Estuarine Forecasting System (NEFS [9]) for the model grid domain and ELM SELFE presented in this thesis.

The focus of this study is to investigate the influence of the choice of advection algorithm and wind inputs from numerical weather models on the generation of a summer plume for the Fraser River using the hydrodynamic model SELFE [1]. The two advection algorithms, Eulerian-Lagrangian Method (ELM, Section 1.4.2) and Upwind Method (UWM, Section 1.4.3), are used to compute the transport of salt; while the datasets produced by the numerical weather models, National Weather Service North American Regional Reanalysis (NARR), National Weather Service ETA-12 (ETA), and the University of Washington Mesoscale Model 5 (MM5), are compared against results from experiments performed without wind inputs. In total, six experiments are performed with varied wind forcing; all four variations of the wind forcing using ELM and two wind forcing variations using UWM. Table 3.1 (p. 112) indicates the variations in the six experiments. Improvements in daily forecasts and future hindcast modeling studies will be guided by an increased understanding of the impact of these model choices.

The remainder of this chapter is composed of five sections. The next section (3.3) describes the methods used during the setup and analysis of the numerical experiments, including a description of each of the wind datasets. Section 3.4 assesses the quality of each of the three atmospheric datasets by comparing the mean speeds/directions, principal axes, and wind stress with those of the measured winds. Section 3.5 presents the results using SELFE for each of the six hydrodynamic experiments. Finally, section 3.6 provides a discussion of these results in the context of the different wind fields and representation of the summertime Fraser River plume.

3.3 Methods

The six experiments presented in this chapter explore the use of the two transport algorithms, ELM and UWM, within SELFE [1] and also the influence of different wind datasets on the development of the Fraser River plume for the summer of 2005. Forcings were applied in a realistic fashion, using forecasted values when available (initial and nudging salinities/temperatures and winds) and climatological values (freshwater input) when necessary. The model domain and individual inputs are discussed within this section.

3.3.1 Model domain

The model domain includes the Fraser River from Hope, British Columbia and extending west through the northern and southern arms to the Strait of Georgia, although tributary inputs below Hope are neither included in the model domain nor used for freshwater inputs. Also included in the domain are Puget Sound, Juan de Fuca Strait, and offshore regions west of Vancouver Island, and the states of Washington and Oregon (Figure 3.1, p. 112). The grid is composed of 24,857 nodes making up 44,189 unstructured triangular elements and 37 S vertical levels. Similar to other experiments using SELFE (see Section 4.3 and 4.5 of [1] and Chapter 2 for a description of the Columbia River simulations using SELFE and realistic bathymetry), realistic bathymetry was used in the grid construction when available. Horizontal resolution varies in the grid from 20km in the offshore regions to 100m inside the mouth of the Fraser River.

A constant bottom friction factor of 0.0025 is used for these experiments, which is a commonly used value in coastal ocean model [8, 10]. This friction factor is the default used for new forecast simulations initialized within NEFS [9], and is currently used for the Fraser Region, Humboldt Bay, Monterey Bay, Siletz/Depoe, Tampa Bay, Tillamook/Nehalem/Netarts, and Yaquina/Alsea forecast simulations. Other modeling studies for the region have used larger friction factors to compensate for energy losses associated with physical processes other than bottom drag, such as those given in [11] (i.e. turbulent mixing, internal tides, side wall friction, etc). A constant bottom friction factor of 0.01 is used for the barotropic simulations of [12], while a larger value of 0.03 is used by [2] within the narrow channels surrounding the San Juan / Gulf Islands (i.e. Haro and Rosario Straits). These calibrations are not explored within the context of the current studies, as this work presents a first effort to understand the influence of certain modeling options for the simulation of the Fraser River summer plume and an example of expansion of the CORIE framework to another large river plume system located in the Pacific Northwest and southern British Columbia.

3.3.2 Forcings

3.3.2.1 Initial and nudging salinities and temperatures

All four of the ELM simulations are initialized from a quiescent state with salinity and temperature values interpolated from the Naval Research Laboratory's (NRL) Navy Coastal Ocean Model (NCOM [13, 14]) forecast model outputs for August 13, 2005. NCOM is operated by NRL as a data assimilated global daily forecast model [14] forced by wind stress and heat flux from the Navy's Operational Global Atmospheric Prediction System (NOGAPS) [14]. NCOM assimilates temperatures and salinities from the

Modular Ocean Data Assimilation System (MODAS) [14]. The resolution of NCOM is 1/8°, or approximately 14km, at the mid-latitude 45°. Use of NCOM in the Fraser Region SELFE experiments allows for the incorporation of ocean dynamics initiated outside of the Fraser Region but moving into the model domain. To decrease the computational time for the two UWM simulations, both are initialized from the conditions at the end of the first week of ELM simulation, on August 20. A transition between oceanic and river salinity values is created in the initial conditions between river kilometer 25 and 31 to facilitate the generation of an August salt wedge for the Fraser River [2]. Salinities and temperatures are nudged to daily NCOM values with a maximum horizontal nudging factor [4] of $5x10^{-4}$ near the open ocean boundaries and decreasing to 0 near the plume (Figure 3.2, p.113). Vertical nudging profile is homogenous. Nudging maintains ambient ocean conditions near the grid boundaries. The maximum nudging factor, $5x10^{-4}$, contributes a weighted portion of the NCOM salinity/temperature value to a SELFE computed value at each model time step (90s for each of these experiments). This nudging scheme is the same as used in Chapter 2 for the Columbia River experiments and again follows [4, 15] as shown in equations 2.1-2.

3.3.2.2 Tidal boundary conditions

Model boundary elevation conditions are forced by 10 tidal constituents (O1, K1, Q1, P1, K2, N2, M2, S2, M4, and M6) and a mean sea level (Z0). The amplitudes and phases for the 10 tidal constituents were from measured water elevations at the Campbell River (8074) and also interpolated from [16, 17]. The tidal conditions were applied to the northern, western, and southern open ocean boundaries, as well as the northern entrance to Johnstone Strait near Port Hardy. Each open boundary node, along the northern Strait of Georgia, is forced by the harmonics of the measured time series of elevation at the Campbell River (8074). Weekly Z0 values are applied from NCOM forecast model outputs to tidal boundary nodes (Figure 3.3, p. 114).

3.3.2.3 Estuarine inputs for the Fraser River

The Fraser River is the dominant source of freshwater for the region of this study, contributing approximately 50% of the total freshwater, and larger percentages during the freshet and also in late summer when less precipitation feeds coastal rivers not receiving input from snowmelt [18]. The period chosen for this model study occurs after the peak freshet and much before when winter rains begin to the smaller coastal rivers. Inputs for the Fraser River are applied from the mean climatological discharge at Hope, BC from 1912-2003 (Figure 3.4, p. 115) and daily river temperature from NCOM model results near the river mouth. Baroclinic solutions to the transport equations are ramped during the first day of simulation. Preliminary discharge measurements at Hope for 2005 were obtained after completion of each of the experiments from Water Survey Canada. For the modeled time period the mean climatological discharge is 27%, or 21,170 m^3 greater than the preliminary discharge. It is also noted that the preliminary discharge was below normal during this time period, falling between 5th and 25th percentile of the mean climatological discharge.

3.3.2.4 Atmospheric conditions

SELFE does not compute atmospheric parameters; therefore these values are needed as inputs for the computation of heat exchange and surface stress at the air-water interface. For the purposes of the sensitivity tests performed in this study, the heat exchange module is neglected for each of the 6 experiments, and atmospheric inputs are used to compute surface stress only. These experiments do not explore the ability of the air sea heat exchange module available within SELFE. Upon initialization of each experiment the inputs from the wind fields are ramped up during the first simulated day from no forcing to full strength.

The sensitivity of simulated coastal processes to three different atmospheric conditions has been assessed for a domain near Point Conception, CA using the hydrodynamic model POM [19]. The atmospheric forcings included two model outputs, the European Centre for Medium-Range Weather Forecasts (ECMWF) and the Coupled

Ocean-Atmosphere Mesoscale Prediction System (COAMPS), and ECMWF blended with remote and in situ observations (SEB). The findings of [19] indicate differences between the modeled circulation from each of the forcings. In particular the lowest resolution wind input, ECMWF (110km), resulted in weaker wind driven circulation. The higher resolution and stronger winds of SEB produced results in better agreement with observations.

Similar to the experiment of [19], the sensitivity of the summertime Fraser River plume to three atmospheric inputs is investigated with SELFE. However, for the current study each of the forcings is taken from different atmospheric datasets and not interpolated from measured winds. The atmospheric datasets (Table 1.1, p. 13) used include output from the University of Washington operated Mesoscale Model 5 (MM5), the National Weather Service ETA-12 model (ETA), and the National Weather Service North American Regional Reanalysis model (NARR).

NARR wind input is derived from the NCAR / NCEP regional analysis data set grid 221, which has a horizontal resolution of 32km and is available at 3h intervals. NARR is a reanalysis product using the ETA numerical code and assimilating measured data. NARR is the lowest resolution product used, and it is coarse when considering its resolution in relation to the size of the Strait of Georgia (on average 30km wide by 210km long). The ETA model inputs are also derived from the ETA grid 218, which is run in forecast mode. ETA has a higher spatial resolution than the NARR at 12km, but is available at the same temporal resolution. MM5 wind inputs have the highest spatial (4km) and temporal resolution (1h) of the three forcings investigated. MM5 is also run in forecast mode. For reference purposes, additional experiments using both the ELM and UWM transport algorithm were performed without forcing.

3.3.3 Observations

Winds measured at 21 observation stations, maintained by the National Oceanic and Atmospheric Administration's (NOAA) National Data Buoy Center (NDBC) and Environment Canada, are used for comparison with the results of the three wind models (Figure 3.5, p. 115). Only nine of these stations (46029, 46041, 46087, 46088, WPOW1, 46146, 46134, 46131, and 46206) fall within the domains of all three models and should be used to compare the quality of each wind model for the specific region being modeled. The other comparisons performed provide a reference for future modeling studies.

Model salinities and zero mean elevations are compared against measured data (Figure 3.5, p. 115). Salinity data is measured along the Tsawwassen-Duke Point (central) BC Ferry route by a hull mounted thermosalinograph. Water elevations are measured by the NOAA's Center for Operational Oceanographic Products and Services (CO-OPS) and Department of Fisheries and Oceans Canada tidal gauge stations (Figure 3.5, p. 115). The tide gauge stations used include: Bamfield (8545), Campbell River (8074), Cherry Point (9449424), Friday Harbor (9449880), Neah Bay (9443090), New Westminster (7654), Port Angeles (9444090), Port Hardy (8408), Port Townsend (9444900), Tofino (8615), Vancouver (7735), Victoria Harbour (7120), and Winter Harbour (8735).

3.3.4 Performance metrics

Similar to the methods of [20] mean speeds (vector and scalar), mean directions and principal axes ([21]; Appendix A.2) for each atmospheric forcing are compared with observed winds. Vector and scalar mean speeds assess each model's ability to represent the long term trend of the observed wind field. Vector means measure the average speed in the average direction of the wind, while scalar means measure the average speed independently of the direction. Using both of these methods reveals if the model represents the magnitude properly and if it accounts for the proper direction. Principal axes serve as a means to compare the magnitude and direction of the maximum and minimum variance of the vector field. Time series of wind stress are also compared.

The results from each of the hydrodynamic experiments will be assessed for their ability to simulate and maintain the freshwater plume of the Fraser River. The comparisons of modeled and measured water elevations are assessed and a sub-experiment forced by tides only is performed to understand how the tidal boundary condition along the northern Strait of Georgia is impacting water elevations with the Straits of Georgia and Juan de Fuca. Time series comparisons of modeled to measured salinities and contours of surface salinities are used to compare the results of each of the experiments. Mean speeds, mean directions, and principal axes are computed for horizontal water currents and used for evaluating differences between the experiments.

3.4 Wind field analysis

Analysis of the MM5 wind fields, for both the 12km and 4km grid versions, has been performed for the summer and fall of 2003 by [20]. Their analysis indicates that both of the models capture a majority of the observed wind fluctuations. However, they also note that the model winds in the central Strait of Georgia have a very low coherence with the observed summer diurnal winds.

Time series means and principal axes, also used in the analysis of [20], are computed for modeled wind fields and compared with and measured winds at 20 moored buoys and one land based site. Average metrics are computed using the 9 stations (Figure 3.5, p. 115) that lie in the domain of all three weather models and are also closest to the Fraser Region. Consistent with the analysis of NARR model winds presented in Chapter 2, adjustments to measured wind speeds for height have not been performed in the analysis presented here and directions are referenced towards the direction of wind movement, as opposed to meteorological angles, to readily place them in context with the directions of water currents. Height adjustments were performed in the study of [20] as a uniform factor of 1.08 using the data of [22]. As for Chapter 2, the adjustments for anemometer height were not applied as heights for all anemometers were not known. Therefore, the presented magnitudes of measured wind speed maybe underestimated by 2-8% using the tables of [22].

3.4.1 Time series means

The seasonal mean winds for the Fraser Region are steered and modulated by the varied topography of the mountain/valley landscape [23]. In particular the summer mean winds are variable in the southern part of this region. These patterns of variability are reflected in the mean wind vectors for the stations 46088, 46134, 46131, and 46146

(Figure 3.6, p. 117). The variability decreases in the northern part of this region, where the mean summer winds are aligned with offshore winds, similar patterns were found in [20]. This is evident when comparing mean wind vectors for stations 46131 and 46132.

Mean values of wind vector and scalar speed and direction are provided for each of the atmospheric models and observed data (Table 3.2, p. 116). MM5 winds are stronger on average than both the NARR and ETA, when compared with the measured data. Using the nine stations coincident in all three of the weather model domains, the average ratio of modeled to observed wind mean vector speed is 2.7, 0.90, and 0.88 for the MM5, ETA, and NARR respectively. The orientation of the mean model wind directions are 2° clockwise for the MM5, 9° counter-clockwise for the ETA, and 14° clockwise for the NARR, all with respect to the mean measured wind directions.

These findings for the MM5 winds are consistent with [20]. For the 4km MM5 results they analyzed, the MM5 model winds were stronger than observations with an average ratio of modeled to observed wind magnitude of 1.55. Another similarity between these findings and [20], is that a large portion of average ratio of mean vector speed for the MM5/data results is attributed to the ratio for the station 46146, which has a ratio of 10.8 for the current analysis. By removing this station and performing the aggregate analysis on the remaining coincident stations the average ratio of model to observed wind magnitudes improves to 1.66 for the MM5 and 0.94 for the ETA; while it degrades slightly for the NARR to 0.85.

3.4.2 Principal axes

Comparison of principal axes serves as an indicator of each model’s ability to predict the variability in the observed wind field. Using this form of analysis, the major and minor axes lie in the directions of the maximum and minimum variance for the wind vector time series. The major and minor axes (λ_1 and λ_2) and direction (θ_p) of the principal ellipses for each of the atmospheric models and the observations are provided (Table 3.3, p. 118) and the ellipses are plotted (Figure 3.7, p. 119-122). MM5 winds have a greater amount of variance than the observed winds in the major axis direction and less variance than the observed winds in the minor axis direction, with an average modeled to observed ratio of 1.09 and 0.97 for the major and minor axes respectively. ETA and NARR both have less variance than the observed winds, with average modeled to observed ratios of 0.80 and 0.66 less in the major axis direction and 0.59 and 0.62 in the minor axis direction, for the ETA and NARR respectively.

3.4.3 Wind stress

Wind stress is proportional to the square of wind speed represented simply by equation 3.1, which retains wind direction.

$$\tau_w = C_d U_w \left| U_w \right| \tag{3.1}$$

SELFE utilizes a module based on the aerodynamic bulk model of [24] to compute wind stress from model inputs and thus supply momentum to the water column. The relationship between wind velocity and wind stress provides for an additional means to compare the MM5, ETA, and NARR weather models. Through time series of the u/v components of wind stress at buoy locations for each of the three atmospheric weather models (Figure 3.8-9, p. 123-124), NARR produces much weaker wind stress (again the resolution of NARR is coarse within the Strait of Georgia) within the Strait of Georgia (Figure 3.8-9g,h, p. 123-124) than either MM5 or ETA. MM5 winds produce the greatest amount of wind stress. Three periods (August 21-25; August 27-31; and September 7-10) of increased wind stress present in the observed data at the two buoys within the Strait of Georgia (46131 and 46146) are represented in the results for both the ETA and MM5 by increased magnitude and reversal in direction from southward to northward from the first to the second event. Such reversals are important in developing alternating upwelling and downwelling favorable circulation patterns and consequently the spreading and mixing of the buoyant fresh water with ambient salt water. Both upwelling and downwelling are important physical processes in the context of biological processes, causing movement and spreading of nutrients and organisms.

3.5 Results of the SELFE experiments

The influence of the three different weather models for atmospheric inputs and also no atmospheric inputs on the simulation the summer Fraser River plume is assessed in experiments 1-4 of this study. The differences in the wind fields for each of the inputs results in differences in plume size/freshness and water velocities. Experiments 3 and 4 were repeated using the UWM solution of the transport algorithm within SELFE as experiments 5 and 6; allowing for additional comparisons of the influence of these algorithmic and wind modeling choices. From Chapter 2 and also this study, using the UWM scheme provides improved results for plume formation than the ELM scheme.

3.5.1 Elevations

Measured and computed water elevations are compared for 13 tide gauge locations distributed throughout the model domain for the time period shared by all experiments (August 20–September 17). The is performed by looking at both raw comparisons of measured to modeled elevations and also looking at comparisons of modeled elevations against synthesized observations following harmonic analysis [26] of the ten modeled constituents. For the harmonic analysis, the P1, K2, and NU2 constituents are inferred for each of the observed time series. Harmonic analysis of the modeled elevations at each station is performed using inference of the P1 and K2 constituents and by using only the modeled constituents. The cross comparison of these two methods for assessing elevations provides a means to judge how much error in the tidal representation is due to missing constituents and how much is due to errors in the forcing and other model parameters.

Small improvements for water elevations are achieved with UWM (Table 3.4, p. 125 and Table 3.5, p. 131). The average difference between RMS errors of zero mean elevations show that the MM5 UWM is approximately 1cm less than the MM5 ELM results, while for the stations inside of the Straits of Juan de Fuca and Georgia (excluding Campbell River as it is near the boundary forcing) the difference indicates MM5 UWM is better than MM5 ELM by approximately 2cm at representing the raw water elevations

(Figure 3.10, p. 126). Similarly the difference between RMS errors of zero mean elevations for the UWM and ELM experiments without wind, UWM is better by approximately 2cm both inside and outside of the Straits of Juan de Fuca and Georgia. Differences in RMS errors of zero mean elevations between results for each of the wind variations are not greater than a few millimeters.

Time series plots of the MM5 ELM and observed zero mean water elevations reveal that the general tidal signal is well represented, including spring/neap variation (Figure 3.11, p. 127-128 and Figure 3.14, p. 133-134). However, both phase and amplitude errors are evident in these results. The tidal nature of these differences is readily apparent in differences of raw elevations (Figure 3.12, p. 139-140), and we note that when comparing the differences in synthesized elevations (Figure 3.15, p. 135-136) that the errors are less for the synthesized results. We also note that the reductions in RMS errors from the raw to the synthesized are larger for offshore stations. This indicates that for these stations the missing tidal harmonics within the model lead to higher errors, while for the other stations the errors are influenced by other factors, including errors in the boundary condition discussed below. RMS errors increase moving east within Juan de Fuca Strait and subsequently reduce moving northward through the Strait of Georgia (Figure 3.10, p. 126 and Figure 3.13, p. 132). The primary source of error for the stations within Juan de Fuca Strait and the Strait of Georgia is the inadequate representation of the tidal boundary forcing along the northern Strait of Georgia. Model simulations of tides for the Strait of Georgia and particularly for the representation of the M2 amphidrome at Victoria Harbour, BC are sensitive to this boundary forcing [25]. The harmonics for the Campbell River tide gauge were applied for each of the open boundaries along the northern Strait of Georgia within the numerical grid. These harmonics vary non-linearly across these channels due to differences in coastline geometry and bathymetric changes (e.g. cotidal plots of [12] for examples of bending of the phase/amplitudes isopleths within narrow channels).

Two barotropic simulations using SELFE and forced only by tides were performed using the horizontal grid (Figure 3.16, p. 137) of [12]. The first, BEXP1, uses boundary conditions of [12] to test the elevation results for an experiment with improved boundary conditions. These boundary conditions were interpolated from previously published cotidal plots and harmonics from nearby tide gauges. The second, BEXP_2, uses boundary conditions interpolated wholly from [16, 17], making it more similar to the larger baroclinic domain experiments and therefore testing differences in water elevations derived from using the higher resolution around the Gulf and San Juan Islands offered by this grid. Both of these simulations use the same 8 tidal harmonics (O1, K1, Q1, P1, K2, N2, M2, and S2). The differences between the two boundary conditions are computed as the distance in the complex plane (Appendix A.1) at each boundary node and are approximately zero for each of the boundaries except across Juan de Fuca Strait (Figure 3.17, p. 138). In spite of these differences along the Juan de Fuca Strait boundary, the water elevations for these two experiments at Victoria Harbour are the same, as discussed below. For both experiments, the domain is smaller and does not suffer from the improper tidal boundary condition along the northern Strait of Georgia present in the baroclinic simulations. Ten vertical S levels are used, while [12] reported results from a simulation using 11 sigma levels.

The results of BEXP1 and BEXP2 are evaluated with those of the MM5 ELM baroclinic simulations. Similar to the analysis for the larger domain experiments, raw comparisons are provided (Figures 3.18-19, p. 139 and Table 3.6, p. 139) and also synthesized observations are used after harmonic analysis [26] (Figures 3.20-3.21, p. 140 and Table 3.7, p. 140). The harmonic analysis again uses inference of the P1, K2, and NU2 constituents for the observed elevations and then synthesizes only the leading 8 constituents as specified in BEXP1 and BEXP2. Harmonic analysis of the model elevations uses inference for the P1 and K2 constituents. Time series of zero mean elevation (Figure 3.18, p. 139) indicate an improved fit to the observed tidal signal for both BEXP1 and BEXP2, each having an RMS error of 0.101m which is similar to the error found at coastal locations in the baroclinic simulations and 46% less than the RMS error for the MM5 ELM experiment. Differences of elevation (Figure 3.16, p. 137 and Figure 3.21, p. 140) indicate that the improvements in the boundary condition result in less errors originating in the major tidal constituents and that increasing the grid resolution within the narrow passage around the Gulf and San Juan Islands does not offer a reduction in errors.

Distances computed in the complex plane (Appendix A.1) between the measured and modeled tidal constituents clearly show (for both the raw observed Table 3.6, p. 139 and the synthesized observed Table 3.7, p. 140) the improvements due to the better boundary conditions of the barotropic experiment. The complex distances also indicate that a larger portion of the error is due to the boundary forcing and not in the lack of tidal constituents used to force the model simulations, as the reduction in error between the raw and synthesized is less than between the use of the different forcings.

3.5.2 Salinities

Contour plots of surface salinities for the final simulated time step, on September 17, 2005, for each of the six experiments reveal the qualitative influence from the wind and algorithmic differences (Figure 3.22, p. 141). Wind mixing is important for the determination of plume size using SELFE, as shown by comparing the results for each of the four wind variations that use the same transport algorithm (ELM). For both of the transport algorithms MM5 winds produce smallest and saltiest plumes out of the 4 wind cases. The experiment without wind (Figure 3.22d, p. 141) produces the largest and freshest plume, extending north along the west coast of Vancouver Island to Brooks Peninsula. NARR winds are weak within the Straits of Juan de Fuca and Georgia, but stronger offshore. Consequently the simulation forced by NARR winds produces a plume that is large in the central Strait of Georgia but extends only to Estevan Point along the west coast of Vancouver Island (Figure 3.22c, p. 141). ETA winds produce plumes that are slightly smaller than those produced using NARR (Figure 3.22b, p. 141). Dramatic differences between using ELM or UWM are evident when comparing the results for either the two MM5 experiments (Figure 3.22a, e, p. 141) or the two experiments without wind (Figure 3.22d, f, p. 141). For both the MM5 and no wind cases the UWM produces much smaller and saltier plumes. However, similar to the comparison of the ELM MM5 and ELM no wind cases, the UWM no wind produces a larger plume than the UWM MM5. Daily (24 hour) averaged salinities from the measured thermosalinograph data and the three Fraser Region experiments started on

August 13, 2006 indicates that the initial model conditions are more salty than those observed by approximately 5psu (Figure 3.23, p. 142).

3.5.2.1 Influence of wind forcing on salinity

Quantitative comparison of the daily (24 hour) averaged measured salinities and the six Fraser Region experiments are used to visualize the lower frequency salinity trends within the Strait of Georgia (Figure 3.23, p. 142). Two increases in salinity occurring August 20-24 and September 9-15 correspond to increased wind stress events within the Strait of Georgia at buoy 46146. These increases are due to mixing associated with the wind events. As evidence, the salinities do not increase during these two periods for the experiments without wind forcing. The amount of increase in salinity for each of the simulations varies with the MM5 results showing the largest increase in salinity due to the greater amount of wind stress provided by the MM5 in this region. However, the model results do not represent the shorter term salinity fluctuations that are apparent in the measured data between the two wind events, from August 25–September 6.

Five separate salinity contours (22, 24, 26, 28, and 30psu) are used to compute plume volume (Figure 3.24-25, p. 143-144) and thickness (Figure 3.26-27, p. 145-146) throughout the duration of each experiment. Plume size grows large throughout the duration of the 4 ELM experiments independently of the choice of wind forcing, as shown by both plume volumes (Figure 3.24, p. 143) and plume thickness (Figure 3.26, p. 145) for each salinity contour. In fact for these experiments, plume volumes do not stabilize. For the salinity contours used to compute plume volumes, the two experiments without wind forcing have larger volumes than the corresponding wind forced experiments. The plume volumes of experiments using MM5 are the smallest, while those for ETA and NARR forced experiments are larger than MM5 and similar to each other.

Although plume thicknesses (Figure 3.26, p. 145), for the 4 wind cases using the ELM, tend to increase throughout the duration of the experiments some response to the mixing events is apparent in depth profiles of salinity at the location of buoy 46146 (Figure 3.28, p. 147). Again, the general increase in plume thickness is apparent in this figure, however the mixing within the water column is shown for the wind event around September 9. The salinities increase in both of the MM5 and the ETA experiments, while very little increase is seen in the NARR experiment and none in the experiment without wind. Following this event, the plume begins once again to grow in thickness and the deeper layers become fresher.

3.5.2.2 Influence of transport algorithm on salinity

Model salinity results are affected dramatically by the choice of different transport algorithms within SELFE. Surface contours of salinity for the final time step of each experiment (Figure 3.22, p. 141) and time series of plume volumes (Figure 3.24-25, p. 143-144) show that the UWM produces much smaller saltier plumes than the ELM. UWM plume volumes are generally more stable, for the freshest salinity contours, than the ELM plume volumes which increase throughout the duration of the experiments. Also, the plume volumes for UWM fluctuate with tidal and wind processes. The wind event around September 9 causes a decrease in plume volume for nearly all of the salinity contours of the MM5 UWM experiment that is not seen in the UWM experiment without wind.

Along the central BC Ferry route (Figure 3.23, p. 142) the increases of daily average model salinities differ with the choice of advection algorithm. ELM produces plumes that are overly fresh independent of the wind forcing and even for the case without wind (Figures 3.23, p. 142). The UWM advection algorithm produces plumes that are less fresh using both MM5 and no wind. In fact the UWM results are saltier than the observed values. MM5 UWM salinities respond to the two wind stress events occurring August 20-24 and September 9-15. The first of these events occurs during the initial week of the UWM simulations; here the increase in salinity can also be attributed to the use of UWM and not wind forcing, as the increase is evident in the UWM no wind case as well. MM5 UWM salinities increase by approximately 3psu during the second wind event, while the observed salinities increase by 8psu.

UWM plume thicknesses are substantially thinner than the ELM, by an average of 30m, except for the 30psu contour (Figure 3.26, p. 145). For the 22-26psu contours, both

UWM experiments have thicknesses less than 5m, while ELM thicknesses are greater than 35m. Similar to the plume volumes, UWM produces mean thicknesses that are more stable at the lower salinity contours than the ELM, which generally continue to increase during each simulation. Increases in the MM5 UWM 28psu thickness correspond to the two wind mixing events, with an approximately 5m increase in thickness during the second wind event (Figure 3.27, p. 146). As the fresher water mixes vertically the next highest contour thickness increases, which subsequently leads to a decrease in the thickness of the fresher contour. This is most evident when comparing the 26-28psu contours. The 28psu contour peak thickness lags the 26psu contour, while the greatest decrease in 26psu thickness corresponds to the peak thickness of the 28psu contour. Also, tidal fluctuations within the 22-26psu contours typically mixes plume over 1m of the water column. Depth profiles of model salinities at buoy 46146 (Figure 3.28, p. 147) further indicate the much shallower saltier plumes generated with UWM than with ELM. UWM maintains more stability of the surface layers than the ELM. As the plume size grows, the salinities decrease throughout the water column with the ELM.

3.5.3 Velocities

The influence of the four variations of wind forcing (MM5, ETA, NARR, and none) and the transport algorithm (UWM and ELM) on the surface water velocities is assessed by comparing the mean magnitudes (both vector and scalar), mean directions, and principal axes at buoy and two reference locations within the model domain. These comparisons are only qualitative, as no observed velocities are used. Velocities for experiments without wind forcing are used as a reference to compare against the velocities from experiments with wind forcing. Although it is important to note that the differences in modeled velocities are due to differences in both the momentum applied as wind stress and the baroclinic pressures arising from the differences in the Fraser River plumes (Section 3.5.2).

The metrics used to compare winds are applied here for velocity comparisons. For a given location, if comparisons between simulations with and without wind forcing yield ratios of scalar magnitudes close to one and also low directional biases, the influence of wind forcing on velocities for this location may be considered minimal. Examples of locations that meet these criteria include those where velocities are dominated by processes other than wind forcing, as in the case for Haro Strait (HS) and Rosario Strait (RS). Water velocities within these two narrow channels are dominated by tides. The degree of polarization for velocities in these two straits is low for all experiments, indicating that the variance is highly rectilinear.

3.5.3.1 Influence of wind forcing on velocities

Differences exist between the model surface velocities computed using the different wind forcings. Using wind forcing and ELM transport algorithm results in larger mean scalar speeds and also differences in the mean direction of surface currents compared to results without wind forcing (Table 3.8a, p. 148 and Figure 3.29, p. 150). The average ratios of the mean scalar speed of the experiment with wind to the experiment without wind are 1.14, 1.12, and 1.08 for the MM5, ETA, and NARR respectively. The analysis of each modeled wind field yielded results similar to one another at locations farther offshore, such as at buoy 46207 (Section 3.4). Consequently, the surface currents at 46207 are similar for each of the different wind forcings used, with mean directions of 247°, 254°, and 256° and mean scalar velocities of 0.137 m/s, 0.137 m/s, and 0.138 m/s, for the experiments forced by MM5, ETA, and NARR respectively. MM5 winds produce the largest bias in mean current direction compared with the experiment without wind, at 25.9° counter-clockwise with respect to the mean current direction of the experiment without wind.

The case without wind is also used as a reference for the effect of different winds on the variance of surface currents using the method of principal axes (Table 3.9a, p. 151 and Figure 3.30, p. 153-154). Differences in surface current variance for each of the wind forced experiments are minimal at the offshore locations west of Vancouver Island, Washington, and Oregon; while the experiment without wind has different amounts of variance in these regions. Within the Straits of Georgia and Juan de Fuca surface current variance between each experiment is most different at buoy location 46146. For each of the wind cases, the MM5 forced experiment has the largest variability in surface currents at this location, with a ratio of major axes for the wind to no wind case of 1.89 and 2.38 for the ELM and UWM respectively.

3.5.3.2 Influence of transport algorithm on velocities

Velocity differences between the ELM and UWM transport algorithms are assessed by comparing the results for both of the experiments using MM5 and also the two without wind forcing. Generally, UWM and ELM usage have a small affect on the average mean directions compared with the influence from using different wind forcings. For the MM5, UWM average mean directions were biased 2° clockwise from the ELM; while for the experiment without wind forcing, UWM average mean directions were biased 8° counter-clockwise from the ELM. The largest bias in the average mean direction occurs at the location of the wind buoy 46146 for both of these comparisons, at 50° clockwise for the MM5 UWM with respect to the MM5 ELM and 55° counter-clockwise for the UWM without wind with respect to the ELM without wind. The average ratios of mean scalar magnitudes of surface currents between the UWM and ELM for both the MM5 and no wind cases do not differ by as much as those from variations in wind forcing. At 46146 for the cases without wind, the ELM has more total surface current variance, at $0.0076 m^2/s^2$, than the UWM, at $0.0046 m^2/s^2$, due to the larger plume forcing of ELM. However, although the increase in total variance between the MM5 ELM and UWM is small, from $0.0272 m^2/s^2$ to $0.0280 m^2/s^2$, it indicates an increase relative to the experiment without wind. Thus, using UWM increases the response of surface currents to winds within the Strait of Georgia.

3.6 Discussion

The influence of wind forcing from each of the three numerical weather models has an effect on the size/freshness of the plume and on the water velocities in the Strait of Georgia. Of the various wind forcings evaluated, the MM5 wind field produces the smallest saltiest plume and the most variability in the water velocities. For this region, the MM5 winds offer the highest spatial and temporal resolution of the three.

From the analysis of [20] and this study of the wind field, it is noted that the MM5 winds are stronger than the observed winds and the other weather models evaluated for the Fraser Region. The deficiencies in the atmospheric datasets are compounded by those of hydrodynamic simulations when used for wind stress inputs.

The MM5 forced experiment yields the most variability in surface currents. The NARR/ETA winds are weaker than observed winds in the Fraser Region producing larger fresher plumes and the least variability in the water velocities near the central Strait of Georgia. MM5 winds provide more wind stress which consequently leads to a greater amount of mixing for the water column. This increased mixing generates smaller volumes and thicknesses for the freshest salinity contours (Figures 3.24a, p. 143 and 3.26a, p. 145). The experiments without wind produce the largest plumes, for both algorithm choices, as no wind energy is provided to mix the water column. Experiments without wind also result in the smallest variance in surface currents, which are subject to baroclinic plume related forcings and the barotropic forcings from changes in mean sea level, tidal water elevations, and river discharge.

RMS errors of zero mean water elevations and apparent phase and amplitude errors increase within the Straits of Juan de Fuca and Georgia. This region consists of many narrow and complex channels which have varying depths; consequently variations in tidal harmonics are non-linear across and along these passages (e.g. cotidal plots of [12]). The increase in these errors is primarily due to an inadequate tidal boundary condition along the northern Strait of Georgia (Section 3.5.1 and [25]). Further decreases in elevation errors may be achieved by improving the representation of bottom friction.

An UWM transport algorithm within SELFE yields much saltier plumes for the Fraser River than the original ELM algorithm. The comparisons of model salinities with observed salinities indicate the UWM algorithm more appropriately represents the observed values than the ELM algorithm. The improvements from using the UWM algorithm outweigh those from using the different wind forcings. The computational cost associated with the UWM algorithm is 28% greater than for the ELM, however the dramatic improvements in salinities and subsequent representation of large river plumes likely warrant this expense. Unfortunately, given the size of the current computational domain the model forecasts for the Fraser Region is limited to the use of ELM, when time required for the downloading of model inputs and daily forecast setup is factored into the operational time costs. A reduction in grid size maybe explored to leverage use of UWM, while recent improvements in the efficiency of the UWM algorithm [10] may help to expand its usefulness to problems occurring over large spatial domains but requiring higher grid resolutions .

3.7 Acknowledgements

We would like to thank the following people and agencies for the availability of the data used for these experiments: Atmospheric model data was obtained from University of Washington and NCAR/NCEP, while measured winds were obtained from NOAA/NDBC and Environment Canada. Bathymetry for the Fraser River was provided by Mick Mills of Water Survey Canada through funding by the Canadian Coast Guard, while Mike Foreman at Institute of Ocean Sciences provide the bathymetry data for the Strait of Georgia and Juan de Fuca Strait. Offshore bathymetry was interpolated from ETOPO2 [27]. Initial and nudging salinities, temperatures, and mean sea levels were interpolated from NRL's NCOM global ocean forecast model results. Salinities measured by the BC Ferry were obtained from the STRATOGEM website (http://www.stratogem.ubc.ca/) and tide gauge data from NOAA/CO-OPS, Canadian Hydrographic Service, and from Lynne Campo at Water Survey Canada. Also, Denny Sinnott of the Canadian Hydrographic Service for providing metadata on water elevations, Dianne Masson for feedback, Water Survey Canada for Fraser River discharge, and additional research staff and students of the Center for Coastal and Land-Margin Research group: Michela Burla, Arun Chawla, Sergey Frolov, Nate Hyde, Aaron Racicot, Charles Seaton, Paul Turner, and Ethan VanMatre.

3.8 References

1. Zhang, Y. and A.M. Baptista, *A semi-implicit Eulerian-Lagrangian finite-element model for cross-scale ocean circulation, with hybrid vertical coordinates.* International Journal for Numerical Methods in Fluids, in-review.

2. Crean, P.B., T.S. Murty, and J.A. Stronach, *Lecture Notes on Coastal and Estuarine Studies. Mathematical Modelling of Tides and Estuarine Circulation: The Coastal Seas of Southern British Columbia and Washington State.*, New York: Springer-Verlag, 1988.

3. Baptista, A.M., *Environmental observation and forecasting systems.*, in *Encyclopedia of Physical Science and Technology*, R.A. Meyers, Editor. New York: Academic Press, 2002. 565-581.

4. Baptista, A.M., Y.L. Zhang, A. Chawla, M. Zulauf, C. Seaton, III E.P. Myers, J. Kindle, M. Wilkin, M. Burla, and P.J. Turner, *A cross-scale model for 3D baroclinic circulation in estuary-plume-shelf systems: II. Application to the Columbia River.* Continental Shelf Research, 2005. **25**: 935-972.

5. Coastal Margin Observatory for the Columbia River (CORIE), www.ccalmr.ogi.edu/CORIE, [Viewed July 2006]

6. Allen, S.E., K. Collins, and R. Pawlowicz. *Construction of the Physical Component of a 1-D Coupled Bio-physical Model for the Strait of Georgia*. in *Eos Trans. AGU 87(36). Ocean Science Meeting Supplement*. 2006. Honolulu, HI.

7. Tinis, S.W. and R.E. Thomson, Operational Modelling of Southwest British Columbia Waters Using the Princeton Ocean Model, http://www.pac.dfo-mpo.gc.ca/sci/juandefuca/brochure.pdf, [Viewed July 2006]

8. Blumberg, A.F. and G.L. Mellor, *A description of a three-dimensional coastal ocean circulation model*, in *Three-Dimensional Coastal Ocean Models*, N. Heaps, Editor. Washington, D.C.: AGU, 1987. 1-16.

9. CCALMR, NEFS/NANOOS Rover, http://nefs.ccalmr.ogi.edu, [Viewed July 2006]

10. Zhang, Y. of Oregon Health & Science University, *Personal communication*. 2006.

11. Foreman, M.G.G., G. Sutherland, and P.F. Cummins, *M2 tidal dissipation around Vancouver Island: an inverse approach.* Continental Shelf Research, 2004. **24**(18): 2167-2185.

12. Foreman, M.G.G., R.A. Walters, R.F. Henry, C.P. Keller, and A.G. Dolling, *A tidal model for eastern Juan de Fuca Strait and the southern Strait of Georgia.* Journal of Geophysical Research, 1995. **100**(C1): 721-740.

13. Martin, P.J., *Description of the Navy Coastal Ocean Model Version 1.0, NRL Formal Report 7322-00-9962*. 2000, Naval Research Laboratory: Stennis Space Center, MS.

14. Rhodes, R.C., H.E. Hurlburt, A.J. Wallcraft, C.N. Barron, P.J. Martin, O.M.Smedstad, S. Cross, J.E. Metzger, J. Shriver, A. Kara, and D.S. Ko, *Navy Real-Time Global Modeling Systems.* Oceanography, 2001. **15**(1): 29-43.

15. Foreman, M.G.G., R.E. Thomson, and C.L. Smith, *Seasonal current simulations for the western continental margin of Vancouver Island.* Journal of Geophysical Research, 2000. **105**(C8): 19,665-19,698.

16. Oakey, S., J. Chaffey, F. Dupont, P. Chapman, C. Hannah, and D. Greenberg, *WebTide Tidal Prediction Model*. 2003, Ocean Science Division, Bedford Institute of Oceanography, Fisheries and Oceans Canada: Dartmouth, N.S., Canada, http://www.mar.dfo-mpo.gc.ca/science/ocean/coastal_hydrodynamics/WebTide/webtide.html [Viewed July 2006].

17. Foreman, M.G.G., W.R. Crawford, J.Y. Cherniawsky, R.F. Henry, and M.R. Tarbotton, *A high-resolution assimilating tidal model for the northeast Pacific Ocean.* Journal of Geophysical Research, 2000. **105**(C12): 28,629-28,651.

18. Ott, M.W. and C. Garrett, *Frictional estuarine flow in Juan de Fuca Strait, with implications for secondary circulation.* Journal of Geophysical Research, 1998. **103**(C8): 15,657-15,666.

19. Dong, C. and L.-Y. Oey, *Sensitivity of coastal currents near Point Conception to forcing by three different winds: ECMWF, COAMPS, and blended SSM/I-ECMWF-buoy winds.* Journal of Physical Oceanography, 2005. **35**(7): 1229-1244.

20. Tinis, S.W., R.E. Thomson, C.F. Mass, and B.M. Hickey, *Comparison of MM5 and Meteorological Buoy Winds from British Columbia to Northern California.* Atmosphere-Ocean, 2006. **44**(1).

21. Emery, W.J. and R.E. Thomson, *Data Analysis Methods in Physical Oceanography*. Amsterdam: Pergamon Press, 2001.

22. Smith, S.D., *Coefficients for Sea Surface Wind Stress, Heat Flux, and Wind Profiles as a Function of Wind Speed and Temperature.* Journal of Geophysical Research, 1988. **93**(C12): 15,467-15,472.

23. Thomson, R.E., *Oceanography of the British Columbia Coast*. Canadian Special Publication of Fisheries and Aquatic Sciences 56. Ottawa: Department of Fisheries and Oceans, 1981. 291.

24. Zeng, X., M. Zhao, and R.E. Dickinson, *Intercomparison of Bulk Aerodynamic Algorithms for the computation of Sea Surface Fluxes Using TOGA COARE and TAO Data.* Journal of Climate, 1998. **11**: 2628-2644.

25. Masson, D. of Institute of Ocean Sciences, *Personal Communication*. 2006.

26. Pawlowicz, R., B. Beardsley, and S. Lentz, *Classical tidal harmonic analysis including error estimates in MATLAB using T_TIDE.* Computers and Geosciences, 2002. **28**: 929-937.

27. U.S. Department of Commerce, National Oceanic and Atmospheric Administration, National Geophysical Data Center, *2-Minute Gridded Global Relief Data (ETOPO2).* 2001.

3.9 Figures and Tables

Table 3.1 Description of numerical experiments for the Fraser River plume 2005 study

Experiment #	Atmospheric forcings	Transport algorithm	Start date	End date
1	NARR	ELM	August 13	September 17
2	ETA	ELM	August 13	September 17
3	MM5	ELM	August 13	September 17
4	-	ELM	August 13	September 17
5	MM5	UWM	August 20	September 17
6	-	UWM	August 20	September 17

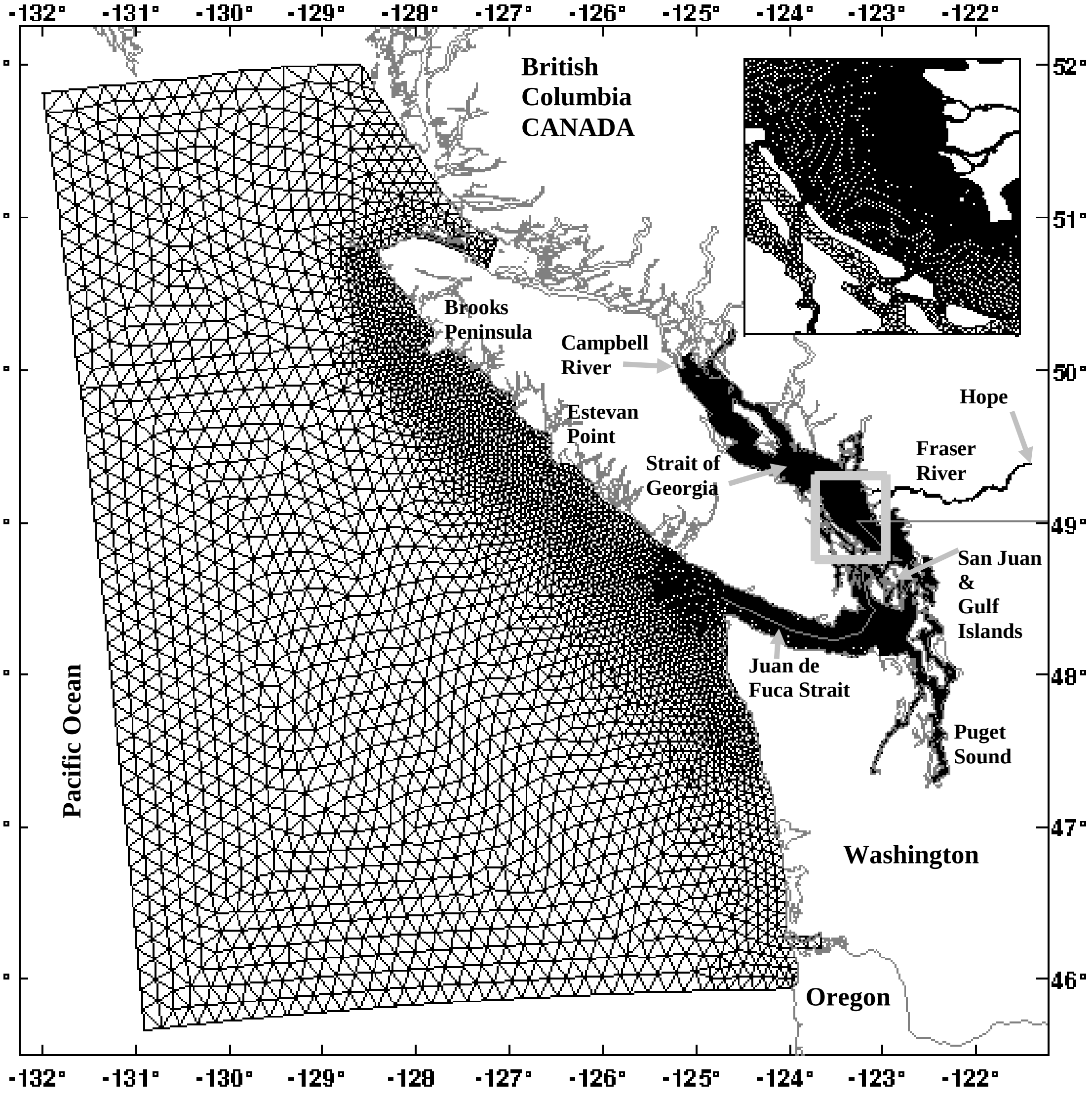

Figure 3.1 Model horizontal grid domain.

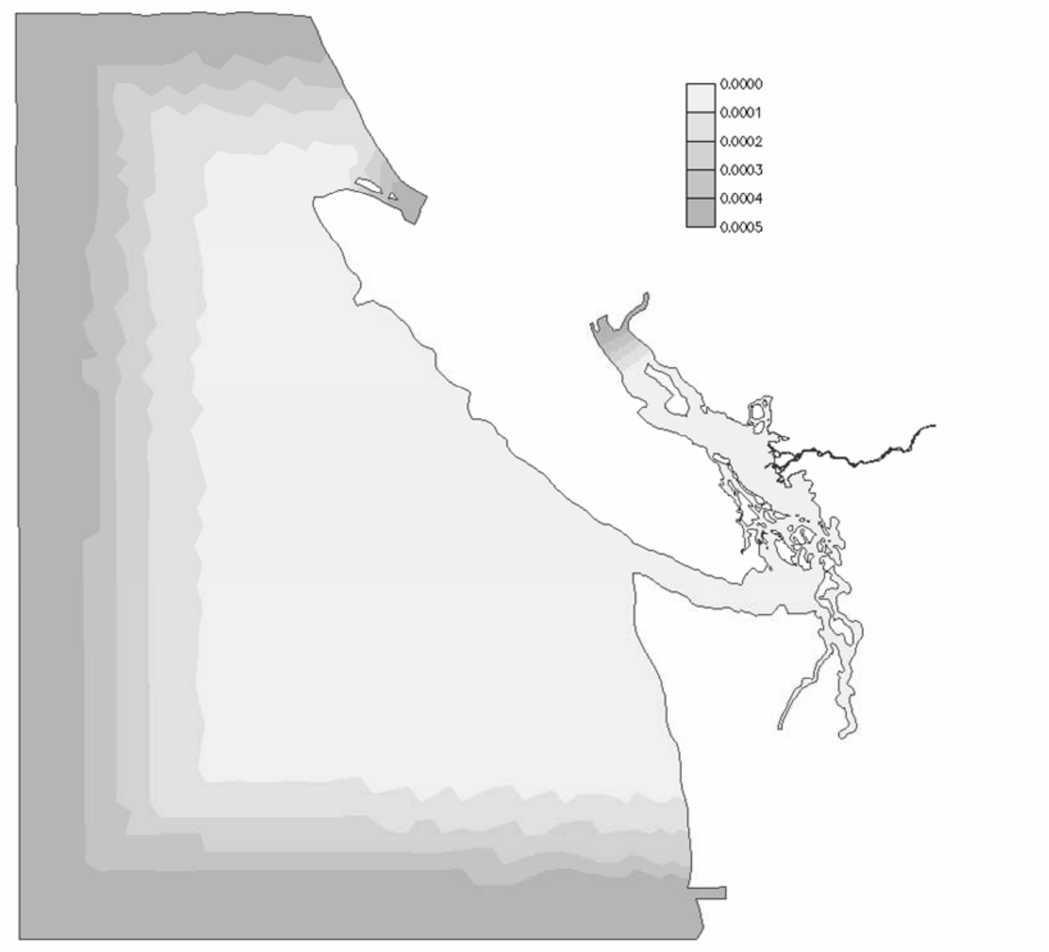

Figure 3.2 Nudging factors (γ) used to enforce baroclinic open ocean boundary conditions for the Fraser Region simulations.

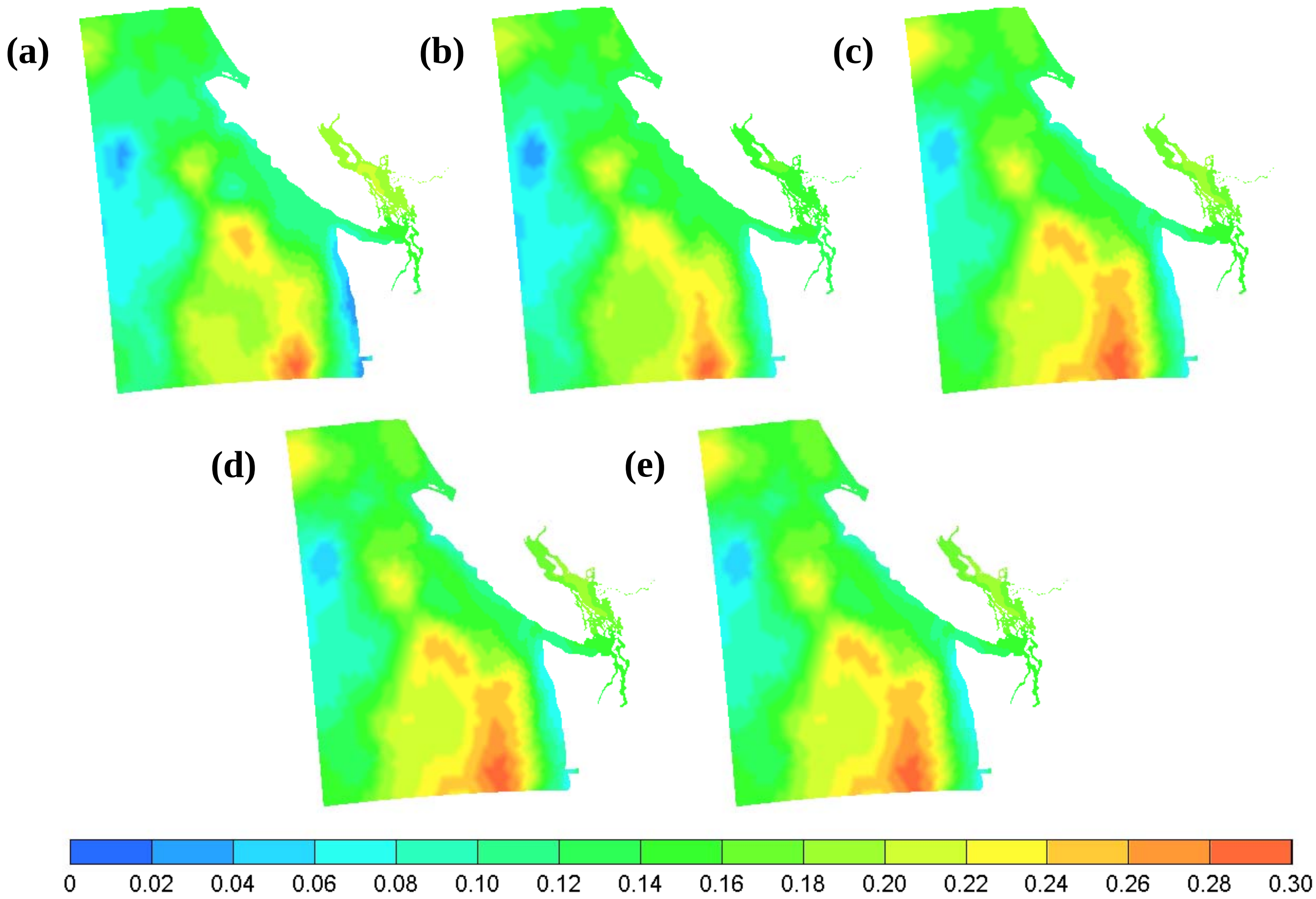

Figure 3.3 Mean sea level (Z0) values (m) interpolated from NCOM results to the Fraser Region numerical grid for the first day of each simulated week as **(a)** August 13, **(b)** August 20, **(c)** August 27, **(d)** September 3, and **(e)** September 10 of 2005.

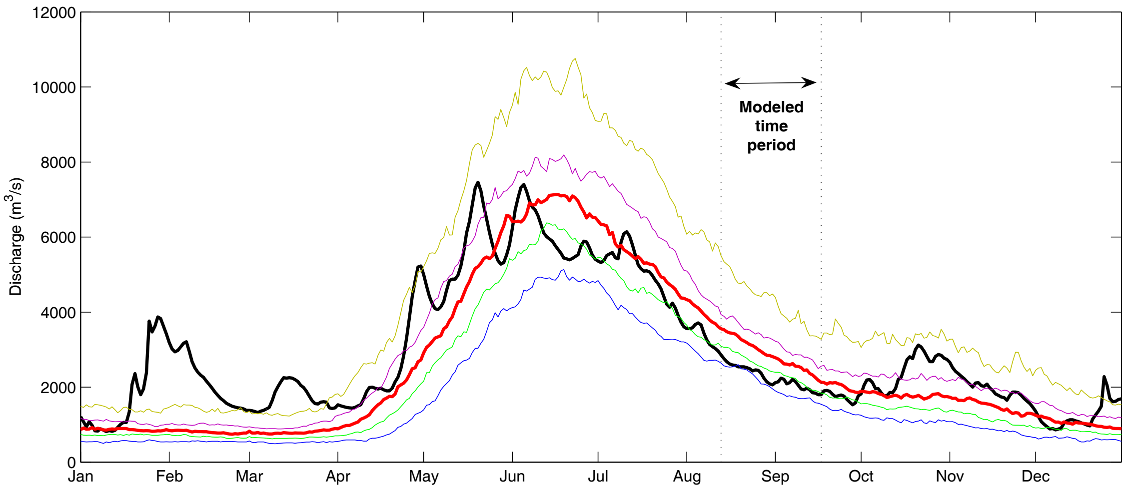

Figure 3.4 Model inputs as mean climatological flow (▬) for the Fraser River at Hope, BC (1912-2003) are shown with preliminary measured values for 2005 (▬) and percentiles of historical flow: 5% (▬), 25% (▬), 75% (▬), and 95% (▬).

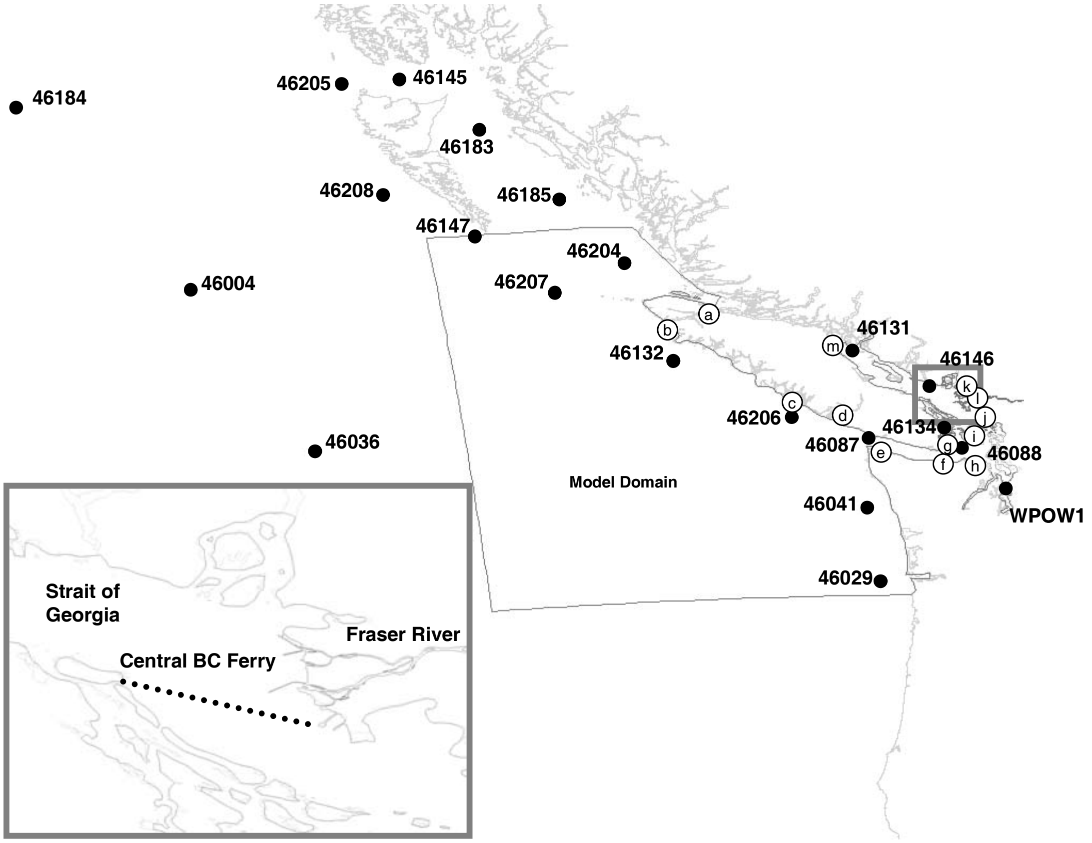

Figure 3.5 The approximate path of the Tsawwassen-Duke Point (central) BC Ferry is shown (**…**) in the inset. Wind buoy locations used for wind and velocity comparisons are shown (●). Tide gauge locations used for comparisons are shown (○) with the letter designation corresponding to their order of comparison with model results as **(a)** Port Hardy, **(b)** Winter Harbour, **(c)** Tofino, **(d)** Bamfield, **(e)** Neah Bay, **(f)** Port Angeles, **(g)** Victoria Harbour, **(h)** Port Townsend, **(i)** Friday Harbour, **(j)** Cherry Point, **(k)** Vancouver, **(l)** New Westminster, and **(m)** Campbell River.

Table 3.2 Mean speeds (m/s) and directions (°clockwise with respect to true north) of modeled and observed winds at measurement locations for the time period August 13 – September 17, 2005. The subscript notation indicates whether a quantity is computed from observed data (d) or model data (m) and whether or not the mean speed is a vector-averaged (v) or scalar-averaged (s). Comparison of model and data speeds ratios are provided for both the vector averaged and scalar averaged mean speeds as well as the bias between the average model direction with respect to the average direction of the data.

	DATA			NARR						ETA						MM5					
Station	$u_{d,v}$	$u_{d,s}$	θ_d	$u_{m,v}$	$u_{m,s}$	θ_m	$u_{m,v} / u_{d,v}$	$u_{m,s} / u_{d,s}$	$\theta_m - \theta_d$	$u_{m,v}$	$u_{m,s}$	θ_m	$u_{m,v} / u_{d,v}$	$u_{m,s} / u_{d,s}$	$\theta_m - \theta_d$	$u_{m,v}$	$u_{m,s}$	θ_m	$u_{m,v} / u_{d,v}$	$u_{m,s} / u_{d,s}$	$\theta_m - \theta_d$
46029	2.57	3.93	151	2.15	3.24	138	0.835	0.824	-13	2.79	4.02	148	1.08	1.02	-3	3.45	4.45	155	1.34	1.13	4
46041	2.06	3.40	139	2.71	3.76	133	1.32	1.11	-6	2.86	3.92	139	1.39	1.15	0	3.74	4.63	142	1.82	1.36	4
46087	1.22	2.72	38.6	2.03	3.14	89.2	1.66	1.16	50.6	1.55	2.10	82.2	1.27	0.775	43.6	2.55	3.80	99.9	2.09	1.40	61.3
46088	3.56	4.32	71.1	0.564	1.42	98.4	0.159	0.329	27.3	2.98	3.22	65.5	0.838	0.746	-5.6	4.74	5.36	80.9	1.33	1.24	9.8
WPOW1	1.23	3.54	241	0.897	2.81	56.0	0.731	0.795	175	0.178	1.94	96.8	0.145	0.548	-144	2.08	3.47	200	1.70	0.981	-41
46146	0.297	3.71	89.7	0.342	0.97	346	1.15	0.26	-104	0.174	3.12	339	0.585	0.840	-111	3.22	4.87	114	10.8	1.31	24
46134	0.732	2.50	233	0.746	1.56	43.3	1.02	0.627	171	1.03	1.94	30.4	1.40	0.776	158	0.891	2.49	144	1.22	1.00	-88
46131	1.97	3.54	140	0.289	1.46	332	0.147	0.412	-168	0.389	2.35	120	0.197	0.665	-20	3.18	4.80	138	1.61	1.36	-2
46206	2.12	4.24	115	1.95	3.29	105	0.918	0.776	-10	2.58	3.86	117	1.21	0.912	2	4.68	5.89	125	2.20	1.39	10
46132	3.53	6.43	137	2.64	5.31	121	0.749	0.826	-16	3.39	5.76	123	0.961	0.895	-15	-	-	-	-	-	-
46207	2.54	5.08	109	2.84	5.46	103	1.12	1.07	-6	3.45	5.84	101	1.36	1.15	-8	-	-	-	-	-	-
46204	1.18	5.58	78.8	1.58	4.30	85.1	1.34	0.770	6.3	2.07	4.87	83.8	1.75	0.873	4.9	-	-	-	-	-	-
46147	3.17	5.56	96.9	3.60	5.82	97.6	1.13	1.05	0.7	3.99	5.86	96.5	1.26	1.05	-0.4	-	-	-	-	-	-
46185	1.65	5.92	83.1	1.98	4.94	76.5	1.20	0.835	-6.6	2.17	5.38	75.9	1.32	0.908	-7.2	-	-	-	-	-	-
46208	3.18	6.11	106	3.12	5.72	104	0.981	0.937	-2	3.39	5.89	99.0	1.06	0.965	-7	-	-	-	-	-	-
46183	0.815	5.59	30.9	0.786	5.01	16.7	0.965	0.896	-14.3	0.945	4.72	39.5	1.16	0.844	8.5	-	-	-	-	-	-
46036	4.60	6.37	108	4.86	6.28	107	1.06	0.986	-1	4.09	5.81	106	0.890	0.913	-2	-	-	-	-	-	-
46004	4.49	6.70	94.4	4.76	6.58	91.7	1.06	0.981	-2.7	4.25	6.26	86.5	0.949	0.934	-7.9	-	-	-	-	-	-
46145	2.03	4.99	73.9	1.81	4.44	60.4	0.889	0.890	-13.5	2.81	5.12	85.2	1.38	1.03	11.2	-	-	-	-	-	-
46205	2.59	5.61	80.2	2.85	4.96	70.9	1.10	0.885	-9.3	3.32	5.47	68.7	1.28	0.975	-11.5	-	-	-	-	-	-
46184	4.25	6.60	85.4	4.39	6.53	72.6	1.03	0.988	-12.8	4.58	6.40	65.4	1.08	0.969	-20.1	-	-	-	-	-	-
Average of stations*							0.88	0.70	14				0.90	0.83	-9				2.7	1.24	-2
Standard error of the sample*							0.50	0.32	112				0.49	0.18	86				3.1	0.17	42

* For stations inside of the MM5 domain

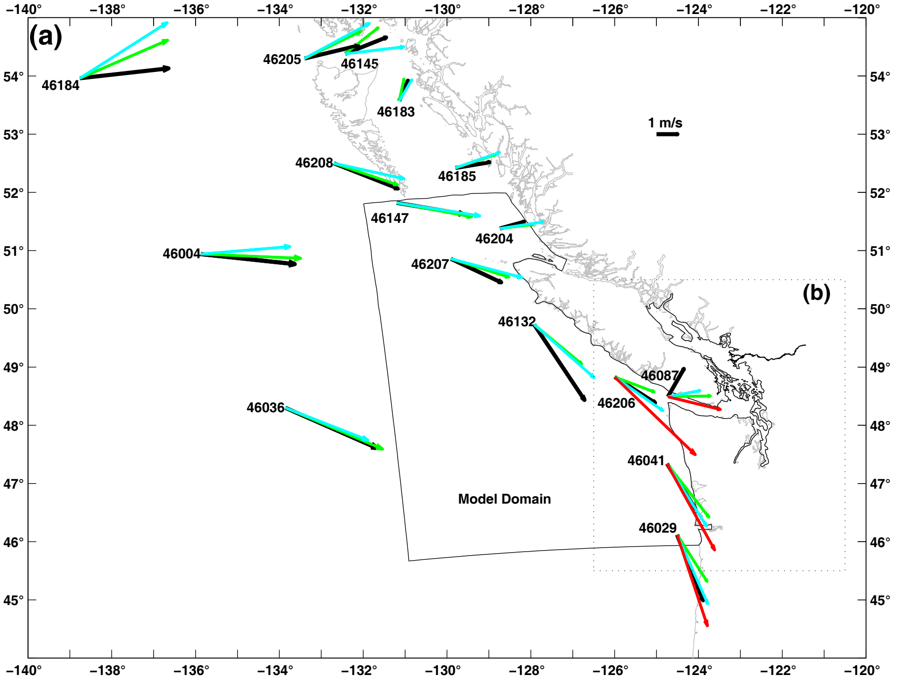

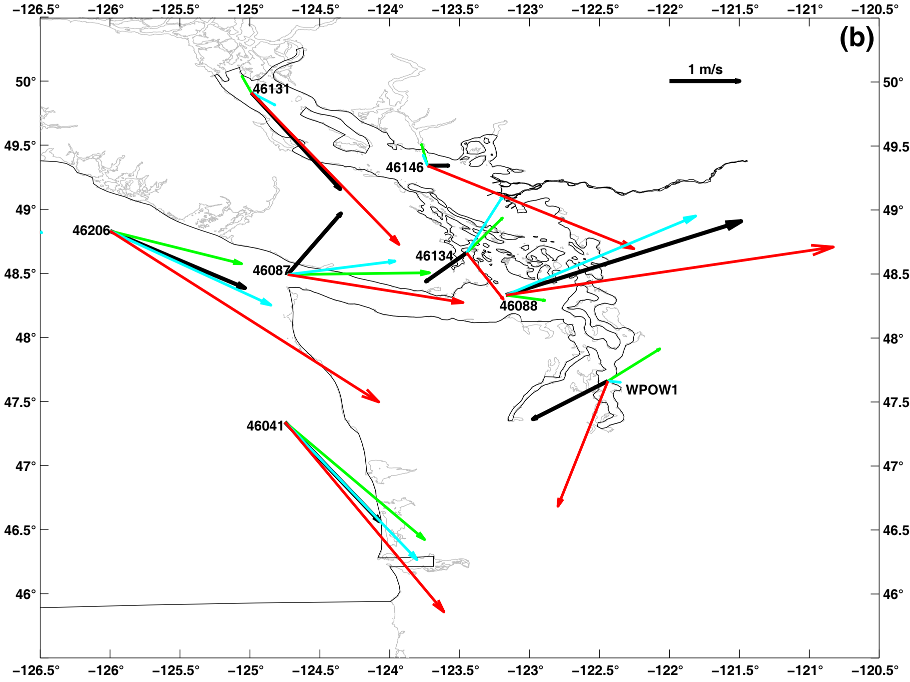

Figure 3.6 Mean vectors of modeled and observed winds for the **(a)** offshore and **(b)** Fraser Region computed for the time period August 13 – September 17, 2005. MM5 (▬), ETA (▬), NARR (▬), and observed winds (**▬**).

Table 3.3 Principal axis analysis including major and minor principal components (m/s), direction of the principal axis (°clockwise with respect to true north), and the degree of polarization of each modeled and observed wind at buoy locations at the during the time period August 13 – September17, 2005.

	DATA				NARR				ETA				MM5			
Station	$\lambda_{1,d}^{0.5}$	$\lambda_{2,d}^{0.5}$	$\theta_{p,d}$	$\lambda_{2,d} / \lambda_{1,d}$	$\lambda_{1,m}^{0.5}$	$\lambda_{2,m}^{0.5}$	$\theta_{p,m}$	$\lambda_{2,m} / \lambda_{1,m}$	$\lambda_{1,m}^{0.5}$	$\lambda_{2,m}^{0.5}$	$\theta_{p,m}$	$\lambda_{2,m} / \lambda_{1,m}$	$\lambda_{1,m}^{0.5}$	$\lambda_{2,m}^{0.5}$	$\theta_{p,m}$	$\lambda_{2,m} / \lambda_{1,m}$
46029	3.64	1.36	166	0.140	2.60	1.35	177	0.271	3.31	1.47	179	0.198	3.35	1.46	178	0.190
46041	3.08	1.36	145	0.194	3.23	1.05	154	0.107	3.28	1.15	157	0.124	3.35	1.39	161	0.171
46087	2.17	1.82	83.8	0.690	2.04	1.78	8.76	0.803	1.60	0.929	110	0.327	3.21	1.43	122	0.187
46088	3.02	1.74	91.0	0.332	1.34	0.657	139	0.236	1.98	0.753	70.5	0.134	3.38	1.53	79.6	0.202
WPOW1	3.64	1.13	5.01	0.0975	2.91	0.672	19.3	0.0532	2.18	0.552	176	0.0638	3.01	1.10	2.12	0.134
46146	4.18	1.23	113	0.0975	0.981	0.395	109	0.160	3.79	0.399	120	0.0111	4.42	1.31	118	0.0815
46134	2.38	1.30	79.8	0.313	1.38	0.871	170	0.392	1.53	1.12	16.9	0.520	2.43	1.33	114	0.285
46131	3.49	1.16	143	0.133	1.79	0.300	122	0.0277	2.94	0.320	140	0.0117	4.87	1.11	137	0.0485
46206	4.49	1.32	121	0.0882	3.40	0.974	132	0.0821	4.03	0.899	134	0.0500	4.69	1.74	139	0.139
46132	5.79	1.81	150	0.0983	5.05	1.12	145	0.0492	5.07	1.40	152	0.0766	-	-	-	-
46207	4.57	1.93	158	0.189	4.85	1.76	163	0.129	4.74	1.98	169	0.172	-	-	-	-
46204	5.65	2.08	153	0.143	4.23	1.45	156	0.116	4.68	1.57	166	0.112	-	-	-	-
46147	4.49	2.50	149	0.311	4.57	2.05	158	0.201	4.17	2.10	160	0.254	-	-	-	-
46185	5.79	2.14	151	0.144	4.59	1.70	156	0.136	5.10	1.69	161	0.110	-	-	-	-
46208	5.26	2.55	160	0.242	5.10	1.73	146	0.115	4.84	2.15	160	0.198	-	-	-	-
46183	5.72	2.02	145	0.132	5.28	1.19	158	0.0501	4.93	1.61	158	0.106	-	-	-	-
46036	4.48	2.50	176	0.311	4.12	2.18	173	0.281	4.14	2.41	172	0.340	-	-	-	-
46004	4.79	2.67	167	0.311	4.46	2.21	167	0.246	4.42	2.36	169	0.285	-	-	-	-
46145	4.70	2.07	124	0.202	4.22	1.46	128	0.118	4.60	1.58	121	0.117	-	-	-	-
46205	4.81	2.70	166	0.320	3.88	2.35	134	0.364	4.19	2.39	158	0.320	-	-	-	-
46184	4.68	3.44	173	0.545	4.43	3.22	158	0.530	4.42	2.65	152	0.360	-	-	-	-
Average of stations*			106	0.232			115	0.237			122	0.160			117	0.160
Standard error of the sample*			48	0.194			60	0.242			52	0.168			52	0.0697

* For stations inside of the MM5 domain

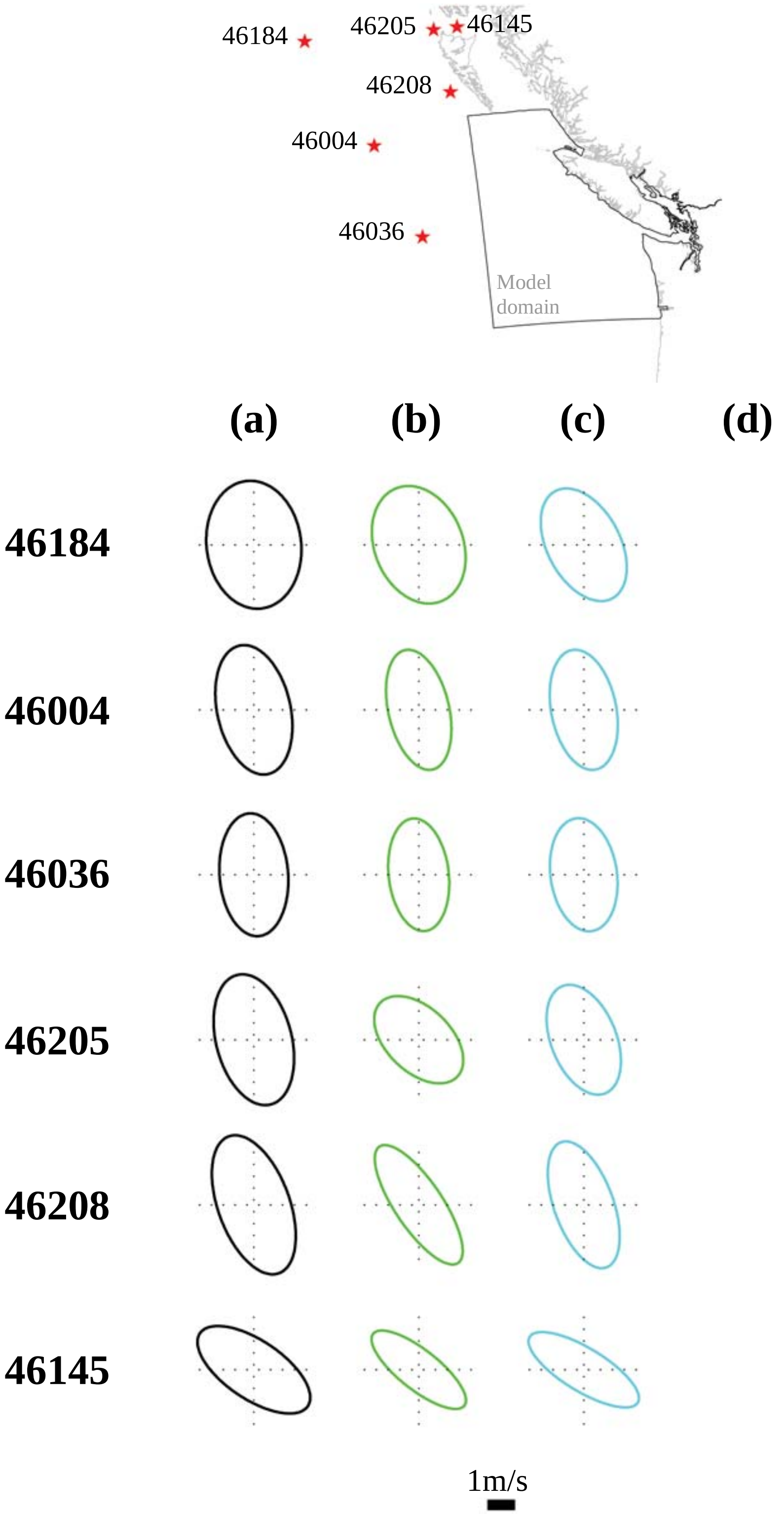

Figure 3.7 Principal ellipses of the **(a)** observed (▬), **(b)** NARR (▬), **(c)** ETA (▬), and **(d)** MM5 (▬) winds computed for the time period August 13–September 17, 2005. Note that the MM5 domain is smaller than the NARR and ETA domains and therefore model winds are not available for comparisons at buoy locations north and west of the Fraser Region.

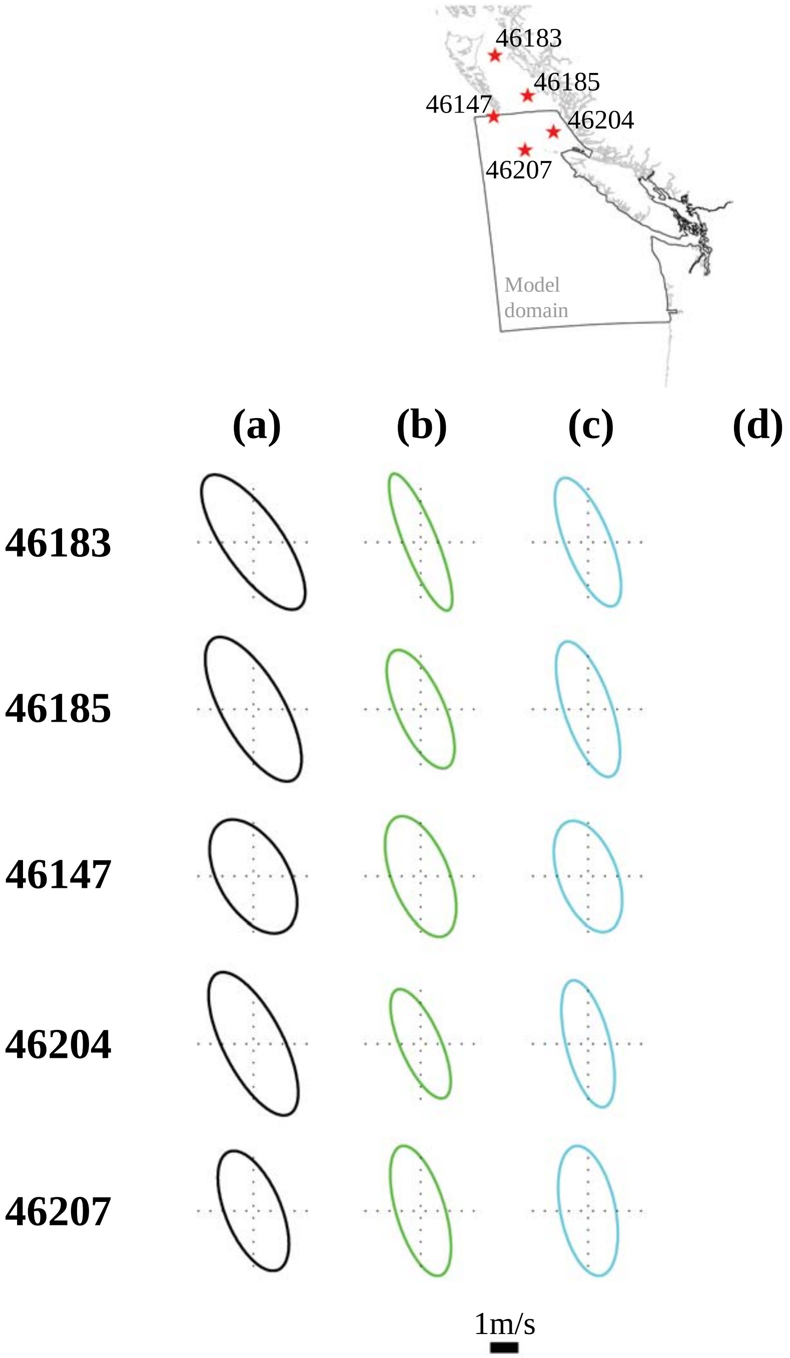

Figure 3.7 Continued.

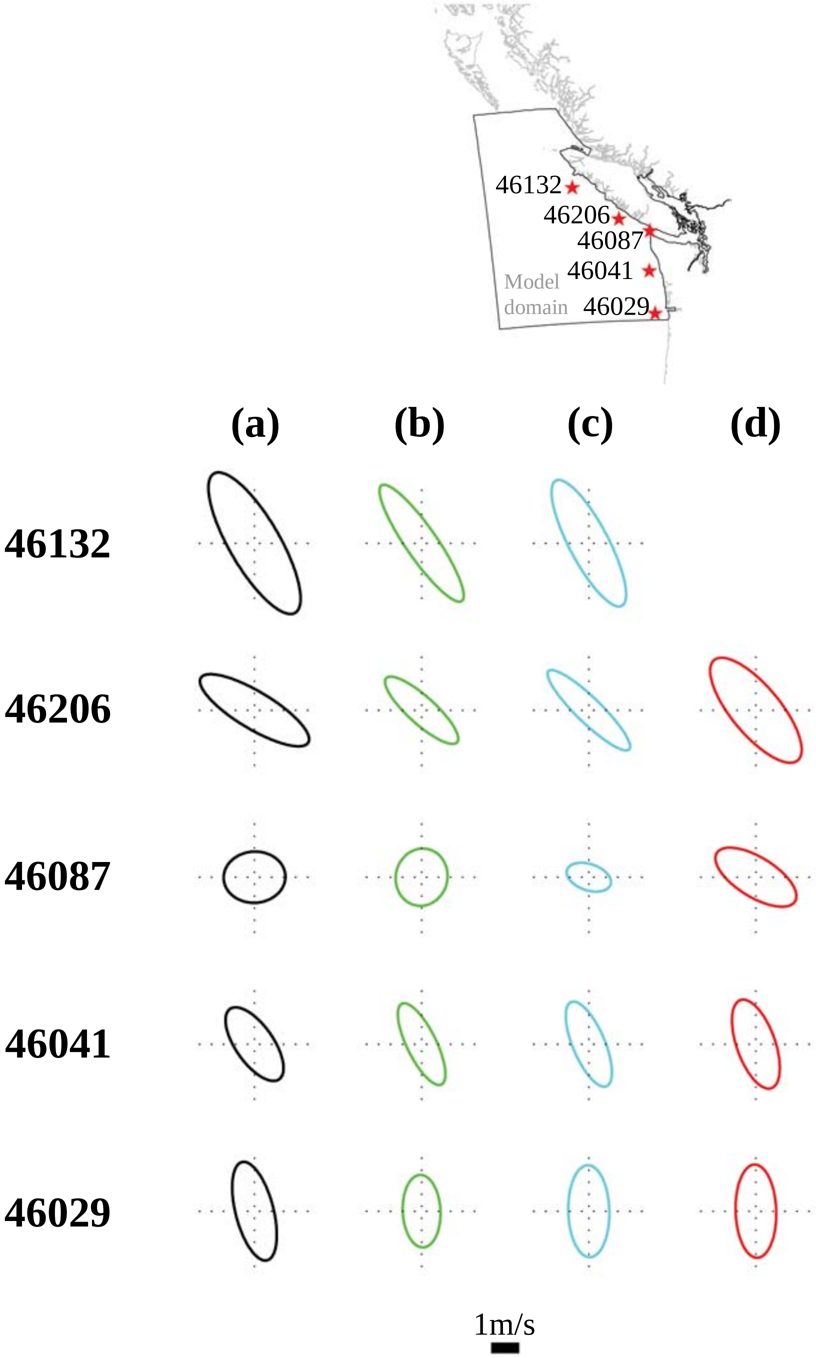

Figure 3.7 Continued.

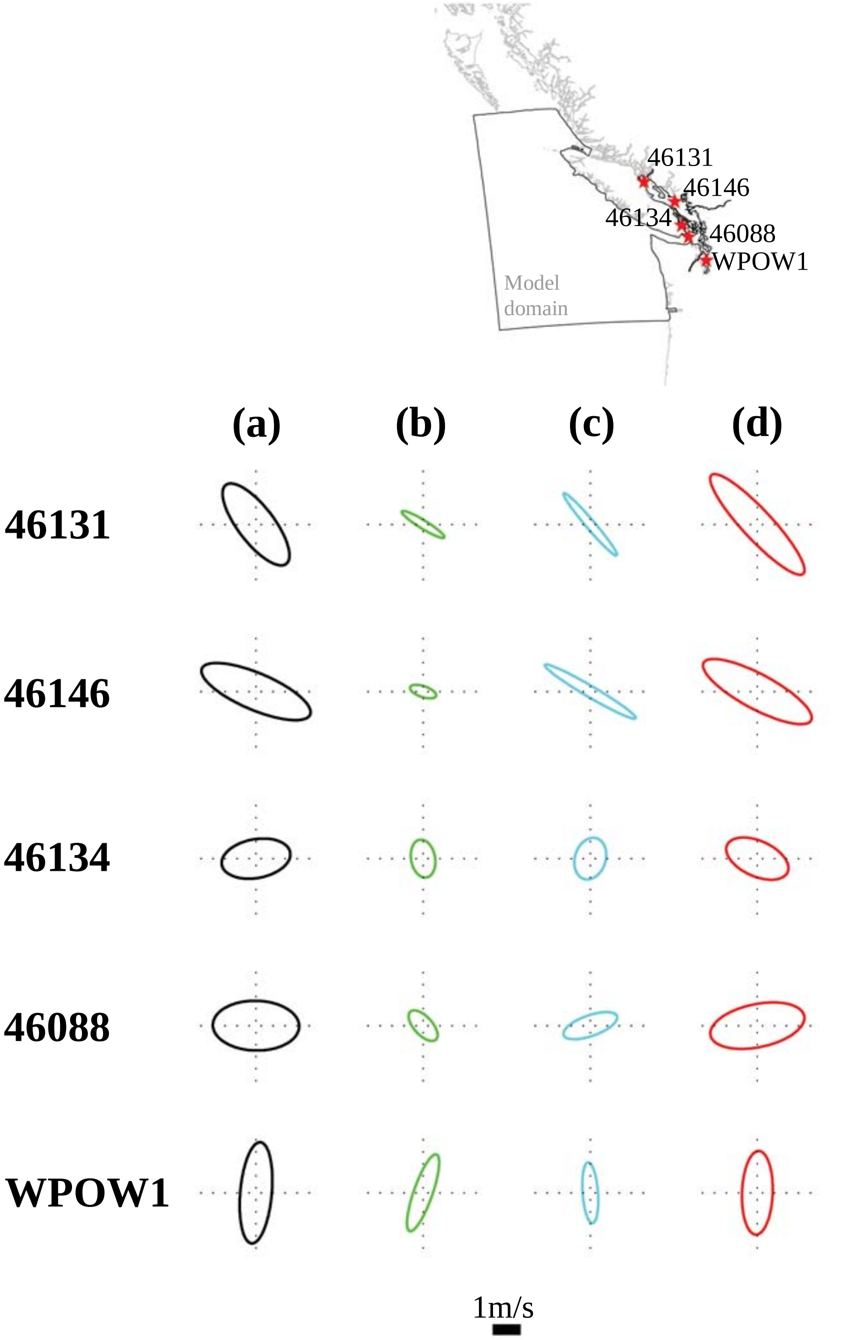

Figure 3.7 Continued.

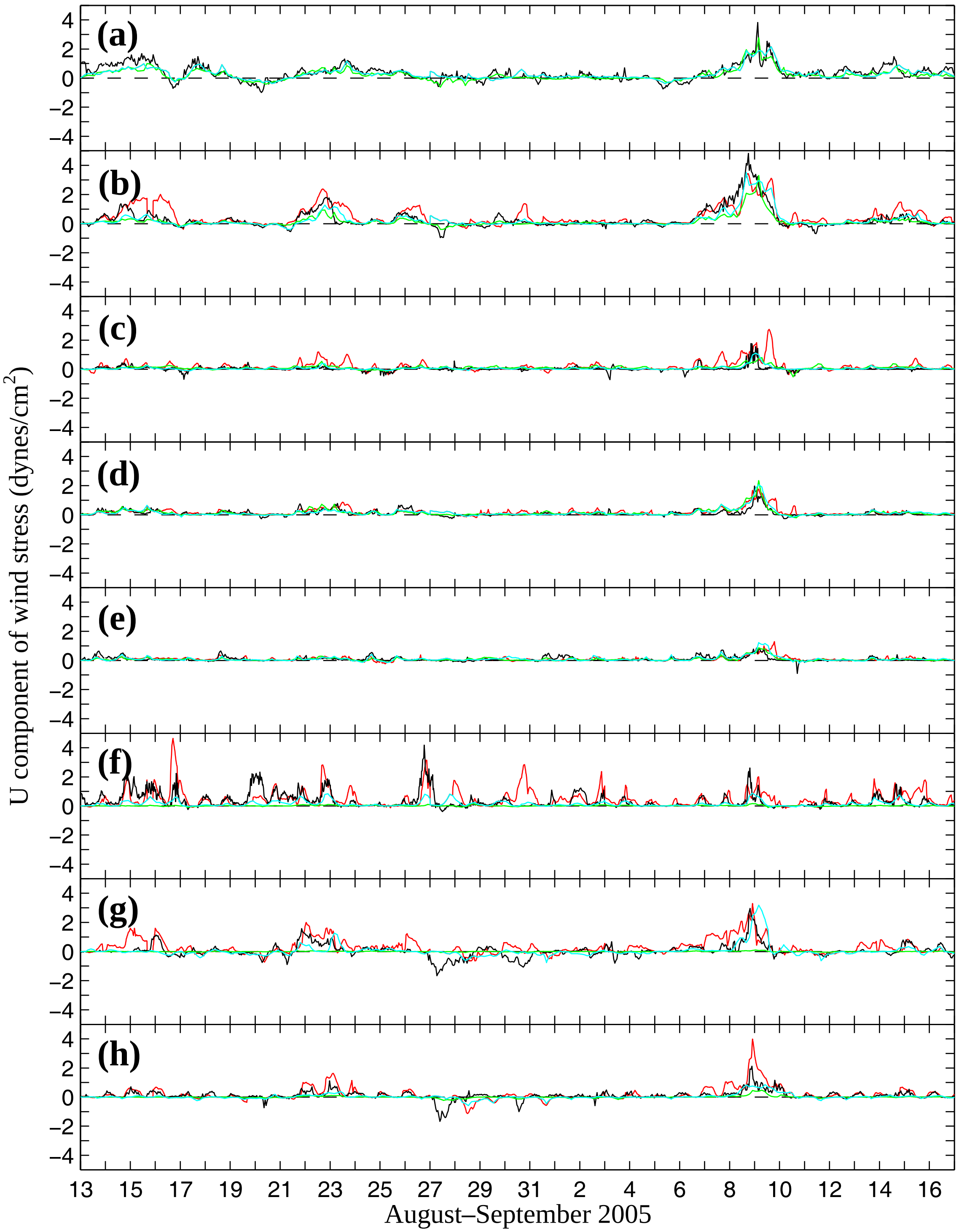

Figure 3.8 Comparison of u component of wind stress for measurements (▬) and the weather models MM5 (▬), ETA (▬), and NARR (▬) at the buoys **(a)** 46132, **(b)** 46206, **(c)** 46087, **(d)** 46041, **(e)** 46029, **(f)** 46088, **(g)** 46146, and **(h)** 46131 over the time period August 13 – September 17, 2005.

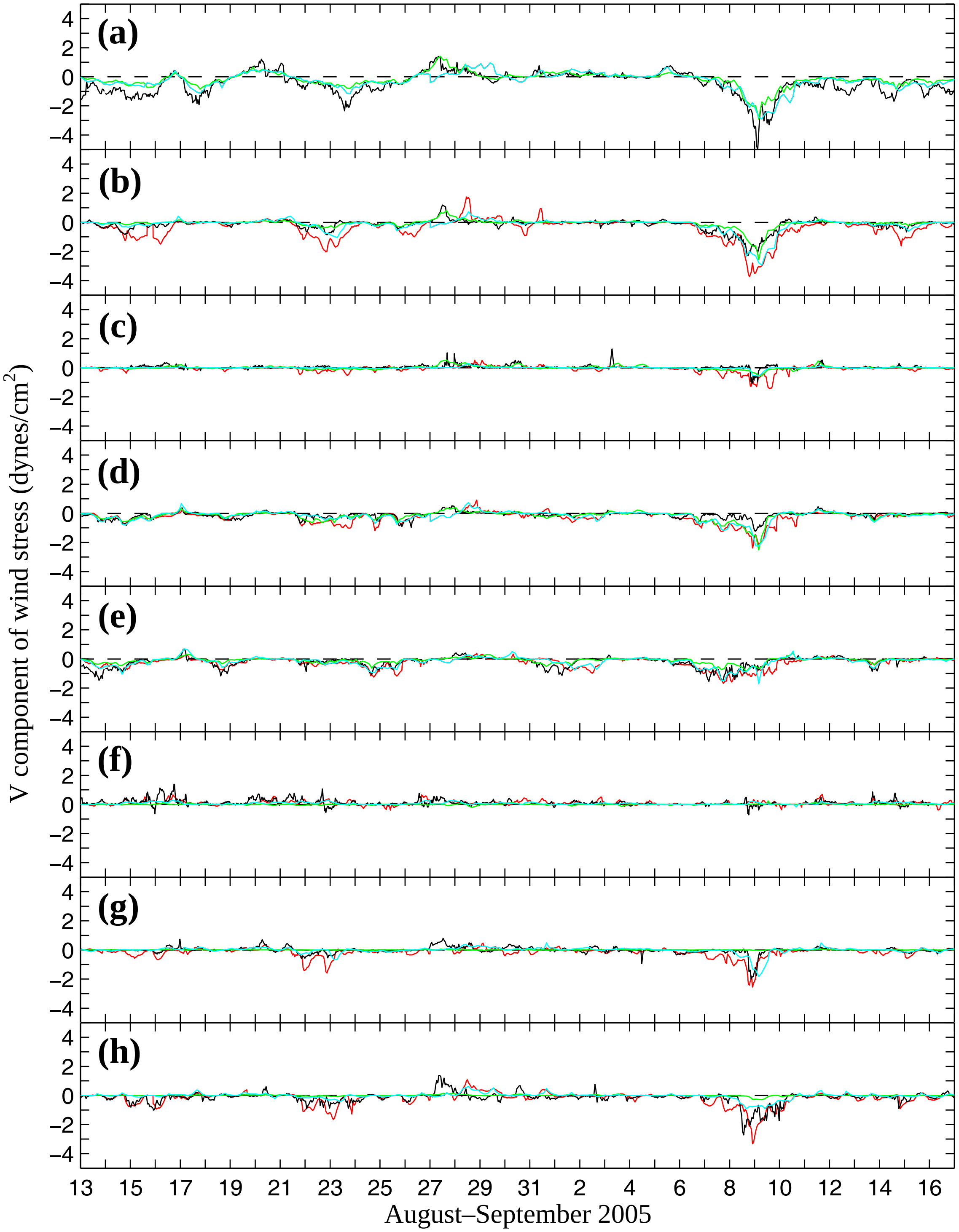

Figure 3.9 Comparison of v component of wind stress for measurements (▬) and the weather models MM5 (▬), ETA (▬), and NARR (▬) at the buoys **(a)** 46132, **(b)** 46206, **(c)** 46087, **(d)** 46041, **(e)** 46029, **(f)** 46088, **(g)** 46146, and **(h)** 46131 over the time period August 13 – September 17, 2005.

Table 3.4 RMS errors (m) of water elevations at tide gauge locations computed for the time period shared by all 6 experiments (August 20 – September 17, 2005).

Tide gauge location	MM5 ELM	ETA ELM	NARR ELM	No Wind ELM	MM5 UWM	No Wind UWM
Port Hardy	0.138	0.138	0.138	0.140	0.138	0.138
Winter Harbour	0.103	0.102	0.0994	0.127	0.0997	0.0959
Tofino	0.111	0.109	0.108	0.127	0.110	0.0843
Bamfield	0.124	0.117	0.118	0.129	0.120	0.0973
Neah Bay	0.117	0.113	0.114	0.125	0.116	0.101
Port Angeles	0.223	0.226	0.223	0.227	0.203	0.199
Victoria Harbour	0.186	0.188	0.187	0.188	0.169	0.163
Port Townsend	0.328	0.329	0.328	0.326	0.310	0.309
Friday Harbor	0.217	0.220	0.219	0.216	0.196	0.194
Cherry Point	0.295	0.293	0.293	0.291	0.285	0.284
Vancouver	0.248	0.247	0.246	0.241	0.230	0.227
New Westminster	0.264	0.266	0.266	0.262	0.253	0.252
Campbell River	0.128	0.128	0.128	0.128	0.128	0.128

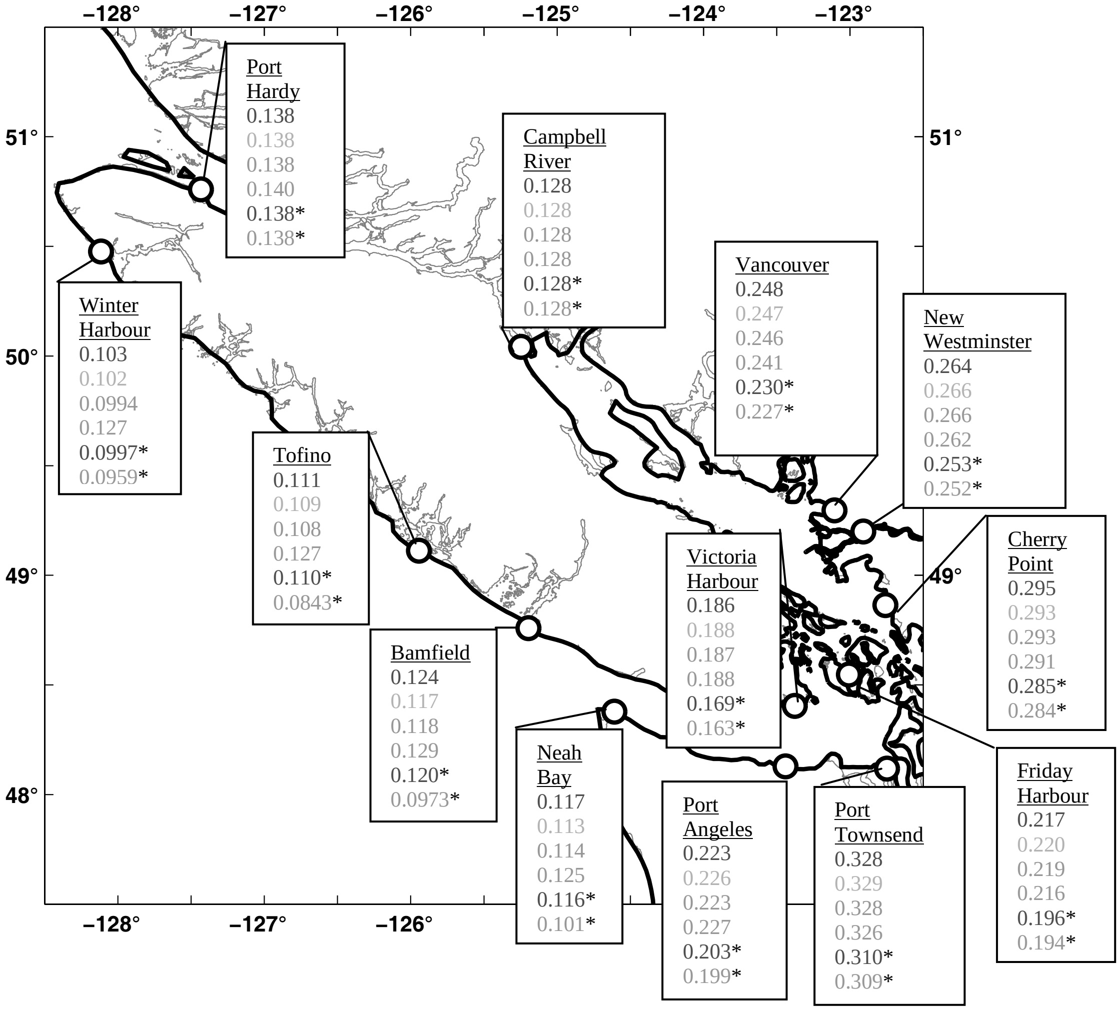

Figure 3.10 RMS errors (m) of water elevations shown at respective tide gauge locations computed for the time period (August 20 – September 17, 2005) shared by all 6 experiments: **MM5**, **ETA**, **NARR**, and **no wind**; * indicate UWM experiments.

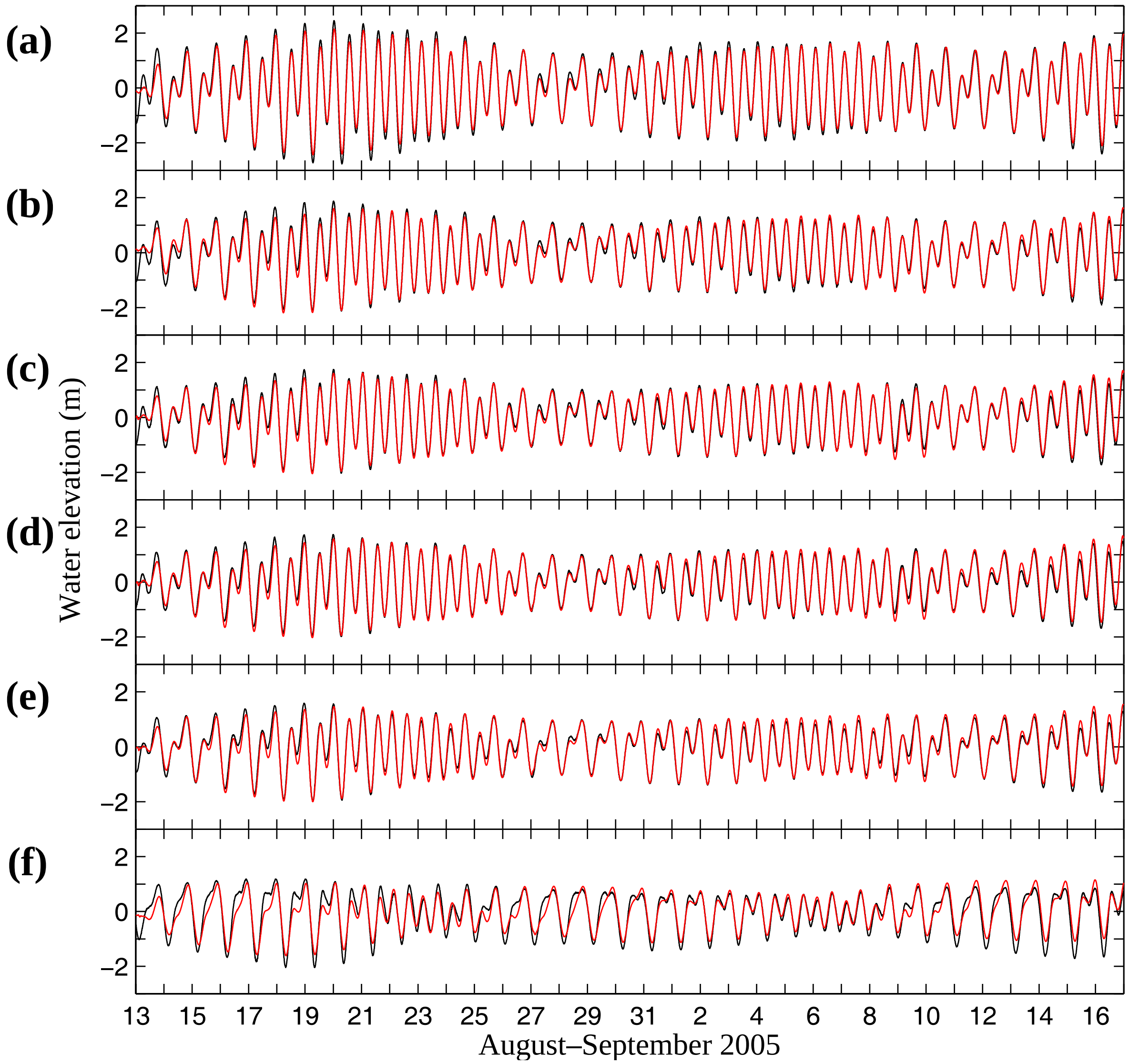

Figure 3.11 MM5 ELM (▬) and measured (▬) zero mean water elevations for the tide gauge locations **(a)** Port Hardy, **(b)** Winter Harbour, **(c)** Tofino, **(d)** Bamfield, **(e)** Neah Bay, **(f)** Port Angeles, **(g)** Victoria Harbour, **(h)** Port Townsend, **(i)** Friday Harbor, **(j)** Cherry Point, **(k)** Vancouver, **(l)** New Westminster, and **(m)** Cambell River.

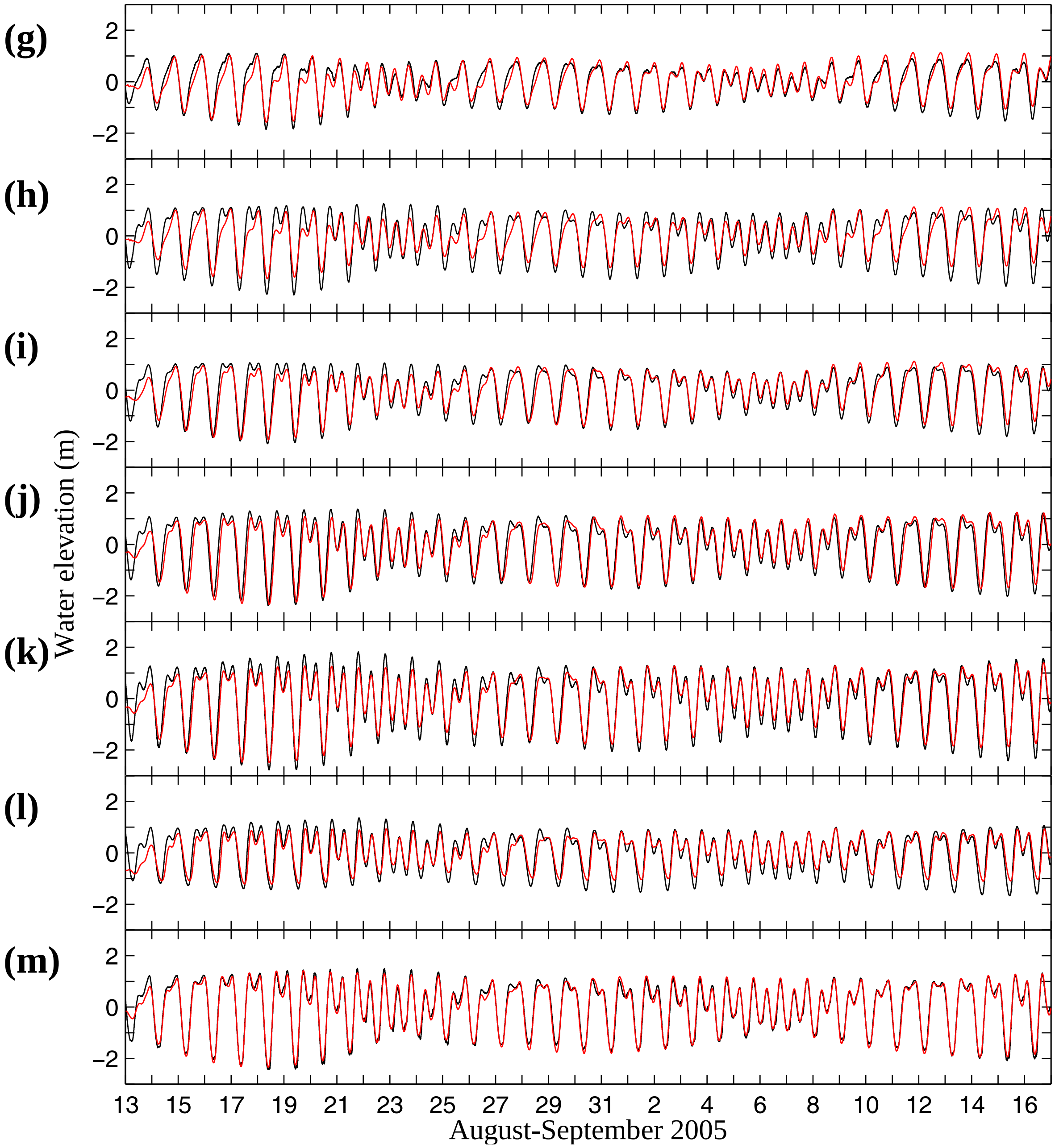

Figure 3.11 Continued.

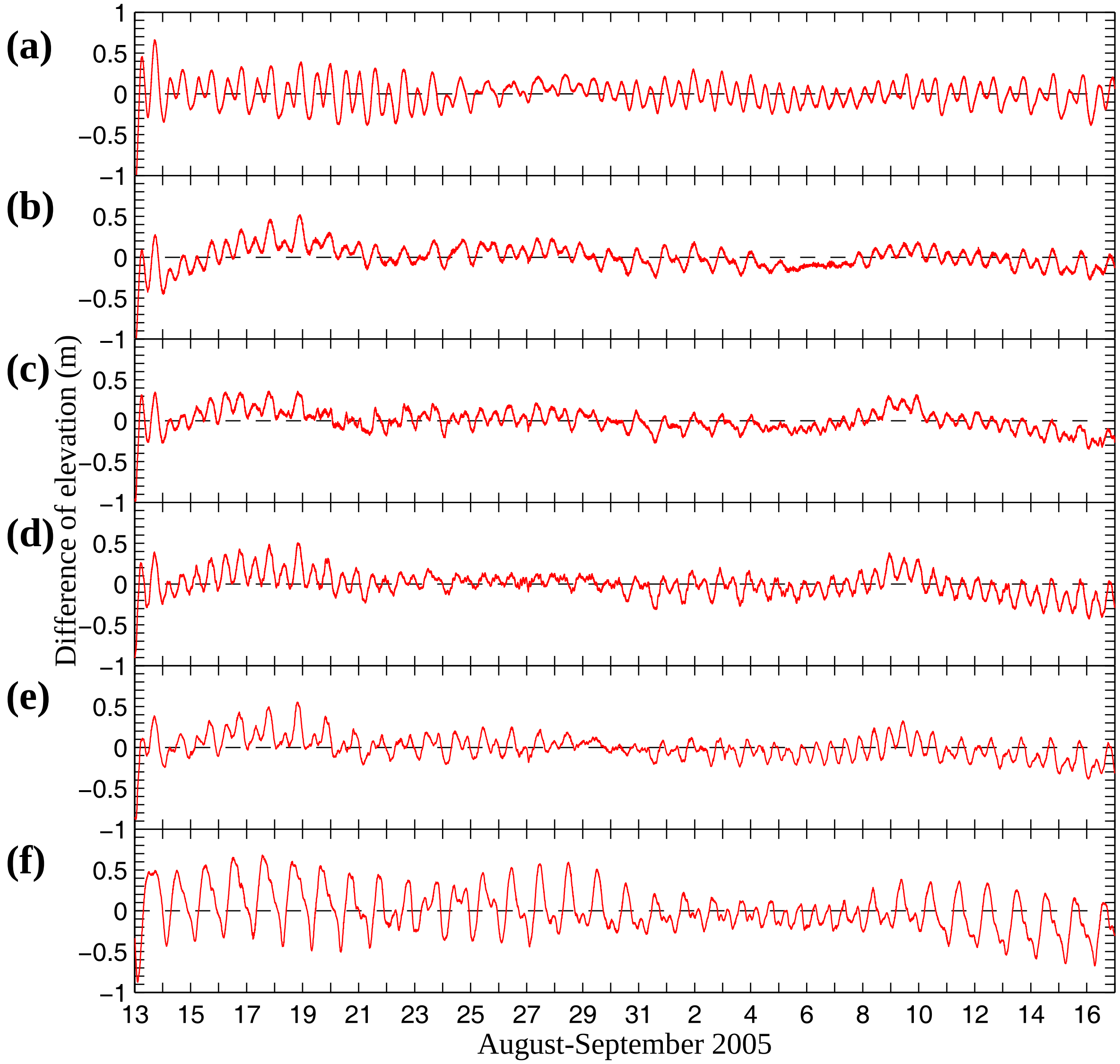

Figure 3.12 Difference [measured–modeled] of water elevations for the MM5 ELM at the tide gauge locations **(a)** Port Hardy, **(b)** Winter Harbour, **(c)** Tofino, **(d)** Bamfield, **(e)** Neah Bay, **(f)** Port Angeles, **(g)** Victoria Harbour, **(h)** Port Townsend, **(i)** Friday Harbor, **(j)** Cherry Point, **(k)** Vancouver, **(l)** New Westminster, and **(m)** Cambell River.

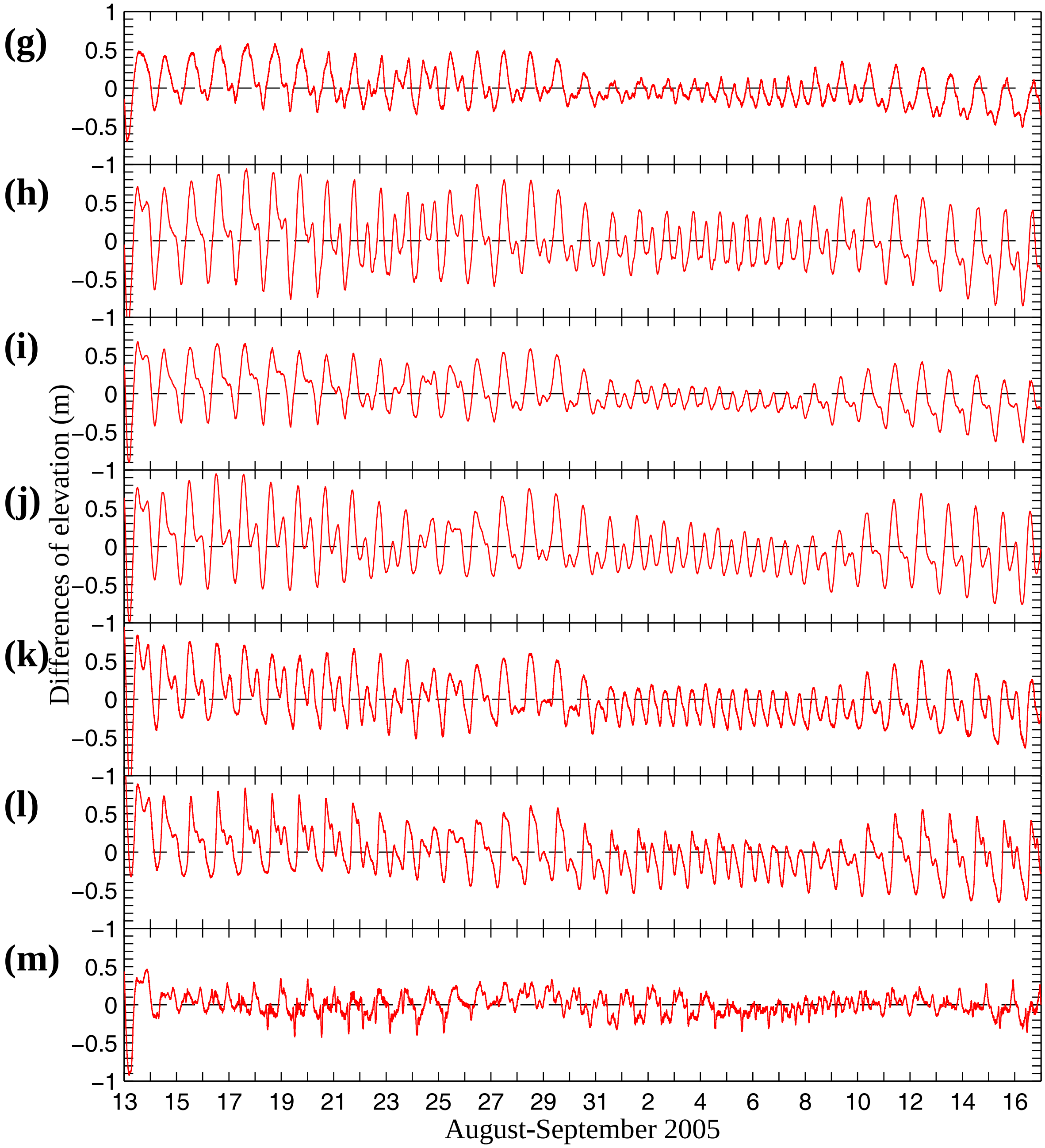

Figure 3.12 Continued.

Table 3.5 RMS errors (m) of synthesized water elevations after harmonic analysis using inference for the P1, K2, and NU2 constituents in the observed time series and fitting only the modeled constituents for the modeled time series at tide gauge locations computed for the time period shared by all 6 experiments (August 20 – September 17, 2005).

Tide gauge location	MM5 ELM	ETA ELM	NARR ELM	No Wind ELM	MM5 UWM	No Wind UWM
Port Hardy	0.0941	0.0941	0.0943	0.0943	0.0939	0.0939
Winter Harbour	0.0356	0.0353	0.0331	0.0317	0.0367	0.0316
Tofino	0.0300	0.0267	0.0279	0.0264	0.0333	0.0255
Bamfield	0.0669	0.0662	0.0651	0.0600	0.0708	0.0617
Neah Bay	0.0726	0.0723	0.0722	0.0671	0.0736	0.0675
Port Angeles	0.187	0.192	0.189	0.186	0.176	0.175
Victoria Harbour	0.149	0.151	0.150	0.143	0.140	0.137
Port Townsend	0.296	0.299	0.298	0.290	0.286	0.287
Friday Harbor	0.173	0.176	0.177	0.172	0.163	0.163
Cherry Point	0.258	0.258	0.260	0.259	0.259	0.259
Vancouver	0.199	0.198	0.199	0.195	0.193	0.191
New Westminster	0.230	0.233	0.232	0.229	0.228	0.227
Campbell River	0.0259	0.0260	0.0260	0.0259	0.0259	0.0257

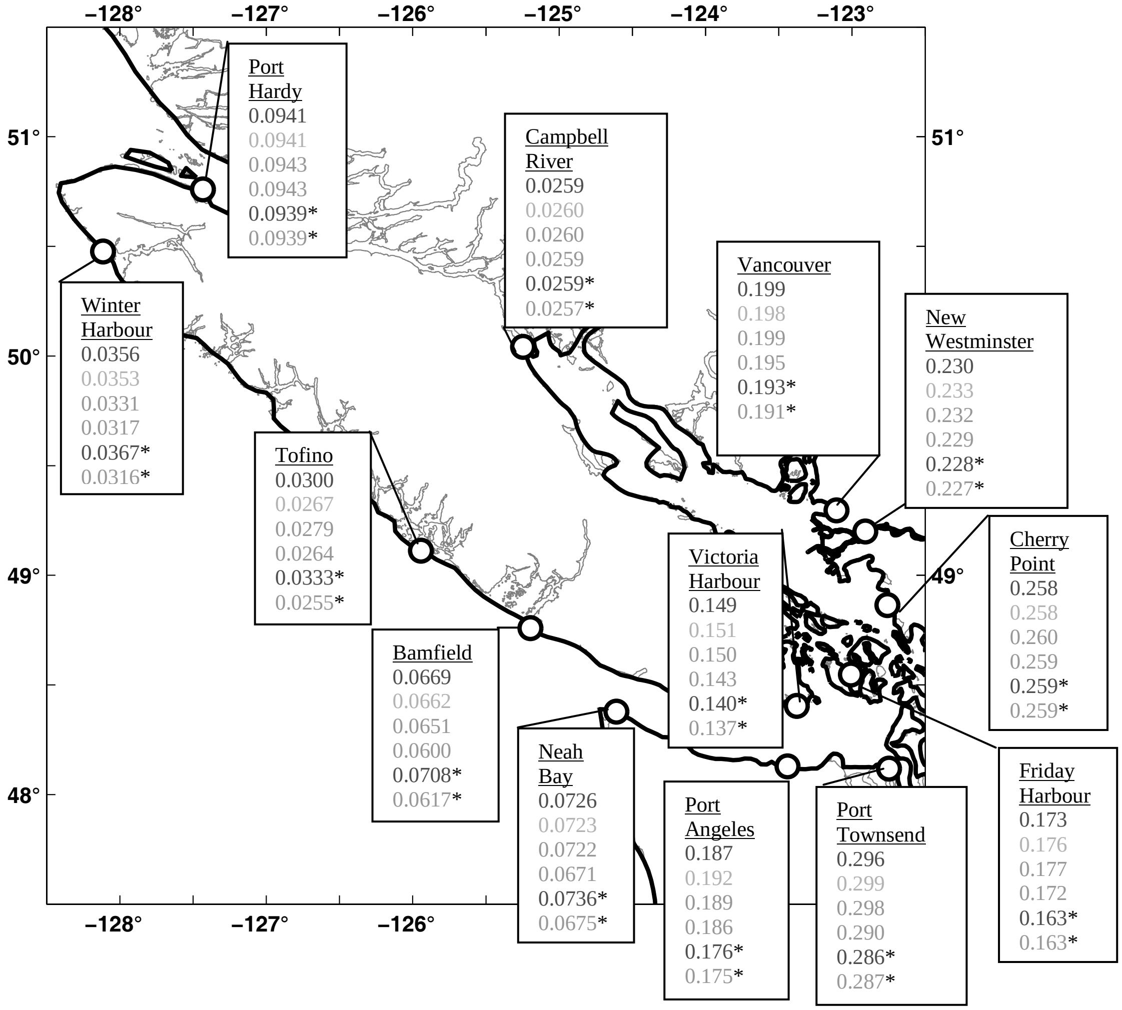

Figure 3.13 RMS errors (m) of synthesized water elevations after harmonic analysis using inference for the P1, K2, and NU2 constituents in the observed time series and fitting only the modeled constituents for the modeled time series shown at respective tide gauge locations computed for the time period (August 20 – September 17, 2005) shared by all 6 experiments: **MM5**, **ETA**, **NARR**, and **no wind**; * indicate UWM experiments.

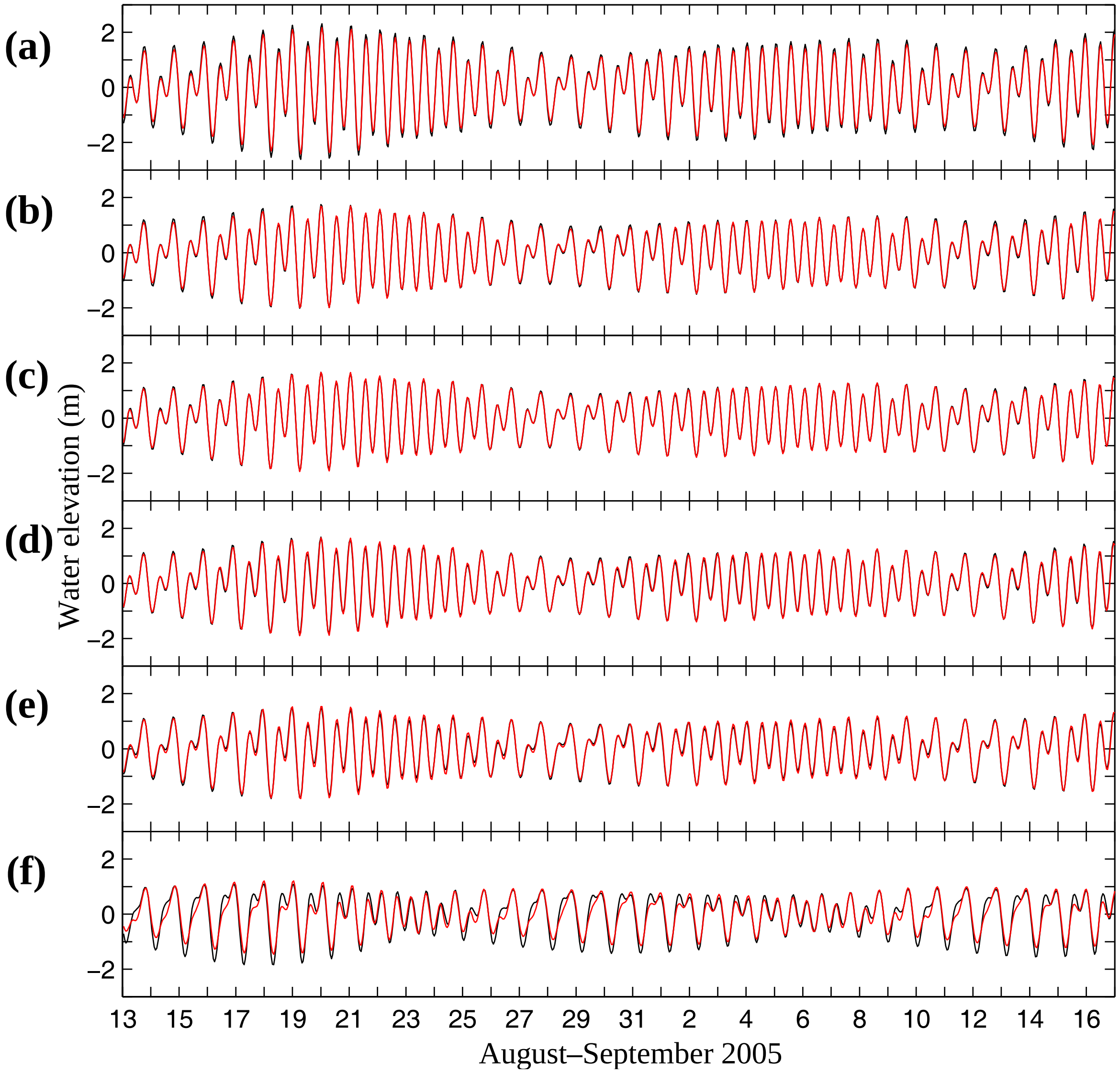

Figure 3.14 MM5 ELM (▬) and measured (▬) zero mean water elevations after harmonic analysis using inference for the P1, K2, and NU2 constituents in the observed time series and fitting only the modeled constituents for the modeled time series for the tide gauge locations **(a)** Port Hardy, **(b)** Winter Harbour, **(c)** Tofino, **(d)** Bamfield, **(e)** Neah Bay, **(f)** Port Angeles, **(g)** Victoria Harbour, **(h)** Port Townsend, **(i)** Friday Harbor, **(j)** Cherry Point, **(k)** Vancouver, **(l)** New Westminster, and **(m)** Cambell River.

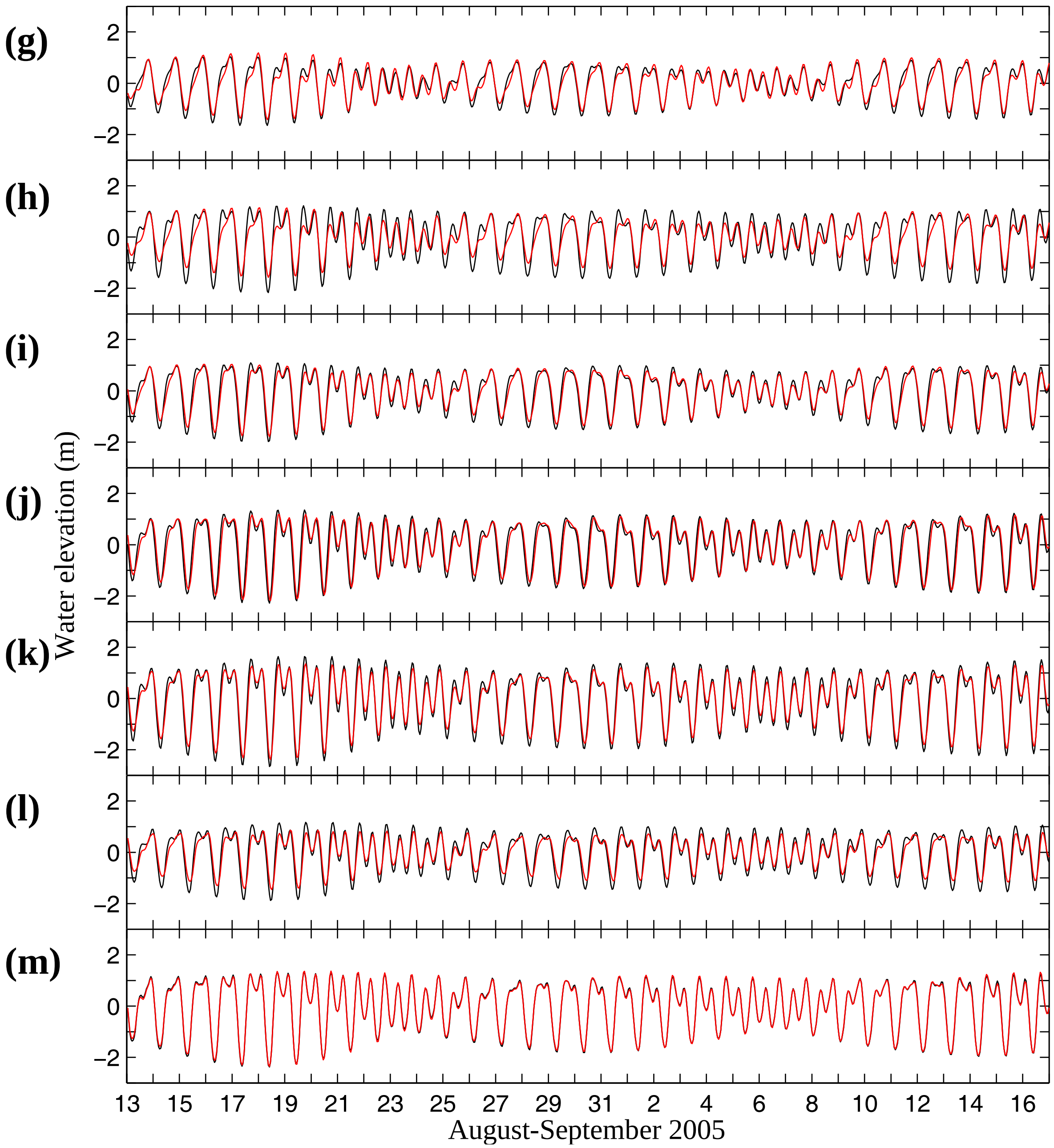

Figure 3.14 Continued.

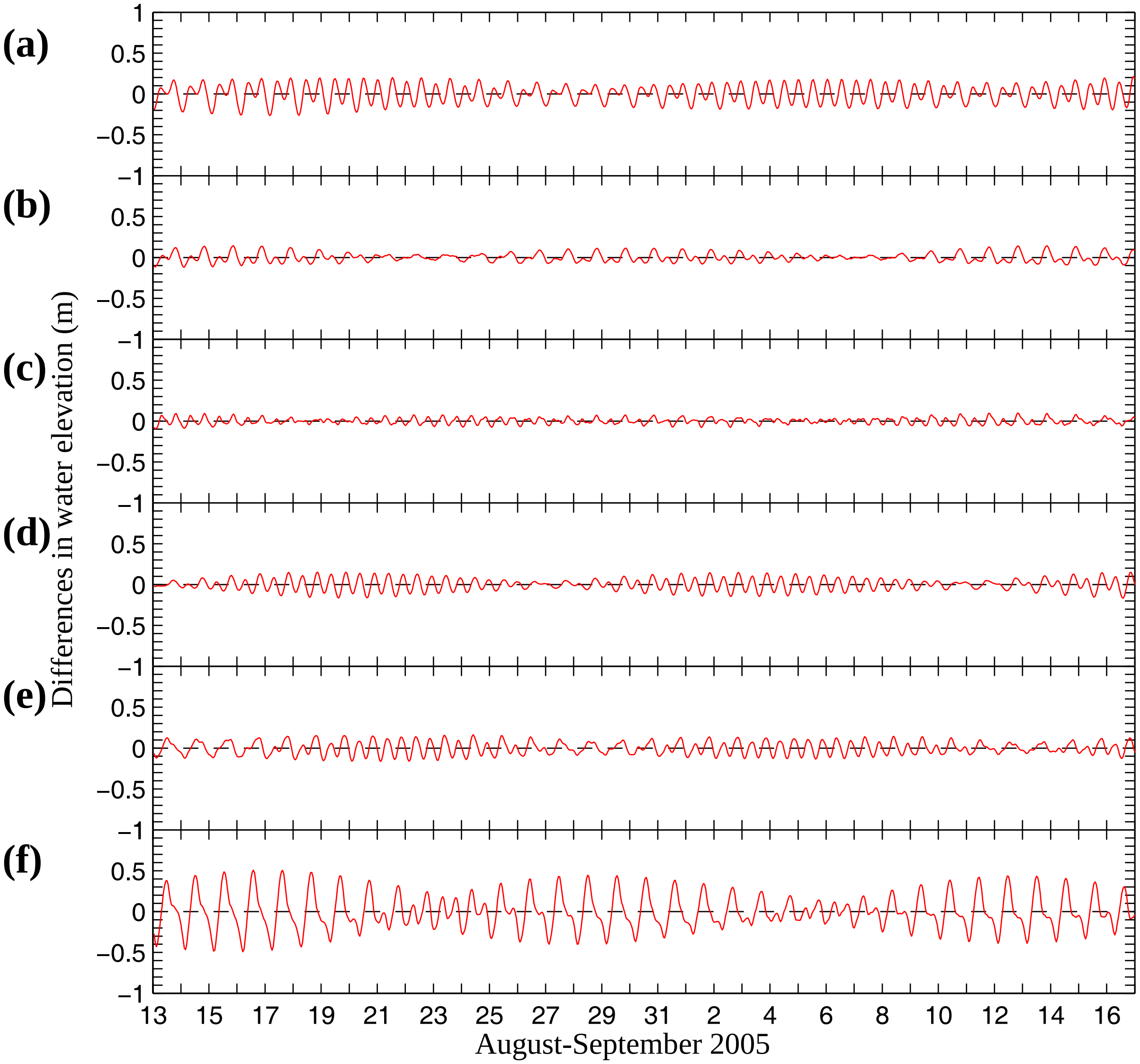

Figure 3.15 Differences [measured–modeled] in water elevations after harmonic analysis using inference for the P1, K2, and NU2 constituents in the observed time series and fitting only the modeled constituents for the modeled time series for the MM5 ELM at the tide gauge locations **(a)** Port Hardy, **(b)** Winter Harbour, **(c)** Tofino, **(d)** Bamfield, **(e)** Neah Bay, **(f)** Port Angeles, **(g)** Victoria Harbour, **(h)** Port Townsend, **(i)** Friday Harbor, **(j)** Cherry Point, **(k)** Vancouver, **(l)** New Westminster, and **(m)** Cambell River.

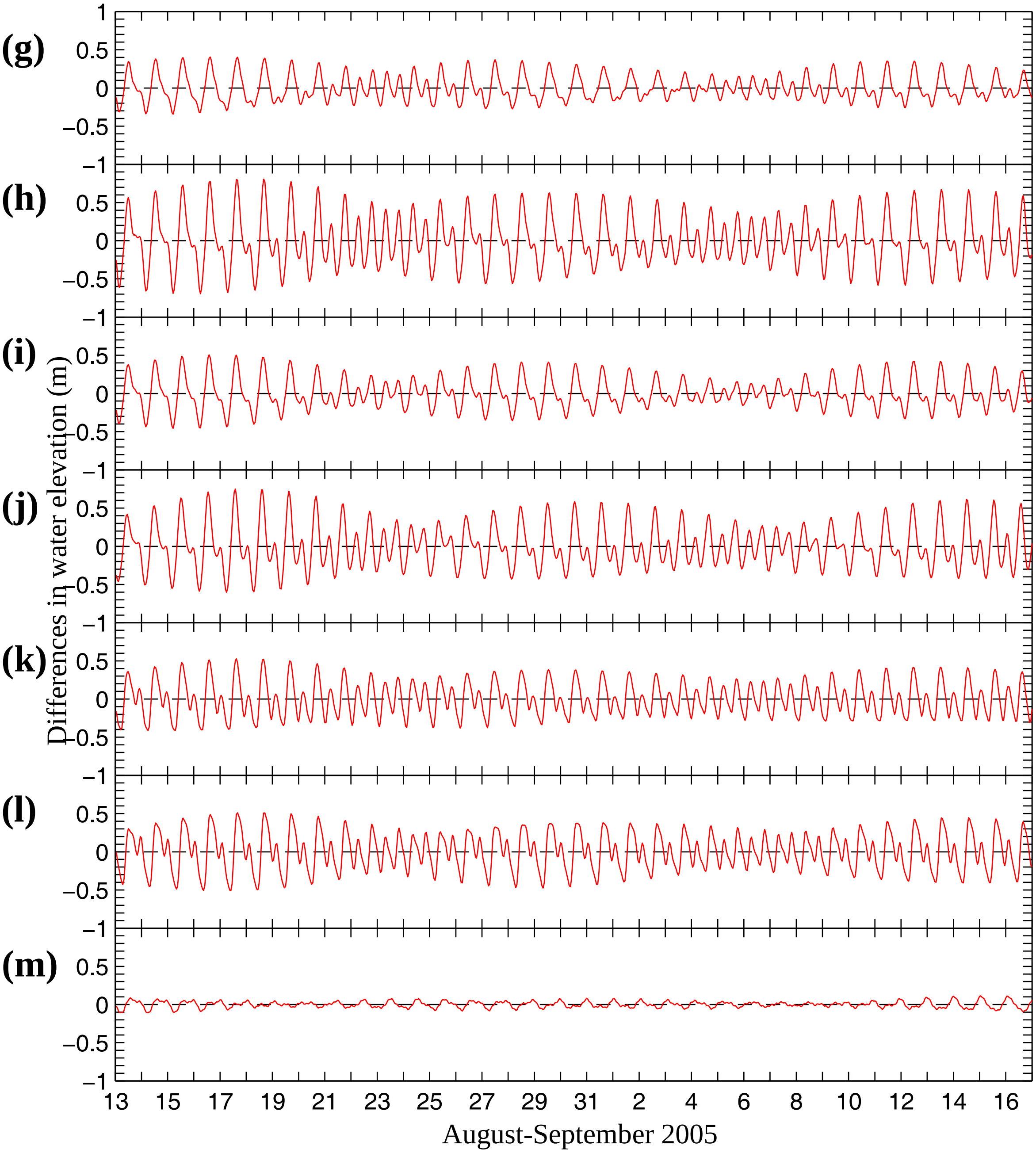

Figure 3.15 Continued.

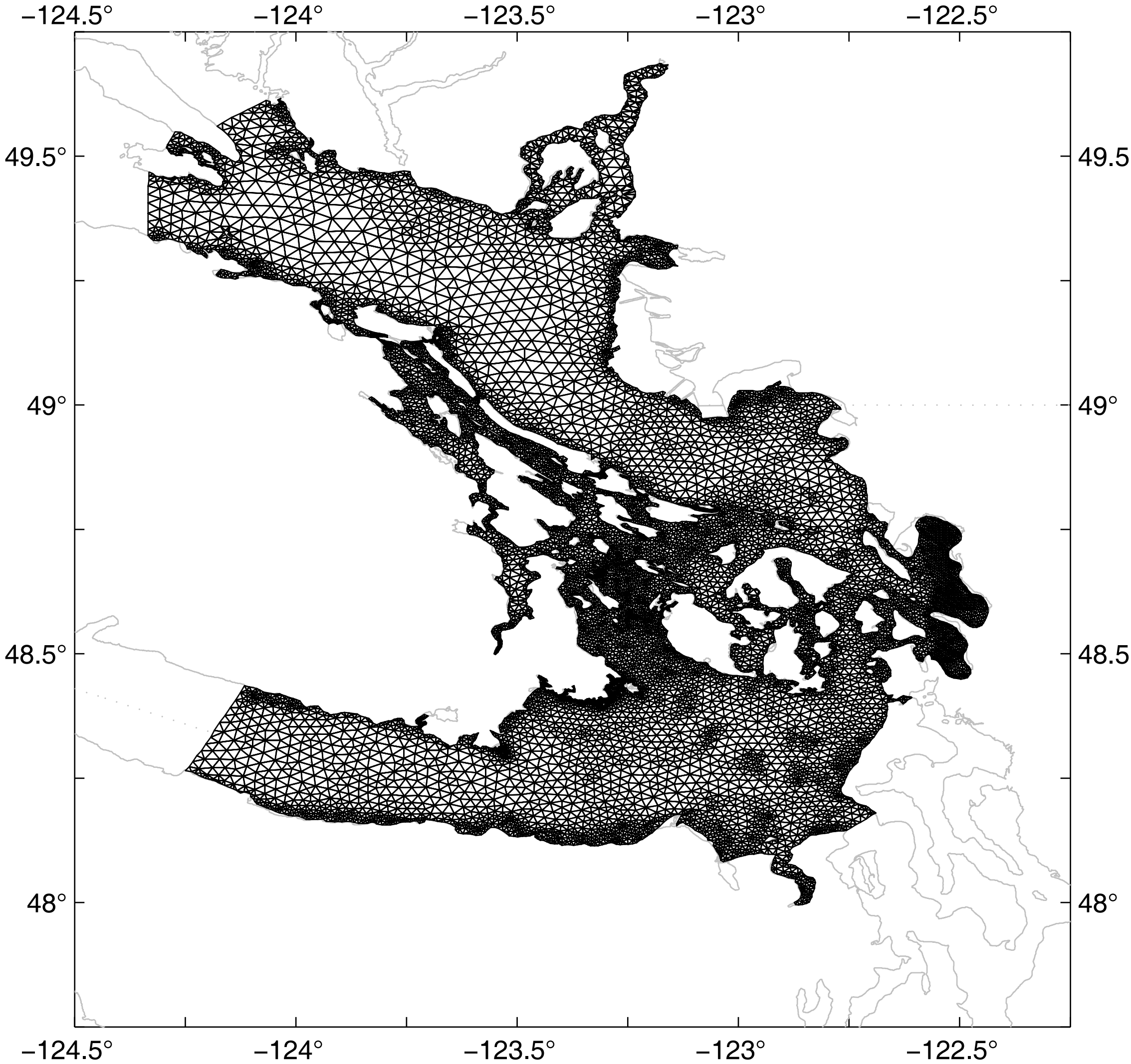

Figure 3.16 Horizontal grid used for the barotropic simulation.

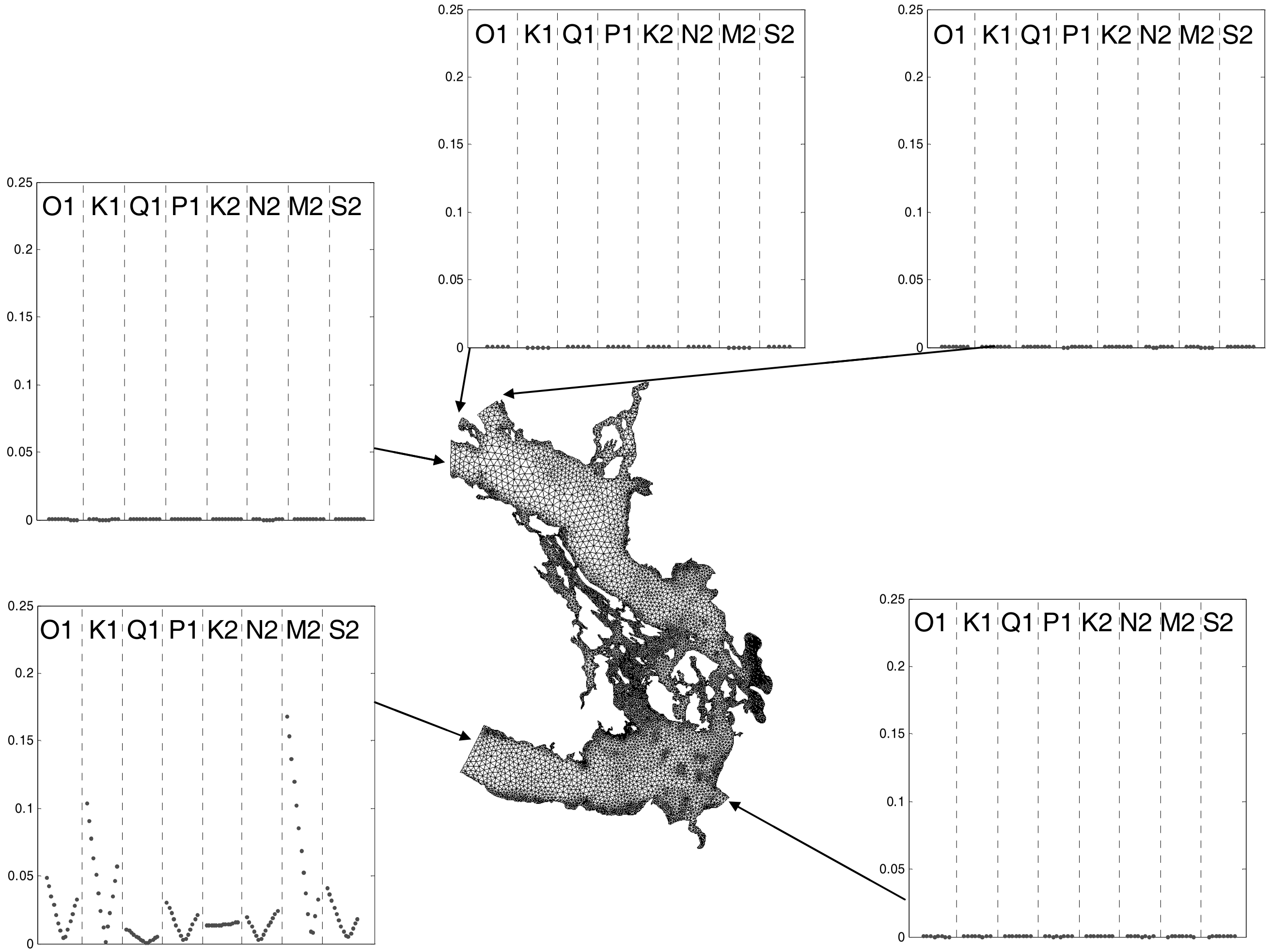

Figure 3.17 Differences in the complex plane (m) between the harmonic constituents of [12] and [15, 16] along each of the 5 tidal grid boundaries of [12].

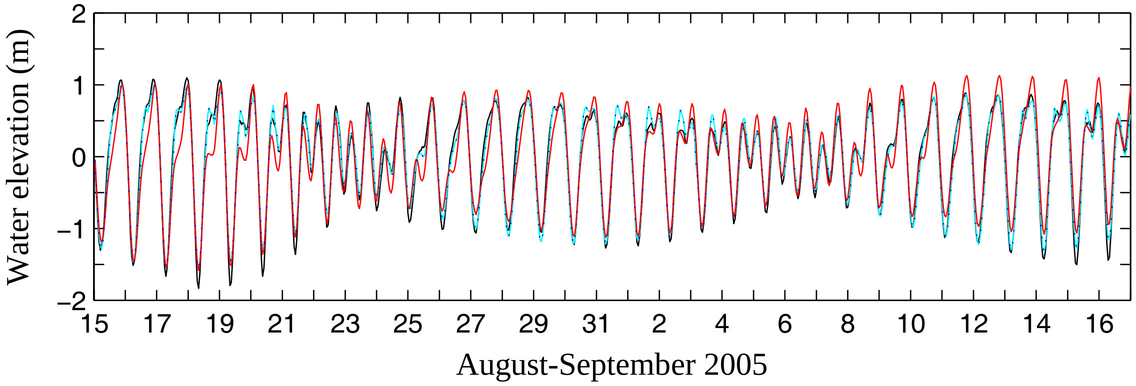

Figure 3.18 Zero mean water elevation at Victoria Harbour for the BEXP1 (—) and BEXP2 (▪▪▪) barotropic, and the MM5 ELM baroclinic (▬) simulations and observations (▬).

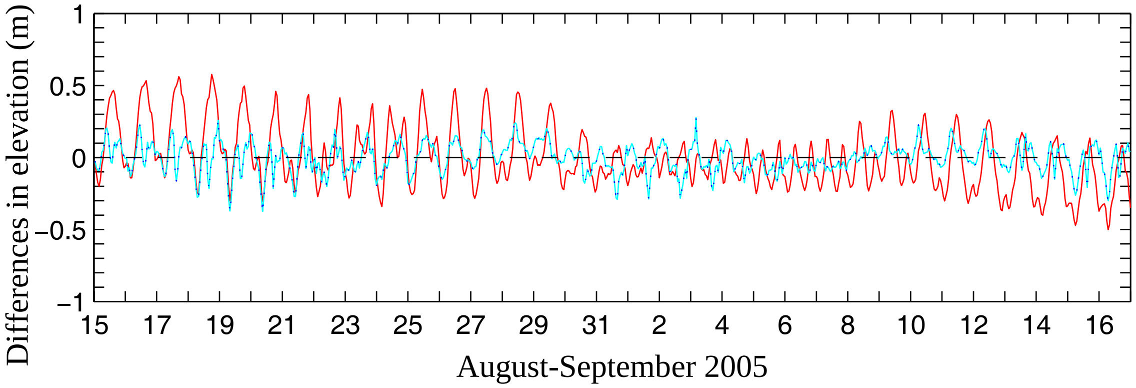

Figure 3.19 Differences [measured-modeled] in water elevation for the BEXP1 (—) and BEXP2 (▪▪▪) barotropic, and the MM5 ELM baroclinic (▬) simulations

Table 3.6 Differences (m) as the distance in the complex plane for the leading 8 harmonic constituents of the measured and modeled water elevations for the BEXP1 and BEXP2 barotropic, and MM5 ELM baroclinic simulations.

	O1	**K1**	**Q1**	**P1**
MM5 ELM	**0.088**	**0.16**	**0.029**	**0.051**
BEXP1	**0.019**	**0.0087**	**0.017**	**0.0029**
BEXP2	**0.019**	**0.0087**	**0.017**	**0.0029**

	K2	**N2**	**M2**	**S2**
MM5 ELM	**0.0097**	**0.027**	**0.12**	**0.036**
BEXP1	**0.0025**	**0.043**	**0.029**	**0.009**
BEXP2	**0.0025**	**0.043**	**0.029**	**0.009**

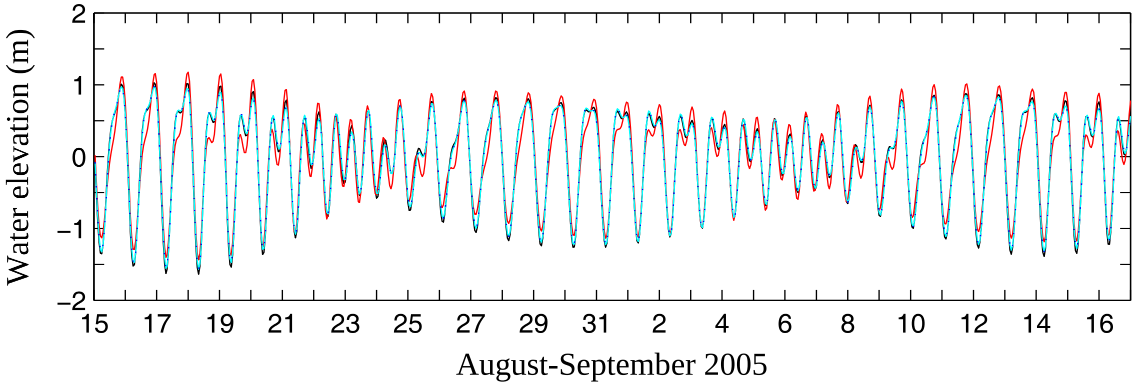

Figure 3.20 Zero mean water elevation after harmonic analysis using inference for the P1, K2, and NU2 constituents in the observed time series and fitting only the modeled constituents for the modeled time series at Victoria Harbour for the BEXP1 (—) and BEXP2 (▪▪▪) barotropic, and the MM5 ELM baroclinic (▬) simulations and observations (▬).

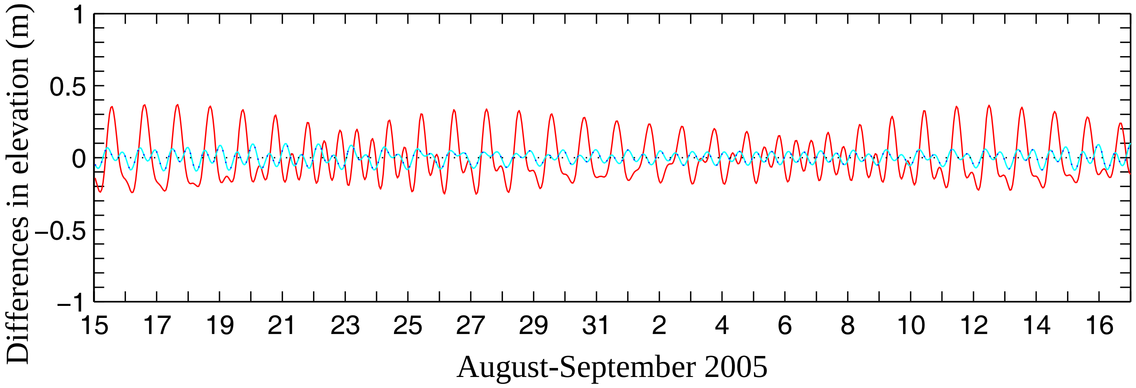

Figure 3.21 Differences [measured-modeled] in water elevation after harmonic analysis as in Figure 3.20 for the modeled time series for the BEXP1 (—) and BEXP2 (▪▪▪) barotropic, and the MM5 ELM baroclinic (▬) simulations

Table 3.7 Differences (m) as the distance in the complex plane for the leading 8 harmonic constituents of the measured and modeled water elevations after harmonic analysis as in Figure 3.20 for the BEXP1 and BEXP2 barotropic, and MM5 ELM baroclinic simulations.

	O1	**K1**	**Q1**	**P1**
MM5 ELM	**0.087**	**0.15**	**0.028**	**0.045**
BEXP1	**0.020**	**0.0078**	**0.017**	**0.0024**
BEXP2	**0.020**	**0.0078**	**0.017**	**0.0024**

	K2	**N2**	**M2**	**S2**
MM5 ELM	**0.0069**	**0.025**	**0.12**	**0.037**
BEXP1	**0.0018**	**0.014**	**0.043**	**0.0093**
BEXP2	**0.0018**	**0.014**	**0.043**	**0.0093**

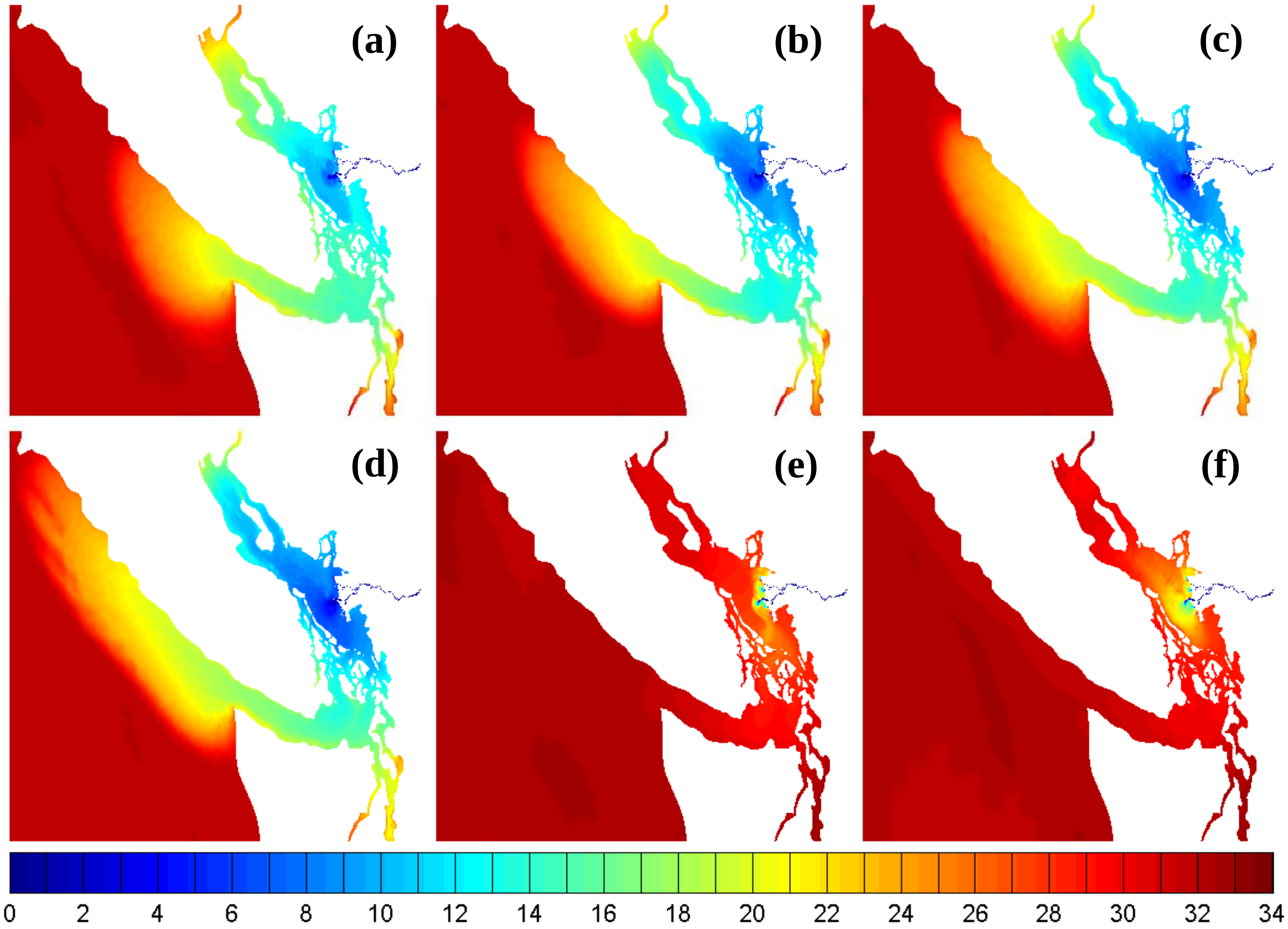

Figure 3.22 Surface salinity contours (psu) for the final time step (September 17, 2005) for each of the 6 model experiments **(a)** MM5 ELM, **(b)** ETA ELM, **(c)** NARR ELM, **(d)** no wind ELM, **(e)** MM5 UWM, and **(f)** no wind UWM.

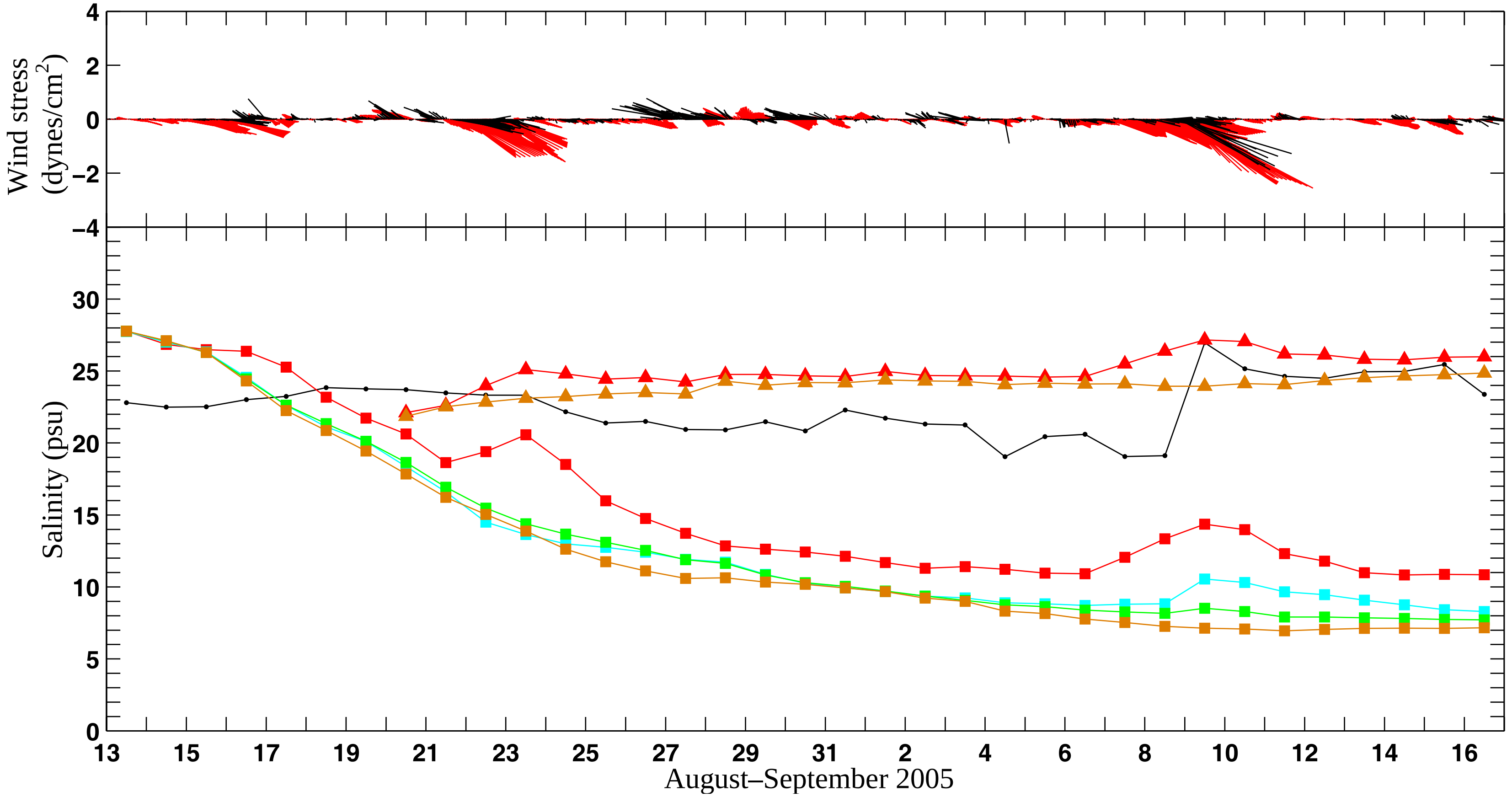

Figure 3.23 Observed (▬) and MM5 (▬) wind stress at the Central Strait of Georgia wind buoy 46146 and daily averaged modeled and measured (▬) salinities collected by the central Strait of Georgia BC Ferry for each of the experiments: MM5 ELM (■), ETA ELM (■), NARR ELM (■), no wind ELM (■), MM5 UWM (▲), and no wind UWM (▲).

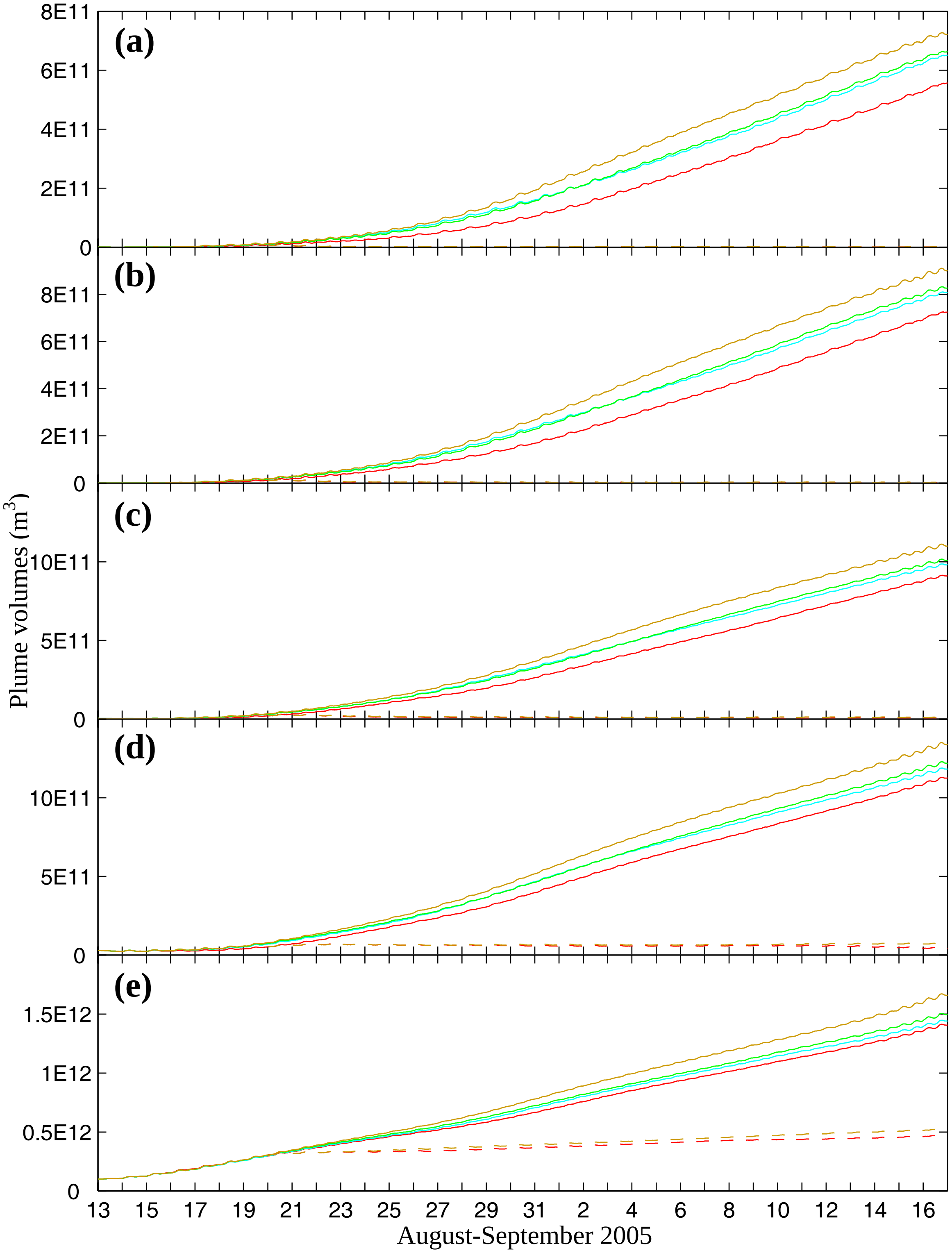

Figure 3.24 Plume volumes (m^3) computed using the **(a)** 22, **(b)** 24, and **(c)** 26, **(d)** 28, and **(e)** 30 psu salinity contours for each of the experiments MM5 ELM (▬), ETA ELM (▬), NARR ELM (▬), no wind ELM (▬), MM5 UWM (▬ ▬), and no wind UWM (▬ ▬). The y-axis scale is adjusted for comparing the wind variations of the ELM experiments.

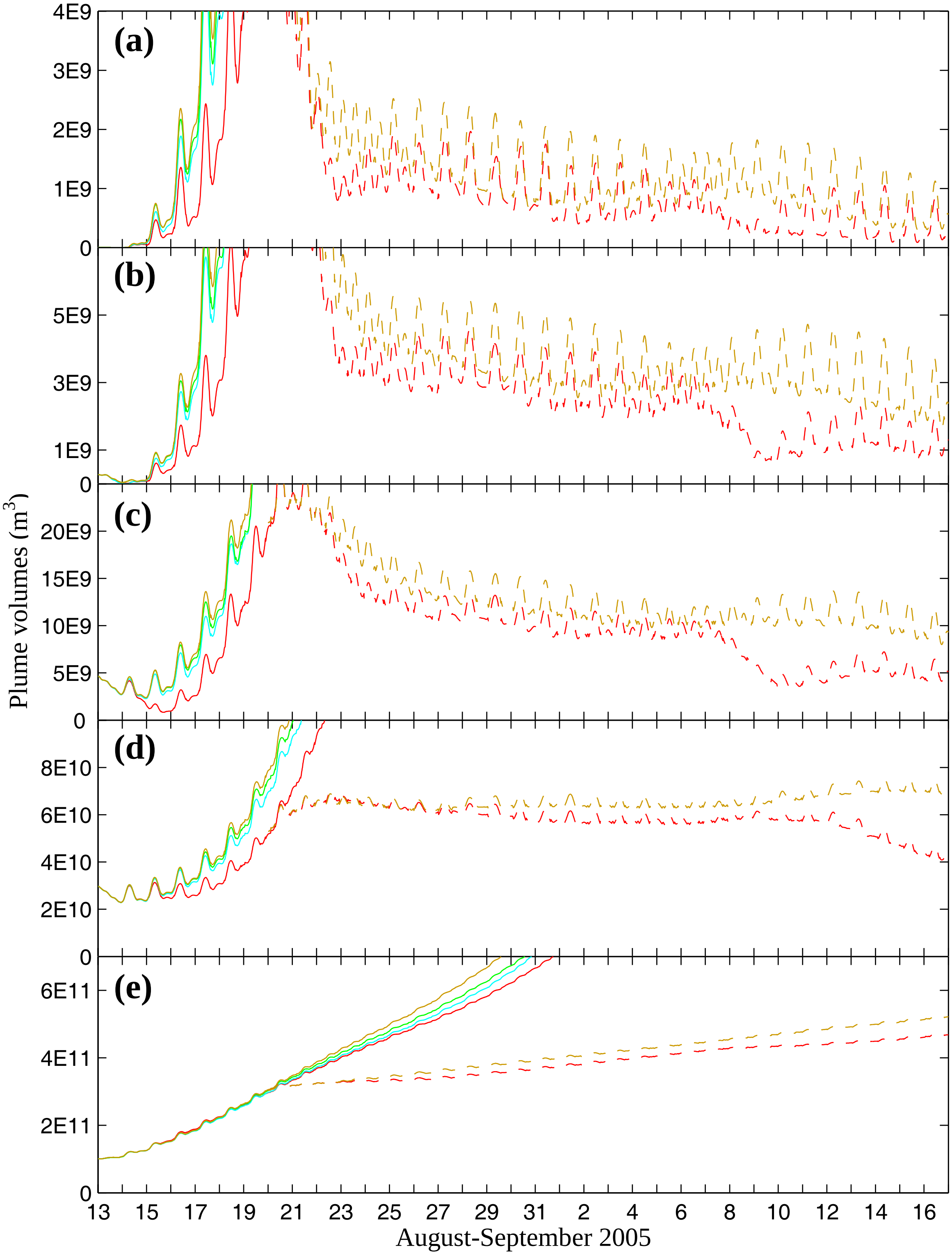

Figure 3.25 Plume volumes (m^3) computed using the **(a)** 22, **(b)** 24, and **(c)** 26, **(d)** 28, and **(e)** 30 psu salinity contours for each of the experiments MM5 ELM (▬), ETA ELM (▬), NARR ELM (▬), no wind ELM (▬), MM5 UWM (▬ ▬), and no wind UWM (▬ ▬). The y-axis scale is adjusted for comparing the wind variations of the UMM experiments.

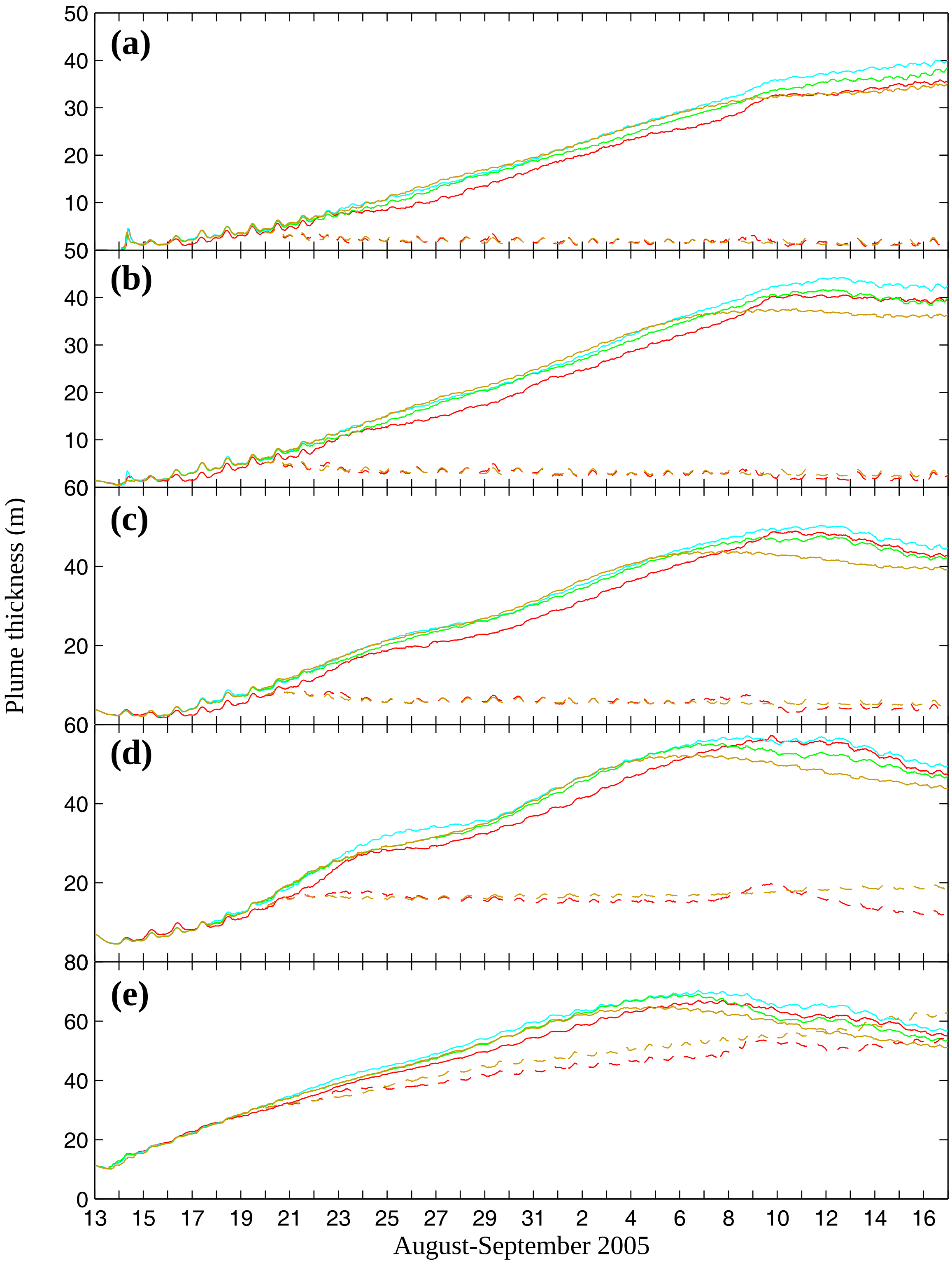

Figure 3.26 Plume thickness (m) computed using the **(a)** 22, **(b)** 24, and **(c)** 26, **(d)** 28, and **(e)** 30 psu salinity contours for each of the experiments MM5 ELM (▬), ETA ELM (▬), NARR ELM (▬), no wind ELM (▬), MM5 UWM (▬ ▬), and no wind UWM (▬ ▬). The y-axis scale is adjusted for comparing the wind variations of the ELM experiments.

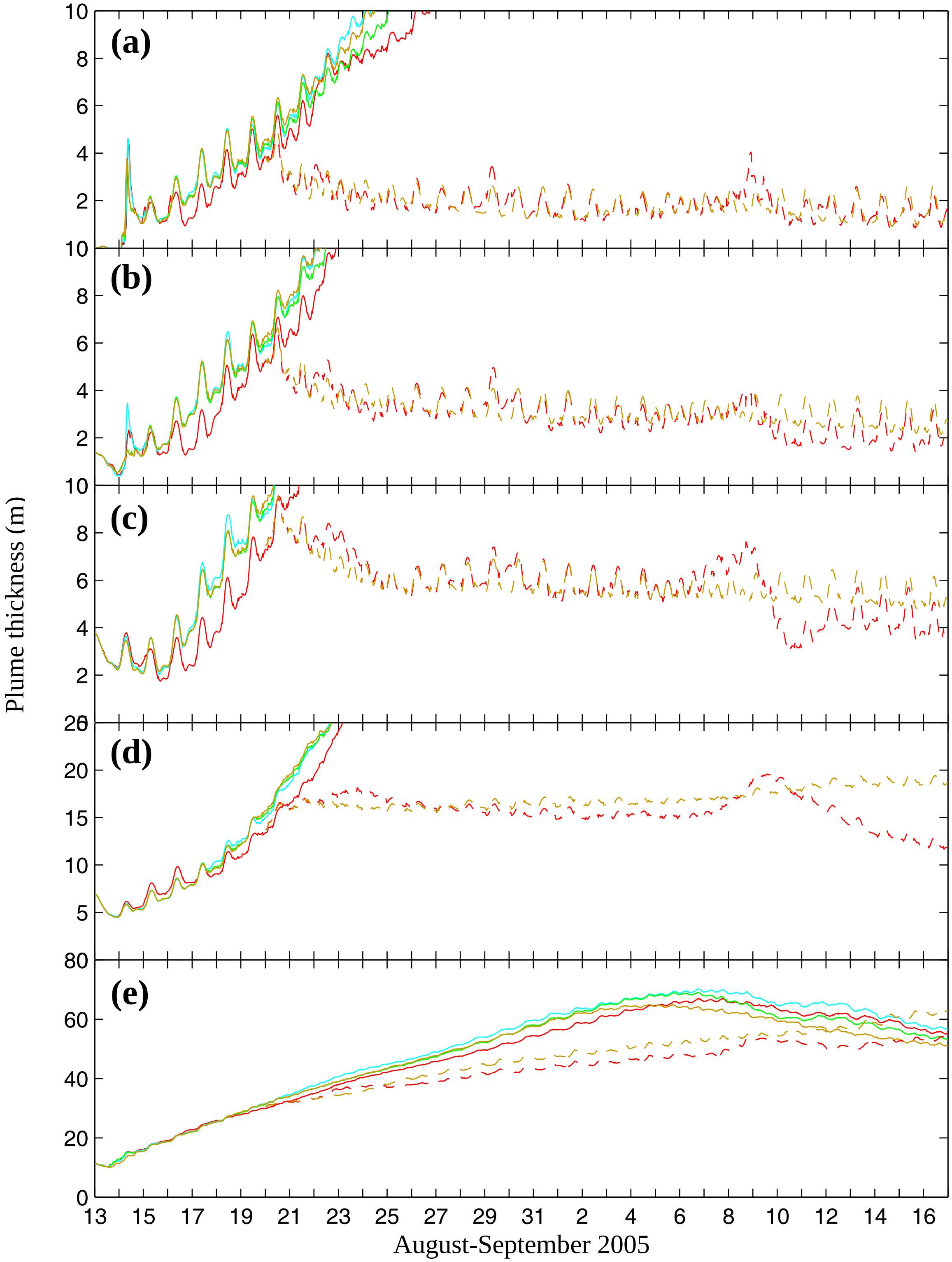

Figure 3.27 Plume thickness (m) computed using the **(a)** 22, **(b)** 24, and **(c)** 26, **(d)** 28, and **(e)** 30 psu salinity contours for each of the experiments MM5 ELM (▬), ETA ELM (▬), NARR ELM (▬), no wind ELM (▬), MM5 UWM (– –), and no wind UWM (– –). The y-axis scale is adjusted for comparing the wind variations of the UWM experiments.

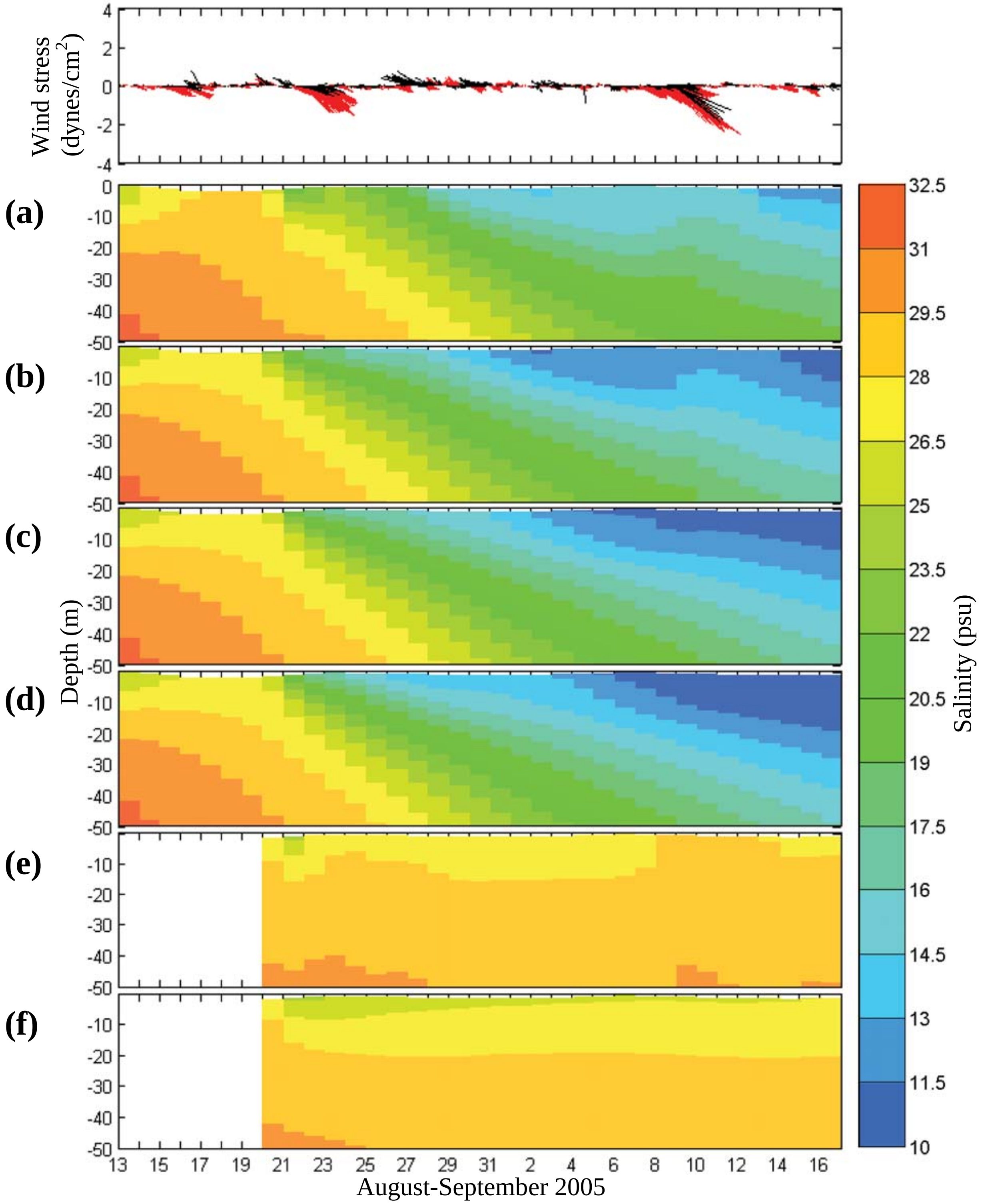

Figure 3.28 Observed (▬) and MM5 (▬) wind stress at the Central Strait of Georgia wind buoy 46146 and depth profiles of daily averaged modeled salinity contours at the buoy location 46146 for **(a)** MM5 ELM, **(b)** ETA ELM, **(c)** NARR ELM, **(d)** no wind ELM, **(e)** MM5 UWM, and **(f)** no wind UWM.

Table 3.8 Surface water current vector (u_v) and scalar means (u_s) and mean directions (θ) for experiments using the **(a)** ELM and the **(b)** UWM transport algorithm at specified wind buoy locations and two virtual locations. The geographic coordinates for HS are -123.22°W 48.52°N and for RS are -122.79°W 48.56°N. The no wind experiments as a reference for comparing the wind choices.

(a)

	No Wind			MM5					
Station	$u_{v,nw}$	$u_{s,nw}$	θ_{nw}	u_v	u_s	θ	$u_v/u_{v,nw}$	$u_s/u_{s,nw}$	$\theta-\theta_{nw}$
46146	0.0640	0.0971	34	0.0194	0.136	244	0.303	1.40	-150
46131	0.248	0.321	321	0.163	0.262	313	0.657	0.816	-8
46087	0.193	0.384	289	0.108	0.367	280	0.560	0.956	-9
46029	0.0664	0.0860	118	0.102	0.133	151	1.54	1.55	33
46041	0.0279	0.0638	129	0.0958	0.132	158	3.43	2.07	29
46207	0.0959	0.129	299	0.0669	0.137	247	0.698	1.06	-52
46204	0.125	0.164	303	0.117	0.178	281	0.936	1.09	-22
46206	0.159	0.171	313	0.0227	0.142	229	0.143	0.830	-84
46132	0.139	0.147	316	0.0243	0.130	318	0.175	0.884	2
46088	0.165	0.367	215	0.168	0.387	178	1.02	1.05	-37
HS	0.107	0.344	196	0.105	0.344	192	0.981	1.00	-4
RS	0.137	0.458	182	0.136	0.445	176	0.993	0.972	-6
				Average			0.953	1.14	-25.9
				Standard error of the sample			0.879	0.364	50.7

	ETA						NARR					
Station	u_v	u_s	θ	$u_v/u_{v,nw}$	$u_s/u_{s,nw}$	$\theta-\theta_{nw}$	u_v	u_s	θ	$u_v/u_{v,nw}$	$u_s/u_{s,nw}$	$\theta-\theta_{nw}$
46146	0.0722	0.125	17.1	1.13	1.29	-16.9	0.0634	0.0918	27.6	0.991	0.946	-6.43
46131	0.230	0.305	320	0.929	0.949	-1.11	0.246	0.314	321	0.993	0.978	-0.0392
46087	0.106	0.362	289	0.548	0.944	0.249	0.123	0.367	283	0.636	0.955	-5.67
46029	0.0942	0.129	142	1.42	1.50	24.4	0.0939	0.122	140	1.41	1.42	22.1
46041	0.0772	0.125	152	2.77	1.96	23.2	0.0784	0.118	151	2.81	1.84	22.2
46207	0.0635	0.137	254	0.662	1.06	-44.9	0.0701	0.138	256	0.731	1.07	-43.2
46204	0.112	0.176	285	0.894	1.07	-17.7	0.112	0.175	284	0.898	1.07	-18.7
46206	0.0572	0.136	303	0.360	0.793	-10.3	0.0749	0.131	310	0.471	0.767	-2.66
46132	0.0479	0.139	304	0.345	0.948	-12.5	0.0625	0.143	309	0.450	0.970	-7.16
46088	0.142	0.367	192	0.858	1.00	-23.1	0.171	0.374	210	1.03	1.02	-4.89
HS	0.0883	0.341	196	0.825	0.990	0.353	0.100	0.343	197	0.935	0.997	1.26
RS	0.111	0.438	178	0.813	0.956	-4.06	0.131	0.451	180	0.959	0.984	-2.08
Average				0.962	1.12	-6.86				1.03	1.08	-3.77
Standard error of the sample				0.644	0.322	19.1				0.621	0.282	17.0

Table 3.8 Continued.

(b)

	No Wind			**MM5**					
Station	$u_{v,nw}$	$u_{s,nw}$	θ_{nw}	u_v	u_s	θ	$u_v/u_{v,nw}$	$u_s/u_{s,nw}$	$\theta-\theta_{nw}$
46146	0.0773	0.0880	339	0.0197	0.139	295	0.255	1.58	-44.4
46131	0.117	0.233	303	0.0809	0.228	277	0.690	0.977	-25.9
46087	0.0567	0.353	312	0.0471	0.362	275	0.831	1.03	-37.1
46029	0.0733	0.0898	131	0.133	0.161	163	1.81	1.79	32.5
46041	0.0172	0.0497	90.2	0.115	0.153	170	6.69	3.07	79.5
46207	0.123	0.144	294	0.0878	0.152	249	0.716	1.05	-44.6
46204	0.169	0.192	296	0.148	0.198	283	0.881	1.03	-13.4
46206	0.153	0.159	319	0.0475	0.163	239	0.311	1.02	-80.8
46132	0.199	0.201	322	0.0784	0.151	325	0.393	0.752	3.33
46088	0.0803	0.351	227	0.119	0.368	173	1.48	1.05	-53.7
HS	0.0430	0.363	180	0.0701	0.368	172	1.63	1.01	-8.16
RS	0.0482	0.369	172	0.0665	0.368	168	1.38	0.997	-4.92
Average							1.42	1.28	-16.5
Standard error of the Sample							1.74	0.630	42.5

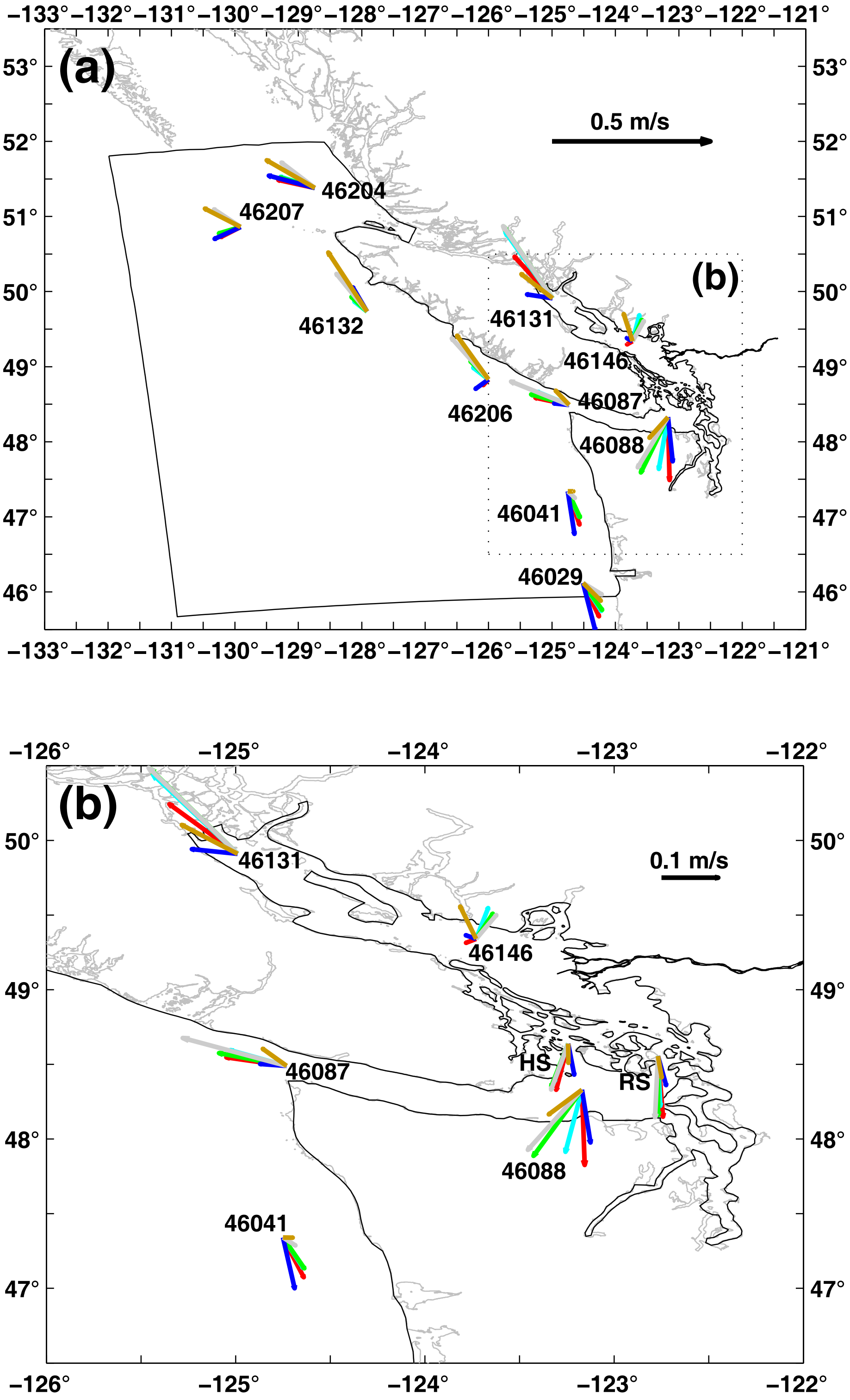

Figure 3.29 Mean vectors of surface currents for each of the experiments: no wind ELM (▬), MM5 ELM (▬), ETA ELM (▬), NARR ELM (▬), no wind UWM (▬), and MM5 UWM (▬).

Table 3.9 Principal axes of surface currents for experiments using the **(a)** ELM and the **(b)** UWM transport algorithm at specified wind buoy locations and two virtual locations. The geographic coordinates for HS are -123.22°W 48.52°N and for RS are -122.79°W 48.56°N. The no wind experiments as a reference for comparing the wind choices.

(a)

	No Wind				MM5						
Station	$\lambda_{1,nw}^{0.5}$	$\lambda_{2,nw}^{0.5}$	$\theta_{p,nw}$	$\lambda_{2,nw} / \lambda_{1,nw}$	$\lambda_1^{0.5}$	$\lambda_2^{0.5}$	θ_p	$\lambda_{2,d} / \lambda_{1,d}$	$\lambda_1^{0.5}/\lambda_{1,nw}^{0.5}$	$\lambda_2^{0.5}/\lambda_{2,nw}^{0.5}$	θ_p-$\theta_{p,nw}$
46146	0.0792	0.0371	144	0.219	0.150	0.0684	141	0.209	1.89	1.84	-2.72
46131	0.294	0.0492	152	0.0280	0.266	0.0489	152	0.0337	0.906	0.994	0.383
46087	0.414	0.0878	110	0.0450	0.415	0.0985	110	0.0565	1.00	1.12	0.0870
46029	0.0590	0.0152	39.3	0.0664	0.0970	0.0302	31.5	0.0973	1.64	1.99	-7.82
46041	0.0559	0.0331	22.6	0.351	0.114	0.0414	5.77	0.131	2.04	1.25	-16.8
46207	0.0844	0.0535	34.5	0.402	0.129	0.0614	24.8	0.228	1.52	1.15	-9.66
46204	0.110	0.0745	70.9	0.459	0.128	0.0979	28.0	0.585	1.16	1.31	-42.9
46206	0.110	0.0521	123	0.224	0.150	0.0721	154	0.232	1.36	1.38	30.6
46132	0.0740	0.0172	142	0.0540	0.142	0.0424	164	0.0897	1.92	2.47	22.3
46088	0.398	0.0486	57.9	0.0149	0.403	0.0914	56.0	0.0514	1.01	1.88	-1.95
HS	0.388	0.0234	176	0.00364	0.396	0.0381	175	0.00923	1.02	1.63	-0.962
RS	0.515	0.0412	173	0.0064	0.504	0.0527	172	0.0109	0.980	1.28	-0.559
Average				0.156				0.144	1.37	1.52	-2.50
Standard error of the sample				0.168				0.161	0.417	0.440	18.2

	ETA							NARR						
Station	$\lambda_1^{0.5}$	$\lambda_2^{0.5}$	θ_p	$\lambda_{2,d} / \lambda_{1,d}$	$\lambda_1^{0.5}/\lambda_{1,nw}^{0.5}$	$\lambda_2^{0.5}/\lambda_{2,nw}^{0.5}$	θ_p-$\theta_{p,nw}$	$\lambda_1^{0.5}$	$\lambda_2^{0.5}$	θ_p	$\lambda_{2,d} / \lambda_{1,d}$	$\lambda_1^{0.5}/\lambda_{1,nw}^{0.5}$	$\lambda_2^{0.5}/\lambda_{2,nw}^{0.5}$	θ_p-$\theta_{p,nw}$
46146	0.123	0.0505	155	0.168	1.55	1.36	10.7	0.0761	0.0342	152	0.201	0.961	0.921	8.06
46131	0.283	0.0531	152	0.0351	0.963	1.08	-0.203	0.282	0.0513	152	0.0330	0.961	1.04	-0.103
46087	0.412	0.0945	109	0.0525	0.996	1.08	-0.675	0.412	0.0954	110	0.0534	0.996	1.09	-0.498
46029	0.0970	0.0323	30.7	0.111	1.64	2.13	-8.57	0.0855	0.0294	31.6	0.118	1.45	1.93	-7.67
46041	0.118	0.0407	5.48	0.120	2.10	1.23	-17.1	0.107	0.0393	3.92	0.136	1.91	1.19	-18.7
46207	0.129	0.0618	24.4	0.230	1.53	1.15	-10.1	0.128	0.0612	22.3	0.230	1.51	1.14	-12.2
46204	0.129	0.0975	26.7	0.575	1.17	1.31	-44.2	0.124	0.0995	26.6	0.645	1.13	1.34	-44.3
46206	0.136	0.0680	149	0.251	1.23	1.31	26.5	0.122	0.0640	144	0.277	1.11	1.23	21.2
46132	0.142	0.0443	163	0.0976	1.92	2.58	21.4	0.140	0.0431	162	0.0952	1.89	2.51	19.7
46088	0.397	0.0637	57.6	0.0258	0.997	1.31	-0.309	0.399	0.0586	57.9	0.0216	1.00	1.21	-0.0320
HS	0.395	0.0312	176	0.00625	1.02	1.33	-0.220	0.391	0.0259	176	0.00437	1.01	1.10	-0.131
RS	0.501	0.0444	172	0.00785	0.973	1.08	-0.637	0.509	0.0458	173	0.00811	0.988	1.11	-0.255
Average				0.140	1.34	1.41	-1.95				0.152	1.24	1.32	-2.90
Standard error of the sample				0.160	0.398	0.461	18.2				0.180	0.357	0.451	17.4

Table 3.9 Continued.

(b)

	No Wind				**MM5**						
Station	$\lambda_{1,nw}^{0.5}$	$\lambda_{2,nw}^{0.5}$	$\theta_{p,nw}$	$\lambda_{2,nw} / \lambda_{1,nw}$	$\lambda_1^{0.5}$	$\lambda_2^{0.5}$	θ_p	$\lambda_{2,d} / \lambda_{1,d}$	$\lambda_1^{0.5}/\lambda_{1,nw}^{0.5}$	$\lambda_2^{0.5}/\lambda_{2,nw}^{0.5}$	θ_p-$\theta_{p,nw}$
46146	0.0636	0.0242	136	0.144	0.152	0.0701	157	0.213	2.38	2.90	21.6
46131	0.251	0.0337	154	0.0181	0.251	0.0383	154	0.0233	1.00	1.14	-0.0436
46087	0.391	0.106	109	0.0733	0.400	0.116	109	0.0839	1.02	1.10	0.781
46029	0.0550	0.0118	39.6	0.0462	0.109	0.0365	31.1	0.113	1.97	3.09	-8.50
46041	0.0445	0.0324	40.6	0.532	0.142	0.0460	8.19	0.105	3.19	1.42	-32.4
46207	0.0791	0.0355	45.2	0.202	0.144	0.0562	37.9	0.152	1.82	1.58	-7.29
46204	0.104	0.0588	66.8	0.319	0.135	0.0802	35.0	0.353	1.30	1.36	-31.8
46206	0.0671	0.0459	139	0.468	0.173	0.0762	163	0.195	2.57	1.66	24.0
46132	0.0322	0.0194	154	0.365	0.147	0.0414	180	0.0794	4.57	2.13	25.5
46088	0.390	0.0652	60.9	0.0279	0.395	0.0823	58.8	0.0434	1.01	1.26	-2.07
HS	0.421	0.0226	175	0.00287	0.427	0.0297	174	0.00484	1.01	1.32	-1.09
RS	0.421	0.0103	167	0.000597	0.418	0.0120	167	0.000816	0.994	1.16	-0.204
Average				0.183				0.114	1.91	1.68	-0.966
Standard error of the sample				0.192				0.102	1.12	0.679	18.8

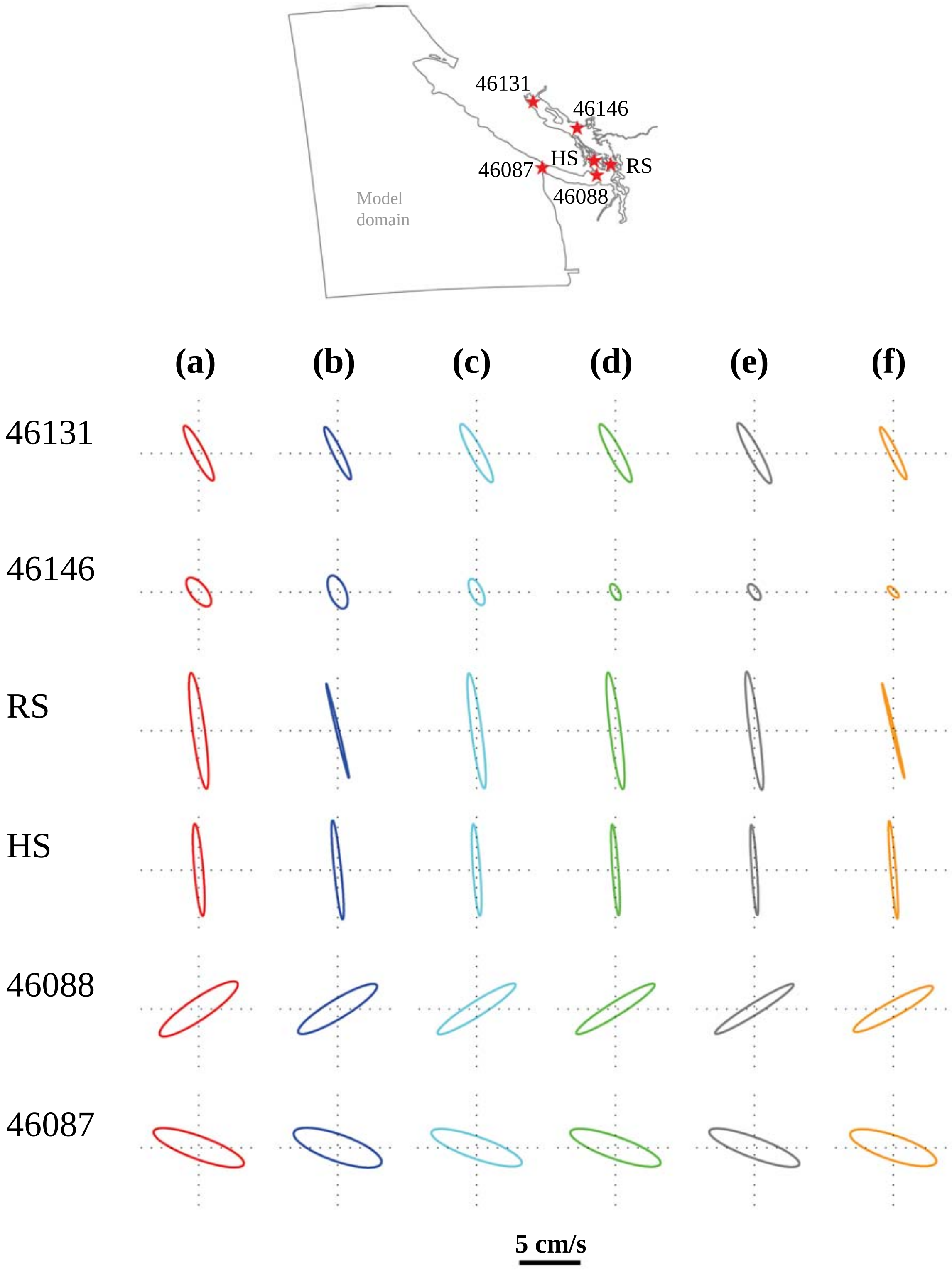

Figure 3.30 Principal axes of surface currents for each experiment **(a)** MM5 ELM (▬), **(b)** MM5 UWM (▬), **(c)** ETA ELM (▬), **(d)** NARR ELM (▬), **(e)** no wind ELM (▬), and **(f)** no wind UWM (▬) at buoy locations.

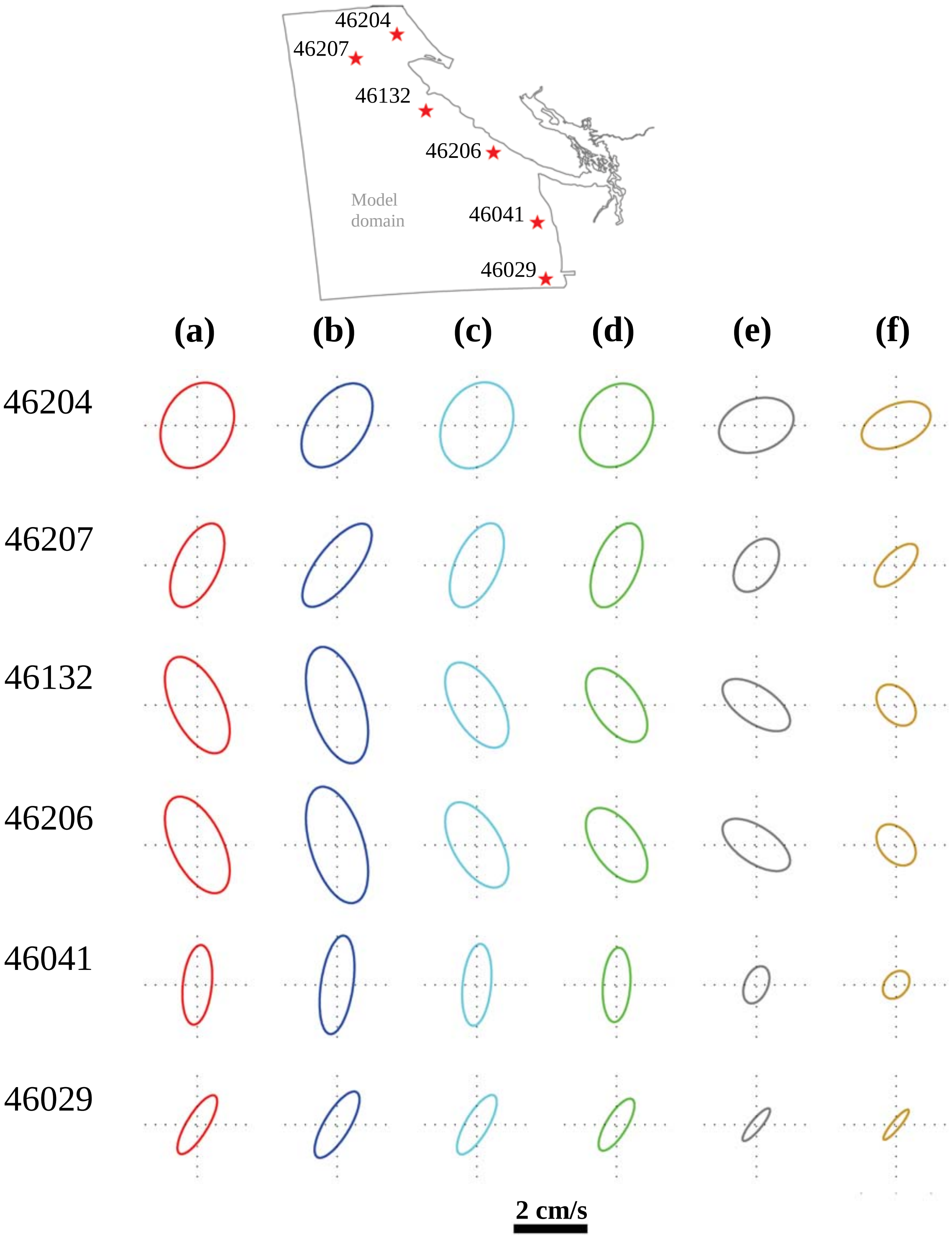

Figure 3.30 Continued.

CHAPTER 4

FINAL CONSIDERATIONS

4.1 Synthesis and conclusions

The modeling framework of a coastal margin observatory for the Columbia River (CORIE [1-3]) was developed to increase the understanding of the Columbia River estuary and plume circulation and has recently been adapted to other estuaries in the Pacific Northwest and southern British Columbia [4], including the Fraser Region presented in Chapter 3 of this thesis. Within the context of modeling, it is important to understand the implications of the many choices of numerical methods, forcings, and input parameters. The first and second of these choices are investigated in this study through model experiments of the Columbia River under the winter conditions of 1990-1991 (Chapter 2) and the Fraser River for the summer of 2005 (Chapter 3). An Upwind Method (UWM, Section 1.4.3) and an Eulerian-Lagrangian Method (ELM, Section 1.4.2) are used to solve for the advection of salt and heat (the heat exchange module is implemented within UWM SELFE only) within the SELFE model [5]; differences of modeled plume formation using forcings from three atmospheric models (Section 1.4.4) and a reference case without wind are also evaluated (Chapter 3).

Several conclusions were similar for both the Columbia and Fraser River experiments. In particular, the superior ability of UWM to simulate large river plume salinities compared with the ELM was demonstrated (Section 2.5.2 and Section 3.5.2.2). The UWM produced smaller and saltier plumes than the ELM (Figures 2.15, p. 52 and 3.17, p. 138) and comparisons with observed values indicated that the UWM results were more realistic than those yielded by the ELM. The accuracy of backtracking and interpolation for ELM algorithms influences mass conservation [6], whereas mass is always conserved in UWM. Therefore, it is believed that mass conservation is crucial in correctly simulating the plume dynamics. Model velocities were different, depending on the advection algorithm used (Section 2.5.4 and Section 3.5.3.2). The UWM yielded less bias in direction with respect to measured currents than the ELM (for the Columbia River experiments, Chapter 2). However, the minimal differences in computed water elevations for each experiment using respective algorithms were primarily attributed to improperly adjusted bottom drag coefficients, not the numerical method used for transport. For the Fraser River simulations, it has also been shown (Section 3.5.1) that an improved tidal boundary condition for the northern Strait of Georgia should improve elevation results.

From Chapter 3, NARR winds were weaker within the Strait of Georgia than either the MM5 or ETA winds. MM5 were the strongest of the three and, in fact, were stronger than the measured winds near the mouth of the Fraser River. Consequently, vertical mixing was greater when using the MM5 and ETA winds. This was particularly apparent during the wind event of September 9, 2005 (Figure 3.23, p. 142). This effect caused the MM5 winds to produce the smallest and saltiest plumes of the wind forcings evaluated. However, the influence of the advection algorithm overshadowed that of the different wind forcings.

4.2 Contributions

Four main contributions have been made to the modeling of large river plume systems in the Pacific Northwest and southern British Columbia through the experiments and analyses. First, the most extensive quantitative validation of two CORIE databases (DB13 and DB14) for the wintertime Columbia River plume (Chapter 2) has been performed utilizing field data from a study during 1990-1991 [7]. Second, the CORIE modeling framework was extended to the Fraser River region through hindcast simulations presented in Chapter 3 and forecast simulations using the National Estuarine Forecasting System (NEFS [4]). Third, the assessment of numerical weather models as inputs to coastal ocean models of the Pacific Northwest and southern British Columbia was furthered from the analysis of [8]. In particular, the impact of using different winds for such simulations was highlighted by the Fraser River experiments. Finally, the use of UWM SELFE was shown to improve simulation results for large river plumes compared with the results of ELM SELFE.

4.3 Implications

The implications of this research support the continued use and investigation of UWM SELFE for the Columbia and Fraser Rivers. Recent increases in the efficiency of UWM SELFE [9] will allow for its application to simulations with larger domains and higher resolutions. Additional investigations should focus on improving both model velocities and the representation of water elevations through the calibration of model parameters and boundary conditions. Attention should be given to improvement of the Fraser River elevations, which can be accomplished with a better boundary condition (Section 3.5.1). Finally, a coupling of the Columbia and Fraser River model domains can be explored in future studies to better understand the interactions between these two systems, such as the winter flow of lower salinity Columbia River water into Juan de Fuca Strait highlighted by [10]. In fact, initial efforts at coupling these domains have begun to further understand the presence of fresh water north of the Columbia River mouth during the summer of 2006 [9].

4.4 References

1. Baptista, A.M., *Environmental observation and forecasting systems.*, in *Encyclopedia of Physical Science and Technology*, R.A. Meyers, Editor. New York: Academic Press, 2002. 565-581.

2. Baptista, A.M., Y.L. Zhang, A. Chawla, M. Zulauf, C. Seaton, III E.P. Myers, J. Kindle, M. Wilkin, M. Burla, and P.J. Turner, *A cross-scale model for 3D baroclinic circulation in estuary-plume-shelf systems: II. Application to the Columbia River.* Continental Shelf Research, 2005. **25**: 935-972.

3. Coastal Margin Observatory for the Columbia River (CORIE), www.ccalmr.ogi.edu/CORIE, [Viewed July 2006]

4. CCALMR, NEFS/NANOOS Rover, http://nefs.ccalmr.ogi.edu, [Viewed July 2006]

5. Zhang, Y. and A.M. Baptista, *A semi-implicit Eulerian-Lagrangian finite-element model for cross-scale ocean circulation, with hybrid vertical coordinates.* International Journal for Numerical Methods in Fluids, in-review.

6. Oliveira, A. and A.M. Baptista, *On the role of tracking on Eulerian-Lagrangian solutions of the transport equation.* Advances in Water Resources, 1998. **21**: 539-554.

7. Hickey, B.M., L.J. Pietrafesa, D.A. Jay, and W.C. Boicourt, *The Columbia River plume study: Subtidal variability in the velocity and salinity fields.* Journal of Geophysical Research, 1998. **103**(C5): 10,339-10,368.

8. Tinis, S.W., R.E. Thomson, C.F. Mass, and B.M. Hickey, *Comparison of MM5 and Meteorological Buoy Winds from British Columbia to Northern California.* Atmosphere-Ocean, 2006. **44**(1).

9. Zhang, Y. of Oregon Health & Science University, *Personal communication.* 2006.

10. Masson, D., *Seasonal water mass analysis for the Straits of Juan de Fuca and Georgia.* Atmosphere-Ocean, 2006. **44**(1): 1-15.

APPENDIX

A.1 Distance in the complex plane

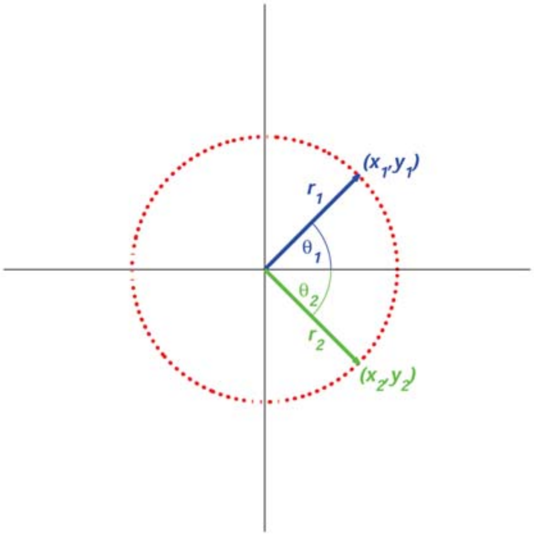

Figure A.1 Example of the phase (θ) and amplitude (r) for a single harmonic constituent for two separate results plotted as phasors in the complex plane.

The distance between two phasor representations of a given harmonic constituent of tidal elevations (Figure A.1) may be computed to evaluate the similarity between the two representations. This method is used for evaluating the ability model results to represent the harmonics of an observed time series of water elevations. The distance is given by the familiar equation A.1.

$$D = \sqrt{\left[\left(x_2 - x_1\right)^2 + \left(y_2 - y_1\right)^2\right]} \qquad \text{(A.1)}$$

The Cartesian coordinates (x_1,y_1) and (x_2,y_2) of a complex number are found using the Polar coordinate relationships

$x = r\cos\left(\theta\right)$

and

$y = ir\sin\left(\theta\right)$,

where r is taken to be the amplitude and θ the phase of a given constituent. Substituting the Polar coordinate representations into equation A.1 yields the equation (A.2) for distance in the complex plane.

$$D = \sqrt{\left[\left(r_2\cos\left(\theta_2\right) - r_1\cos\left(\theta_1\right)\right)^2 + \left(ir_2\sin\left(\theta_2\right) - ir_1\sin\left(\theta_1\right)\right)^2\right]} \tag{A.2}$$

By factoring $-i$ from the second difference, equation A.2 may be written more simply as

$$D = \sqrt{\left[\left(r_2\cos\left(\theta_2\right) - r_1\cos\left(\theta_1\right)\right)^2 + \left(r_2\sin\left(\theta_2\right) - r_1\sin\left(\theta_1\right)\right)^2\right]}.$$

A.2 Principal axes

Principal axes [1] may be computed to asses the magnitude and direction of variance for time series of vector quantities. Using this form of analysis, the magnitudes of the major (λ_1) and minor (λ_2) axes lie in the directions of the maximum (θ_p) and minimum variance for the vector time series. The summation of the major and minor axes yields the total variance. Computation of these values is achieved by finding the eigenvalues which satisfy the covariance matrix comprised of the zero mean components of the vector as in [1] which may be solved for as such

$$U' = (u_1 - \overline{u_1}, u_2 - \overline{u_2}) = (u_1', u_2')$$

$$\det\left|C - \lambda I\right| = \det\begin{vmatrix} \overline{u_1'^2} - \lambda & \overline{u_1'u_2'} \\ \overline{u_2'u_1'} & \overline{u_2'^2} - \lambda \end{vmatrix} = 0$$

$$\lambda_1 = \tfrac{1}{2}\left\{\left(\overline{u_1'^2} + \overline{u_2'^2}\right) + \left[\left(\overline{u_1'^2} - \overline{u_2'^2}\right)^2 + 4\left(\overline{u_1'u_2'}\right)^2\right]^{\frac{1}{2}}\right\}$$

and

$$\lambda_2 = \tfrac{1}{2}\left\{\left(\overline{u_1'^2} + \overline{u_2'^2}\right) - \left[\left(\overline{u_1'^2} - \overline{u_2'^2}\right)^2 + 4\left(\overline{u_1'u_2'}\right)^2\right]^{\frac{1}{2}}\right\}.$$

The principal direction is found by

$$\theta_p = \tfrac{1}{2}\,\mathrm{atan2}\left(2\overline{u_1'u_2'}, \overline{u_1'^2} - \overline{u_2'^2}\right).$$

Within the context of the research presented in this thesis, we compute principal axes to quantify the amount of observed variability represented by a given wind or hydrodynamic model, for either wind or water velocity fields respectively. Within the body of the thesis, the square root of the principal axes variance, or standard deviation, are reported for consistency of units between this metric and the velocities, and denoted in the tables as $\lambda_1^{0.5}$ and $\lambda_2^{0.5}$. For visualization, we plot the ellipses in a geographic reference. As an example, the time series (Figure A.2) and principal axes (Figure A.3) are shown for observed and NARR modeled winds at the buoy location 46010 (Figure 2.4).

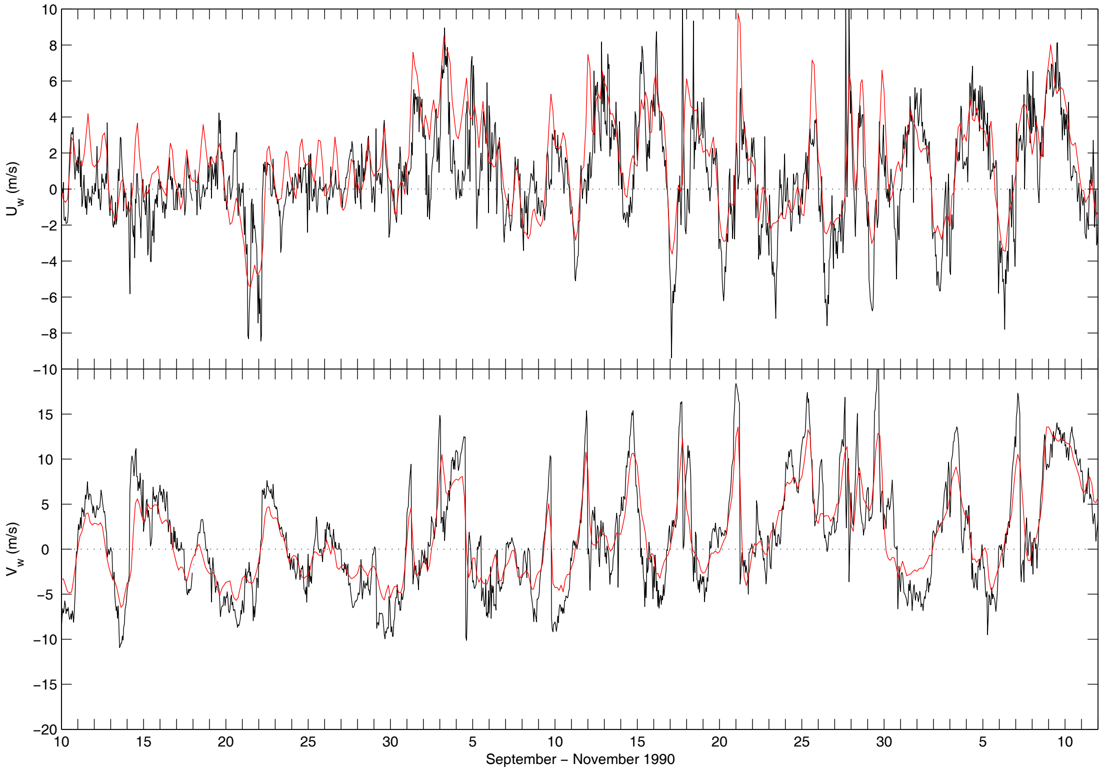

Figure A.2 Time series of the u and v vector components of observed (▬) and NARR modeled (▬) winds for buoy 46010.

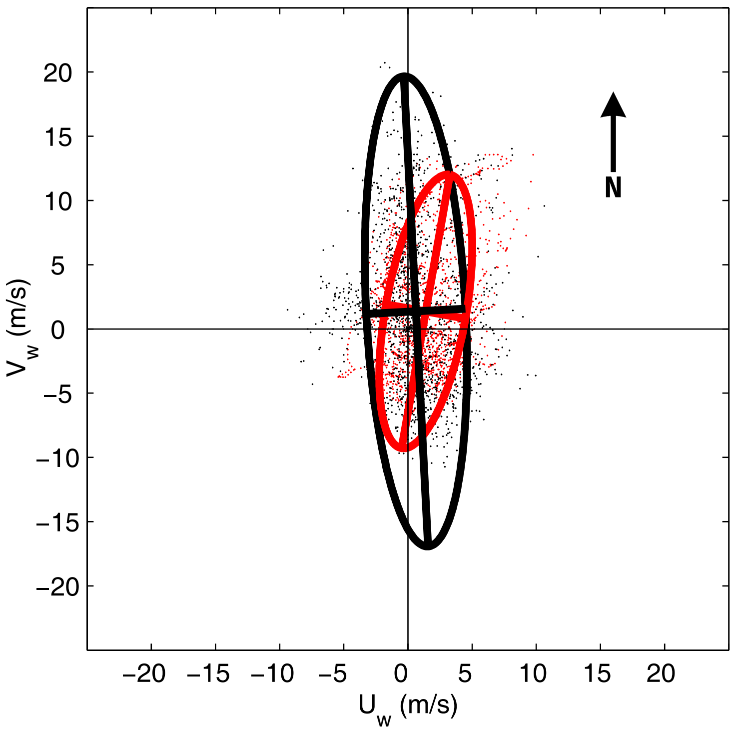

Figure A.3 Observed (●) and NARR modeled (●) u and v vector components and the respective principal axes shown as variance ellipses (m^2/s^2).

The ratio of the minor axis to the major axis for a principal ellipse provides a measure of the degree of polarization for the ellipse [2]. As the degree of polarization approaches zero, the variance is rectilinear; this is also to say that the major axis variance will approach the total variance. Conversely, as the degree of polarization approaches 1, the variance is highly polarized, indicating that the magnitudes of major and minor axes variances are similar.

A.3 References

1. Emery, W.J. and R.E. Thomson, *Data Analysis Methods in Physical Oceanography*. Amsterdam: Pergamon Press, 2001.
2. Tinis, S.W., R.E. Thomson, C.F. Mass, and B.M. Hickey, *Comparison of MM5 and Meteorological Buoy Winds from British Columbia to Northern California.* Atmosphere-Ocean, 2006. **44**(1).

BIOGRAPHICAL SKETCH

Ryan Kilgren was born in Marshall, Michigan on August 1, 1980. His passion for water related activities, science, and service oriented careers was fostered from an early age through the guidance of family and Marshall Middle and High School teachers. This exposure provided him motivation to obtain a Bachelors of Science in Environmental Engineering from Michigan Technological University in 2003, graduating *summa cum laude*. He began his studies at the OGI School of Science & Engineering at Oregon Health & Science University in September of 2003 in Portland, Oregon. His opportunity to perform research with Dr. António M. Baptista has been both challenging and rewarding; and he is very thankful for this experience. He was awarded his Master of Science degree in Environmental Science and Engineering in October of 2006.